

INAUGURAL – DISSERTATION

zur
Erlangung der Doktorwürde
der
Naturwissenschaftlich - Mathematischen
Gesamtfakultät
der
Ruprecht - Karls - Universität
Heidelberg

vorgelegt von
Dipl. Phys. Kai Hebestreit
aus Braunschweig

Tag der mündlichen Prüfung: 25. April 2001

Halogenoxide in der planetaren Grenzschicht mittlerer Breiten

Gutachter: Prof. Dr. Ulrich Platt
Prof. Dr. Frank Arnold

Dissertation
submitted to the
Combined Faculties for the Natural Science and for Mathematics
of the Ruperto Carola University of
Heidelberg, Germany
for the degree of
Doctor of Natural Science

Halogen Oxides
in the
Mid-Latitudinal Planetary Boundary Layer

presented by:

Diplom-Physicist: Kai Hebestreit
born in: Braunschweig

Heidelberg, April 25, 2001

Referees: Prof. Dr. Ulrich Platt
Prof. Dr. Frank Arnold

Halogenoxide in der planetaren Grenzschicht mittlerer Breiten

Die Bedeutung reaktiver Halogenverbindungen (RHS) in der Troposphäre ist durch plötzlich auftretende, sehr schnell ablaufende Ozoneinbrüche während des polaren Sonnenaufgangs dokumentiert. Ob RHS jedoch auch in mittleren Breiten signifikante Auswirkungen auf die Chemie der Troposphäre haben, war bisher unklar, da außerhalb der Polarregionen noch keine Halogenoxide nachgewiesen werden konnten. Im Verlauf der vier im Rahmen dieser Arbeit durchgeführten Messkampagnen gelang es erstmalig, Halogenoxide in der planetaren Grenzschicht (PBL) mittlerer Breiten nachzuweisen und ihren eindeutigen Einfluss aufzuzeigen.

An der westirischen Atlantikküste wurden Jodoxide (IO und OIO) in der marinen PBL nachgewiesen und von Makroalgen emittierte, kurzlebige jodierte Kohlenwasserstoffe als primäre Quelle reaktiven Jods (re-I) identifiziert. Es zeigte sich eine deutliche Abhängigkeit der IO Konzentration sowohl von der solaren Einstrahlung als auch vom Tidenhub, während ein Zusammenhang mit der NO_x Belastung nicht beobachtet wurde. Ein direkter Einfluss von re-I auf die Ozonkonzentration wurde nicht nachgewiesen. Dies liegt vermutlich an der hohen natürlichen Variabilität dieses Parameters, denn Modellberechnungen belegen, dass die Ozonzerstörung durch re-I die Größenordnung anderer Ozonverlustprozesse, wie z.B. Deposition, besitzt und deshalb nicht vernachlässigt werden darf.

Während der Messkampagne am Toten Meer gelang es, BrO in der PBL außerhalb der Polarregionen zu detektieren. Seine ozonzerstörende Wirkung spiegelte sich in periodischen Tageszyklen wider, deren Regelmäßigkeit zum einen durch die Topographie des Toten-Meer-Grabens, zum anderen durch die Meteorologie des Messortes bedingt war. Die Freisetzung reaktiven Broms aus Salzablagerungen entlang des Toten Meeres konnte als primäre Bromquelle identifiziert werden.

Halogen Oxides in the Mid-Latitudinal Planetary Boundary Layer

The importance of reactive halogen species (RHS) in the troposphere has been revealed when they were found to cause sudden, rapid ozone depletion during the polar sunrise. However, whether or not RHS play a significant part in mid-latitude tropospheric chemistry was still unclear, as no halogen oxides had been detected outside the polar regions so far. In the course of the four measurement campaigns carried out within the framework of this thesis the first detection of halogen oxides in the mid-latitude planetary boundary layer (PBL) succeeded, and their impact could be clearly demonstrated.

At the Western Irish Atlantic coast iodine oxides (IO and OIO) have been detected in the marine PBL, and short-lived iodinated hydrocarbons released by macroalgae were found to act as the primary source of reactive iodine (re-I). IO turned out to depend closely on solar radiation and tidal height, but not on NO_x concentration. A direct effect of re-I on ozone has not been observed, possibly owing to the natural variability of this parameter. Model calculations indicate that the overall influence of re-I is comparable to known ozone loss processes, such as ozone deposition, and should therefore not be neglected.

During a measurement campaign at the Dead Sea the detection of BrO in the PBL outside the polar regions succeeded. Its ozone-destroying effect was reflected by recurring diurnal cycles, the periodicity of which is due to the topography of the Dead Sea Valley on the one hand and to the meteorology of this region on the other hand. The release of reactive bromine from sea salt deposits along the Dead Sea has been identified as the primary source of BrO.

Table of contents

Halogen Oxides in the Mid-Latitudinal Planetary Boundary Layer

Chapter 1	Introduction	1
Chapter 2	Halogen Chemistry in the Troposphere	5
2.1	Overview of the role of Halogens in the Troposphere	5
2.1.1	The Main Reaction Patterns of RHS	6
2.1.2	Tropospheric Sources of RHS	11
2.1.3	Tropospheric Sinks of RHS	14
2.1.4	Influence of RHS on Tropospheric NO _x and HO _x Chemistry	15
2.2	Reactive Bromine in the Troposphere	16
2.2.1	Historical Overview	16
2.2.2	Main Reactions and Release of Reactive Bromine	17
2.2.3	Sinks of Reactive Bromine	19
2.3	Reactive Iodine in the Troposphere	20
2.3.1	Primary Sources of Reactive Iodine	21
2.3.2	Main Reactions of Reactive Iodine	21
2.3.3	Sinks of Reactive Iodine	22
Chapter 3	The DOAS Technique	29
3.1	Absorption of Light	30
3.1.1	The Basics of Absorption Spectroscopy	30
3.1.2	Spectroscopy in the Atmosphere	31
3.1.3	The Basics of the DOAS Technique	34
3.1.4	Principle of Evaluation of DOAS Spectra	36
3.2	The Instrumental Set-up	40
3.2.1	Light Sources	42
3.2.2	The Telescopes	43
3.2.3	The Quartz-Fibre Mode Mixer	44
3.2.4	The Spectrographs	44
3.2.5	The Detector Systems	45

Chapter 4	Field Observations and Results	49
4.1	The Weybourne Campaign 1996	50
4.1.1	The Weybourne Measurement Site	50
4.1.2	The Meteorological Conditions at WB96	51
4.1.3	Results of the Weybourne Campaign	52
4.2	The Mace Head Campaign 1997	55
4.2.1	The Mace Head Measurement Site	55
4.2.2	DOAS Light Path at Mace Head	58
4.2.3	The Meteorological Conditions at MH97	59
4.2.4	The DOAS Measurement Routine of MH97	61
4.2.5	Results of the Mace Head Campaign 1997	62
4.3	The Mace Head Campaign 1998	67
4.3.1	The Meteorological Conditions at MH98	68
4.3.2	The DOAS Measurement Routine of MH98	70
4.3.3	Wavelength calibration	71
4.3.4	Recording and Convolution of Reference Spectra	71
4.3.5	Evaluation of the IO Wavelength Region	74
4.3.6	Evaluation of the BrO Wavelength Region	77
4.3.7	Evaluation of the OIO Wavelength Region	78
4.3.8	Overview of the DOAS Measurements of MH98	79
4.3.9	Non-DOAS Measurements of MH98	83
4.4	Results of MH98: Iodine Oxide in the Marine Planetary Boundary Layer	86
4.4.1	Data Processing	86
4.4.2	Potential Precursors of Iodine Oxides	88
4.4.3	IO Dependence on its Precursors and other Parameters	97
4.4.4	Iodine – Ozone Interactions at Mace Head, a Modelling Study	104
4.4.5	Influence of Iodine Oxide on the Leighton Ratio	109
4.4.6	IO - NO ₂ Interactions	116
4.4.7	The Formation of OIO	121
4.5	The Dead Sea Campaign 1997	129
4.5.1	The Dead Sea Measurement Site	129
4.5.2	Chemical Composition of the Dead Sea Water	131
4.5.3	The Meteorological Conditions at the Dead Sea	132
4.5.4	The DOAS Measurements of DS97	135
4.5.5	Non-DOAS Measurements of DS97	138
4.6	Results of DS97: Bromine Oxide – Ozone Interactions at the Dead Sea	141
4.6.1	Average Daily Cycles BrO and Ozone	141
4.6.2	Identification of BrO as the O ₃ -Destroying Agent	143
4.6.3	Identification of the Sources of Reactive Bromine at the Dead Sea	146
4.6.4	Modelled Description of the BrO and O ₃ Observations of DS 97	150
4.6.5	Bromocarbons at the Dead Sea	154
4.6.6	Total Atmospheric Bromine and Chlorine in the Dead Sea Valley	155
4.6.7	Subsequent Air-Plane Study: The Extent of the Ozone Destruction Phenomenon	156
Chapter 5	Summary and Outlook	159
5.1	Mace Head	159
5.2	Dead Sea	160
5.3	Outlook	161
Chapter 6	References	163
Chapter 7	Appendix	i
(A 1)	PF vs. SR and UVA	ii
(A 2)	Individual calculation of average values	iii
(A 3)	Reactions of iodine compounds in the BL included to the model	iv
(A 4)	Reactions of Bromine Compounds in the BL Included in the Chemical Box Model	v

Chapter 1

Introduction

Only in the course of the last three decades it has become known that halogen species play an important part in the atmosphere. In the 1970s it was shown that chlorine could be involved in a catalytic cycle resulting in ozone (O₃) destruction [Stolarski and Cicerone, 1974]. Another important step was the identification of chlorofluorocarbons [Molina and Rowland, 1974] and bromocarbons [Wofsy *et al.*, 1975] as major sources of ozone-destroying halogens in the stratosphere¹. It became obvious that the model predictions underestimated the real influence of halogens on the ozone layer when the ‘polar stratospheric ozone hole’ - the temporary depletion of the stratospheric ozone layer after polar sunrise - was described by Farman *et al.* [1985] for the first time. Field observations, laboratory and modelling studies showed that halogen species are involved in the catalytic cycles responsible for the ozone destruction [Crutzen and Arnold, 1986; McElroy *et al.*, 1986; Solomon *et al.*, 1986; Molina and Molina, 1987].

The typical O₃ mixing ratio² in the maximum of the stratospheric ozone layer at 25 – 30 km altitude is of the order of 6 - 8 ppm corresponding to a concentration of $4 - 5 \times 10^{12} \text{ molec cm}^{-3}$ [WMO, 1998]. Due to catalytic reaction cycles involving *reactive*

¹ The Earth’s atmosphere is characterised by variations of temperature and pressure with height. Therefore the variation of the average temperature profile with altitude is the basis for distinguishing the layers of the atmosphere:

The *Planetary Boundary Layer* (PBL) is the lowermost part of the *Troposphere* (*see below*). It is defined as the part of the atmosphere where the air still interacts with the earth’s surface by exchanging vertical impulses. Therefore the PBL is relatively well mixed; the typical height is some 0.1 - 1 km.

The *Troposphere* extends from the earth’s surface up to the tropopause, which is at an altitude of 8 to 18 km depending on latitude and season, characterised by decreasing temperature with height and rapid vertical mixing.

The *Stratosphere* extends from the tropopause to the stratopause (~ 45 – 55 km altitude). Its temperature increases with altitude, which leads to a slow vertical mixing of this layer.

² number of molecules per absolute number of molecules in a volume, given in ppm = parts per million = 10⁻⁶; ppb = parts per billion = 10⁻⁹; ppt = parts per trillion = 10⁻¹²

halogen species, *RHS*, the stratospheric ozone concentration is temporarily reduced by in average of up to 65 % [WMO, 1998], in the ozone hole even by 100 %. The ozone layer protects the earth from harmful ultra-violet (UV) radiation, for high UV encumbrance increases the risk of skin cancer. Thus the dramatic halogen-induced decrease of by now 5 % per decade on average at mid latitudes [WMO, 1998] has caused stratospheric halogen chemistry to become a matter of public concern.

In the stratosphere *RHS* are released from mostly man-made precursors like CFCs³ that are photolysed by light in the UV region below 320 nm (e.g. *DeMore et al.* [1997]). In the troposphere these fully halogenated CFCs are photostable because the intensity of the UV sunlight reaching this lowermost layer of the atmosphere is insufficient to dissociate these molecules. For that reason fully halogenated hydrocarbons are thought to play a negligible part in the PBL chemistry.

Since the beginning of the 1980s periodical ozone depletion during springtime has also been detected in the troposphere of polar regions. During these *Low-Ozone Events (LOE)*, which may last for several hours or even days, polar boundary layer ozone decreased from background values of ~ 40 ppb ($\sim 1 \times 10^{12}$ molec cm^{-3}) to values below the detection limit [Bottenheim *et al.*, 1986; Oltmans and Komhyr, 1986]. In the late 80s *Barrie et al.* [1988] found a negative correlation of filterable bromine compounds (f-Br) and ozone mixing ratios. This was the first indication that halogen atoms, setting off reactions similar to those observed in the stratosphere, can also explain the polar tropospheric ozone loss.

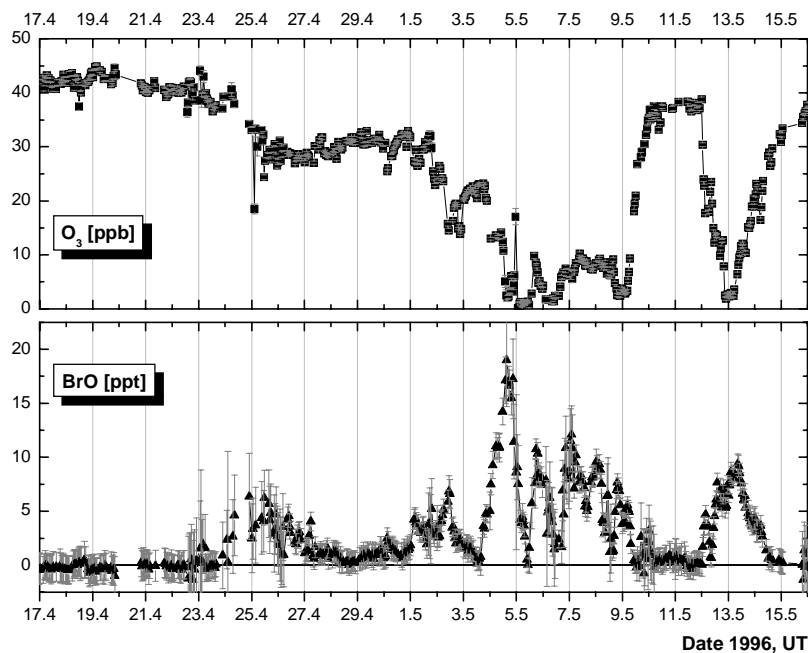


Figure 1.1 Bromine monoxide and ozone mixing ratios measured in April and May 1996 at Ny Ålesund (Spitzbergen), adapted from Tuckermann *et al.* [1997].

³ chlorofluorocarbons

Bromine monoxide (BrO) in the troposphere was first detected by *Hausmann and Platt* [1994] during a LOE in Alert, Canada, using the DOAS⁴ technique. Their measurements, which were performed during the *Polar Sunrise Experiment 1992*, confirmed the theory that BrO is the key species of LOE.

Figure 1.1 shows BrO and ozone mixing ratios measured by *Tuckermann et al.* [1997] during the ARCTOC campaign 1996 at Ny-Ålesund, Spitzbergen, using a long path DOAS instrument. During further ground-based investigations in the Arctic [*Platt and Lehrer*, 1997; *Martinez-Harder*, 1998] and Antarctic [*Murayama et al.*, 1992; *Kreher et al.*, 1997; *Wessel et al.*, 1998] and via world wide satellite mapping [*Richter et al.*, 1998; *Wagner and Platt*, 1998] polar LOE correlated with high tropospheric BrO mixing ratios have been detected several times.

The phenomenon of LOE, also described as *polar tropospheric ozone hole* [*Platt*, 1999a; *Lehrer*, 2000], was first observed only in the Arctic. The question was discussed whether man-made or natural emissions are responsible for the amount of RHS in the arctic troposphere. In that remote polar area anthropogenic effects may occur due to polluted air masses from mid-latitudinal industrial regions reaching the Arctic - but not the Antarctic - in springtime [*Lehrer et al.*, 1997; *Wagenbach et al.*, 1998]. Since measurements also revealed tropospheric BrO in the Antarctic, which is in general largely free from man-made influence, it has become obvious that natural sources are responsible for the existence of halogen compounds in the polar troposphere.

Two primary natural sources of RHS have been identified so far:

1. Halogen release from sea-salt-covered surfaces via different heterogeneous mechanisms [*Fan and Jacob*, 1992; *Tang and McConnell*, 1996; *Vogt et al.*, 1996] is known as the primary source of reactive bromine species: The oxidation of sea salt halides, which are widely spread in the polar regions as salt covered (ice-) surfaces and as aerosol particles, have become well known as ‘bromine explosion’ mechanism [*Platt and Lehrer*, 1997]. This autocatalytic mechanism, which releases RHS from sea salt, was originally suggested by *Fan and Jacob* [1992] as a recycling mechanism of hypobromous acid (HOBr). The bromine explosion leads to an exponential growth in the BrO concentration, which represents a ‘chemical instability’ of the atmosphere.
2. Emissions of short-lived partly halogenated organic compounds as e.g. alkyl-halides by macroalgae are well known to photolyse in the PBL within seconds to hours, leading to reactive halogen and especially iodine compounds [*Lovelock et al.*, 1973; *Lovelock*, 1975; *Cicerone*, 1981; *Berg et al.*, 1983; *Klick and Abrahamsson*, 1992; *Schall and Heumann*, 1993; *Roehl et al.*, 1997; *Carpenter et al.*, 1999].

No successful measurements of halogen oxides had been reported from the mid-latitudinal troposphere so far. It was still unclear whether or not significant concentrations of RHS also exist outside the polar regions.

⁴ Differential Optical Absorption Spectroscopy

- ⇒ The primary aim of this thesis was to investigate the presence of RHS in the mid-latitude planetary boundary layer. As the conditions there differ from polar regions concerning the availability of salt-covered ice surfaces and the meteorological conditions, it was not clear whether one could expect halogen oxides to be present in the mid-latitude boundary layer in detectable concentrations of some ppt.
- ⇒ In the case of the detection of halogen oxide the primary sources of RHS as well as their influence on the chemistry of the mid-latitude boundary layer in general had to be investigated. Due to the differences between mid latitudes and polar regions it was not clear whether one could expect the same or other release mechanisms and effects on boundary layer chemistry.
- ⇒ Moreover it had to be analysed whether the observations made were only single events, representing the atmospheric situation at the respective site and time, or whether it was possible to interpret the measurements as valid on a regional or even global scale.

In order to clarify these questions, four measurement campaigns at three different sites were carried out between 1996 and 1998. Even at mid latitudes sea salt on the one hand and short-lived halogenated organic compounds emitted by marine algae on the other hand are regarded as potential sources of RHS. Taking into account these expected sources, the first two measurement sites were above all chosen due to their marine character, indicated by:

- ⇒ rural European background conditions, where anthropogenic emissions could be expected to be negligible.
- ⇒ sea salt, which is available in form of sea spray, aerosols or deposits on the ground.
- ⇒ macroalgae, which are expected to release halogenated hydrocarbons.

The third site stand out for

- ⇒ widely spread salt-covered surfaces.

In detail, the first field campaign relating to this thesis was carried out in autumn 1996 at the Atmospheric Observation Centre Weybourne, a semi-polluted site associated with the University of East Anglia, located at the northeast coast of England.

Two campaigns were performed at the Atmospheric Research Station of Mace Head on the western coast of Ireland in spring 1997 and in autumn 1998. This site represents European clean-air background conditions and is associated with the National University of Ireland, Galway.

The fourth campaign was carried out in co-operation with the Hebrew University of Jerusalem at the Dead Sea, Israel in late spring 1997. At this location with its unique topography – 400 m below sea level, the lowest land area on the earth's surface – expansive saltpans were expected to be an important source of RHS.

Chapter 2

Halogen Chemistry in the Troposphere

The following chapter gives an introduction to the role of halogen species in tropospheric chemistry. Halogens are the elements of the 7th column of the periodic table of elements. They are characterised by 7 electrons on the valence shell. Therefore they need to take up only one more electron to obtain inert-gas configuration. In general there are 5 halogens: Fluorine, Chlorine, Bromine, Iodine and Astatine with the chemical symbols F, Cl, Br, I and At respectively. Mostly only the first 4 elements (of which F and Cl are in a gaseous, Br is in a liquid and I is in a solid state of aggregation under standard conditions) are considered. As will be explained below, only Cl, Br and I are of importance in tropospheric chemistry.

In section 2.1 halogen chemistry in the troposphere will be described in general and the ozone destruction cycles involving halogenated species and their tropospheric sources and sinks will be dealt with. The influence of *reactive halogen species, RHS*, on NO_x and HO_x chemistry is the subject of subsection 2.1.4. After that the chemical effects of the most important tropospheric halogen species, bromine monoxide, BrO, and iodine monoxide, IO, will be recapitulated in sections 2.2 and 2.3.

2.1 Overview of the role of Halogens in the Troposphere

In field campaigns and laboratory investigations the halogen atoms X, Y and their oxide radicals⁵ XO and YO (X, Y = Cl, Br, I) were found to be the key species in the chemical mechanisms responsible for the destruction of PBL ozone [Barrie and Platt, 1997; Finlayson-Pitts et al., 1990; LeBras and Platt, 1995; Platt, 1996; Tuckermann et al., 1997; Wayne et al., 1995]. RHS comprise the halogen atoms X, their oxides XO_n, the hypohalous

⁵ Radicals are molecules or fragments of molecules with at least one free electron in the valence shell. Therefore radicals are very reactive. For further information about the part of radicals in atmospheric chemistry in general see e.g. Platt [1999a].

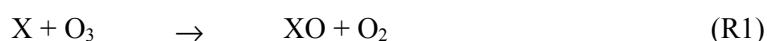
acids HOX, as well as the halogen molecules X₂ and the interhalogens⁶ XY_n. In contrast to RHS the rate coefficients of reservoir species like halogen-NO_x compounds (XNO_x) or halogen halides (HX) are comparably slow. As will be described in the next section, there are two main reaction cycles involving halogens that are destroying ozone in the PBL: Cycle A is based on the XO self- or cross-reaction, cycle B on the reaction of XO with hydroperoxyl radicals, HO₂.

A number of recent field campaigns, e.g. within the framework of the *ACSOE* and the *HALOTROP* projects (see chapter 4), were aimed at studying the influence of halogen oxides at the mid-latitudinal PBL [*Alicke et al.*, 1999; *Carpenter et al.*, 1999; *Hebestreit et al.*, 1999; *Stutz et al.*, 1999]. It has been confirmed by all these studies that RHS are indeed present in certain parts of the troposphere and the PBL.

2.1.1 The Main Reaction Patterns of RHS

The main reaction schemes of the three halogens⁷ Chlorine (Cl₂), Bromine (Br₂) and Iodine (I₂) appear to be the similar regarding tropospheric chemistry. As will be discussed later, there are differences in the rate constants and different quantum yields concerning their photochemical reaction channels (see e.g. Table 2.1). Therefore, if the reactions given are similar for the different halogens involved⁸, X and Y will be used instead of the chemical symbols Cl, Br or I. Several rate constants and photolysis frequencies of RHS, which are important with regard to the two different ozone destruction cycles involving halogens, are listed in Table 2.2.

Halogen atoms (X, Y) and their monoxides (XO, YO) are the key species in the ozone destruction cycles [*Crutzen and Arnold*, 1986; *Garcia and Solomon*, 1994; *Hausmann and Platt*, 1994; *LeBras and Platt*, 1995], by which halogen oxides are formed in reaction with ozone (see R1 and R4 below). Accordingly the most prominent reaction of halogen atoms is the reaction with ozone, followed by the photolysis of the halogen oxide molecule:



Nevertheless this sequence leads to a ‘null cycle’⁹ with respect to O₃ destruction as the atomic oxygen regenerates O₃ in the reaction with O₂ immediately:



⁶ In general, interhalogens are defined as XY_n with n as odd number and X heavier than Y.

⁷ As can be seen in Table 2.2 and will be explained below, the halogen ‘Fluorine (F)’ does not seem to be of importance in tropospheric chemistry.

⁸ The main difference is the reactivity concerning the reactions with VOC (volatile organic compounds)

⁹ Reaction sequence that shows no net chemistry but leads to a steady state of the species involved.

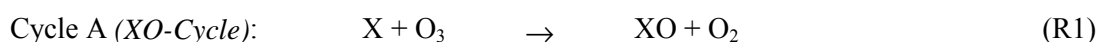
¹⁰ M notes a collision partner. Due to the atmospheric composition N₂ and O₂ are most probable.

Table 2.1 Several prominent halogen rate coefficients and photolysis rates

Halogen Retion Educt → Product		Overall Rate Constant k ($\text{molec}^{-1}\text{cm}^3\text{s}^{-1}$) or Photolysis Frequency* J (s^{-1})	Reference
BrO + BrO	Products	$k = 3.3 \times 10^{-12}$	[DeMore et al., 1997]
BrO + IO	Products	$k = 8.5 \times 10^{-11}$	[Cox et al., 1999]
BrO + HO ₂	HOBr + O ₂	$k = 2.3 \times 10^{-11}$	[DeMore et al., 1997]
BrO + ClO	Products	$k = 1.4 \times 10^{-11}$	[DeMore et al., 1997]
Br + O ₃	BrO + O ₂	$k = 1.1 \times 10^{-12}$	[DeMore et al., 1997]
BrO + hv **	Br + O ₃	$J = 0.0025$	[DeMore et al., 1997]
Br ₂ + hv	2 Br	$J = 0.02$	[Sander, 2000]
BrCl + hv	Br + Cl	$J = 0.008$	[DeMore et al., 1997]
IO + IO	Products	$k = 8.2 \times 10^{-11}$	[Cox et al., 1999]
IO + HO ₂	HOI + O ₂	$k = 8.4 \times 10^{-11}$	[DeMore et al., 1997]
I + O ₃	IO + O ₂	$k = 1.1 \times 10^{-12}$	[DeMore et al., 1997]
IO + hv **	I + O ₃	$J = 0.25$	[Lazlo et al., 1995]
I ₂ + hv	I	$J = 0.13$	[Tellinghuisen, 1973]
IO + ClO	Products	$k = 1.3 \times 10^{-11}$	[DeMore et al., 1997]
IBr + hv	I + Br	$J = 0.05$	[Seery and Britton, 1964]
ClO + ClO	Products	$k = 1.3 \times 10^{-14}$	[DeMore et al., 1997]
Cl + O ₃	ClO + O ₂	$k = 1.4 \times 10^{-11}$	[DeMore et al., 1997]
ClO + HO ₂	HOCl + O ₂	$k = 5.5 \times 10^{-12}$	[DeMore et al., 1997]
ClO + hv **	Cl + O ₃	$J = 1.4 \times 10^{-5}$	[Röth et al., 1996]

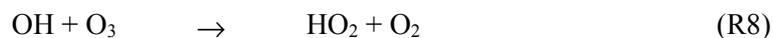
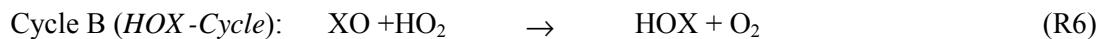
* Values for 45° SZA adapted from [Sander, 2000] ** followed by the reaction of O with O₂

If a self- or cross-reaction of XO occurs instead of the photolysis, two ozone molecules are converted into three dioxide molecules with no net loss of RHS. This corresponds to the catalytic destruction of ozone. Assuming a concentration of $\sim 10^7 \text{ molec cm}^{-3}$ of XO, the tropospheric lifetime of halogen oxides concerning photolysis and interhalogen oxide reactions is of the same order of magnitude, as can be seen from Table 2.1.



The most probable product of R5 is $\text{X} + \text{Y} + \text{O}_2$. Therefore the halogen atoms X and Y are recycled and do not get lost from the cycle. As long as the ozone mixing ratio is high enough ($40 \text{ ppb} > [\text{O}_3] > 1 \text{ ppb}$) R1 and R4 are fast (the time constant for $\text{X} \rightarrow \text{XO}$ is of the order of 0.1 to 1 seconds for $\text{X} = \text{Cl}, \text{I}$ or Br) compared with the halogen self- or cross-reaction R5. Therefore R5 is the rate-determining step of cycle A. Depending on the different rate constants (see e.g. Table 2.1 or the review of Atkinson et al. [1997] or DeMore et al. [1997]), the resulting (tropospheric) ozone destruction potential increases from chlorine reactions via bromine to reactions involving iodine monoxide.

Cycle B is initiated by the reaction of XO with HO₂, the hydroperoxyl radical, forming hypohalous acid HOX, with $k_{R6} = 0.7, 4.5, \text{ and } 8.4 \times 10^{-11} \text{ cm}^3 \text{ molec}^{-1} \text{ s}^{-1}$ for X = Cl, Br, I. HOX may be photolysed again (R7), leading to halogen atoms, which have a high affinity to react with ozone (R1). The second product, the hydroxyl radical OH, can react with ozone, too. Thereby HO₂ is recycled and ozone is converted into O₂. The net reaction shows that XO and HO₂ are recycled while two ozone molecules are converted into three oxygen molecules.



Therefore, taking into account only the relevant ozone levels above 1 ppb, the ozone destruction rate is independent of the ozone concentration. Presuming that halogen atoms react only with ozone, an ozone reduction rate of

$$-\frac{d[\text{O}_3]}{dt} = 2 \left\{ \sum_{i,j} k_{X_i\text{O}+X_j\text{O}} [\text{X}_i\text{O}] [\text{X}_j\text{O}] \right\} + \sum_i k_{X_i\text{O}+\text{HO}_2} [\text{X}_i\text{O}] [\text{HO}_2] \quad \text{Equ 1}$$

can be calculated with $i, j \leq 3$, considering Cl, Br and I. In this equation the first summand considers the halogen cross reactions of cycle A, while the second represents the destruction via cycle B.

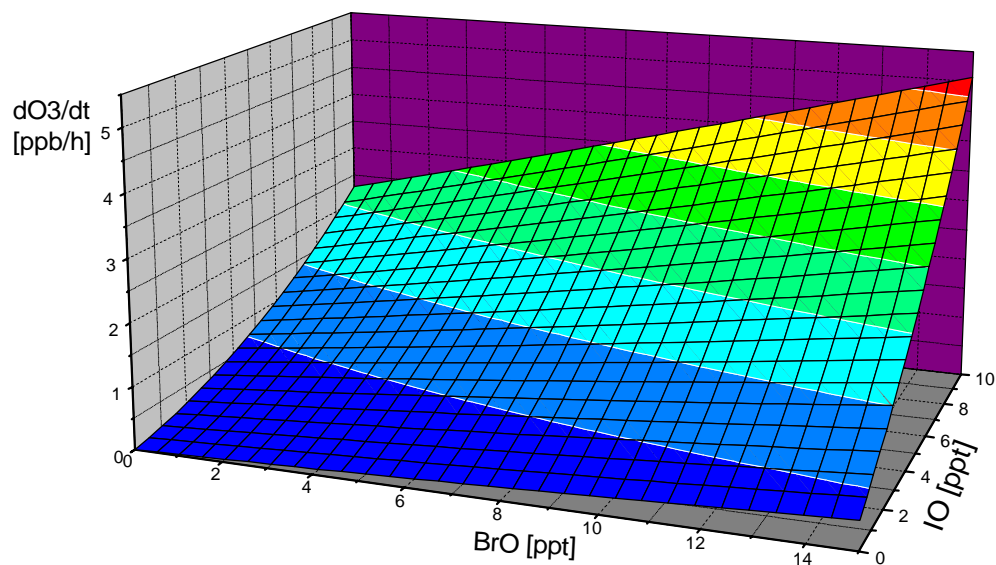


Figure 2.1 Ozone depletion rates calculated according to Equ 1 in consideration of 10 ppt HO₂ for varying IO and BrO mixing ratios.

Figure 2.1 shows the ozone depletion per hour calculated according to Equ 1 for various BrO and IO concentrations (case $i,j = 2$), assuming an HO₂ mixing ratio of 10 ppt. It is important to note that all product channels of the XO reactions were assumed to lead to O₃ destruction. Therefore the given values are upper limits of dO_3/dt . However, Figure 2.1 indicates that 4 ppt of BrO are needed to destroy as much ozone as is destroyed by only 1 ppt of IO. The branching ratio of the IO + XO reactions will be discussed in section 2.3.3.

Apart from its importance for the destruction of ozone the reaction of halogen oxides with hydroperoxyl radicals (R6) followed by the photolysis of the product from this reaction, the hypohalous acids HOX (R7), also have a strong influence on the ratio of OH/HO₂ [Stutz *et al.*, 1999], as will be discussed in section 4.4.4.

Analogous to R6, XO also reacts with organic peroxy radicals (RO₂, R = organic group) as e.g. the methyl peroxy radical, CH₃O₂, instead of HO₂. It has been shown in laboratory experiments that this reaction occurs for X = Br as well [Aranda *et al.*, 1997]. HOBr was formed in about 80 % of the reactions:

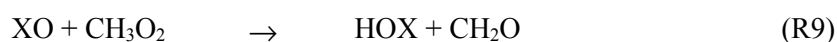


Table 2.2 Rate constants and reaction frequencies of halogen atoms (X) with different reaction partners (RP): different hydrocarbons (RH), H₂O, HO₂, and O₃.

Halogen X	RP	K_{X+RH}^a (k_{X+RH}) ($cm^3 s^{-1}$)	typ. Trace gas conc. (cm^{-3})	$R_{RH}=k_{X+RH}$ (s^{-1})	$\frac{R_{O_3}}{R_{O_3} + \sum R_{RH}}$	$\frac{R_{O_3}}{\sum R_{RH}}$
F	H ₂ O	1.4×10^{-11}	2.0×10^{17}	2.8×10^6	3.3×10^{-6}	3×10^{-7}
	CH ₄	8.0×10^{-11}	4.0×10^{13}	3.2×10^3		
	H ₂	2.6×10^{-11}	1.2×10^{13}	312		
	HNO ₃	2.3×10^{-11}	1.0×10^{10}	23		
	O ₃	1.3×10^{-11}	7.2×10^{11}	$\Sigma R_{RH} = 2.8 \times 10^6$ 9.4		
Cl	CH ₄	1.0×10^{-13}	4.0×10^{13}	4.0	0.45	0.86
	C ₂ H ₆	5.9×10^{-11}	3.0×10^{10}	1.8		
	C ₃ H ₈	1.4×10^{-10}	1.0×10^{10}	1.4		
	CH ₂ O	7.3×10^{-11}	1.0×10^{10}	0.73		
	C ₂ H ₂	1.0×10^{-10}	1.0×10^{10}	1.0		
	C ₂ H ₄	3.0×10^{-10}	5.0×10^9	1.5		
	O ₃	1.2×10^{-11}	7.2×10^{11}	$\Sigma R_{RH} = 10$ 8.6		
Br	CH ₂ O	1.0×10^{-12}	1.0×10^{10}	0.01	0.988	41
	C ₂ H ₂	1.5×10^{-13}	1.0×10^{10}	1.5×10^{-3}		
	HO ₂	2.0×10^{-12}	1.0×10^8	2.0×10^{-4}		
	O ₃	1.2×10^{-12}	7.2×10^{11}	$\Sigma R_{RH} = 2.1 \times 10^{-2}$ 0.86		
I	HO ₂	3.8×10^{-13}	1.0×10^8	3.8×10^{-5}	0.99994	1.9×10^4
	O ₃	1.0×10^{-12}	7.2×10^{11}	0.72		

^a rate constants taken from Platt and Stutz [1998], calculated for 298 K

Ozone depletion takes place depending on the branching ratio of the reaction of halogen atoms with ozone (R1) vs. the reactions with various hydro carbons, RH (R19) or HO₂

(R20). The relative reaction rate ($R_{O_3}/(R_{O_3} + \Sigma R_{RH})$), given in column 6 of Table 2.2, indicates the different contributions of the 4 halogens to the ozone destruction. R_{RH} corresponds to the rate constant of RHS with different hydrocarbons (RH). Because of its high affinity to the reaction with water, forming HF, which will not be reconverted FO_X , Fluorine has no impact on tropospheric chemistry.

Column 7 of Table 2.2 gives the ratio of the reaction destroying ozone and the sum of the rate constants of the reactions leading to a deposition of halogens. Therefore this ratio indicates the number of ozone-destroying cycles for a halogen atom before it is deposited. This value is equivalent to the average number of ozone molecules converted to molecular oxygen per halogen atom. As can be seen clearly, bromine and especially iodine pass through many more cycles than chlorine before being deposited.

As an approximation the ratio of the halogen oxide XO to the corresponding halogen atom X is determined by the relative rates of the reactions which convert X into XO (the halogen reaction with ozone (R1) and the reaction with hydrocarbons (HC) (R19)) and back (NO reaction, self- or cross-reaction and photolysis (R2, R26)):

$$\frac{[XO]}{[X]} = \frac{[O_3] \cdot k_{X+O_3} + [HC] \cdot k_{X+HC}}{[NO] \cdot k_{XO+NO} + 2 \cdot [XO] \cdot k_{XO+XO} + [YO] \cdot k_{YO+XO} + J_{XO}} \quad \text{Equ 2}$$

Due to the fast photolysis of the IO radical the IO/I ratio is about 1 - 10 depending on NO_x and O_3 levels (e.g. [Platt and Janssen, 1995; Vogt et al., 1996]). This is significantly lower than that of the other halogens. BrO/Br and ClO/Cl are of the order of 100 and 1000 respectively [Barrie et al., 1988]. Figure 2.2 shows a schematic overview of the halogen chemistry of the troposphere adapted from Platt and Janssen [1995].

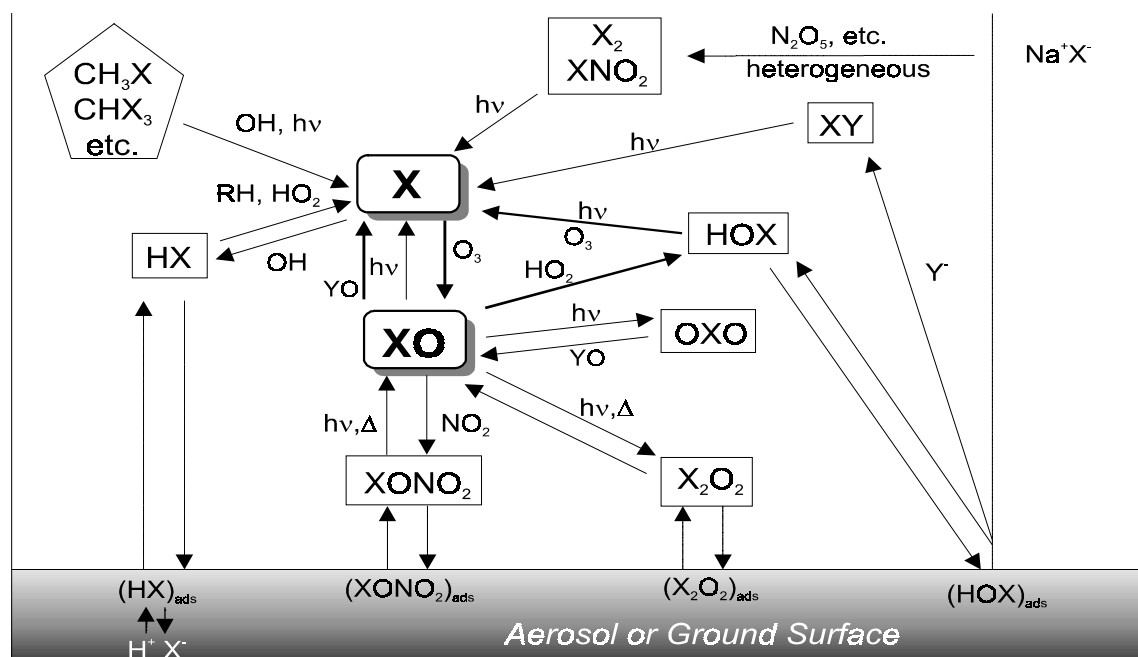


Figure 2.2 Overview of boundary-layer halogen chemistry ($X = Cl, Br, I$), adapted from Platt and Janssen [1995]. Fat lines indicate ozone-destruction sequences. Sources of RHS are the release from sea salt and the photolysis of halocarbons.

2.1.2 Tropospheric Sources of RHS

Halogen release mechanisms have been the subject of a number of computational, laboratory and field investigations. Even if there are still several uncertainties, two main sources have been identified so far: Halogen release from sea salt and the photolysis of unstable halogenated organic compounds. First the halogen release from sea salt and second from photolytically unstable halogenated organic compounds will be discussed as relevant sources of RHS in the troposphere.

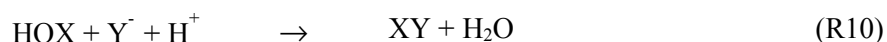
a) *Halogen Release from Sea Salt*

The release of halogens from sea salt via heterogeneous reactions was introduced by *Holland* [1978] two decades ago. In the early 1990s the first release mechanisms were described by *Fan and Jacob* [1992], followed by *Mozurkewich* [1995], *Platt and Lehrer* [1997], *Sander and Crutzen* [1996] and *Vogt et al.* [1996] or *Oum et al.*, [1998], *Behnke et al.* [1999] *Fickert et al.* [1999] and *Kirchner et al.* [1997] in the mid and late 90s.

By weight sea salt contains 55.7 % Cl⁻, 0.19 % Br⁻, and 2 x 10⁻⁵ % I⁻ [*Holland*, 1978]. As coated surfaces and as aerosol particles sea salt is in contact with the atmosphere. It represents a large reservoir of halogens, is available at almost every coastline and – in form of aerosols – present on the open sea. However, the absolute atmospheric halogen input from sea salt remains uncertain [*Platt and Lehrer*, 1997; *Wennberg*, 1999].

Halogen-catalysed RHS Liberation From (Sea) Salt, the ‘Bromine Explosion Mechanism’

One interesting process is based on the uptake of gaseous HOX (e.g. product of R6 or R9) on acidic salt surfaces [*Fan and Jacob*, 1992; *Tang and McConnel*, 1996; *Vogt et al.*, 1996] followed by the formation of an (inter-) halogen molecule:



XY (e.g. Br₂ or BrCl) returns to the gas phase where it is quickly photolysed (see e.g. Table 2.1) and oxidised to XO or YO (R1 or R4) again. Including R1 and R6 the reaction sequence for X = Y can be summarised as:



Platt and Lehrer [1997] introduced this process - as it can lead to an exponential growth in the BrO concentration - as ‘bromine explosion’ mechanism: The halogen oxide molecule acts like a catalyst promoting the oxidation of Br⁻ to Br by O₃. This reaction sequence has been demonstrated in several laboratory [*Rudich et al.*, 1996] and modelling (see e.g. [*Lehrer*, 2000]) investigations. Our current understanding shows that bromine is released by the autocatalytic process, while chlorine is a by-product as Br release is preferred to Cl, even if it is much less abundant in a sea salt solution [*Fickert et al.*, 1999].

The required acidity (this reaction occurs only at pH < 6.5 [*Fickert et al.*, 1999]) could be supplied by strong acids, such as HNO₃ and H₂SO₄ (see below).

Halogen release via the attack of strong acids

The attack of strong acids such as H_2SO_4 on sea salt aerosols is known to release gaseous halogen compounds as e.g. HX:



These species are very soluble (see section 2.1.3 ‘Tropospheric Sinks of RHS’).

A recycling of gaseous HX via heterogeneous reactions is possible and is supposed to be of mayor importance in polar regions [McFiggans *et al.*, 2000; Sander *et al.*, 1999; Vogt *et al.*, 1999] and in the remote marine boundary layer [Seisel and Rossi, 1997]. On the surface of sea salt aerosols the reaction of HOX with HX is followed by the release of X_2 to the gas phase [Abbatt, 1994; Abbatt, 1995; Abbatt and Nowak, 1997], as originally suggested by Fan and Jacob [1992]. Afterwards the (inter)halogen molecule is rapidly photolysed (Table 2.1):



Seisel and Rossi [1997] discovered a reaction that requires cold and acidified aerosol surfaces. Therefore this reaction of nitrous acid (HONO) and HBr:



could be of importance at the polar regions but not at mid latitudes.

Halogen release via NO_y species¹¹

Man-made trace gases like NO_2 and N_2O_5 have been found to release halogens from sea salt [Finlayson-Pitts *et al.*, 1989; Mozurkewich, 1995]. In the presence of nitrogen oxides heterogeneous reactions on aerosol surfaces¹² like R15 are known to produce halogenated nitrogen oxides which are photolabile (R16) or which may also react directly with sea salt (R17) [Schweizer *et al.*, 1999]:



Under atmospheric conditions reaction R15 is very slow [Mozurkewich, 1995]. However, in contrast to the other halogen release mechanisms described at the beginning of this section, the formation of XNO_2 and X_2 can proceed without light, leading to an accumulation of these photolabile species before sunrise (‘dark source’ of RHS). Nagao *et al.* [1999] observed O_3 depletion events in the sub-tropical marine boundary layer and made responsible night-time halogen release followed by photolysis at sunrise for these events. Nevertheless, this source is the more effective the higher the NO_x values are, i.e.

¹¹ NO_y : family of the reactive inorganic nitrate species

¹² in chemical reactions marked as index s

the more polluted the atmosphere is. Therefore it cannot be expected to be the dominant process of halogen release in the remote marine boundary layer.

The uptake of NO_3 by aqueous solutions¹³ of NaX leads to another night-time mechanism [Gershenson *et al.*, 1999]:



The absorption coefficient was found to be near 0.01 for sea water by Rudich *et al.* [1996], while Seisel *et al.* [1997] found 0.05 for dry NaCl.

b) Halogenated Hydrocarbons as a Source of RHS

Halogenated hydrocarbons (HHC), or halocarbons for short, are emitted by a number of natural and anthropogenic sources. The most important natural source is the emission from algae in the oceans [Schall and Heumann, 1993].

In total the source strength of methyl halides CH_3X is [DeMore *et al.*, 1997] about $(100 - 400) \times 10^9 \text{ g CH}_3\text{Br}$ and $4 \times 10^9 \text{ g CH}_3\text{I/year}$.

In addition, there are emissions of polyhalogenated hydrocarbons like bromoform (tribromomethane, CHBr_3) or iodoform (triiodomethane, CHI_3), dibromo- and diiodomethane (CH_2Br_2 , CH_2I_2) of a short photolytic lifetime (order of seconds in the marine boundary layer, see e.g. Carpenter *et al.* [1999]) or short-chained organic halogens including different halogen species such as CH_2ClI or CH_2IBr [Wayne *et al.*, 1995] that have been detected in the atmosphere in significant amounts (see Table 2.3). Especially in the tropics biomass burning is the most important anthropogenic source of halogenated hydrocarbons. Manö and Andreae [1994] estimate the man made-amount of methyl bromide to be $(10 - 50) \times 10^9 \text{ g CH}_3\text{Br/year}$.

Table 2.3 Typical mixing ratios and lifetimes of several important organic hydrocarbons in the planetary boundary layer

Species	Typical mixing ratio (ppt)	Photolytic tropospheric lifetime
CH_3Cl	~ 630	~ 1 year ^a
CH_2Cl_2	~ 32	~ 3 month
CH_3Br	10 - 20 ^f	1 - 2 years ^b
CH_2Br_2	0.2 - 3	2 - 5 month ^c
CHBr_3	2 - 20 ^f	Some days ^a
CH_3I	1 - 30 ^e	1 - 5 days ^d
CH_2I_2	< 1 ^e	Some minutes ^e
CH_2ClI	< 1 ^e	~ 1 day ^d
CH_2BrI	< 1 ^e	45 minutes ^f

a [Yvon and Butler, 1996]

b [Mellouki *et al.*, 1992]

c [Davis *et al.*, 1996]

d [Sander, 2000]

e [Carpenter *et al.*, 1999]

f [Brown *et al.*, 1990]

¹³ in chemical reactions marked as index aq

In contrast to CFCs¹⁴ halocarbons can be photolysed even at low UV intensity in the planetary boundary layer or the upper troposphere. Table 2.3 shows the typical mixing ratios and tropospheric photolytic lifetimes of several halogenated hydrocarbons of tropospheric importance.

The comparatively short lifetimes of the iodinated hydrocarbons are particularly conspicuous. Especially as the iodide content of sea salt is only of the order of $10^{-5}\%$ [Holland, 1978], HHC photolysis deserves more attention as a RHS source than the iodine release from sea salt. As an example the photolytic lifetime of CH_3I is about hundred times shorter than its lifetime with respect to the reaction with OH [DeMore *et al.*, 1997] and photolysis of the alkyl iodides occurs on a much shorter timescale than for the equivalent bromo or chloro compounds [Carpenter *et al.*, 1999].

2.1.3 Tropospheric Sinks of RHS

In general a distinction is made between wet (after dissolution in water-droplets of clouds or fog or on aerosol surfaces) and dry deposition (in the gaseous form) on the earth's surface, which includes not only soil but grass, trees, buildings etc. As a result gaseous species are removed, at least temporarily, from the atmosphere.

The most important loss process of RHS in the troposphere is their reaction with hydrocarbons (RH, R = organic radical, e.g. CH_3) or peroxy radicals (Hydroperoxyl, HO_2 , and organic peroxy radicals, RO_2). As shown in R19 and R20, these reactions cause the formation of hydrogen halides, HX, which are readily soluble in water. This leads to a wet deposition on the ground or on aerosol surfaces and thus - at least preliminarily - to a removal of RHS from the atmosphere:



The different halogens show different behaviour concerning their reaction with hydrocarbons: Cl also reacts with saturated, Br only with unsaturated hydrocarbons or carbonyls leading to the formation of HX. Owing to their low reactivity iodine atoms are not taken up by unsaturated organic molecules and are unable to abstract H atoms from saturated hydrocarbons [Miyake and Tsnogai, 1963].

Additionally, Br atoms can add to the $\text{C}=\text{C}$ double bond of olefins leading to organic bromine species or to HBr. In the absence of heterogeneous recycling processes reactive Br and Cl reacts with formaldehyde, HCHO, forming hydrogen halides within a few hours [Platt and Lehrer, 1997]. Especially concerning the reaction with hydrocarbons, the different halogens show a diverse behaviour. For a detailed description cf. the reviews of DeMore *et al.* [1997] or Atkinson *et al.* [1997].

¹⁴ CFCs (chlorofluorocarbons) are photolytically stable in the troposphere and are cracked by the short-wave UV radiation in the stratosphere where they are the most important (anthropogenic) halogen source [WMO, 1998].

The most effective chlorine removal process is R19, the reaction of chlorine atoms with hydrocarbons which is very fast and very often limited by gas-kinetics rate constants [Atkinson *et al.*, 1997]. For more details concerning loss processes of bromine and iodine species see section 2.2.3 and 2.3.3 respectively.

In principle, a recycling of hydrogen halide is possible via the gas-phase reaction with a hydroxyl radical (OH):



As shown in Table 2.4 the reaction enthalpy of the different halogens decreases from fluorine to iodine. The positive value of 15 kcal/mol shows that HF cannot be recycled by OH.

Table 2.4 Reaction enthalpy of reaction R21 after Atkinson *et al.* [1997]

Halogen	Reaction Enthalpy ΔH (kcal mol ⁻¹)
F	15.0
Cl	-18.2
Br	-33.7
I	-49.9

2.1.4 Influence of RHS on Tropospheric NO_X and HO_X Chemistry

In the boundary layer the interconversion of the NO_X species (NO and NO₂) is dominated by the following null cycle where ozone is involved:



In a rural atmosphere the Leighton ration, *L*, the ratio of NO₂ to NO, can be approximated as

$$L = \frac{[\text{NO}_2]}{[\text{NO}]} = \frac{k_{\text{NO}+\text{O}_3} \cdot [\text{O}_3]}{J_{\text{NO}_2}} \quad \text{Equ 3}$$

also referred to as ‘*photostationary state*’, *PSS*, which is established within about 2 minutes [Leighton, 1961]. *L* is disturbed by peroxy radicals under certain conditions (e.g. smog), because HO₂ and RO₂ are transforming NO to NO₂ while no ozone is destroyed:



where $k_{R24} = 8.3 \times 10^{-12} \text{ cm}^3 \text{ molec}^{-1} \text{ s}^{-1}$ and $k_{R25} = 8 \times 10^{-12} \text{ cm}^3 \text{ molec}^{-1} \text{ s}^{-1}$ for $\text{RO}_2 = \text{CH}_3\text{O}_2$ or $k_{R25} = 9.2 \times 10^{-12} \text{ cm}^3 \text{ molec}^{-1} \text{ s}^{-1}$ for $\text{RO} = \text{C}_2\text{H}_5\text{O}_2$ [DeMore *et al.*, 1997].

Therefore these reactions, in combination with the subsequent photolysis of nitrogen dioxide (R23), lead to a net production of ozone via reaction R3. Since the early 1990s these conditions have been a matter of public interest and are known as *photo smog conditions*. With respect to HO_2 (R24) and RO_2 (R25) the modified Leighton ratio, L_{RO_2} , can be written as [Parrish *et al.*, 1986]:

$$L_{\text{RO}_2} = \frac{[\text{NO}_2]}{[\text{NO}]} = \frac{k_{\text{NO}+\text{O}_3} \cdot [\text{O}_3] + k_{\text{RO}_2+\text{NO}} \cdot [\text{RO}_2] + k_{\text{HO}_2+\text{NO}} \cdot [\text{HO}_2]}{J_{\text{NO}_2}} \quad \text{Equ 4}$$

In parts of the troposphere, which are affected by halogens, the rapid reaction of XO with NO ($k_{R26,\text{Cl}} = 1.7 \times 10^{-11} \text{ cm}^3 \text{ molec}^{-1} \text{ s}^{-1}$ and $k_{R26,\text{Br,I}} = 2.1 \times 10^{-11} \text{ cm}^3 \text{ molec}^{-1} \text{ s}^{-1}$ (X = Br, I)) will generate halogen atoms and convert NO to NO_2 while no O_3 is destroyed or produced:



The X-atom generated in R26 (or e.g. in the photolysis of XO as mentioned at the beginning of the chapter on page 6 as R2) can degrade volatile organic compounds (VOC). Therefore halogen oxide radicals can influence the photochemical equilibrium as well, which is usually interpreted in terms of concentration of peroxy radicals. As a result the Leighton ratio affected by peroxy radicals and halogen chemistry, $L_{\text{RO}_2,\text{RHS}}$, can be calculated as [Platt and Janssen, 1995]:

$$L_{\text{RO}_2,\text{RHS}} = \frac{[\text{NO}_2]}{[\text{NO}]} = \frac{k_{\text{NO}+\text{O}_3} \cdot [\text{O}_3] + k_{\text{HO}_2+\text{NO}} \cdot [\text{HO}_2] + k_{\text{RO}_2+\text{NO}} \cdot [\text{RO}_2] + k_{\text{XO}+\text{NO}} \cdot [\text{XO}]}{J_{\text{NO}_2}} \quad \text{Equ 5}$$

The ratio and the absolute concentrations of OH and HO_2 are also affected by the presence of RHS. Besides R24, HO_2 can also be converted to OH by the production of HOX followed by its photolysis (R7+R6). Model calculations related to the field measurements of this thesis [Stutz *et al.*, 1999] show for the case X = I that the OH/ HO_2 ratio increases by a factor of 3.5, while the Leighton ratio increases by 25 to 30 %, which has previously been discussed by Davis *et al.* [1996], Jenkin [1992] and Sander *et al.* [1997]. It is important to note that most of the change in L is caused by the XO + HO_2 cycle and not by the XO self-reaction ([Stutz *et al.*, 1999], see also section 4.4.4).

2.2 Reactive Bromine in the Troposphere

2.2.1 Historical Overview

The dramatic effect of bromine species in the remote planetary boundary layer was discussed for the first time after the measurements of Barrie *et al.* [1988]. The measurements of Hausmann and Platt [1994], Tuckermann *et al.* [1997] and [Martinez-Harder *et al.*, 1999] showed that bromine monoxide is the key species in the ozone destroying cycles

discussed above (see Cycle A and B on page 7). Via satellite remote sensing systems (e.g. GOME, **G**lobal **O**zone **M**onitoring **E**xperiment) these episodes of low ozone in the troposphere were detected in the polar regions of both hemispheres [Richter *et al.*, 1998; Wagner, 1999; Wagner and Platt, 1998]. Within the framework of this thesis LOE correlated with high values of bromine monoxide were detected at mid latitudes for the first time: At the Dead Sea, Israel, ozone depletion in the planetary boundary layer (PBL) correlated with BrO mixing ratios of up to 178 ppt was observed [Hebestreit *et al.*, 1999; Matveev *et al.*, 2001; Stutz *et al.*, 1999].

Airborne measurements performed in April 1997 during polar sunrise showed BrO vertical-column densities (VCDs) of $1 - 3 \times 10^{14} \text{ cm}^{-2}$ in the North American Arctic [McElroy *et al.*, 1999]. Since there was no correlation with altitude, solar zenith angle (SZA) and geographical latitude the interpretation of McElroy and co-workers was that most of the BrO was present below a height of 8 km and therefore in the troposphere. Assuming that all of the BrO was located in the PBL they calculated a mixing ratio of 50 - 100 ppt, which was higher by a factor of 2 - 3 than it was measured before in the polar troposphere (e.g. Harder *et al.* [1998], Tuckermann *et al.* [1997]). The more sophisticated interpretation was that the bromine monoxide was spread over the free troposphere, leading to mixing ratios of 10 - 30 ppt depending on their distribution during the measurements. In the case of effective recycling processes of reactive bromine (Br, Br₂, BrO and HOBr; for short r-Br:) BrO could have a devastating effect on the ozone budget of the free troposphere. McElroy *et al.* [1999] assumed cracks in the arctic pack-ice followed by convective transport processes to be the source and the recycling platform of the r-Br compounds, while Wennberg [1999] suspected recycling processes on background sulphur aerosols.

1 - 2 ppt BrO background values are assumed in the free troposphere, as a result of balloon-borne measurements [Harder *et al.*, 1998], [Fitzenberger *et al.*, 2000], while Fries *et al.* [1999] find 0.75 - 2 ppt BrO in the free Arctic troposphere by comparing their ground-based measurements of scattered sunlight with model calculations.

This short introduction shows that a considerable number of measurements of BrO have been carried out. On the other hand, there are still quite a few open questions concerning tropospheric bromine chemistry. Especially the source and sink mechanisms and the influence of r-Br at mid latitudes, where no measurements were reported before the beginning of this thesis, are uncertain. The following section deals with a more detailed description of the sources and sinks of r-Br, especially at mid latitudes. Recycling processes and reaction cycles of bromine species in the PBL will be described.

2.2.2 Main Reactions and Release of Reactive Bromine

In comparison with the BrO observations made in polar regions, where bromine release from salt brines on the pack-ice surface is supposed to be the primary bromine source (e.g. [Sander and Crutzen, 1996; Tang and McConnel, 1996; Vogt *et al.*, 1996]), there are different conditions at mid latitudes. The salt brines on the missing ice shields can be

‘replaced’ by salt-covered surfaces as available on almost every coast line and at salt lakes such as the Dead Sea or the big continental salt lakes of North and South America, Africa or Asia. But there is still a difference in temperature. Furthermore, there have been no publications about observations of regularly recurrent LOE at mid latitudes or successful measurements of tropospheric bromine oxide, before the measurements reported in this thesis were carried out at the Dead Sea, Israel (see sections 4.5 and 4.6).

As described in section 2.1.2 inorganic bromine, Br_Y (= Br, Br₂, BrX, BrO_n, HBr, HOBr, BrONO₂ for X = Cl, I), is released to the atmosphere either by degradation of organic bromine compounds or by oxidation of sea salt bromide. The most probable mechanism at mid latitudes and especially at the Dead Sea is the ‘bromine explosion’ [Platt and Lehrer, 1997; Wennberg, 1999]. Strong oxidising agents were proposed to oxidise Br⁻ to Br₂ or – in the presence of Cl⁻ – to BrCl. In more detail, gaseous HOBr is dissolved in the aqueous phase of the (aerosol) surface where it can react with halogen ions (Br⁻ or Cl⁻) forming highly soluble Br₂ or BrCl:



To sum up: one HOBr molecule can release up to 2 Br atoms per cycle, while the second halogen atom is derived by the oxidation of the salt halogenides. Sea salt represents an almost endless reservoir of halogenides. As a consequence, the number of gas-phase bromine containing molecules (i.e. BrO) can increase exponentially, if less than 50 % of the bromine is lost from the cycle (‘bromine explosion’).

As can be seen from R27 acidity is needed to promote the oxidation of Br⁻ by HOBr. In fact, Fickert *et al.* [1999] showed that this reaction in the liquid phase only proceeds at pH ≤ 6.5 (on ice, however, acidity appears to have little effect). Thus the halogen release from the surface of bulk sea water (pH ≈ 8.2) is unlikely. In contrast to that the surface of solid salt can relatively easily be acidified by acids such as H₂SO₄ or HNO₃ of anthropogenic or natural sources.

Besides its importance concerning ozone destruction (see Cycle A on page 7 for the case X = Br) BrO is an important oxidising agent of the marine atmosphere. Sulphur emission from algae is one of the most important sulphur sources of the marine environment. Dimethylsulphide (CH₃SCH₃ = DMS) is one of the key species of these emissions. Already in 1994 Toumi [1994] assumed that BrO might be one of the important oxidising agents of DMS:



DMSO (dimethylsulphoxide, (CH₃)₂SO) is formed with $k_{\text{R28}} = 2.6 \times 10^{-13} \text{ cm}^3 \text{ molec}^{-1} \text{ s}^{-1}$ [Atkinson *et al.*, 1997]. Assuming a Br₂ emission rate of 0.5 ppt h⁻¹ in model calculations, BrO was shown to be an important sink of DMS (in the contribution of NILU¹⁵ to the final report of the HALOTROP project, edited by Platt and Stutz [1998]). So far there have been no publications about simultaneous measurements of halogen oxides and DMS/DMSO in

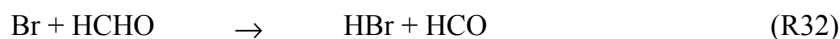
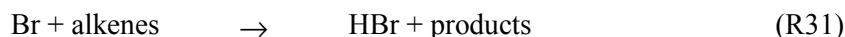
¹⁵ Norwegian Institute for Luftforskering

the marine PBL. First simultaneous measurements of both species are planned within the framework of the EU project EL CID. The reaction of IO with DMS forming DMSO and I does not seem to be relevant in the marine atmosphere with regard to DMS oxidation, as the rate constant is by one order of magnitude lower compared to BrO ($k_{DMS+IO} = 1.2 \times 10^{-14} \text{ cm}^3 \text{ molec}^{-1} \text{ s}^{-1}$ [Atkinson *et al.*, 1997]). The oxidation rate constant of DMS via OH is by one order of magnitude higher. The reaction proceeds by two channels: abstraction of a hydrogen from a methyl group and addition of OH to the sulphur atom with $k_{R29} = 4.8 \times 10^{-12} \text{ cm}^3 \text{ molec}^{-1} \text{ s}^{-1}$ and $k_{R30} = 1.7 \times 10^{-12} \text{ cm}^3 \text{ molec}^{-1} \text{ s}^{-1}$ respectively [Atkinson *et al.*, 1997]. Since typical daytime OH levels are of the order of $2 \times 10^6 \text{ molec cm}^{-3}$, a BrO concentration of only $2 \times 10^7 \text{ molec cm}^{-3}$ ($\cong 1 \text{ ppt}$) would be enough to oxidise the same amount of DMS:



2.2.3 Sinks of Reactive Bromine

Under typical tropospheric conditions bromine reacts only with unsaturated hydrocarbons such as alkenes or with those of a higher oxidation state such as formaldehyde, HCHO [Bedjanian *et al.*, 1998b]:



While the rate coefficient of R31 varies between $k_{propene} = 1.2 \times 10^{-14} \text{ cm}^3 \text{ molec}^{-1} \text{ s}^{-1}$ and $k_{2,3\text{-dimethyl-2-butene}} = 2.0 \times 10^{-11} \text{ cm}^3 \text{ molec}^{-1} \text{ s}^{-1}$ [Sauer *et al.*, 1999], the rate constant of the reaction of bromine with formaldehyde is $k_{R32} = 1.1 \times 10^{-12} \text{ cm}^3 \text{ molec}^{-1} \text{ s}^{-1}$. Under typical atmospheric conditions of 0.2 ppb HCHO and alkenes mixing ratios of some 10^{th} of a ppt (which is 4 orders of magnitude below the estimated HCHO concentration) both reactions are of the same importance concerning their HBr production. Even if the reactions of bromine are slow compared to the reactions of chlorine [Atkinson *et al.*, 1997], most of the bromine will be deposited as HBr. Furthermore, HBr is produced in the reactions of bromine with hydroperoxyl radicals (R20) or in heterogeneous reactions with strong acids such as H_2SO_4 (R12).

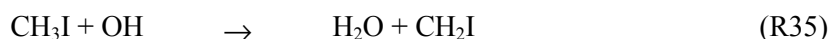
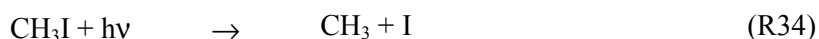
Theoretically a recycling of HBr to r-Br is possible via the gas-phase reaction of HBr with OH with $k_{R33} = 1.1 \times 10^{-11} \text{ cm}^3 \text{ molec}^{-1} \text{ s}^{-1}$ [Bedjanian *et al.*, 1998a; Cox *et al.*, 1999]:



Assuming a typical OH concentration of $2 \times 10^6 \text{ molec cm}^{-3}$, the lifetime of HBr is of the order of $\tau = \frac{1}{2}$ day and therefore too long to be an effective recycling mechanism, as in the PBL the exchange processes with the ground are much faster. Thus - because of the high solubility of hydrogen bromide forming hydrobromic acid - its wet (or dry) deposition is much more likely.

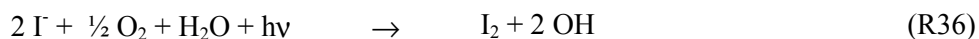
2.3.1 Primary Sources of Reactive Iodine

Unlike the other halocarbons, the photolytic lifetime of iodohydrocarbons is comparatively short (of the order of days or even less, see Table 2.3 in section 2.1.2 b)). To give an example, the photolysis of methyl iodide (= iodomethane, CH₃I) under daylight conditions is by a factor of 100 faster than the rival reaction with OH:



The rate constant of $k_{\text{R35}} = 7.2 \times 10^{-14} \text{ cm}^3 \text{ molec}^{-1} \text{ s}^{-1}$ [DeMore *et al.*, 1997] leads to a lifetime of CH₃I of the order of months via the reaction with OH. Because of the low energy content of the H-I bond iodine atoms formed by photolysis via R34 do not abstract hydrogen atoms from alkanes [Jenkin *et al.*, 1985] as described above.

Apart from the emission by algae the oxidation of iodide in sea water may be an additional source of atmospheric iodine. As was found in laboratory studies of Miyake and Tsnogai [1963], volatile iodine species such as I₂ or HOI are released to the atmosphere. Free iodine might escape to the gas phase according to the overall reaction:



The mechanism is still unclear, however, Miyake and Tsnogai [1963] estimated emissions of 0.4 Tg iodine per year to be released photochemically from the oceans.

Regarding anthropogenic sources of iodine, CF₃I is discussed as one possible halon replacement to reduce the stratospheric ozone-depleting compounds which have been applied e.g. in fire extinguishers. The photolytic lifetime of CF₃I is of the order of 2 days and it is therefore not expected to penetrate to the stratosphere. If CF₃I was applied as a widespread halon replacement, the amount of iodine released to the atmosphere would be 3 - 7 % of the global natural sources of iodocarbons [Solomon *et al.*, 1994].

In a low NO_x environment the heterogeneous mechanisms assumed by Mozurkewich [1995] and Vogt *et al.* [1996],



are possible, but unlikely because of the low iodide content of sea salt (0.00002 %) in general [Holland, 1978].

2.3.2 Main Reactions of Reactive Iodine

The most probable pathway of I atoms is the reaction with ozone forming iodine monoxide:

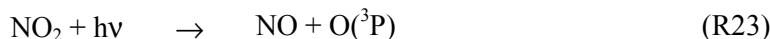


Assuming an ozone mixing ratio of ~ 30 ppb (as it is typical for the marine boundary layer) the time scale of this reaction with $k_{R38} = 1.2 \times 10^{-12} \text{ cm}^3 \text{ molec}^{-1} \text{ s}^{-1}$ [DeMore *et al.*, 1997] is ~ 1 second.

At low NO_x levels of less than 50 ppt - as observed in the remote oceanic boundary layer - the major fate of IO is the photodissociation to regenerate I atoms with a photolysis frequency of $J_{IO} = 0.2 \text{ s}^{-1}$ at 45° SZA (Table 2.1). This cyclic interchange of I and IO results in no net chemistry, since O_3 is also regenerated by the reaction of O with O_2 (R3). Up to about 1 ppb NO_x the regeneration of the I radicals is also possible via the reaction of IO with NO,



with $k_{R39} = 2.0 \times 10^{-11} \text{ cm}^3 \text{ molec}^{-1} \text{ s}^{-1}$ [DeMore *et al.*, 1997], which is able to compete with the photodissociation of IO. The photolysis of NO_2 , the product of the IO + NO reaction R39, again leads to the regeneration of both NO and O_3 (R23, R3). Therefore this reaction results in a null cycle with no net chemistry [Jenkin, 1992]. The two null cycles are summarised below:



Unlike these 2 cycles with no net chemistry, the reactions of IO with HO_2 or YO (R5 and R6) lead to the destruction of O_3 and a change in the Leighton ratio (see sections 2.1.1, 4.4.4 and 4.4.5).

2.3.3 Sinks of Reactive Iodine

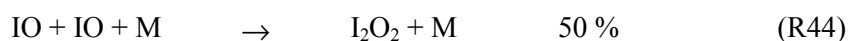
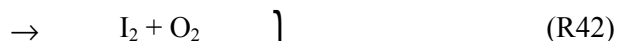
Compared with the other halogens, iodine atoms are not taken up by unsaturated organic molecules and are unable to abstract H atoms from saturated hydrocarbons owing to their low reactivity, as mentioned above [Miyake and Tsnogai, 1963]. In the following several re-I loss processes and the respective recycling reactions, leading to a reactivation of the deactivated iodine, will be presented.

a) *The IO self-reaction*

Based on the first detection of IO and OIO in the atmosphere within the framework of this thesis (see section 4) the reaction of IO with other halogen oxides and the IO self-reaction became the subject of a number of laboratory studies [Cox *et al.*, 1999; Ingham *et al.*, 2000] once again. The major loss process of IO radicals in the remote environment under

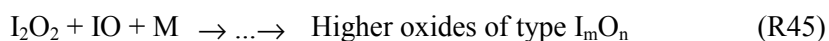
low NO_X conditions is its photolysis (R40), which consequently leads to a recycling of the I atom via the reaction with ozone and the reaction with HO_2 (R6).

Thus the IO self-reaction can become an important loss process when NO_X is low and sufficient IO is present. It leads to three different reaction channels:



Recently the overall rate constant $k_{\text{IO}+\text{IO}} = 8.2 \times 10^{-11} \text{ cm}^3 \text{ molec}^{-1} \text{ s}^{-1}$ and the branching ratio 38:12:50 was determined by *Cox et al.* [1999] at room temperature. Their results are in good agreement with other recent literature values of e.g. *Gilles et al.* [1997], *Harwood et al.* [1997], *Ingham et al.* [2000] and *Lazlo et al.* [1997 and 1995]. As can be seen from the branching ratio, at the most 12 % of the IO self-reactions (R42 and R43) are producing 2 iodine radicals (assuming the fast photolysis of the I_2 atom $\tau \approx 10 \text{ s}$ [Tellinghuisen, 1973]) and are thus leading to ozone destruction.

The fate of the other products is still uncertain. The dimer I_2O_2 can be photolysed forming 2 IO radicals or 2 I and O_2 [Chatfield and Crutzen, 1990] or forms higher iodine oxides (I_mO_n), which leads to a removal of re-I via reactions of aerosols or the formation of micro-particles [Jenkin, 1992; Vogt et al., 1999]:



This pathway is still subject to laboratory and field investigations and is not well understood yet.

The third product, iodinedioxide (OIO) was detected in the atmosphere for the first time within the framework of this thesis. The first absorption spectrum of OIO was published by *Himmelman et al.* [1996], showing structures between 480 and 660 nm in the visible wavelength region. The value of the absorption cross section of between $2 - 5 \times 10^{-17} \text{ cm}^2$ at 549.1 nm was published later by the same group [Spietz et al., 1998]. If this absorption were dissociative, cross section values of that magnitude would result in a very short photolytic lifetime.

Another absorption cross section was published by *Cox et al.* [1999]. They found $\sigma = (1.09 \pm 0.21) \times 10^{-17} \text{ cm}^2 \text{ molec}^{-1}$ at 548.6 nm for a spectral resolution of 1.13 nm FWHM. The value determined by *Ingham et al.* [2000] in a later work is higher by approximately a factor of three, which compares better with the cross section published by *Spietz et al.* [1998].

Misra and Marshall [1998] used *ab initio* methods to calculate standard thermodynamic constants of a number of iodine species. They found OIO to be the major product of the IO self-reaction with a formation enthalpy of $\Delta_f H^\circ(\text{OIO}) = 76.7 \text{ kJmol}^{-1}$. Using this information, an O-IO bond strength of 288.2 kJmol^{-1} can be calculated. The threshold for the photodissociation via the reaction



was computed to be 418 nm [*Cox et al.*, 1999]. Because of the weak absorption of OIO below 480 nm photolysis in the near UV resulting in IO + O(³P) will not occur as it does for OCIO.

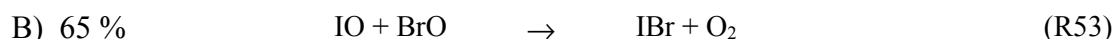
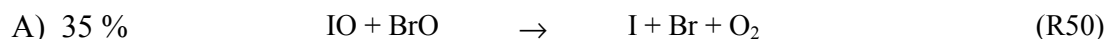
In general, there is an alternate photolysis channel of OXO to form O₂ and X. This has only been observed for OCIO under collision-free conditions [*Vaida and Simon*, 1995]. In analogy to OCIO *Cox et al.* [1999] conclude that one could expect negligible reactions of OIO with closed shell molecules and rather slow rate coefficients ($k < 1 \times 10^{-12} \text{ cm}^3 \text{ molec}^{-1} \text{ s}^{-1}$) for the reaction with NO or polyatomic radicals such as HO₂. The OIO lifetime with respect to chemical reactions was calculated to be at least one hour. Therefore OIO can be an important reservoir species for re-I compounds (see section 4.4.7 c) for the OIO lifetime calculations of this work).

The halogen oxide cross reaction IO + ClO was analysed by *Bedjanian et al.* [1997]:



The overall rate constant was determined to be $k_{\text{IO}+\text{ClO}} = 1.1 \times 10^{-11} \text{ cm}^3 \text{ molec}^{-1} \text{ s}^{-1}$ at 298 K. The first channel where OCIO is formed does not lead to O₃ destruction.

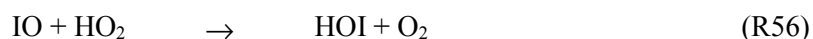
The cross reaction of IO and BrO was analysed by *Gilles et al.* [1997]. They divided the reaction in group A), where atomic I was formed, and B), where I was always bound in molecules.



The branching ratio was determined to be 0.35 (type A) to 0.65 (type B), with a rate constant of type A) of $k_A = 2.5 \times 10^{-11} \text{ cm}^3 \text{ molec}^{-1} \text{ s}^{-1}$ and $k_{\text{tot}} = 7.1 \times 10^{-11} \text{ cm}^3 \text{ molec}^{-1} \text{ s}^{-1}$. In a recent study *Cox et al.* [1999] determined the overall rate constant of the IO + BrO reaction to be $k_{\text{IO+BrO}} = 8.5 \times 10^{-11} \text{ cm}^3 \text{ molec}^{-1} \text{ s}^{-1}$, which is in agreement with the one of *Gilles et al.* [1997] and other literature values [*Bedjanian et al.*, 1998a; *Harwood et al.*, 1997; *Lazlo et al.*, 1997]. The branching ratio for the formation of OIO was found to be 0.65 - 1 in the study of *Bedjanian et al.* [1998a]. Therefore, besides the IO self reaction, the reaction of IO with BrO significantly contributes to the formation of OIO and therefore the formation of gas-phase reservoir species.

b) Reactive Iodine Removal via HO₂

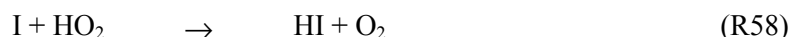
The reaction of IO with the hydro peroxy radical HO₂ ($k_{R56} = 8.4 \times 10^{-11} \text{ cm}^3 \text{ molec}^{-1} \text{ s}^{-1}$ [*Bedjanian et al.*, 1997], Table 2.1) is supposed to be an important loss process as it leads to the formation of the reservoir species hypoiodous acid (HOI):



Assuming a concentration of 3.5 ppt HO₂, the iodine oxide lifetime concerning the attack of HO₂ is $\tau \approx 2$ min. On the other hand, HOI has a strong absorption spectrum and is rapidly photolysed, leading to the same lifetime of $\tau \approx 2$ min in the case of its photolysis with a quantum yield of ~ 1 at 355 nm [*Bauer et al.*, 1998b]:



The reaction of the resulting I atom with HO₂, forming hydrogen iodide (in aqueous solution hydroiodic acid) is rather slow ($k_{R58} = 3.8 \times 10^{-13} \text{ cm}^3 \text{ molec}^{-1} \text{ s}^{-1}$ [*Atkinson et al.*, 1997], Table 2.2):



A recycling of iodine from HI is theoretically possible with the aid of OH radicals:



Even if the rate constant $k_{R59} = 3.0 \times 10^{-11} \text{ cm}^3 \text{ molec}^{-1} \text{ s}^{-1}$ [*Atkinson et al.*, 1997] is comparably fast, one has to consider the low concentration of OH radicals. Assuming $[\text{OH}] = 2 \times 10^6 \text{ molec cm}^{-3}$ the lifetime of HI vs. OH attack is of the order of $\tau_{\text{HI+OH}} = 11 \text{ hr}$. Therefore the (wet or dry) deposition of hypoiodous and hydroiodic acid is the most probable fate of HI.

c) Iodine removal via NO_x reactions

In a more polluted troposphere the reaction of IO with NO₂, forming iodine nitrate, IONO₂, with a rate constant of $k_{R60} = 3.5 \times 10^{-12} \text{ cm}^3 \text{ molec}^{-1} \text{ s}^{-1}$ [*DeMore et al.*, 1997], becomes more important than the reaction with NO (R39):



The partitioning of HI, HOI, IONO₂ and I₂O₂ depends upon the ambient levels of the iodine precursors (iodinated hydrocarbons) and NO_x. IONO₂ and HOI are present in comparable concentrations for NO_x = 1 ppb, whereas HOI is the major gas reservoir of inorganic iodine at low NO_x [Jenkin, 1992; Stutz *et al.*, 1999].

In the daytime iodine nitrate is supposed to be photolysed rapidly, forming I atoms and NO₃:



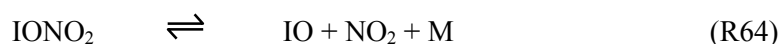
The photolysis rate is somewhat uncertain because no absorption spectrum of iodine nitrate has been published yet. By red shifting the absorption spectrum of ClONO₂ and BrONO₂ J_{R61} can be calculated to be about $(1.5 - 6.4) \times 10^{-3} \text{ s}^{-1}$ as estimated e.g. by Stutz *et al.* [1999], Jenkin [1992] and Chameides and Davis [1980] respectively. The deposition of IONO₂ on the ground or on aerosol surfaces is an important iodine sink. At night two different pathways for IONO₂ are possible. For the uptake on aerosols Jenkin [1992] assumes an uptake coefficient of $\gamma = 0.05$, resulting in $k_{loss} = 1 \times 10^{-5} \text{ s}^{-1}$. In the liquid phase nitric acid, HNO₃, and HOI can be formed:



The second night-time pathway is the thermal decomposition, leading to the production of IO and NO₂ with $k_{R63} = 3 \times 10^{-2} \text{ s}^{-1}$ Jenkin [1992]:



To sum up, IONO₂ is a significant reservoir species at NO_x levels above ~1 ppb. The major reaction pathway of IO under these conditions is the reaction with NO₂. Both species are regenerated immediately after the decay of IONO₂, setting up an equilibrium between IO, NO₂ and IONO₂:



Depending on the absolute levels of IO and HO₂, IO can be removed in the form of HOI or I₂O₂. Taking into consideration the dynamic steady state of R64, IONO₂ will decrease as well.

To sum up the last section, Figure 2.4 illustrates the atmospheric iodine cycle in the marine boundary layer where short-lived alkyl iodides are supposed to be the major source of reactive iodine, as found by Carpenter *et al.* [1999].

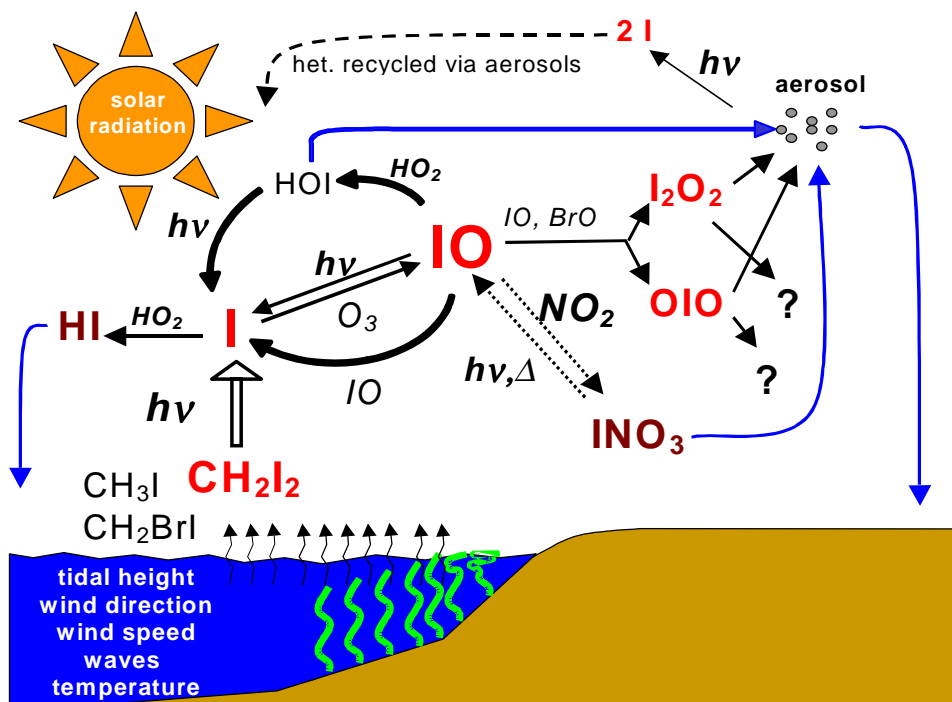


Figure 2.4 Scheme of the atmospheric iodine cycle in the marine boundary layer. Thick arrows indicate ozone destruction cycle, open arrow indicates the primary source of iodine atoms.

Chapter 3

The DOAS Technique

Due to their high reactivity and their low concentration in the boundary layer halogen oxide radicals are very difficult to detect. On the one hand radicals cannot be sampled as they undergo (surface) reactions. On the other hand different halogen oxide radicals show spectroscopic absorption features from the near UV to the visible electromagnetic spectrum. In the open atmosphere *DOAS (Differential Optical Absorption Spectroscopy)* [Platt *et al.*, 1979] is the most common technique to detect halogen oxides, as it allows direct and absolute in-situ measurements.

With the DOAS technique the absorption of light, which is specific for different trace gases, is measured. Atoms and molecules are absorbing light, whereby electronic transitions are induced. In addition, molecules are excited to higher rotational and vibrational levels. As they differ in their moments of inertia and their strength of bonding, they show different rotational and vibrational levels. That is why the absorption in dependence of the wavelength is characteristic of each compound like a fingerprint.

The following section starts with a description of the absorption of light by matter, leading to *Beer-Lambert's law*, the fundamental equation of the DOAS technique. The second part of the chapter gives an introduction to the DOAS instruments used in two of a total of four field campaigns performed within the framework of this thesis, including a discussion of the measurement and evaluation routines. The instruments of the two other campaigns (Weybourne 1996 and Mace Head 1997) are very similar to the instruments portrayed and have already been described in great detail by *Alicke* [1997].

3.1 Absorption of Light

3.1.1 The Basics of Absorption Spectroscopy

The law of Beer-Lambert describes the decrease of the light intensity by dI while passing through an infinitesimally thin layer dl of an absorbing trace gas. The change in intensity dI is directly proportional to the intensity of light before the absorbing matter I_0 , the concentration of the trace gas that might not be constant over the absorbing path $c(l)$, the absorption cross section of the trace gas $\sigma(\lambda, T)$ and the length of the absorbing layer dl :

$$dI = -I_0(\lambda) \cdot c(l) \cdot \sigma(\lambda, T) \cdot dl \quad \text{Equ 6}$$

The negative sign reflects the reduction of intensity with an increase in path length. The integration of this equation leads to:

$$I(\lambda) = I_0(\lambda) \cdot e^{-\sigma(\lambda, T) \int c(l) dl} \quad \text{Equ 7}$$

The exponent is similar to the natural logarithm¹⁶ of the ratio of the light intensities before and after passing through absorbing mater, $\ln(I_0/I)$. It is known as optical density τ :

$$\tau := \ln\left(\frac{I_0}{I}\right) = -\ln\left(\frac{I}{I_0}\right) = \sigma(\lambda, T) \int c(l) dl \quad \text{Equ 8}$$

The integral of Equ 8 is known as column density, CD . Applying an average concentration c or assuming c to be constant along the light path CD is equal to $c \cdot L$,

$$\begin{aligned} \tau &:= \ln\left(\frac{I_0}{I}\right) = -\ln\left(\frac{I}{I_0}\right) = \sigma(\lambda, T) \int c(l) dl \\ &= \sigma(\lambda, T) \cdot c \cdot L \\ &= \sigma(\lambda, T) \cdot CD \end{aligned} \quad \text{Equ 9}$$

Knowing the absorption cross section of the trace gas, which can be measured in the laboratory, the average trace gas concentration over the light path of the length L can be calculated from the measured ratio $I_0(\lambda, T)/I(\lambda, T)$:

$$c = \frac{CD}{L} = \frac{\tau}{\sigma(\lambda, T) \cdot L} = \frac{\ln\left(\frac{I_0(\lambda, T)}{I(\lambda, T)}\right)}{\sigma(\lambda, T) \cdot L} \quad \text{Equ 10}$$

Figure 3.1 describes Beer-Lambert's law. In the upper panel the exponential decrease of light intensity with increasing path length is plotted, while the lower panel illustrates the experimental approach to Beer-Lambert's law.

¹⁶ Note that in literature the decadic logarithm is used as well. In this thesis the natural logarithm is used without exception.

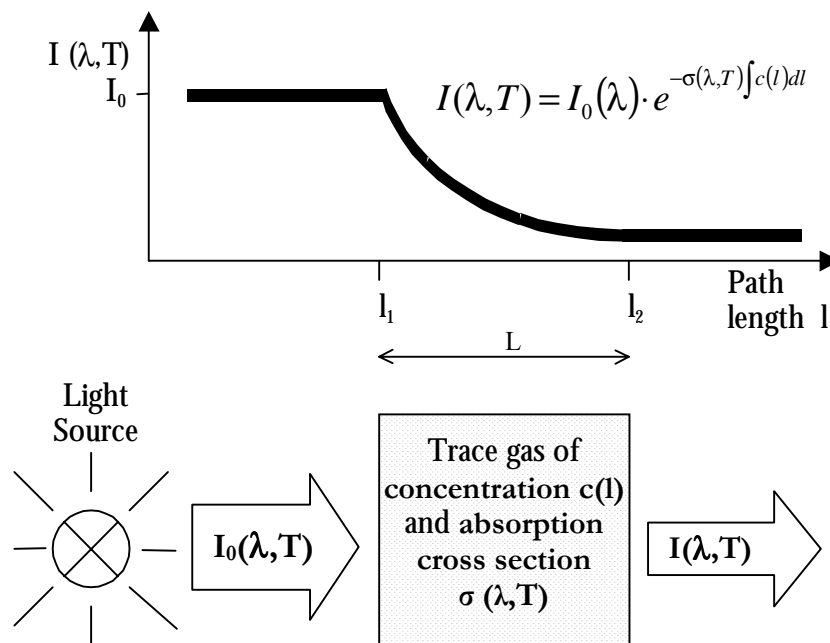


Figure 3.1 Illustration of Beer-Lambert's law. The upper panel shows the exponential decrease of the intensity of light passing through a volume of absorbing matter (lower panel).

3.1.2 Spectroscopy in the Atmosphere

Many trace gases of atmospheric interest show relatively large absorption cross sections in the UV/visible wavelength range. The typical middle wavelength of the near UV applied during the measurements carried out at the Dead Sea was 337.5 nm, which corresponds to 3.7 eV, while the biggest wavelength (lowest energy) interval used at Mace Head was around 555 nm, the yellow/green visible range, which corresponds to 2.2 eV.

Figure 3.2 shows the differential absorption cross sections σ' of a number of trace gases measurable with DOAS. To determine concentrations of these species in the open atmosphere Beer-Lambert's law as it is given in Equ 7 needs to be applied to the specific conditions of the atmosphere and the light sources used. Some important points to be mentioned are:

- More than one absorbing species is present in the atmosphere.
- Light scattering by molecules (Rayleigh-) and aerosols (Mie-extinction) occurs.
- Absorption cross sections are dependent on temperature, which needs to be considered in general. As within the framework of this thesis measurements were only carried out in the troposphere parallel to the ground, only one cross section (at a given temperature) per species was adapted.
- Instead of $c(l)$ the average concentration c along the total light path L will be determined.
- The artificial light source used shows a) spectral features and b) variations in time.

- The detection and digitalisation of light defines a characteristic instrumental function due to features of the spectrograph, the electronic compounds used, and the sensitivity of the different diodes of the photo-diode-array detector.

By applying Equ 7 to these conditions the atmospheric absorption of light can be expressed as:

$$I(\lambda) = I_0(\lambda) \cdot A(\lambda) \cdot e^{-L[\sum(\sigma_i(\lambda)c_i) + \sigma_{Ray}(\lambda)\lambda^{-4} \cdot c_{Air} + \sigma_{Mie}(\lambda)\lambda^{-n} \cdot N_{Aerosol}]} \quad \text{Equ 11}$$

The attenuation factor $A(\lambda)$ summarises the slowly varying wavelength dependence of the optical system. $\sigma_i(\lambda)c_i$ denote the absorption cross section and concentration of the i^{th} species respectively, and c_{Air} the concentration of molecules of air, that is $2.46 \times 10^{19} \text{ molecules cm}^{-3}$ at standard conditions of 20 °C and 1 atm. $\sigma_{Ray}(\lambda)\lambda^{-4}$ and $\sigma_{Mie}(\lambda)\lambda^{-n}$ describe the wavelength dependence of Rayleigh and Mie extinction, while the exponent n varies from one to three depending on the aerosol size distribution. Therefore the variation in wavelength is slow compared to molecular absorptions, which are the features of interest. $N_{Aerosol}$ indicates the average aerosol number density.

Although Rayleigh and Mie scattering are not absorption processes, their contribution to the reduction of light intensity can be treated as if they were. The typical value at 300 nm of $\sigma_{Ray}(\lambda)\lambda^{-4} = \epsilon_{Ray}(\lambda)$ is $1.3 \times 10^{-6} \text{ cm}^{-1}$. This reduces the light intensity by about 12 % in each kilometre. As $\sigma_{Mie}(\lambda)\lambda^{-n} = \epsilon_{Ray}(\lambda)$ strongly varies with aerosol loading, 1×10^{-6} is a typical value in the marine environment with no sea spray, while $1 \times 10^{-5} \text{ cm}^{-1}$ is typical in rural continental air.

Figure 3.2 represents some examples of differential trace gas absorption cross sections, which are typically applied in DOAS measurements. The right column shows the average detection limit calculated for the given light path length.

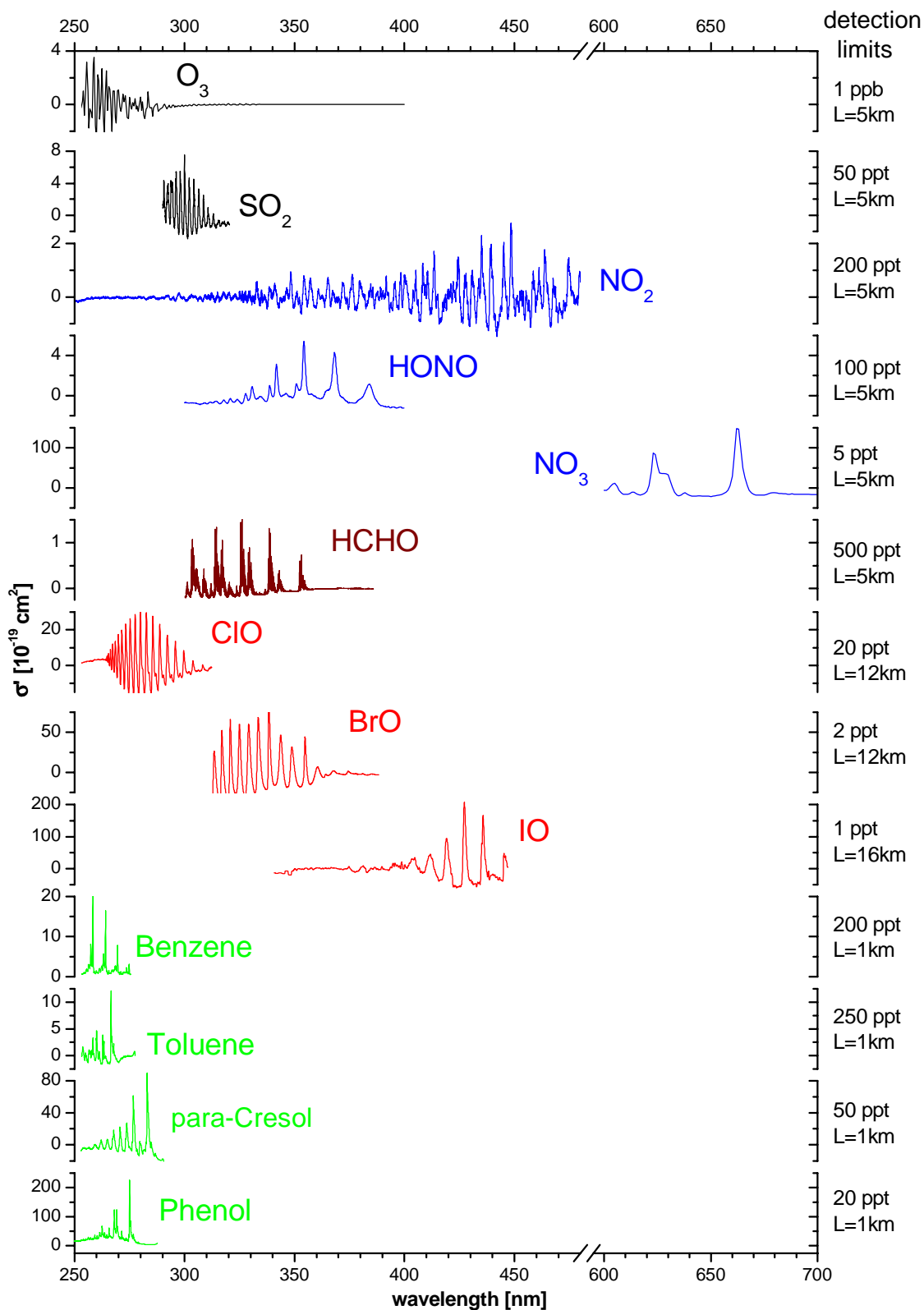


Figure 3.2 Selected differential absorption cross sections σ' of species that are measurable by DOAS. The right-hand scale shows the detection limit for the given light path length L . Please note the interrupted wavelength scale.

3.1.3 The Basics of the DOAS Technique

One missing point in the enumeration of problems of atmospheric measurements above is that it is difficult to determine the true intensity $I_0(\lambda)$ that would be received from the light source without any extinction. The fundamental idea of the DOAS is only to determine the ‘differential’ absorption of trace gases by breaking the total absorption cross sections σ_i of a single trace gas i down into a contribution from the structures portion, $\sigma'_i(\lambda)$, that shows rapid variations in wavelength and from the broadband absorption, $\sigma^B_i(\lambda)$, that varies slowly in wavelength:

$$\sigma_i(\lambda) = \sigma^B_i(\lambda) + \sigma'_i(\lambda) \quad \text{Equ 12}$$

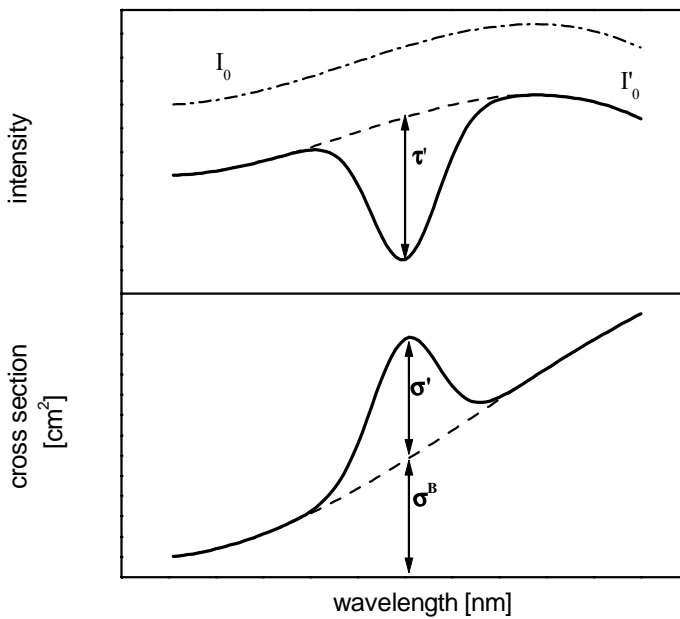


Figure 3.3 Principle of DOAS. The absorption is broken down into two contributions. Part one is slowly varying in wavelength, while the second part shows rapid variations in λ (adapted from Stutz and Platt [1996]). The differential absorption τ' corresponds with the differential optical density σ' .

$\sigma^B_i(\lambda)$ describes the general slope caused by Rayleigh or Mie scattering, while $\sigma'_i(\lambda)$ indicates the rapid variations in λ due to absorption lines. This principle of DOAS is illustrated in Figure 3.3.

‘Rapid’ and ‘slow’ variations of the absorption cross sections are in fact a question of both the observed wavelength interval and the width of the absorption bands that needs to be detected. The nitrate radical NO_3 shows relatively slow variations in λ around 640 nm, while the aromatics show very sharp bands in the UV at about 260 nm. Both can be detected using the

DOAS technique. Inserting Equ 12 in Equ 11 one obtains:

$$I(\lambda) = \left\{ I_0(\lambda) \cdot A(\lambda) \cdot e^{-L \cdot [\sum (\sigma_i^B(\lambda) c_i) + \epsilon_{Ray}(\lambda) + \epsilon_{Mie}(\lambda)]} \right\} \cdot e^{-L \sum (\sigma'_i(\lambda) c_i)} \quad \text{Equ 13}$$

The exponential function behind the brace describes the rapid variation of the spectrum, the so-called *differential absorption*, while the first exponential function considers the broadband variations of the cross sections and the effects of Rayleigh and Mie scattering. The transmission of the optical system, which is varying slowly with wavelength, is summarised in the attenuation factor $A(\lambda)$. Finally one can define a quantity I_0' summarising the brace of Equ 13:

E
q
u
1
4

$$I(\lambda) = I_0(\lambda) \cdot e^{-L \sum (\sigma'_i(\lambda) c_i)}$$

Therefore the *differential optical density* τ' can be calculated taking the natural logarithm:

E
q
u
1
5

$$\tau' = \ln\left(\frac{I_0}{I}\right) = L \sum \sigma'_i(\lambda) c_i$$

In analogy to Equ 10 the trace gas concentration can be calculated by substituting the differential optical density τ' and the differential absorption cross section and column density respectively:

E
q
u
1
6

$$c = \frac{\ln I_0(\lambda, T) / I(\lambda, T)}{\sigma(\lambda, T) \cdot L} = \frac{\tau'}{\sigma'(\lambda, T) \cdot L} = \frac{CD'}{L}$$

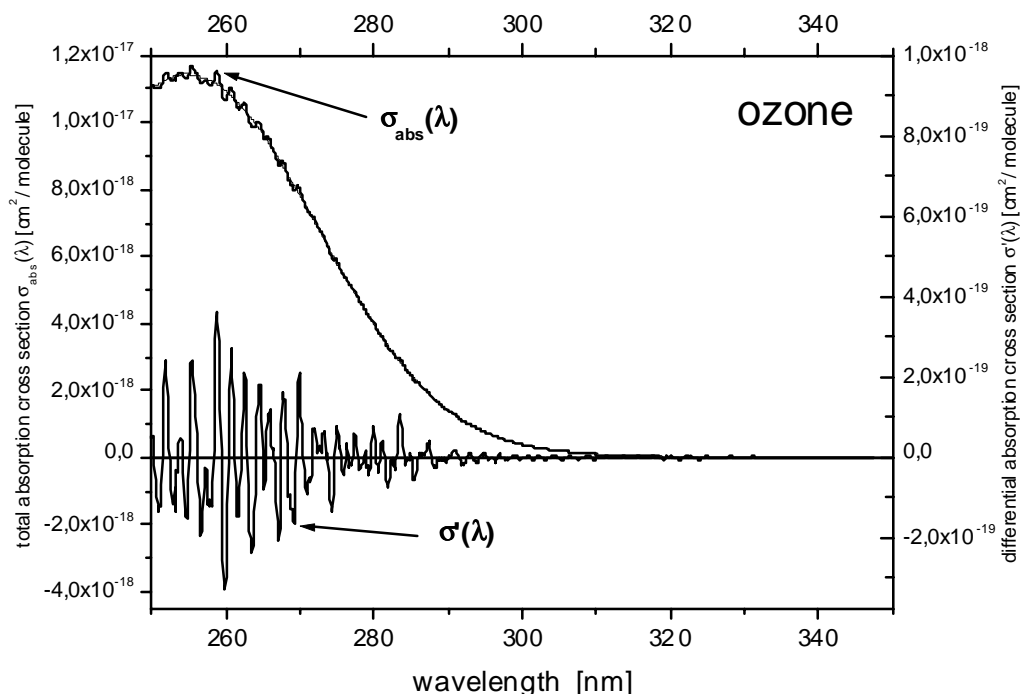


Figure 3.4 Absolute (σ) vs. differential (σ') absorption cross section of ozone. Note the different scales on the left hand (σ) and on the right hand side (σ').

Figure 3.4 shows the absolute and differential absorption cross section of ozone. In practice σ_{abs} is smoothed or a polynomial is adapted to gain a spectrum, which represents the part of σ_{abs} slowly varying in wavelength. As a next step σ_{abs} is divided by this spectrum. This leads to the differential absorption cross section σ' , which represents only the part rapidly varying in wavelength.

3.1.4 Principle of Evaluation of DOAS Spectra

The recorded atmospheric spectra $S(\lambda)$ are made up of 4 different parts: the real intensity spectra $I(\lambda)$, perturbations like the electronic offset O , the dark current D of the detector system and the scattered light $SL(\lambda)$ reaching the detector:

$$S(\lambda) = I(\lambda) + O + D + SL(\lambda) \quad \text{Equ 17}$$

For further analysis the atmospheric spectra need to be debugged by subtraction of suitable offset, dark current and scattered light spectra respectively. In the following ‘measured spectra’ means the intensity spectra $I(\lambda)$ corrected for O , D and $SL(\lambda)$.

As a first step of the evaluation, the narrow absorption lines of the trace gases need to be separated from the broadband structures of e.g. aerosol extinction, as explained above. This corresponds to the change from I_0 to I'_0 in Figure 3.3.

In practice a measured atmospheric spectrum $I(\lambda)$ should extend over at least two absorption bands in order to reduce interference effects of different absorbers. Furthermore, instead of measuring the differential depth of an absorption band of one species, a combination of a linear and non-linear least-square fitting procedure is used to determine the concentrations of a number of species simultaneously [Stutz and Platt, 1996]. The negative argument of the first exponential function of Equ 13 and Equ 14 can be written as:

$$L \sum \sigma_i'(\lambda) c_i + L \left(\sum \sigma_i^B(\lambda) c_i + \varepsilon_{\text{Ray}}(\lambda) + \varepsilon_{\text{Mie}}(\lambda) \right) = L \sum \sigma_i'(\lambda) c_i + f(\lambda) = \wp(\sigma_i, \lambda)$$

$$\text{Equ 18}$$

Therefore the differential optical density τ' (Equ 15) can be expressed as a linear combination of differential trace gas cross sections σ_i and a function $f(\lambda)$ characterising the broadband extinction processes. The most common approximation of $f(\lambda)$ was adapted by Platt *et al.* [1979], who suggested a polynomial of a specified degree. Depending on the wavelength interval and the shape of the structures that need to be adapted, different orders of polynomial (from 1st to 9th) are used today. Besides the approach of a polynomial, other high-pass filter algorithms like triangular smoothing and Savitzky-Golay smoothing [Savitzky and Golay, 1964] are applied. For detailed information about the filter behaviour of various algorithms refer to Volkamer [1996].

Using the software MFC [Gomer *et al.*, 1993; Stutz and Platt, 1996], up to nine reference spectra and a polynomial of the order of up to nine can be adapted to the logarithm of the measured spectrum $I(\lambda)$. This fitting algorithm uses the *Levenberg-Marquard* method

[Levenberg, 1943; Marquardt, 1963], which is an iterative combination of a linear part for the retrieval of the trace gas absorptions and a non-linear part which accounts for possible spectral shifts between the measured spectrum and the reference spectra in order to minimise the integral given below:

$$\int_{\lambda_{\min}}^{\lambda_{\max}} (\tau'(\lambda) - \rho(\lambda))^2 d\lambda = \text{Min} \quad \text{Equ 19}$$

A number of differential absorption cross sections that are typically applied in DOAS evaluations are shown in Figure 3.2. Note that the whole electromagnetic spectrum from the UV to the visible red region is covered by the DOAS technique, allowing a huge number of species to be measured in the atmosphere.

As will be described in section 3.2.5, the spectra are recorded with a slotted-disk spectral scanning device (*SSD*) or a photo-diode-array detector (*PDA*) system. Both systems have in common that the light passing through the spectrograph is divided into a given number of discrete channels. In the following ‘channel’ and ‘diode’ will be used synonymously even if there is only one diode in a SSD detector system. The typical number of channels is 810 for a SSD and 1024 for a PDA system respectively. The signal obtained by a single channel represents the integrated intensity over the wavelength range $\lambda_{i,\text{low}}$ to $\lambda_{i,\text{high}}$ with the central wavelength λ_i :

$$I(\lambda_i) = \int_{\lambda_{i,\text{low}}}^{\lambda_{i,\text{high}}} I'(\lambda') d\lambda' \quad \text{Equ 20}$$

The aim of the fitting process is to minimise the difference between the measured optical depth τ' and the sum of the reference spectra for every single pixel i . Taking into account the possibility of fitting an additional polynomial (to remove broad structures), the integral of equation Equ 19 can be written as

$$\sum_i^n \left(\tau'(\lambda_i) - \sum_j \alpha_j \sigma_j'(\lambda_i) - \sum_k \beta_k \lambda_i^k \right)^2 = \text{Min} \quad \text{Equ 21}$$

where i is the channel number and n the number of channels. α_j denotes the fitting coefficient of the j^{th} reference absorption cross section σ_j' , while β_k are the coefficients of an additional polynomial that can be adapted to correct broad structures that have not been removed by the primary high-pass filter process described above. The difference between the measured optical density and the result of the fitting routine, the residual or residual structure, is an indicator for the quality of the spectral fitting results. When the optical density of the residual is small compared with the trace gas absorption derived in the fitting procedure, the respective trace gas can be detected easily. After minimising the residual, the average concentration of trace gas j along the light path can be determined by dividing the fitting coefficient by the length of the light path L . As will be shown in part d) of this section, the residual plays an important part in the calculation of errors and, consequently, regarding the quality of the fitting results.

a) 'Shift' and 'Squeeze'

It is possible to vary the wavelength calibration of the spectrum which means to allow shifts¹⁷ and squeezes¹⁸ of the reference spectra versus each other and versus the atmospheric spectrum in order to minimise the residual in an iteration process. In the next step of the fitting process the algorithm optimises the residual by varying the shift and squeeze parameter, while the number of iterations and stopping criteria can be defined. In this thesis neither automatic shift nor squeeze processes were applied in the evaluation of the spectra recorded at Mace Head. In the case of the spectra recorded at the Dead Sea the shift parameters had to be determined non-automatically because of their relatively large amounts of up to 50 channels, as will be discussed later.

b) Self-Recorded Reference Spectra

The quality of the specific reference spectra is very important for the quality of the evaluation. Even if cross sections of most of the common trace gases are available in literature, it might be better to record the reference spectra with the same instrument (especially spectrograph and detector) as the atmospheric spectra. Doing so, the logarithm of an absorption spectrum taken from a direct measurement through a quartz cell is used in the fitting routine. In this case the instrumental function, such as features caused by the diode array or the spectrograph, is automatically adapted to the reference.

If possible these 'individual references' need to be determined during the field campaigns in order to take into account variations of the instrumental function, such as of the aperture, that may be caused by transport or other vibrations, a new alignment or temperature variations. It is self-evident that the individual references should be treated like the atmospheric spectra. Therefore the same measuring routines and band-pass filter processes are applied.

c) Literature Cross Sections

Reference spectra have to have the same resolution and wavelength calibration as the atmospheric spectra. In order to make use of literature cross sections one has to convolute these data with the individual instrumental function. Here only a short summary of the simulation of DOAS reference spectra is given, for a more comprehensive description please refer to *Stutz* [1996].

From the mathematical point of view the recording of a spectrum with a spectrograph is in accordance with a convolution process. The continual and ideal dispersed intensity spectrum $J(\lambda)$ is convoluted with the instrumental function of the spectrograph:

$$J^*(\lambda) = J(\lambda) \otimes H(\lambda) = \int J(\lambda - \lambda') \cdot H(\lambda') d\lambda' \quad \text{Equ 22}$$

¹⁷ The relative position of the spectra vs. each other is changed by a number of channels

¹⁸ The spectra can be linear 'squeezed' by keeping channel a fixed while channel b is squeezed/expanded to another channel-position b+s.

$H(\lambda)$ denotes the instrumental function that can be approximated by a mercury or neon emission line. These atomic lines show a full width at half maximum (FWHM) of 10^{-3} nm, which can be assumed as a delta function compared with the typical DOAS resolution of 0.1 to 1 nm. After recording such a mercury line with the DOAS instrument, the same convolution process can be carried out mathematically by means of a literature cross section. As *Stutz* [1996] pointed out, the resolution of the literature cross section needs to be much better than the resolution of the spectrograph.

First of all the literature cross section and the instrumental function need to be interpolated to a linear dispersion. After that, as the literature cross sections σ are given as absolute values, σ needs to be multiplied with a typical column density, and the exponential function natural base e needs to be calculated, as the convolution requires an intensity spectrum. This spectrum can be convoluted with the normalised atomic emission line. The result can be used as a self-recorded reference spectrum after adapting the wavelength-channel relation of the atomic line spectrum. With a literature cross section σ , a typical column density CD and a mercury emission line H the reference spectrum σ^* is given by:

$$\sigma^*(\lambda) = \sigma(\lambda) \otimes H(\lambda) = \int e^{-\sigma(\lambda')CD} H(\lambda - \lambda') d\lambda' \quad \text{Equ 23}$$

Due to temperature variations and other disturbances the instrumental parameters are not constant over the period of a campaign. Therefore it is necessary to record a number of instrumental functions per measuring period depending on the stability of the instrumental set-up.

d) Error Determination

The overall error of DOAS measurements is composed of errors made by the recording of the spectra, the so called instrumental errors, and errors made by the analysis of the spectra. Divided into ‘systematic’ and ‘statistical’ the following errors need to be taken into consideration:

Systematic Errors:

- Depending on the species to be determined the error of the literature cross section is typically 1 to 15 %.
- Due to the convolution process and differences in the wavelength-channel relation an error of up to 2-3 % occurs.
- *Stutz* [1996] determined the error made by the DOAS measuring instrument to be approximately 3 %.
- Using a laser range finder or two GPS instruments, the error in determining the atmospheric light path, which is of the order of some kilometres, is better than 1 %.

Statistical Errors

The statistical error for the derived concentrations can be determined from the random structures of the residual according to *Stutz and Platt* [1996] and *Stutz* [1996]: Within the MFC fitting process a statistical error is determined for every reference spectrum adapted and stated as a 1σ -error. This error takes into account the number of absorption bands, the number of channels of the evaluation, the intensity of the recorded spectrum and some related quantities as well as uncertainties in the wavelength-channel relation.

However, especially measurements in the troposphere with artificial light sources may produce residuals containing persistent spectral structures which can be caused by errors in the spectral calibration of the reference spectra, the temperature dependence of the cross sections, several effects arising from scattering processes in the atmosphere or by absorption of so far unidentified species. Furthermore, variable emission features of the light source and from instrumental artefacts can generate systematic spectral features. Such structures have to be considered carefully in order to optimise the spectral fitting procedure and to determine the uncertainty of the derived concentrations [*Ferlemann*, 1998].

For that purpose the statistical error of an evaluated concentration calculated from the least-square fitting algorithm underestimates the real error if the average width of the absorption structure and the residual are considered. In this thesis a correction factor of 2 was considered.

Detection Limit

The detection limit is dependent on the statistical error. Commonly it is given as the 2σ -error. As the statistical errors are varying for every single reference spectrum for every atmospheric spectrum, the detection limit is not constant in time. Furthermore, different light paths are used depending on visibility and weather conditions. The concentration of the trace gases, as well as the statistical errors, are calculated by dividing the coefficients by the length of the light path L (Equ 16). This leads to a negative correlation of the detection limit and L . In addition, the signal-to-noise ratio is higher at high visibility and therefore on the long light. Consequently, the statistical errors are bigger at low visibility and on short light paths. Therefore, in general the statistical error is a) variable and b) negatively correlated with the length of the light path L .

3.2 The Instrumental Set-up

Two different DOAS-long-path (DOAS-LP) systems were used within the framework of this thesis. The first one, applied during the Dead Sea campaign, was a system which was developed in the late 1970s by *Platt et al.* [1979]. It consists of two separate telescopes, one as an emitting and one as a receiving telescope. A SSD was used as a detector. A detailed account of all components of the original SSD set-up can be found at *Platt and Perner* [1983] or *Heintz et al.* [1996].

The second DOAS-LP system is a modern version of the original set-up and consists of one double Newtonian telescope and a photo-diodearray as a detector. Both systems will be described in the following sections, starting at the light sources and following the light through the emitting telescope out through the atmosphere and back to the detector. A detailed description of the modern set-up, using a PDA detector system, is provided in *Stutz [1991]*, *Platt [1994]* and *Stutz [1996]*. Figure 3.5 represents the set-up of the two LP-DOAS instruments. Part A shows the older system used at the Dead Sea, part B shows the schematic set-up of the system which was used at Weybourne and Mace Head.

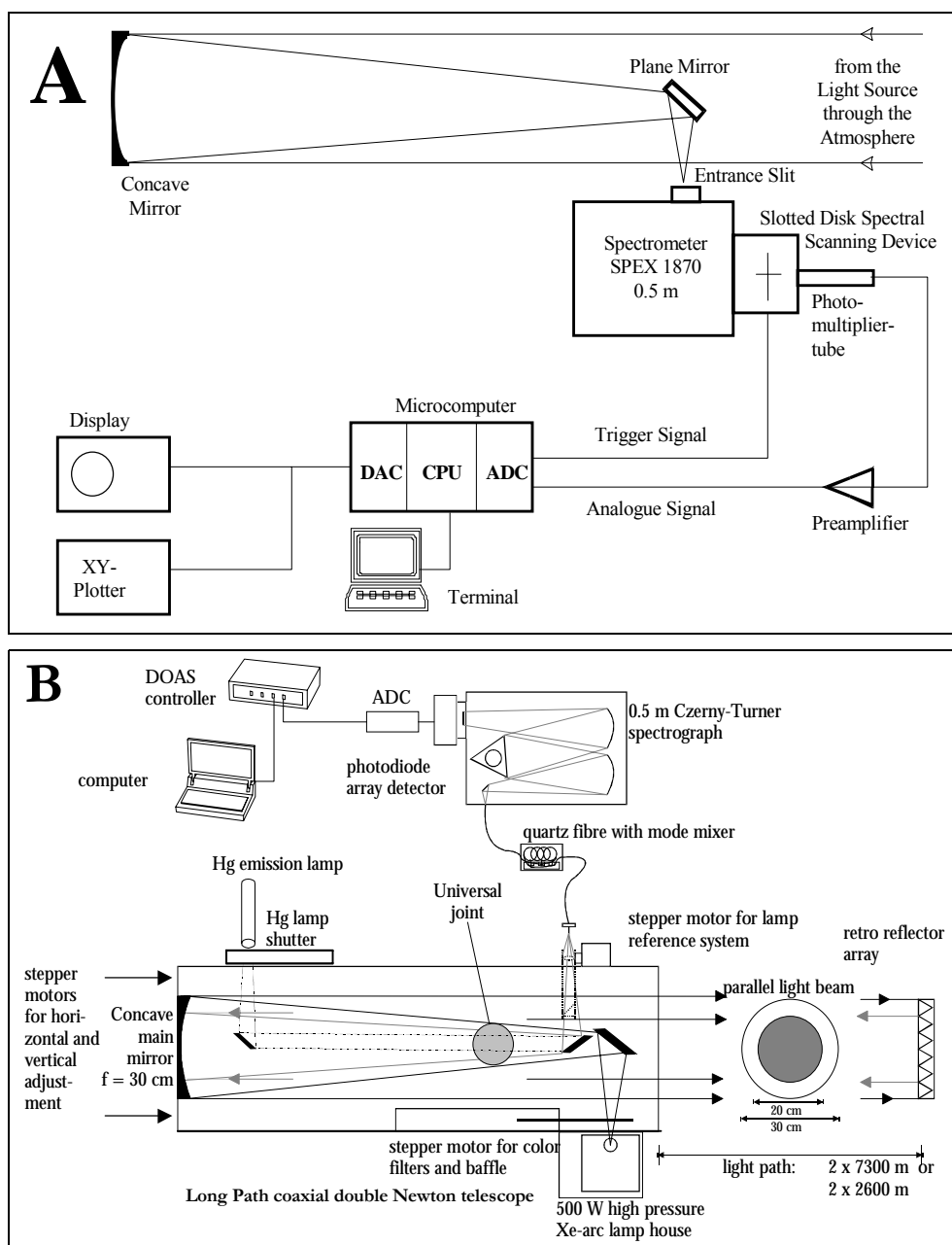


Figure 3.5 Typical set-up of the DOAS-LP systems as they were used within the framework of this thesis (panel A : Dead Sea campaign, panel B: Weybourne and Mace Head campaigns)

3.2.1 Light Sources

The light sources used for the DOAS measurements within the framework of this thesis are high-pressure Xenon arc lamps, as they are commercially available for the use of cinema film projectors. A high-voltage ignition discharge plasmasizes the Xe-gas and produces a light arc of approximately one millimetre diameter between the anode and the cathode. The typical spectrum of a Xe arc lamp is a superposition of the thermal emission according to Max Planck's law and single Xe emission lines. Under operating conditions the Xe gas is under high pressure of up to 100 bar in the lamp body. Therefore the atomic emission lines are broadened by pressure and temperature. The colour temperature of the lamps is approximately 6000 K, which is similar to that of the sun. A high local light intensity and a small divergence of the emitted light beam can be attained because the small distance of the electrodes results in a small arc length.

Table 3.1 Characteristic parameters of the lamps used within the framework of this thesis.

Parameters	Dead Sea Campaign	Weybourne 1996 and Mace Head Campaigns 1997/98
Manufacturer	Osram GmbH, München	Canrad-Hanovia, Newark. N.J
Type	Osram XBO 450W	Hanovia 500W
Power	450 W	500 W
Voltage	17 V	17 V
Current	25 A	29 A
Typical life time	2000 h	200 h
Size of light arc	2.7 x 0.9 mm ²	0.3 x 0.3 mm ²

As the flask of a Xe lamp consists of a quartz glass which is extremely resistant to pressure and temperature relatively high light intensity in the UV region can be attained. The electrodes are made of tungsten with endowments depending on the lamp type. The cathode has a spiky peak to focus the electron emission, while in contrast to that the anode is made of massive material which is to absorb the kinetic energy of the incoming electrons. Within the framework of this thesis two different kinds of Xe arc lamps were used. A comparison of the lamps is given in Table 3.1.

A number of lamps including the two types used here were analysed in an extensive study of *Hermes* [1999]. As also observed during the measurements for this thesis, his study underlines that both types showed variability of the emission features caused by flickering lamp plasma. Xe emission lines were observed at several wavelengths, while the emission strength and pressure broadening were found to change in time. Therefore the lamp structures are difficult to remove from a spectrum. *Hermes* [1999] found that lamp structures are easier to remove in the case of the *Hanovia* lamp, as its Xe emission bands are broader and therefore can be reduced more effectively by high-pass filter routines.

The system used at the Dead Sea did not allow the recording of lamp spectra as the *Osram XBO* lamps and the emitting telescope used were located 3.75 km away from the receiving telescope and the detector. Therefore no clear lamp spectra could be recorded without sending light through the atmosphere.

Hanovia lamps were used at Weybourne and at Mace Head where the set-up allowed to record lamp reference spectra. These spectra are pure lamp emission spectra, recorded with a short-cut system integrated into the telescope. As the light did not pass through the atmosphere (except the length of the telescope), it is possible to record the clear lamp emission spectra without the influence of atmospheric absorbing matter. However, compared to the 'normal' atmospheric spectra this short-cut system causes faults due to the use of lenses and due to the fact that not the whole light arc is reproduced onto the entrance slit of the spectrograph.

3.2.2 The Telescopes

The instrument used at the Dead Sea consists of two Newtonian telescopes for emitting and receiving the DOAS light beam. The transmitting telescope ($f = 265$ mm, diameter = 300 mm) was set up on the rooftop of a hotel at a distance of 3.75 km from the receiving telescope. The receiving telescope with a parabolic main mirror of a focal length of $f = 1800$ mm, diameter = 300 mm, and the spectrograph and detector unit (see Figure 3.5 A) were placed inside a van, the mobile laboratory of the Hebrew University of Jerusalem. On the optical axis of the receiving telescope an elliptic plane mirror was located to reflect the incoming light by 90 degrees right on the 200 μm entrance slit of the spectrograph. The incoming light was focused on the entrance slit by adjusting the main mirror with two stepper motors along its longitudinal and lateral axis. These two stepper motors were also used to defocus the light from the entrance slit if background spectra were recorded.

The telescope unit which was used at Mace Head consists of only one coaxial Newtonian telescope with transmitting and receiving optic combined in one device. As can be seen in Figure 3.5 B, two elliptic plane mirrors are mounted on the optical axis of the telescope. The first reflects the light coming from the lamp by 90 degrees to the 300 mm parabolic main mirror with a focal length of $f = 150$ cm. A parallel outgoing light beam is obtained if the light source is placed in the focal point of the main mirror. A retroreflector array at a distance of several kilometres is used to reflect the parallel light beam exactly back into the telescope, where it is focused via the main mirror and the second elliptic plane mirror onto a quartz fibre. The quartz fibre passes a mode mixer and transmits the light into the spectrograph.

The optical image, however, is not perfect as the light source is no real point source, but shows an expansion of about one square millimetre. Therefore the light beam slightly diverges along its path through the atmosphere, resulting in a loss of light depending on the distance from the retroreflectors. Furthermore, caused by the two plane mirrors along the optical axis of the telescope, only a ring of light can be sent out to the atmosphere, leading to a loss of light intensity of 50 %.

The retroreflectors used in this case are Quartz triple prisms of 63 mm diameter, which are mounted in a thin metal or plastic housing. Within a precision of 2 arc sec the incoming light is reflected back to the telescope. Usually a number of retroreflectors is arranged very close to each other, forming a ‘retroreflector array’.

Overall 6 stepper motors were mounted to the telescope:

- Two main motors were used to align the telescope in the horizontal and vertical direction in order to focus the light beam onto the retroreflector array.
- One stepper motor carried a number of attenuation filters (25 % and 50 % grey filter, *Schott, Germany*) to reduce the absolute light intensity.
- One stepper motor carried a *OG570* and a *GG395* filter (*Schott, Germany*) to cut off at the respective wavelengths in order to reduce the influence of stray light in the spectrograph and a baffle to record background spectra.
- One stepper motor was used as a shutter for the Hg-atomic emission lamp which is used as a wavelength calibration.
- One stepper motor was used to move the optical ‘reference shortcut system’ into the outgoing light beam. It consists of an elliptical plane mirror which reflects part of the outgoing light beam onto a quartz lens from which it is focused onto the quartz fibre.

3.2.3 The Quartz-Fibre Mode Mixer

Unlike the system used in Israel, a quartz fibre combined with a quartz-fibre mode mixer was used at Weybourne and Mace Head to transfer the light from the telescope into the spectrograph. Especially during field campaigns, where the set-up of a LP-DOAS system may be relatively unstable compared with laboratory set-ups, the application of fibres is useful to ensure the illumination of the entrance slit of the spectrograph. The quartz fibre used was a multi-mode step-index fibre with a numerical aperture of 1:8.

The light leaving the fibre shows interference fringes (‘modes’) produced by the total reflections inside the fibre. *Stutz and Platt* [1997] found that this heterogeneous illumination of the grating and the PDA leads to high residual structures in data evaluation. That is why a quartz-fibre mode mixer [*Stutz and Platt, 1997*] is supplemented to the modern DOAS systems. This mode mixer combines a specific squeezing with a random deformation of the fibre, which leads to an equally spread illumination and therefore to a reduction of the residual structures. In spite of the incorporation of the mode mixer, the residual noise is generally higher compared with laboratory tests of the spectrograph-detector system with direct light transition.

3.2.4 The Spectrographs

The spectrograph used at the Dead Sea was a 0.5 m Czerny-Turner instrument (*SPEX 1870C*, 1200 groves/mm, leading to 0.0306 mm/channel) based on a set-up developed by *Czerny and Turner* [1930]. The light beam was received directly through an open window

and focused by the receiving telescope onto the 200- μm entrance slit of the spectrograph. Inside the spectrograph the light was paralleled by the spherical mirror and reflected to a plane diffraction grating. The dispersed light was then focused by a second convex spherical mirror onto the detector unit. The spectrograph was located in the air-conditioned mobile laboratory of the Hebrew University Jerusalem. Due to the open window the temperature in the van was varying by ~ 10 K. The limited individual thermal stabilisation of the spectrograph caused periodic variations and especially shifts in the wavelength-to-channel relation (dispersion) over time (see section 4.5.4 a)).

The spectrograph used for the measurements carried out at Weybourne and at Mace Head was an *ACTON spectra Pro 500*, which is based on a set-up of *Czerny and Turner* [1930] as well. The quartz fibre, which transmits the light from the telescope to the spectrograph, ends in the focal plane (entrance slit) of a convex mirror. The width of the entrance slit was adjusted to 200 μm . As in the case of the *SPEX1870C* described above the light was paralleled by the spherical mirror and reflected to a plane diffraction grating. In contrast the grating was mounted on a turnable table. Therefore the wavelength of a spectrum focused by a second convex spherical mirror onto the detector unit could be changed automatically by a computer-controlled stepper motor (tolerance 0.5 steps). The focal length of the spectrograph was 500 mm, its aperture 1:6.9. The dispersion of the grating used at Weybourne and Mace Head 1997 (600 grooves/mm) was -0.078 nm/channel. In order to minimise thermal misalignment the whole spectrograph unit was thermally isolated and the temperature stabilised at 30 ± 0.2 °C by a PID controller.

3.2.5 The Detector Systems

Two different approaches have been used within the framework of this thesis. As the systems are totally different, they are described in two separate sections. The one that will be described first in section a) is an optomechanical scanning device. In this arrangement the exit slit of the spectrograph is replaced by a rotating disc including typically 60 slits. This system is called *slotted-disc spectral scanning device (SSD)* and was used at the Dead Sea. The second, more common system is a *photo-diode-array detector (PDA)* system that was used during the campaigns at Weybourne and Mace Head. It will be described in section b).

a) *Slotted-Disc Spectral Scanning Device*

After the light has been dispersed in the spectrograph, the spectrum is focused on the exit focal plane of the monochromator. Instead of only one exit slit 60 movable exit slits are used. These slits are radially etched in a thin metal wheel, rotating behind a mask that allows a segment of typically a few of up to 100 nm of the spectrum to pass (Figure 3.6). A photo multiplier tube (PMT) is used as a detector .

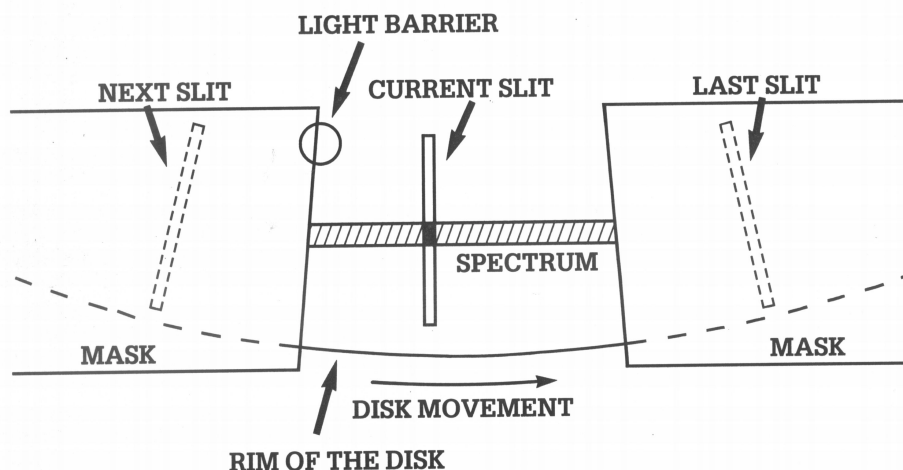


Figure 3.6 Schematic diagram of a slotted-disk spectral scanning device used during the Dead Sea campaign [Platt and Perner, 1983].

Its output signal is digitised by a high-speed analogue-to-digital (A/D) converter, allowing measurements (read-outs) at several hundred locations per scan. 820 read-outs were made during the measurements related to this thesis. This corresponds to 820 wavelength intervals. Simultaneously only one rotating slit is in the aperture. The beginning of a scan¹⁹ is signalled by a light barrier at the edge of the mask that sends a trigger signal to the computer to accommodate data. The amounts of the different intervals are stored in corresponding channels by a computer. As the next rotating slit crosses the light barrier, the next scan is performed and the signals are stored in the appropriate channels. Typically, some 10,000 scans are averaged, resulting in an increase in the signal-to-noise ratio. For a more detailed description please refer to Platt [1994] and Platt and Perner [1983].

b) Photo-Diode-Array Detector System

Instead of only one PMT the principal item of the detector unit used at Weybourne and Mace Head is a photo-diode-array (PDA). Two different types were applied within the framework of this thesis. In the first two campaigns at Weybourne and Mace Head a *EG&G reticon RL 1024R random access* was used. In the second campaign at Mace Head in 1998 a *Hamamatsu* PDA (Type S3904-1024) was applied. Both types have 1024 Si photo diodes (CMOS) of a width of 25 μm and a height of 2.5 mm each. The PDA is located in a steel can, which is evacuated and filled with 1.2 bar of Ar 5.0. Inside the can a *Peltier element cascade* is used to cool the PDA down to -15 to -35 $^{\circ}\text{C}$. The capacity of a diode is 10 pF, full charge corresponds to 1.3×10^8 photo electrons²⁰. A detailed discussion of the usage of PDAs as DOAS detectors is given by Stutz [1991] and Senne [1996], for a comparison please refer to Kah [1998].

Each photo diode represents a n-p junction. During operation an inverse voltage of 2.06 V is applied to the diode inducing a depletion layer which is almost as large as the whole

¹⁹ one pass of one slit over the aperture of the mask

²⁰ $Q = C U = 10^{-11} \text{ F } 2 \text{ V} = 2 \times 10^{-6} \text{ As}$; $N = Q/q_e = 2 \times 10^{-6} / 1.6 \times 10^{-19} = 1.3 \times 10^8$

diode area. Incoming light excites a number of electrons proportional to the light intensity into the conducting layer of the semiconductor. These mobile charge carriers reduce the applied inverse voltage. The voltage is also reduced by the transition of thermally activated electrons into the conducting layer. This dark-current effect must be considered in the evaluation procedure especially at low light intensities. In order to reduce dark current, which decreases exponentially with decreasing temperature [Stutz 1996], the PDA was cooled down to temperatures between -15 and -35 °C by a *Peltier cascade*. As the dark current depends also on the integration time an integration-time-corrected dark-current spectrum is subtracted from every atmospheric spectrum within the evaluation.

After the PDA has been read out, the signals are electronically amplified. To exclude negative signals under low light conditions an offset signal is added to every PDA signal. As the final spectrum can be composed of a number of single scans, it is obvious that the offset-correction of the final spectra must be performed with respect to the number of scans. The signals are then digitised by a 16-bit analogue-to-digital converter (ADC) with full saturation of $2^{16} = 65536$ counts. Finally the spectra are transmitted to a computer.

The PDA is covered with a thin quartz window, which can lead to *Fabry-Perot etalon* structures in the spectra (cf. Stutz [1991]). These structures are caused by the interference of multi-reflected light inside this surface layer. Furthermore, even if the detector unit has been evacuated and filled with dry argon as inert gas, residual water vapour could freeze out on the cooled PDA. This may cause etalon or other structures in the spectra as well.

Another effect of PDAs is the memory effect. That means that structures of a former spectrum can be seen in the following spectra. This effect was discussed in detail by Stutz [1996]. However, its origin is unclear to date. Usually the memory effect can be significantly reduced by multiple readouts of the PDA without light exposure or by an adequate relaxation between the scans.

c) *The Multi-Channel Scanning Technique*

In order to avoid spectral features due to the varying sensitivity of the individual diodes of the PDA detector the *Multi-Channel Scanning Technique (MCST)* was applied. It was published first by Knoll *et al.* [1990] and later adapted to the DOAS technique by Brauers *et al.* [1995]. Within the framework of this thesis the MCST was adapted at the campaign in Weybourne and the two campaigns in Mace Head.

In general, the spectra recorded with PDAs show two kinds of variations: Structures that are varying in wavelength like (i) rapid varying absorption features of trace gases $A(\gamma, i)$, (ii) broad structures due to Rayleigh and Mie extinction $B(\gamma, i)$, (iii) noise $N(\gamma, i)$ and (vi) the primary intensity $I_0(\gamma, i)$. Furthermore, PDAs show structures that are only dependent on the channel number $E(i)$ due to the individual sensitivity of the diodes. Assuming a linear dispersion one gets:

$$i = \gamma(\lambda) = a \cdot \lambda + b \quad \text{Equ 24}$$

$$I(\gamma, i) = E(i) \cdot A(\gamma, i) \cdot B(\gamma, i) \cdot I_0(\gamma, i) \cdot R(\gamma, i) \quad \text{Equ 25}$$

Here i denotes the number of channels, γ the wavelength-channel relation and λ the wavelength of channel i .

The fundamental idea of the MCST is to record not only one spectrum of the type given in Equ 25, but k spectra, which are slightly shifted vs. each other. These spectra $I_k(\gamma_k, i)$ are added afterwards. During the measurements at Mace Head a series of $k = 9$ spectra was recorded with a shift of 0.4 nm rum, which corresponds to a shift of ~ 5 channels. By adding these spectra I_k to a summation-spectrum $I_S(i)$ the features that are fixed to different individual diodes are relatively reduced due to the summation. In the mathematical description one can extract this contribution from the summation as it is independent of wavelength. Now the summation consists only of broad-banded functions that can be replaced by one spectrum $I_b(i)$:

$$\begin{aligned} I_S(i) &= \sum_{k=1}^9 I_k(\gamma_k, i) \\ &= E(i) \cdot \sum_{k=1}^9 A(\gamma_k, i) \cdot B(\gamma_k, i) \cdot I_0(\gamma_k, i) R(\gamma_k, i) = E(i) \cdot I_b(i) \end{aligned} \quad \text{Equ 26}$$

Finally, the spectra I_k are divided by the summation spectrum I_S , leading to k single spectra \hat{I}_k . These spectra \hat{I}_k are shifted back to their original wavelength position and summarised to the resulting MCST spectrum I_{MCST} :

$$\hat{I}_k(\gamma_k, i) = \frac{I_k(\gamma_k, i)}{I_S(i)} = \frac{I_k(\gamma_k, i)}{E(i) \cdot I_b(i)} \quad \text{Equ 27}$$

$$I_{MCST} = \sum_{k=1}^9 \frac{A(\gamma_k, i-k) \cdot B(\gamma_k, i-k) \cdot I_0(\gamma_k, i-k) \cdot R(\gamma_k, i-k)}{I_b(i)} \quad \text{Equ 28}$$

I_{MCST} is extensively reduced by channel-fixed structures as every channel includes the average intensity of a number (here 9) of diodes. *Stutz* [1996] pointed out that channel-fixed structures could be reduced by some orders of magnitudes applying the MCST. The disadvantage of the MCST is the unintentional reduction of the differential optical density that occurs by dividing the spectra I_k by the broad-banded spectra I_b . Furthermore, the shape of the absorption bands changes significantly. In general this operation is comparable to a high-pass filter process. To equalise this effect the reference spectra have to be treated in the same way. In the case of self-recorded reference spectra (see 3.1.4 b)) one has to use the same application as it is used for the atmospheric case; for the literature cross sections one has to use a MCST simulation routine.

Chapter 4

Field Observations and Results

The aim of this thesis was to investigate whether or not halogen oxides are detectable in the mid-latitudinal troposphere and - if this is the case - what the implications are for atmospheric chemistry. Four field campaigns have been carried out in order to investigate the role of halogens in this region. This chapter reports the conditions we found during the campaigns at three different sites and in three different seasons. Table 4.1 gives an overview of the campaigns and a description of the different measurement periods, sites and projects related to these campaigns.

Table 4.1 Overview of the campaigns performed within the framework of this thesis.

Place/Name	Period	Characteristics of Site & Campaign
Weybourne 1996 WB96	10.10. – 27.10.96	Maritime site at the north-east coast of England, facing the North Sea. Co-operation with the <i>University of East Anglia (UEA)</i> within the framework of the EU-project <i>HALOTROP</i>
Mace Head 1997 MH97	17.04. – 01.06.97	Most famous European clean-air site at the west coast of Ireland facing the Atlantic Ocean. Measurements were performed within the framework of <i>HALOTROP</i> in co-operation with the British <i>ACSOE</i> project.
Dead Sea 1997 DS97	26.05. – 21.06.97	Continental/urban site at the salt lake of the Dead Sea Valley. Measurements were performed in co-operation with the <i>Hebrew University Jerusalem, Israel (HUJI)</i> , funded by the <i>German-Israelite-Foundation (GIF)</i> .
Mace Head 1998 MH98	07.09. – 07.10.98	Same site as <i>MH97</i> , measurements were performed within the framework of the British <i>PARFORCE</i> project.

¹ Contributions of Reactive **H**alogen Species to the **O**xidation Capacity of the **T**roposphere

² Atmospheric Chemistry Studies in the **O**ceanic **E**nvironment

³ New **P**article **F**ormation and Fate in the **C**oastal **E**nvironment

The first two campaigns, carried out at Weybourne, England, in autumn 1996 (**WB96**) and at Mace Head, Ireland, in spring 1997 (**MH97**), have been described in great detail by *Alicke* [1997]. Therefore only a short overview of the measurements performed there and

the fundamental results obtained will be given in section 4.1 and 4.2. For more details, especially concerning the evaluation of the data, refer to *Alicke* [1997] and *Alicke et al.* [1999]. The third campaign performed in a coastal environment was again carried out at the Atmospheric Research Station of Mace Head in late summer 1998 (**MH98**) and will be reported in section 4.3. The Mace Head measurement site will be described only once in section 4.2.1. In section 0 the results of MH98 will be presented. The fourth campaign was carried out at the Dead Sea, Israel in early summer 1997 (**DS97**). It will be described at the end of this chapter in section 4.5 and not in the actual chronological order, as it differs from the three other campaigns concerning its geographical location (continental/urban vs. marine/European background) and its main species of interest (BrO vs. IO). Finally, section 4.6 presents the results of DS97.

4.1 *The Weybourne Campaign 1996*

The campaign was carried out within the framework of the EU project *HALOTROP* and in co-operation with the British project *ACSOE*. In this section the Weybourne measurement site will be described first, followed by an outline of the meteorological conditions. A summary of the results of the campaign will be given in section 4.1.3.

4.1.1 The Weybourne Measurement Site

From Oct 10 to Oct 27, 1996 measurements were carried out at the atmospheric observatory of the University of East Anglia (UEA) at Weybourne. The site is located at the north coast of England (coastline straight east to west direction) and faces the North Sea. Northerly conditions are regularly observed at this station. This permits to analyse clean air masses representing European background conditions as the air is of polar origin, reaching England after passing over the North Sea between Scandinavia and Great Britain. Figure 4.1 A shows the geographical location of the observatory, which is located in a rural environment right beside the small village of Weybourne.

The DOAS measurements were basically carried out with the same set-up described in section 3.2 regarding the Mace Head campaign 1998. Together with the DOAS group of the UEA we used two DOAS-LP instruments to measure along the same folded light path of 5 km path length in total. The beam extended parallel to the water line in a distance of 200 m at a height of 10 to 3 m above sea level. Part B and C of Figure 4.1 show the site and the light path as sectional and as top view respectively.

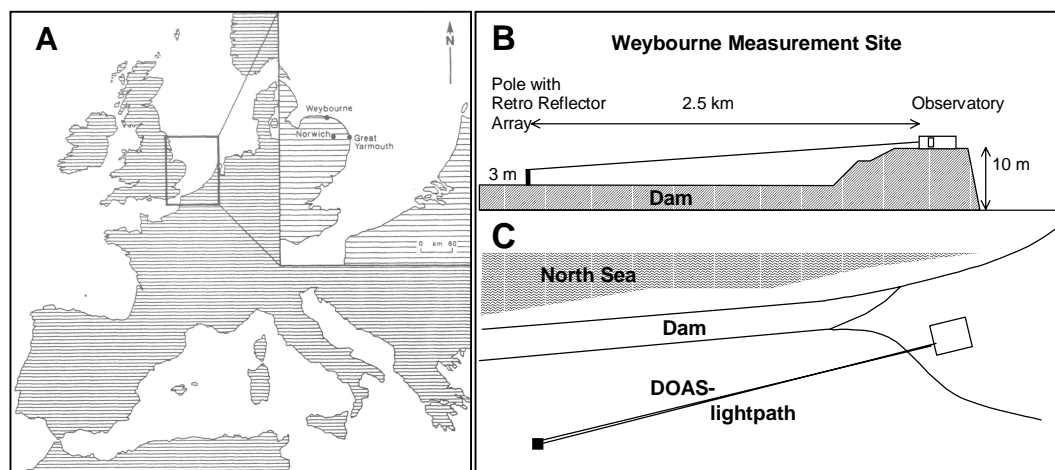


Figure 4.1 (A) Map of the atmospheric observatory of the University of East Anglia, Norwich. (B) Sectional view and (C) top view of the Weybourne site.

4.1.2 The Meteorological Conditions at WB96

The meteorological conditions during the two-week campaign were dominated by a stable anticyclone. Figure 4.2 shows the relative frequency of wind directions subdivided into 10° average values. Contrary to our expectations of northerly conditions only wind directions between 150 and 210° (SE-SW) were observed.

Figure 4.3 represents the meteorological parameters measured during the campaign. The upper panel again underlines the almost constant southerly conditions, while the second panel shows the variations in wind speed between zero and 18 ms^{-1} . It can be seen that the wind speed was very slow on the days with northerly wind directions. The temperature varied between 6 and 19°C and showed the expected daily cycle, well correlated with the solar radiation and negatively correlated with the relative humidity.

In the daytime there was a good visibility most of the time, apart from only a few hazy days. The temporary low intensity in our spectra even during the clear days may have been due to a high aerosol concentration which was not measured during the campaign.

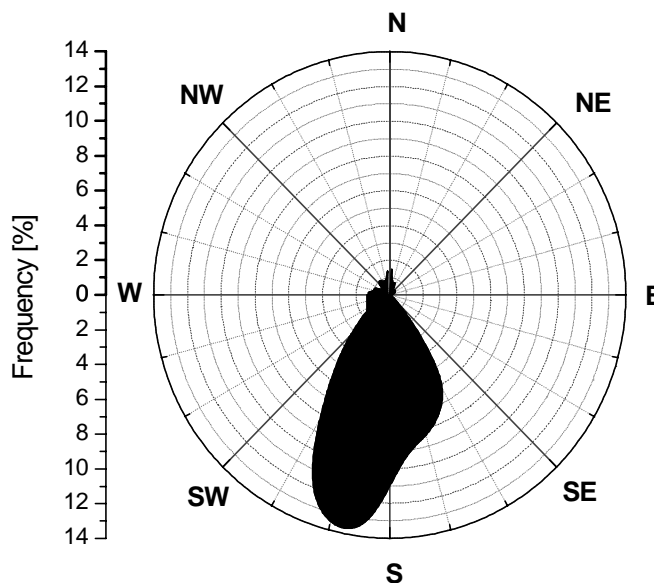


Figure 4.2 Distribution of wind directions at WB96, 10° average values (adapted from Alicke [1997]).

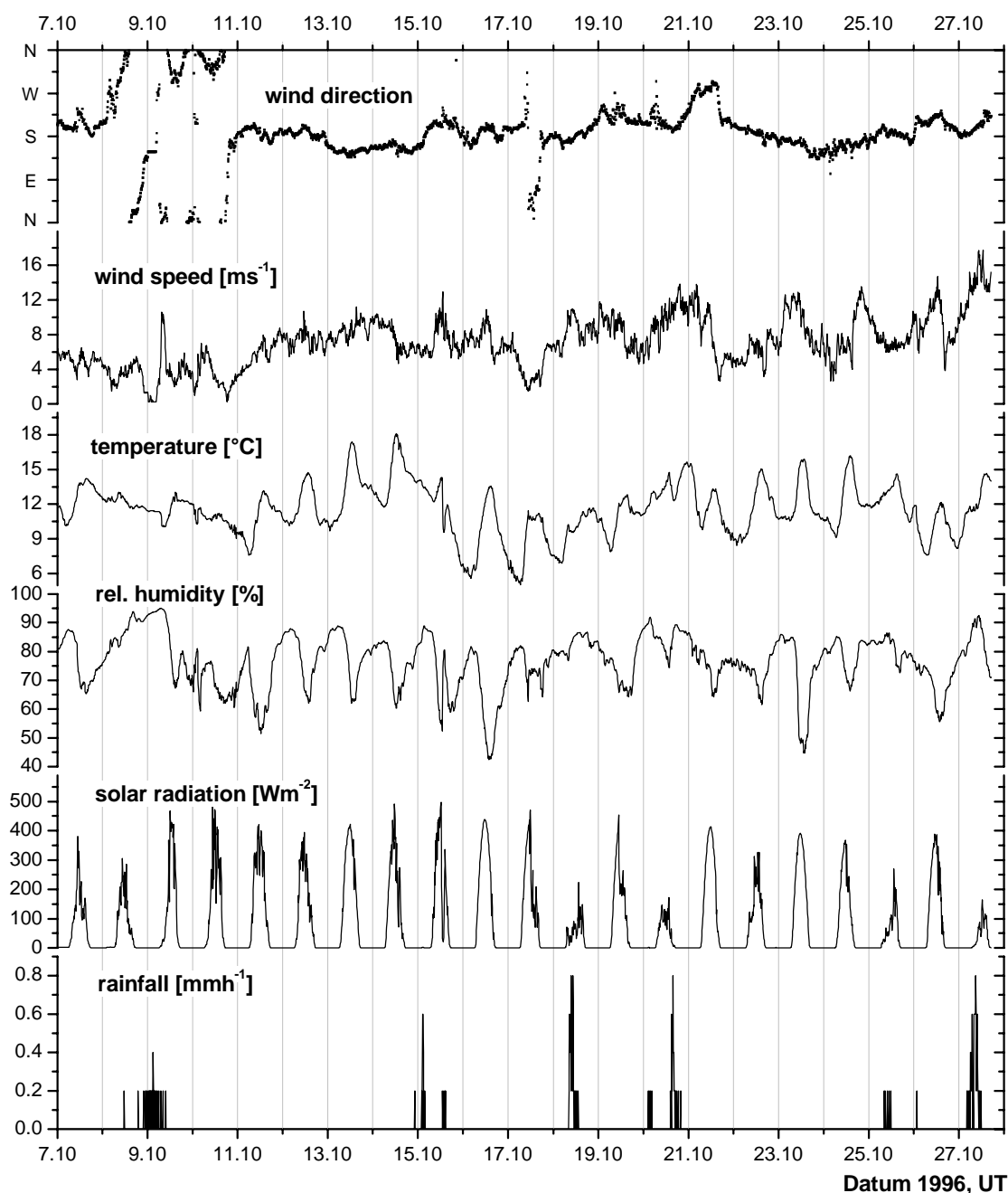


Figure 4.3 Data of the Weybourne meteorological station. On almost all days the air masses reached the site from southerly directions. The few days of northerly flow periods show very low wind speeds (adapted from Alicke [1997]).

4.1.3 Results of the Weybourne Campaign

Measurements were carried out at three different wavelength regions. We intended to measure ClO (292.4 nm), BrO (328 nm) and IO (432.4 nm) in a 40-nm interval. The temperature of the PDA and the spectrograph was held constant over the campaign at $-35 (\pm 0.3)^\circ\text{C}$ and $+25 (\pm 0.3)^\circ\text{C}$ respectively. Table 4.2 shows the different wavelength regions and trace gases adapted during the Weybourne campaign in 1996. For details of the analysis of the spectra refer to Alicke [1997] and Alicke *et al.* [1999].

Table 4.2 Wavelength intervals of the Weybourne campaign 1996, adapted from Aliche [1997].

XO of interest	Wavelength interval (nm)	Trace gas references applied
ClO	287 – 308	O ₃ , SO ₂ , ClO, HCHO, NO ₂
BrO	313 – 336	O ₃ , BrO, SO ₂ , NO ₂ , HONO, HCHO
IO	424 – 444	IO, NO ₂ , H ₂ O

During the two weeks of measurements in autumn 1996 the coastal site was influenced by relatively polluted, continental air masses. Therefore, as the possible sources of RHS, sea salt and emissions of algae, are of oceanic origin, the probability of detecting halogen oxide radicals was very low due to the meteorological conditions of low wind speed and southerly wind directions.

Table 4.3 shows maximum and average detection limit of the trace gases measured at Weybourne. Even if some data points of the time series are above the average detection limit of 13.85 ppt ClO, 2.59 ppt BrO and 2.99 ppt IO, no XO could actually be identified in any of the spectra recorded during the campaign.

Table 4.3 Statistics of trace gases measured at the Weybourne campaign 1996, adapted from Aliche [1997].

Species	Maximum	Detection limit
ClO	29.3 ± 10.5 ppt	13.85 ppt
BrO	3.0 ± 1.5 ppt	2.59 ppt
IO	6.4 ± 2.2 ppt	2.99 ppt
O ₃	37.6 ± 0.4 ppb	1.32 ppb
NO ₂	27.19 ± 0.07 ppb	0.12 ppb
SO ₂	9.88 ± 0.03 ppb	0.04 ppb
HCHO	2.1 ± 0.3 ppb	0.41 ppb
HONO	0.4 ± 0.25 ppb	0.27 ppb

Figure 4.4 shows the time series of these species. Even if the O₃ mixing ratio drops from almost 40 ppb to 5 ppb – which looks like a low ozone event at polar regions - this effect cannot be related to halogen chemistry. Not even the high values of XO allow to see the reference in the atmospheric spectrum as the residual is too high, which would lead to a high error. To summarise one can say that no halogen oxides were found significantly above the respective detection limits given in Table 4.3.

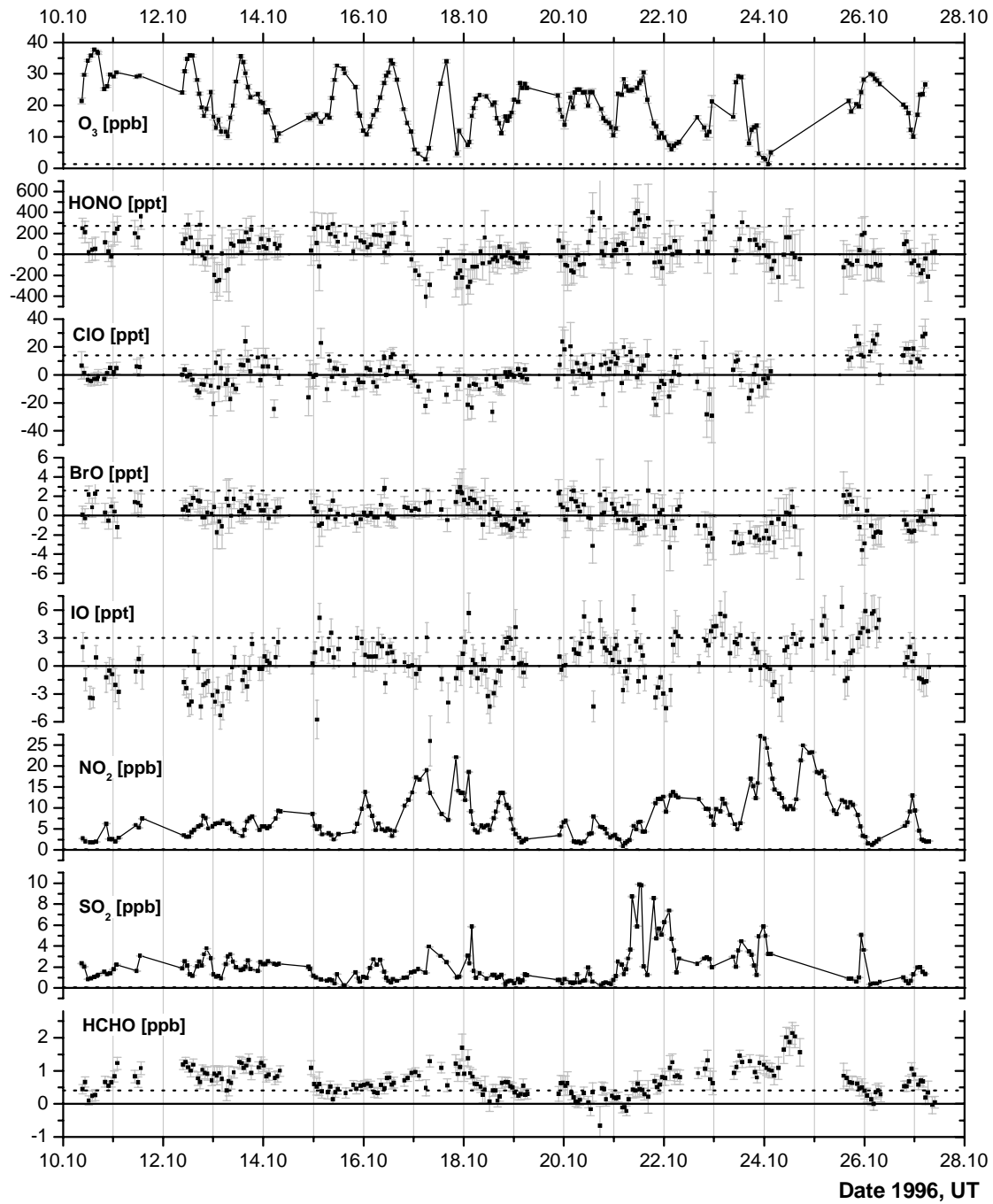


Figure 4.4 DOAS data of the Weybourne campaign 1996 (adapted from Alicke [1997]). Dotted lines indicate the average 2σ -detection limits. The variations in O_3 show no correlation with the halogen oxide concentrations, but are – as expected – negatively correlated with NO_2 . Due to the air mass transport over land the values of NO_2 and SO_2 are relatively high, especially for a marine site.

4.2 The Mace Head Campaign 1997

As mentioned at the beginning of this chapter, two campaigns related to this thesis have been carried out at the *Atmospheric Research Station of Mace Head, Carna, County Galway, Ireland*. The site which is associated with the National University of Ireland, Galway (NUIG) and the used DOAS light paths will be described in the following subsections. The meteorological conditions and the DOAS measurements and results of MH97 will be described in the sections 4.2.3 - 4.2.5.

4.2.1 The Mace Head Measurement Site

The European clean-air site of Mace Head at 53 degrees 20 minutes N, 9 degrees 54 minutes W is located in the path of the mid-latitude cyclones which frequently traverse the North Atlantic (see Figure 4.5). Galway city with a population of ~55,000 is the nearest major conurbation at a distance of 88 km eastward. The main Atlantic shipping routes are more than 150 km, the transatlantic air corridors more than 80 km away. The site shows westerly exposure to the North Atlantic Ocean, the clean-air sector reaches from 180 to 300° west. Significant pollution events only occur at the site when European continental air masses, generally originating from easterly directions, reach Mace Head. This location offers the opportunity to study the composition of the atmosphere under northern hemispheric background conditions in direct comparison with European continental emissions, depending on the wind direction

Local industrial emissions are negligible as the main source of income is fishing and fish farming. Lobster pots are set ~500 m offshore, but boat traffic is minimal and does not seriously affect any of the sampling programs there. All local fish farms are located outside the clean sector and their activities also appear to have little or no impact on the measurements carried out at the site. The second main local employment is agricultural activity, which is limited to stock-farming in this area. In springtime some agricultural burning of gorse occurs. Occasionally, plumes of smoke will pass over the site, however, as this burning generally only occurs during calm periods, the disturbance is probably minimal. Furthermore, no motorised traffic was allowed on the site. Therefore, when the wind blows from the clean sector, no disturbing influences of industrial emissions are expected to affect the measurements of European atmospheric background conditions.

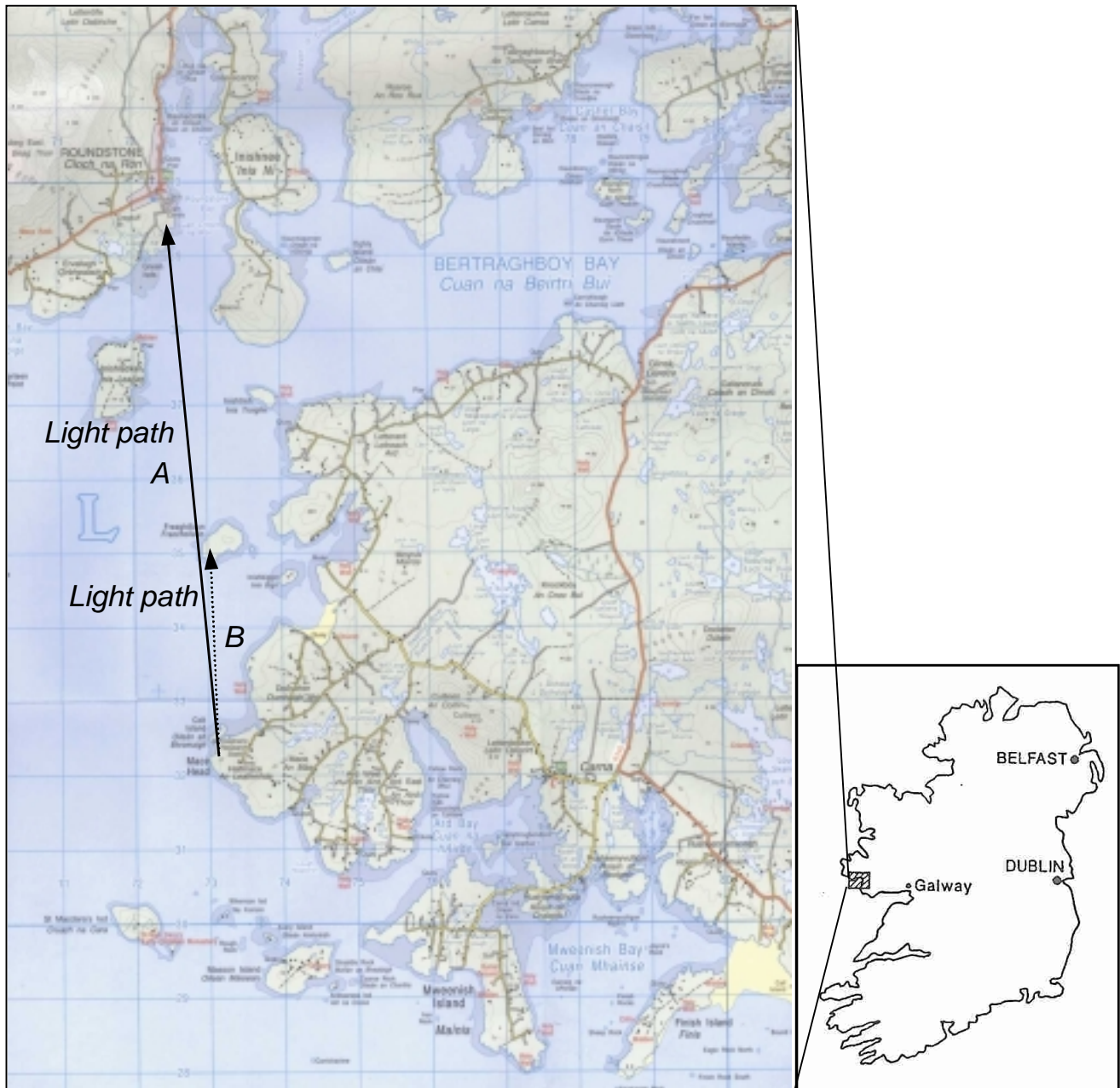


Figure 4.5 The Mace Head site on a local scale in the county of Galway facing the open Atlantic Ocean. Two almost identical light paths have been used in both of the Mace Head campaigns (length 7.27 km and 2.63 km one way in 1998). A third path (further west) has been applied in 1997 for only two days (see text).

The climate of Mace Head is dominated by maritime air masses and is therefore mild and moist. The meteorological records show that an average of more than 60 % of the air masses arrive at the station via the clean sector. Annual rainfall is approximately 1200 mm, October to December are the wettest, April and May the driest and sunniest months. Relative humidity is generally high, at about 80 %.



Figure 4.6 View from the upper cottage westwards to the Atlantic Ocean. The DOAS instrument was set up in the right cottage.

As can be seen from the sectional view of the site (Figure 4.7) it consists of three laboratory buildings, one at ~300 m and two at ~90 m from the shore (~50 m from high water). Other ancillary constructions include a 10-m meteorological tower where data such as wind speed, wind direction, pressure, temperature, relative humidity and rainfall are measured. Solar radiation and UV levels are recorded continuously. Figure 4.6 shows the view from the upper cottage straight west down to the lower buildings.

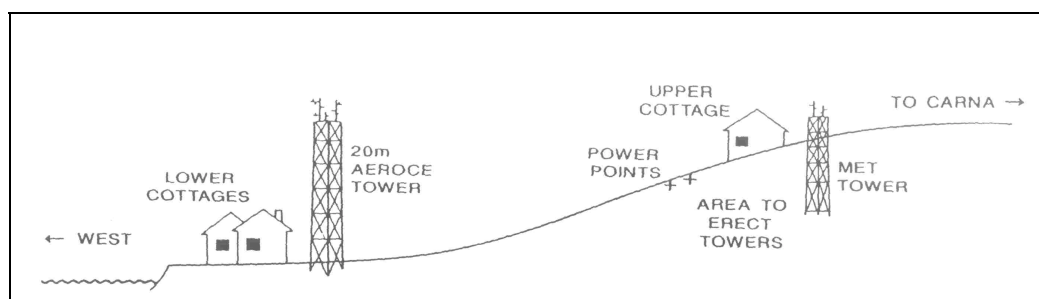


Figure 4.7 West-to-East sectional view along the Mace Head Research Station. In 1998 a second tower of a height of 10 m was set up right behind the lower cottages.

During both of the campaigns the DOAS instrument was set up in the northern lower cottage, at a distance of 20 m from the shore, in a room usually used as a clean laboratory (right building shown in Figure 4.6). We replaced the front door by a special door the lower part of which could be opened separately. The upper part was fixed to send out the DOAS light beam without disturbance. In front of the hole in the door a windbreaker was installed to protect the telescope from being sprayed with rainwater. The hole was kept open over the period of the campaigns, so that the temperature stabilisation of the spectrograph was set at 20°C instead of 25°C, which had been the setting during the Weybourne campaign.

4.2.2 DOAS Light Path at Mace Head

In expectation of totally different visibilities from misty to very clear conditions we decided to set up two different light paths. The short light path was to give us the opportunity to continue the measurements in case of rain or fog, the long light path was to be as long as possible in order to optimise the detection limit under the auxiliary condition of an acceptable time resolution. As RHS are expected to be released close to the shoreline due to i) breaking waves causing sea spray and ii) emission of halocarbon by algae, another auxiliary condition was that the light path was to be close to the sea level and, if possible, parallel and close to the coastline.

On the first light path, which we adapted in 1997, we measured only for two days. The limited angle of view of the telescope caused by the door frame did not allow to turn the telescope to another (shorter) light path. However, ultimately two light paths were established. The long light path (line A in Figure 4.5) of 2×7.27 km was used in both of the campaigns. The retroreflector array that consists of 60 (37 in 1997) single reflectors was fixed on a statue. For the short light path of 2×2.63 km (line B in Figure 4.5) a retroreflector array with 19 reflectors was set up on a small island. As no fixed location was used for the array, the light path in 1998 was a little longer (~ 100 m) than the one used in 1997. The long and the short path were almost at the same angle to the station. Therefore the telescope had only to be turned slightly, which allowed a quick change of the light path. Figure 4.8 shows the view along the light paths.

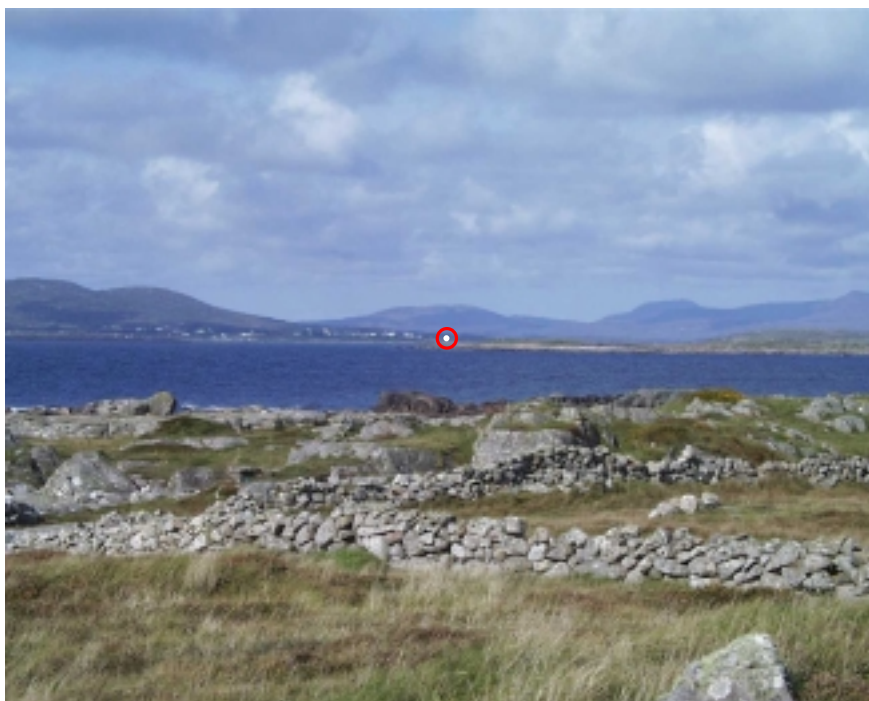


Figure 4.8 View along the DOAS light paths from North to South. Red circle marks the light reflex of the long path at a distance of 7.27 km.

4.2.3 The Meteorological Conditions at MH97

Over a 7-week period from April 17 until June 1, 1997 LP DOAS measurements of the halogen oxides ClO, BrO and IO and the other atmospheric trace gases absorbing in the related wavelength regions were performed within the framework of the EU project *HALOTROP*. The site was very crowded because our measurements were performed in co-operation with a huge campaign of the British *ACSOE* project. The following section describes the meteorological conditions we found during MH97, followed by a portrayal of the measurement routine adapted in 1997. Section 4.2.5 presents the data and summarises the results of MH97.

During the 7 weeks of the campaign the meteorological conditions ranged from quick showers of hail and snowfall to some days of warm and sunny weather. Figure 4.9 shows an overview of the meteorological parameters from April 23 to June 1. The temperature varied between 4 and 22 °C, the wind direction temporarily varied between the westerly clean air sector (180° – 300°) and the other (possibly polluted) directions and back within hours. The overall variation of the wind speed reached from approximately 0 to 20 ms⁻¹ and up to 100 ms⁻¹ in squalls. The lower panel shows the solar radiation, indicating clear sky and very cloudy days.

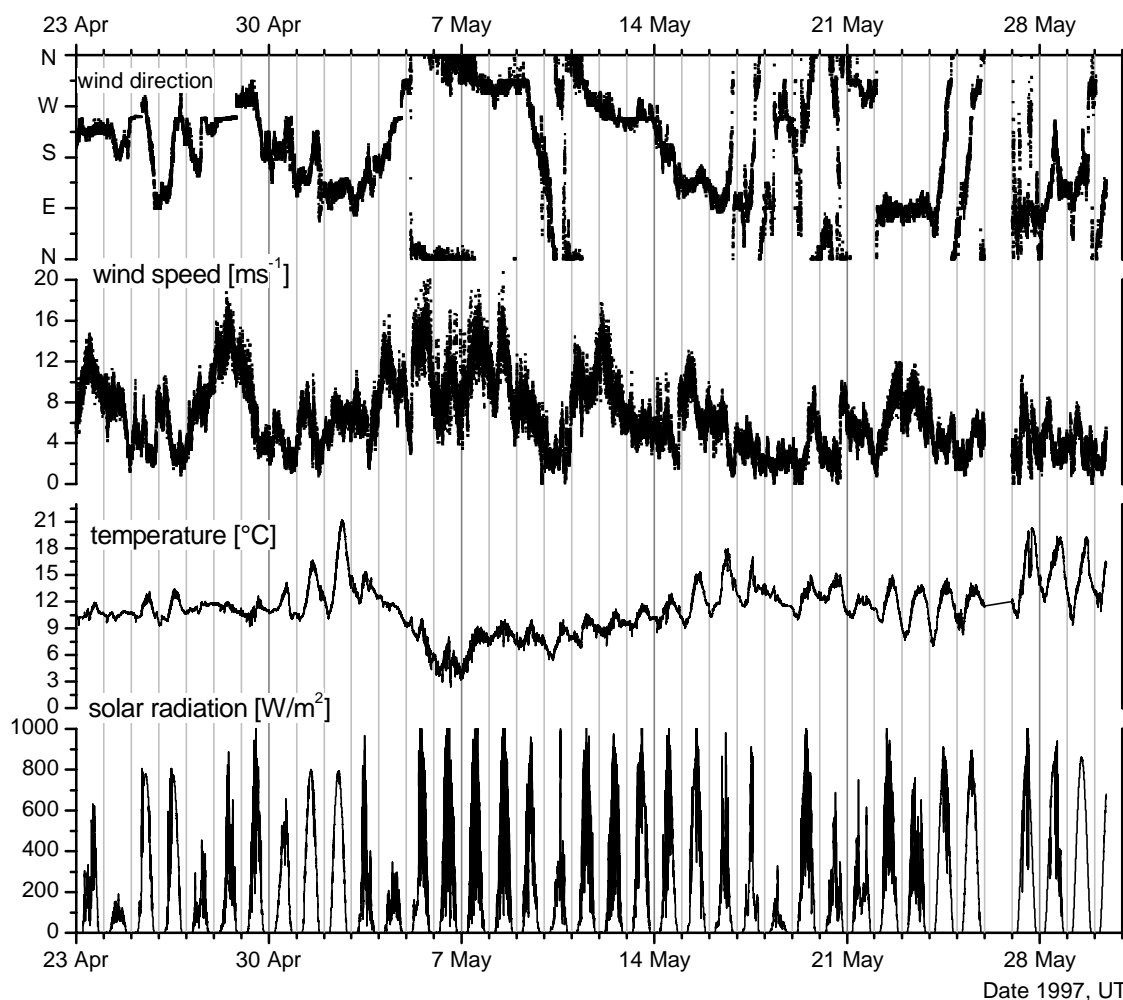


Figure 4.9 Meteorological conditions of the Mace Head 1997 campaign.

Especially a cold period around May 6 attracts attention. As can be seen from the wind direction panel these low temperatures were caused by air masses reaching Mace Head from northerly directions with extreme high wind speeds of $10 - 20 \text{ ms}^{-1}$ causing high breaking waves and a rough sea. Figure 4.10 A shows a 5-day-back trajectory, reaching Mace Head on May 6 0:00, underlining that the air masses observed during these days were of polar origin. Graph B shows a typical trajectory of a relatively polluted period.

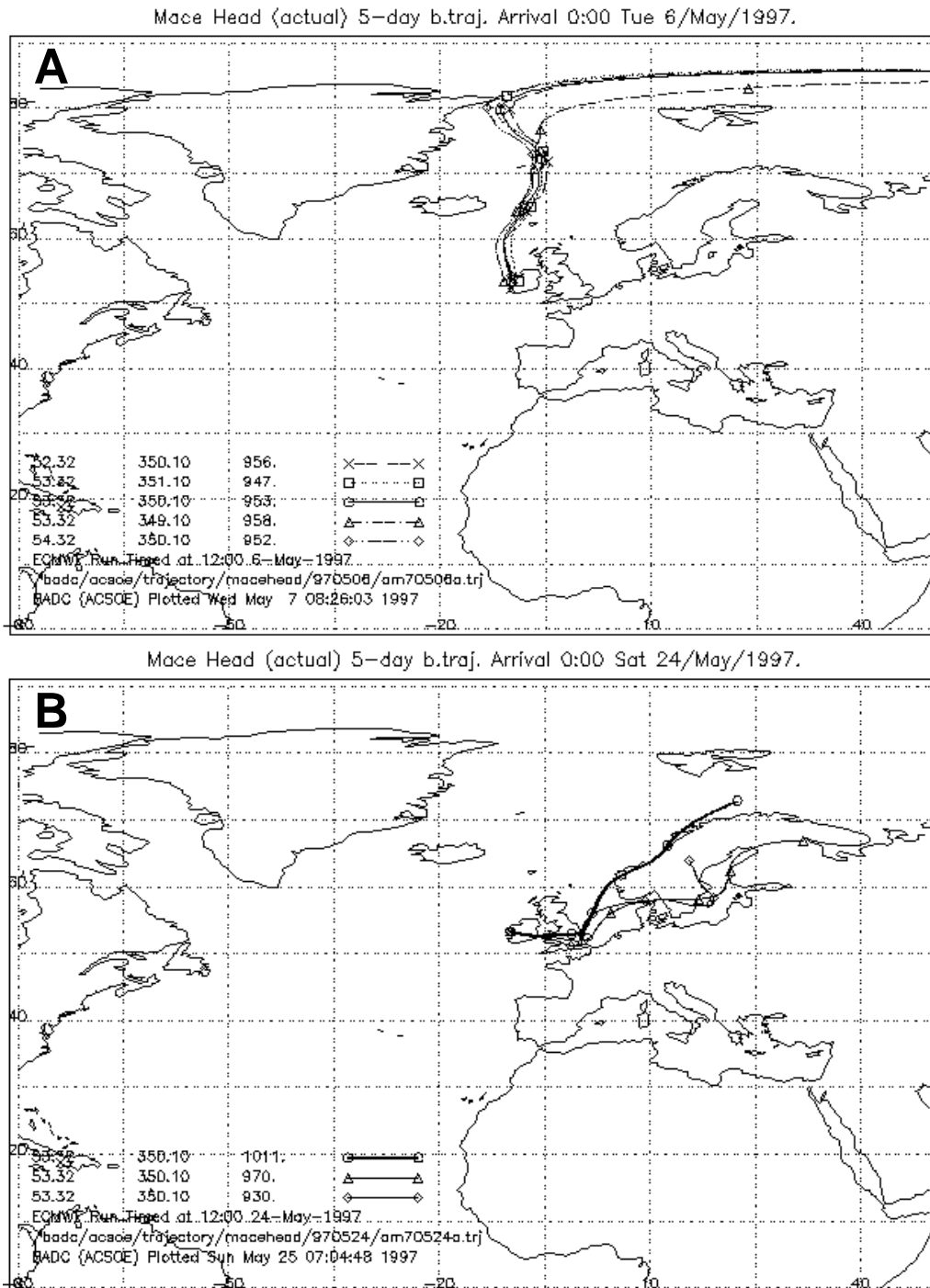


Figure 4.10 Two representative 5-day-back trajectories. A shows a clean-air trajectory of polar origin, reaching Mace Head at 0:00 on May 6 1997. In comparison B shows the arrival of polluted air masses passing over the South of England and Ireland.

4.2.4 The DOAS Measurement Routine of MH97

We had no other experience in measuring halogen oxides at mid latitudes than the unsuccessful campaign of Weybourne 1996 where no XO could be detected above the detection limit. Therefore we decided to measure all three relevant wavelength regions as we did at Weybourne before. Table 4.4 summarises which species was measured in which wavelength interval.

Figure 4.11 shows a flow diagram of the measurement routine. The UV region, where ClO shows its major absorption structures, requires long integration times due to high O₃ absorption bands. This region was skipped in case of low visibility to retain a sufficient time resolution. All measurements were performed applying the MCST (see section 3.2.5 c)).

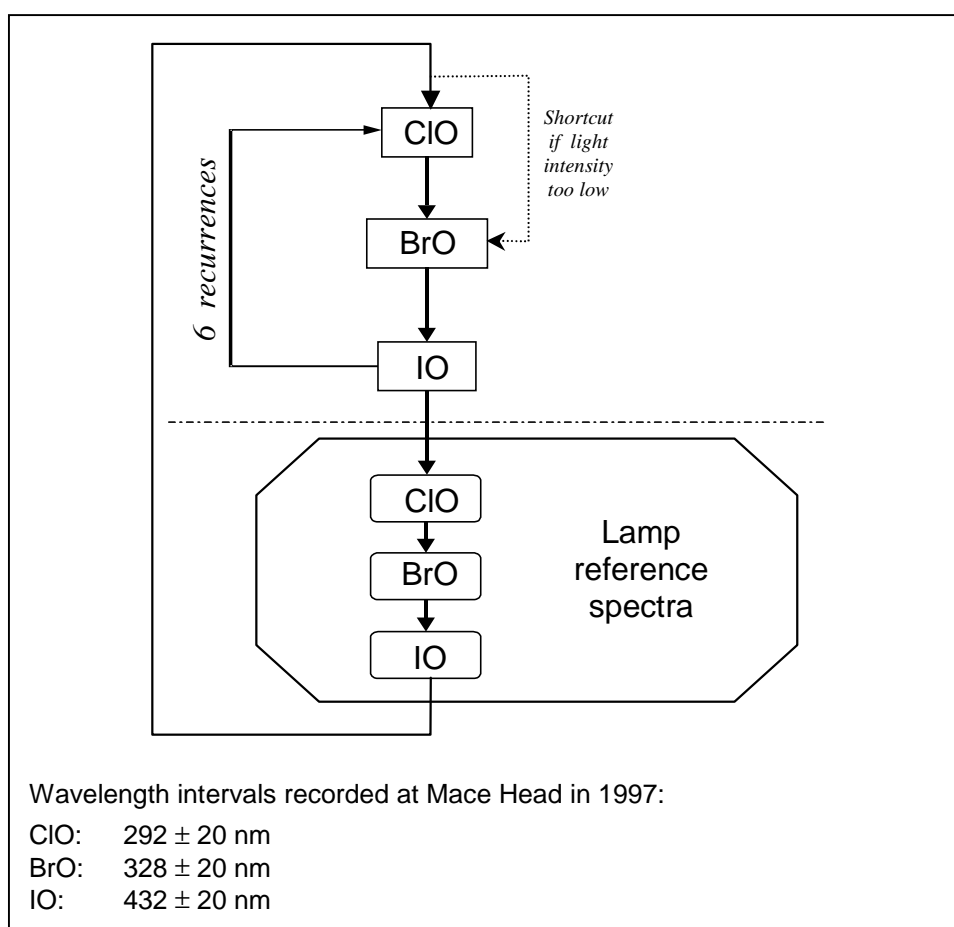


Figure 4.11 Scheme of the Mace Head 1997 measurement application. We attempted to measure the halogen monoxides ClO, BrO and IO. As the ClO region in the UV requires long integration times, this region was automatically skipped if the visibility was too low (adapted from Aliche [1997]).

Depending on the weather conditions, the integration time as well as the light path was adapted. This causes a varying time resolution and, as the path length and the recording level influence the fit error, a varying detection limit. The whole LP DOAS system ran in a fully automated way and was realigned about once a day.

Table 4.4 Wavelength intervals of the MH97 (adapted from Alicke [1997]).

XO of interest	Wavelength interval used for the evaluation (nm)	Trace gas references applied
ClO	300 – 311	O ₃ , SO ₂ , ClO, HCHO, NO ₂
BrO	317 – 342	O ₃ , BrO, SO ₂ , NO ₂ , HONO, HCHO
IO	423 – 445	IO, NO ₂ , H ₂ O

4.2.5 Results of the Mace Head Campaign 1997

Table 4.5 lists maximum and the average detection limit of the trace gases measured at Mace Head. The time series of the species measured with DOAS are shown in Figure 4.12. The statistics of the trace gases as well as the time series emphasise the clean-air character of the site.

Table 4.5 Statistics of trace gases measured at Mace Head in spring 1997 (adapted from Alicke [1997]).

Species	Maximum	Detection limit
ClO	83.2 ± 18.3 ppt	34.0 ppt
BrO	4.5 ± 1.2 ppt	1.7 ppt
IO	6.7 ± 0.5 ppt	1.7 ppt
O ₃	50.7 ± 1.2 ppb	3.1 ppb
NO ₂	5.43 ± 0.07 ppb	0.14 ppb
SO ₂	18.3 ± 1.95 ppb	1.0 ppb
HCHO	3.0 ± 0.7 ppb	0.7 ppb
HONO	761 ± 217 ppt	276 ppt

a) Non-Halogen Species

The upper panel of Figure 4.12 shows the time series of the NO₂ mixing ratio, ranging from European background values around and below the detection limit of 0.14 ppb to a single emission peak of almost 5.5 ppb. As expected, the SO₂ mixing ratio (6th panel) shows parallel variations and ranged from values scattered around zero to values above 9 ppb as is regularly observed in urban areas. The O₃ values remained relatively constant over periods of the order of a few days: between May 8 and May 24 the mixing ratio was 32 ± 4 ppb. The HONO and HCHO values remained below the detection limit of 276 and 700 ppt most of the time. At the end of the campaign HCHO rose to values of the order of 2 ppb for a few days.

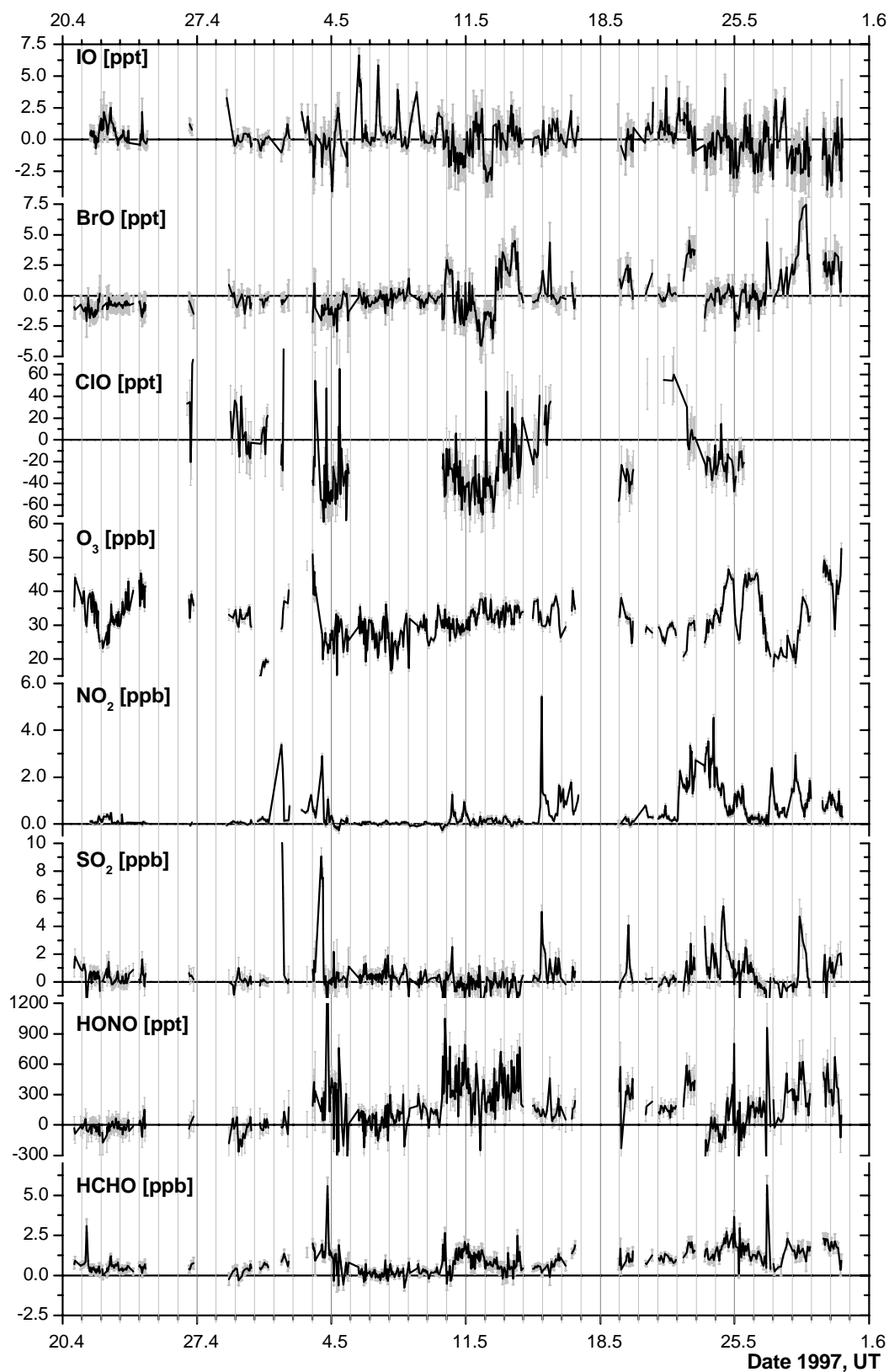


Figure 4.12 Time series of the species measured at Mace Head in 1997 (adapted from Alicke [1997]).

b) *BrO, ClO*

Even if a number of data points seem to be above the detection limit, neither BrO nor ClO absorption features could be found in the recorded spectra. Although May 12 and 13 look like days with periodic BrO cycles with mixing ratios above the average detection limit of 1.7 ppt, no BrO was identified in the spectra. Taking into account the fit errors of this period, the detection limit is elevated as the spectra were recorded on the short light path (compare with 3.1.4 d) ‘Error Determination’).

c) *IO*

During the 7-week campaign IO could be observed in the troposphere for the first time. Figure 4.13 gives an example of an atmospheric spectrum showing clearly visible iodine oxide absorption structures. The absorption features of all other species that have been applied in this region have already been removed.

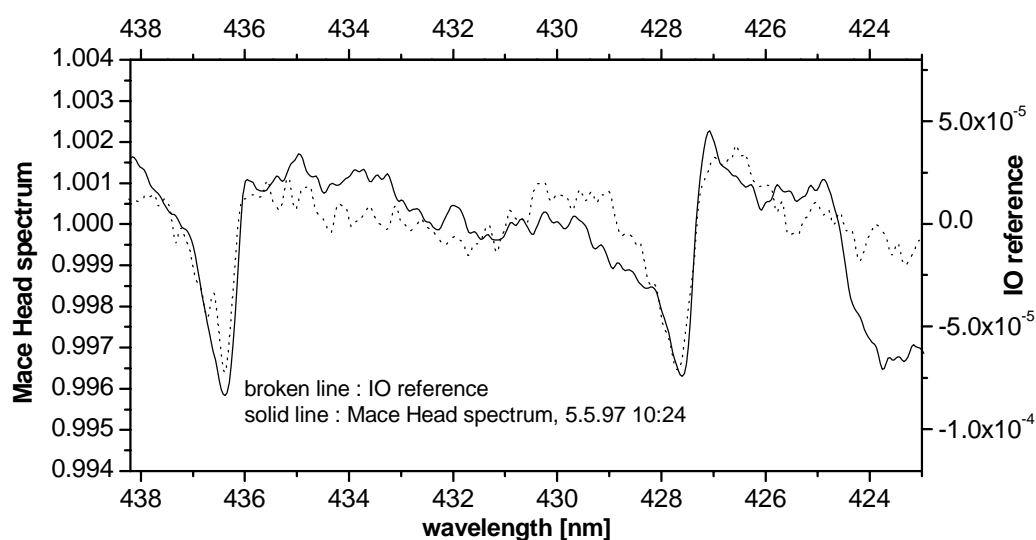


Figure 4.13 Example of an atmospheric IO spectrum recorded at MH97. The structures of other trace gases have already been removed (adapted from Alicke [1997]).

From May 5 – 8 the IO mixing ratios show daily recurring cycles peaking at noon. The maximum value of 6.7 ppt was reached on May 5. On May 4 this cycle is clearly visible in the time series, even if the mixing ratios did not exceed the detection limit. Thus a daily periodic repetition of iodine oxide mixing ratios, which has never been observed in the boundary layer before, was recorded over a period of 5 days. Besides the clearly visible spectral feature the daily recurring signal underlines the existence of iodine monoxide in the marine boundary layer.

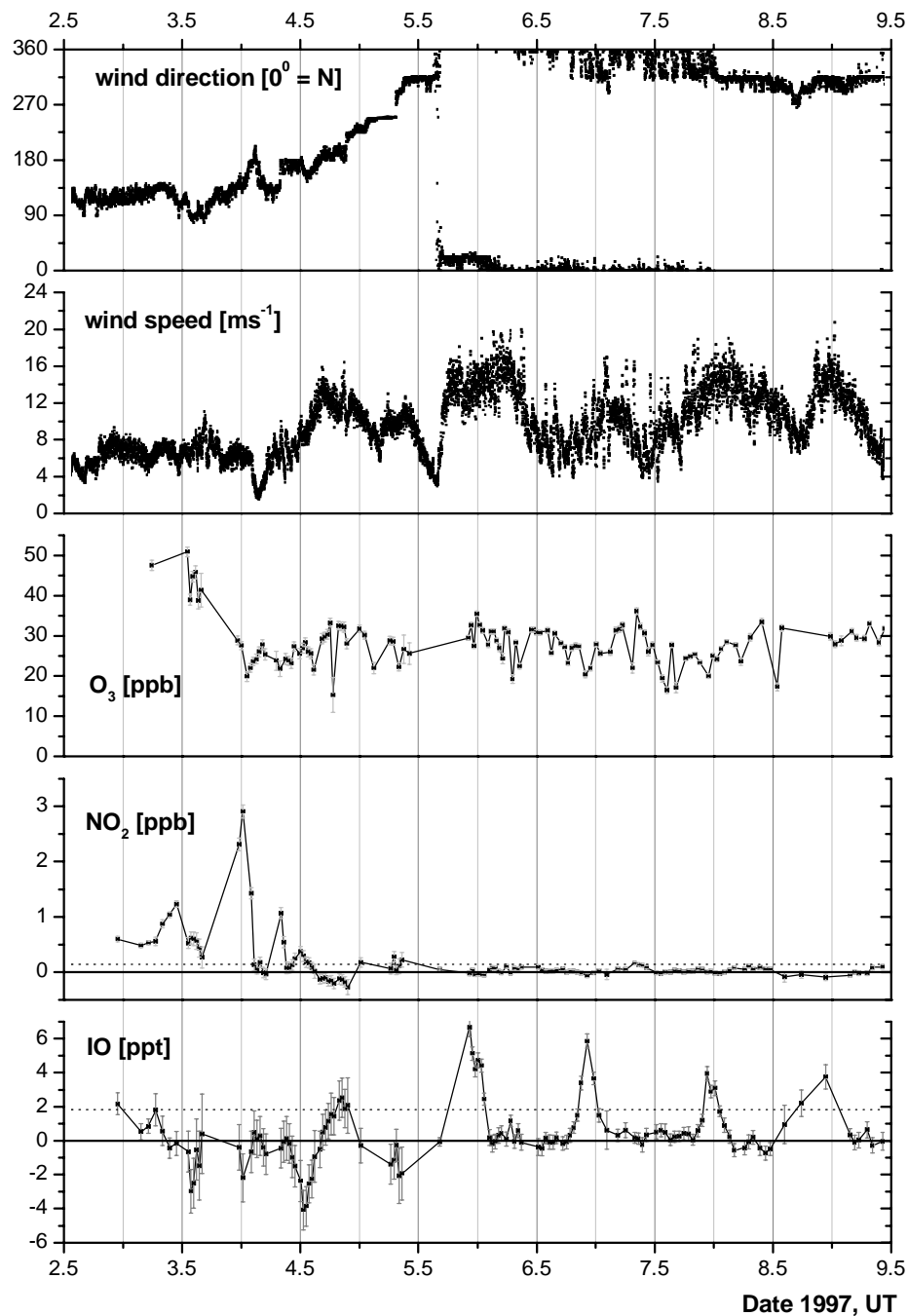


Figure 4.14 Period of cyclic elevated IO mixing ratios during MH97, dotted line indicates 2σ -detection limit (adapted from Alicke [1997]).

d) Halocarbons

Halocarbons are a potential source of RHS in the boundary layer (see section 2.1.2 b)). A number of these species have been measured during MH97 by Carpenter *et al.* [1999] using a GCMS (Gas Chromatography Mass Spectrometer). Figure 4.15 shows the time series of these measurements. A conspicuous peak of CH_2ClI (photolytic lifetime ~ 10 h) can be found in the early morning hours of May 5, the day of the highest IO event, which fits in quite well with the theory of halocarbons as precursors of RHS and halogen oxides respectively. On the other hand there are no noticeable halocarbon peaks in the night before the other IO events.

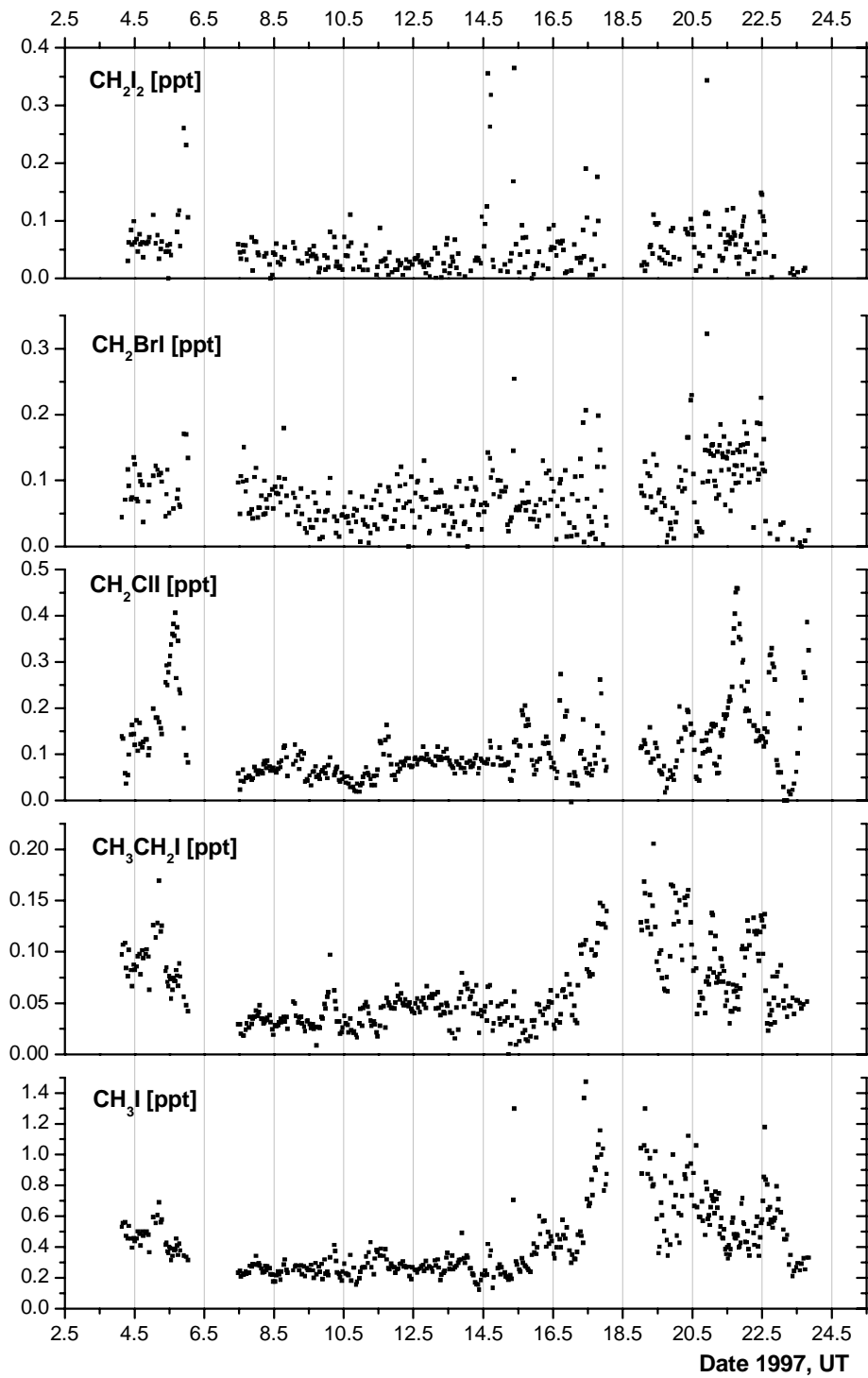


Figure 4.15 Halocarbon mixing ratios measured at MH97(adapted from Carpenter et al., [1999]).

4.3 The Mace Head Campaign 1998

Over a 1-month period from Sept 8 until Oct 8, 1998 LP DOAS measurements of the halogen oxides IO, OIO and BrO and also of other atmospheric trace gases like NO₂, O₃, HCHO, HONO and NO₃ were carried out at Mace Head in co-operation with the *PARFORCE* project. For a detailed description of the measurement site and the DOAS light paths applied see section 4.2.1 and 4.2.2 above.

The primary aim of the *PARFORCE* project was to investigate the formation and size distribution of micro particles. Elevated aerosol nucleation is observed when low tide occurs near and around the solar radiation intensity peak. Exactly under those conditions the formation of halogen oxides can be expected: The emission by algae increases at low tide because the plants are stressed when they are exposed to the atmosphere, especially under daylight conditions. Furthermore, the higher the intensity of the sunlight the faster the photolysis of the emitted halocarbons will occur, leading to the formation of RHS. Figure 4.16 shows the prediction of solar radiation and tidal height for the period of the *PARFORCE* campaign.

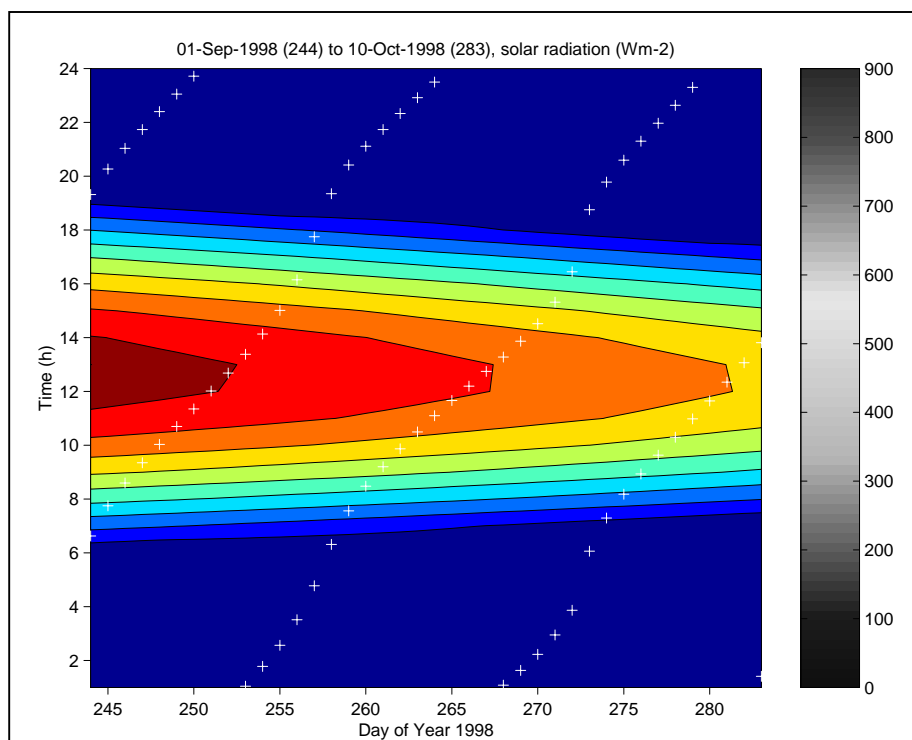


Figure 4.16 Tidal height and solar radiation prediction for MH98. Under conditions of low tide during high solar radiation particle and halogen oxide formation was expected. White crosses mark the time of low tide. Abscissa shows day of the year (250 = Sept 7, 280 = Oct 7), ordinate shows time of day.

Besides the particle and DOAS measurements and the recording of meteorological parameters in-situ monitors were operated to measure O₃ and NO. Halocarbons were measured by *Carpenter et al.* [1999] using the *GC-MS* (*gas chromatography - mass spectrometer*) technique. *Lewis* [1999] measured NMHC (Non-Methane Hydrocarbons)

using a GC instrument improved for this application. More details concerning the instrumentation may be found in *Lewis et al.* [1998, 1996].

In the next section I will focus on the description of the meteorological conditions we found in autumn 1998. After that the evaluation of the IO region and the problems caused by spectral lamp and water features of this wavelength region from 390 to 470 nm will be described. As the analyses of the other wavelength intervals were performed and partly published previously by *Hönninger* [1999], *Geyer* [2000] and *Stutz* [1999], only the IO evaluation will be presented in detail.

4.3.1 The Meteorological Conditions at MH98

During the 4-week campaign in late summer 1998 the meteorological parameters showed variations between midsummer and typical autumn values. The Mace Head site was influenced by more or less polluted continental as well as clean marine air masses, representing European background conditions.

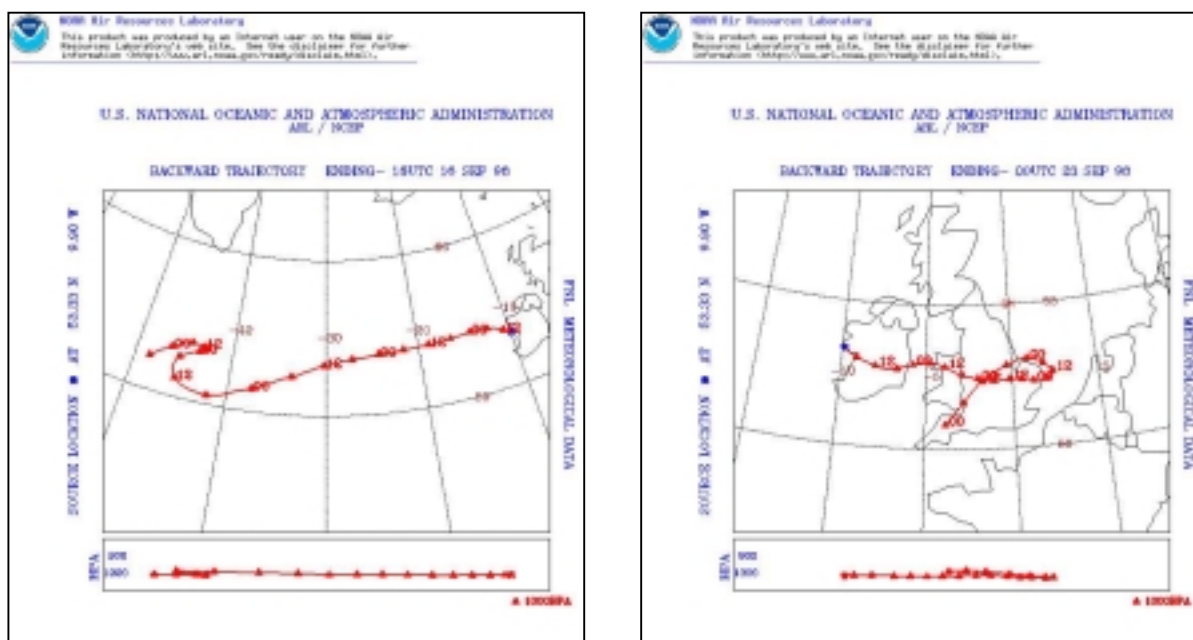


Figure 4.17 5-Day-Back Trajectory of MH98. Typical clean-air (left) and polluted (right) conditions.

Figure 4.17 shows two representative 5-day-back trajectories of the campaign. The one on the left hand side shows the path of the air masses reaching the site during the first, very clean period of the campaign on Sept 16. The second trajectory shows the path of the air masses reaching Mace Head on Sept 23, during the polluted period in the middle of the campaign.

Figure 4.18 gives an overview of several meteorological parameters which have been determined during the campaign. The temperature varied between 8 and 23 °C with an average of 15 °C. The relative humidity shows typical marine variations of 60 to 100 %. Photopic measurements, which can be interpreted in terms of an index of solar radiation, varied between zero and almost 90 klx. The overall variation of wind speed reached from

approximately zero to 20 ms^{-1} and up to 100 ms^{-1} in squalls. Most of the time the changes in wind direction occurred relatively slowly. The change of the length of the DOAS light path can be taken as an indication for the visibility²¹. Moreover the tidal height is shown with maximum values of 5 to 6 m.

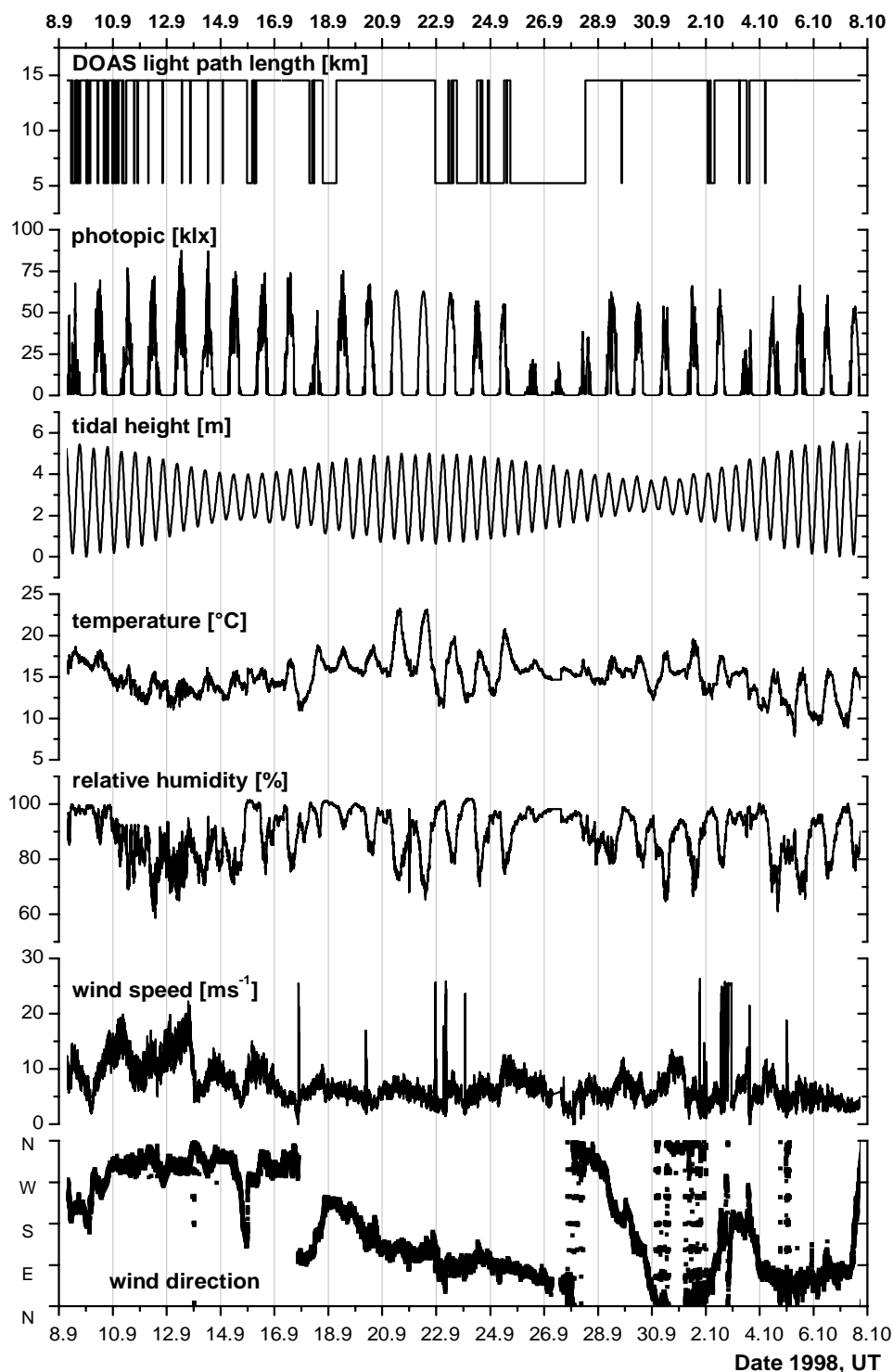


Figure 4.18 Overview of the meteorological conditions, tidal height and the changes between the two DOAS light paths during MH98.

²¹ On the one hand the a self adjustment routine was working properly, besides the late night hours the DOAS instrument was permanently cared for.

4.3.2 The DOAS Measurement Routine of MH98

In 1998 we focused on the detection of iodine oxides, taking into account the results of the 1997 campaign. For a better time resolution of the IO area we did not attempt to measure ClO, because it shows absorption structures in the UV region where integration times are likely to be comparatively long due to Rayleigh and Mie extinction (see section 3.1.2). Furthermore, we emphasised the IO region as we measured IO at least twice as much as the other regions. Figure 4.19 gives the scheme of the measurement routine applied at MH98.

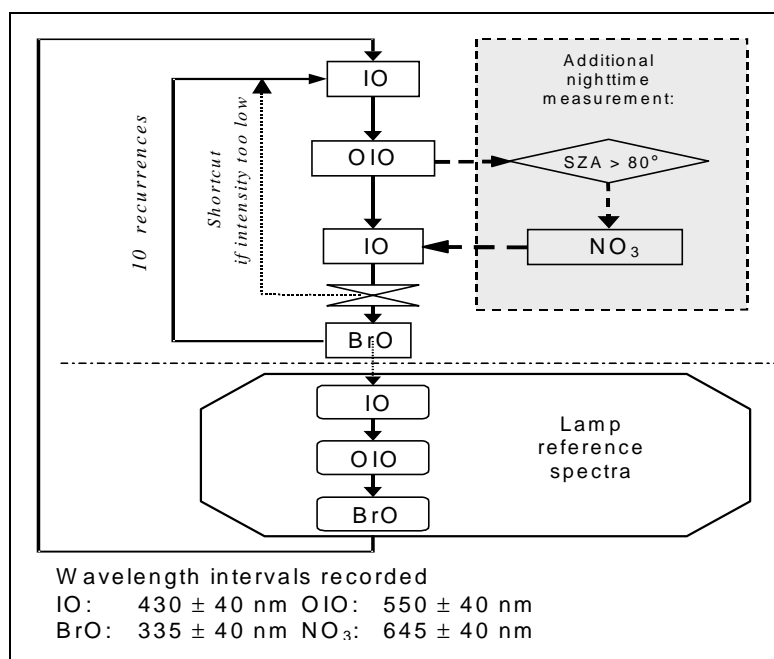


Figure 4.19 Scheme of the Mace Head 1998 measurement application. As we focused on the IO measurements particular emphasis was put on the wavelength region of 390-470 nm. Before the measurements in the BrO region were executed, a test scan was performed. If the integration time was expected to be too long, the BrO measurements were skipped.

LP DOAS measurements were performed in four wavelength regions. In three of these intervals the species of major interest were the halogen oxides IO, BrO and OIO. Table 4.6 summarises which species was analysed in which wavelength interval. The fourth wavelength region was applied to measure the nitrate radical (NO₃), which is produced by the reaction of NO₂ with O₃. NO₃ is photolytically unstable under daylight conditions. As Mace Head is a clean-air site with low NO₂ concentrations, the detection of NO₃ in the daytime is very unlikely. For this reason, and as our main interest was to measure halogen oxides, the region from 605 to 685 nm was operated for a solar zenith angle (SZA) > 80° only (see Figure 4.19). The measurements of the nitrate radical were performed to support the work of my colleague Andreas Geyer, who analysed these data, which were not related to the halogen oxide measurements performed for this thesis. Therefore the NO₃ time series will not be represented here. For details about these and other NO₃ measurements cf. Geyer [2000].

Table 4.6 Wavelength intervals of MH98 halogen oxide evaluation.

XO of interest	Wavelength interval applied for the evaluation (nm)	Trace gas references applied
BrO	312 – 364	BrO, O ₃ , SO ₂ , NO ₂ , HCHO, HONO
IO	414 – 437	IO, NO ₂ , H ₂ O
OIO	546 – 565	OIO, NO ₂ , H ₂ O

4.3.3 Wavelength calibration

Employing the MCST (see section 3.2.5 c)), every single spectrum recorded has to be shifted by a specific amount. Afterwards it has to be shifted back to the position of the middle wavelength spectrum. This shift is realised by turning the grating of the spectrograph. In order to minimise errors in the back-shift procedure atomic mercury emission lines were recorded after every single multi-channel spectra set (atmospheric spectrum and corresponding background). Therefore the sequence of recording a MCST series is as follows: atmospheric spectrum (AS), background (BG), mercury line (Hg); turning grating (CG), AS, BG, Hg; CG, ...

Another possibility of realising the MCST is to use regular repeating spectral features of atmospheric trace gases instead of mercury emission lines as a wavelength calibration. Depending on the wavelength region strong absorption structures of water can be used. Within the framework of this thesis this less common version of the MCST has not been applied for atmospheric measurements but for reference spectra, as will be explained below.

The MCST was applied in the IO, OIO and BrO region, while in the NO₃ region only one atmospheric, one background and one mercury calibration spectrum were recorded.

4.3.4 Recording and Convolution of Reference Spectra

As described in section 3.1.4 reference spectra for DOAS evaluation can be recorded in the field using a quartz cell filled with the respective trace gas. Afterwards these spectra are calibrated using literature cross sections of a given concentration. On the other hand references can be convoluted from literature cross sections and a recorded instrumental function represented by an atomic emission line. Both techniques have in common that lamp reference spectra as well as Hg emission lines are mandatory for the evaluation.

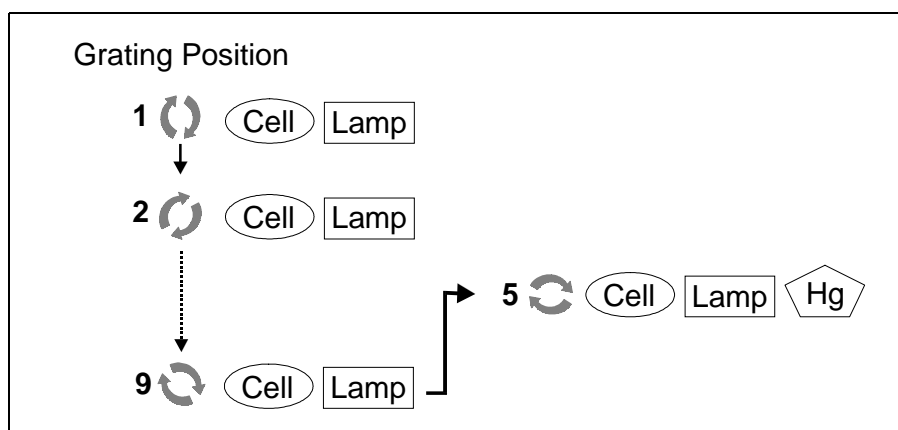


Figure 4.20 Recording-scheme of the cell reference spectra

The *lamp shortcut system* used for the recording of reference spectra consists of a quartz lens imaging the light arc on the quartz fibre (see 3.2.2). When recording the cell reference spectra, we did not change the position of the shortcut system to avoid spectral artefacts due to changes in the lens position. The recorded series was as follows (see Figure 4.20): Cell, lamp; turning grating (CG), cell, lamp; CG... After one complete series the grating was changed to the middle multi-channel position and as an additional wavelength calibration three spectra were recorded: Lamp, cell, Hg. This version of the MCST was used to record reference spectra of NO_2 (IO, BrO and OIO region) and SO_2 (BrO region), while the measurements of the NO_3 region were carried out without using the MCST at all [Geyer, 2000].

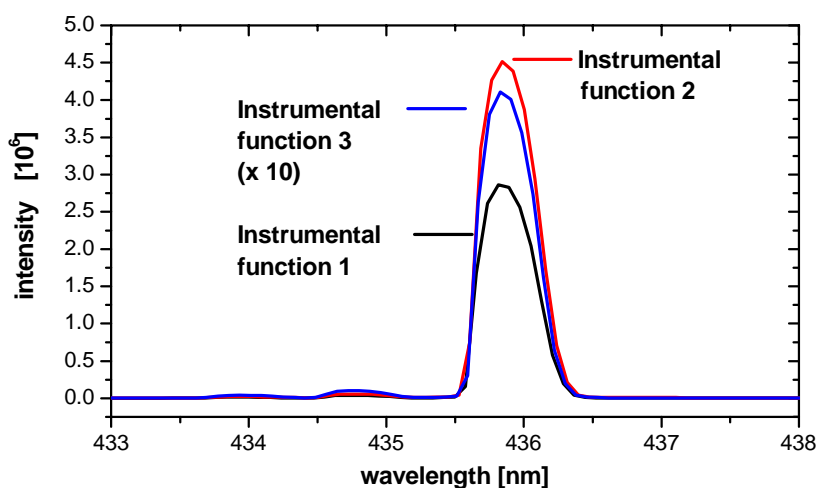


Figure 4.21 435.84 nm mercury convolution lines recorded at Mace Head in 1998. Instrumental function 3 is scaled up by a factor of 10. With ~ 6 channels FWHM and a dispersion of 0.078 nm/channel the spectral resolution can be calculated to be 0.5 nm.

During the Mace Head campaign the high pressure Xe arc lamp had to be changed three times because the spectral lamp structures became too big or the light intensity decreased. As every lamp shows differences in its specific spectral features and as the telescope had to be realigned after the lamp changing procedure (which changes the optical imaging of the system) at least one set of references per lamp has to be recorded. In general, lamp

structures are removed due to the MCST. However, because of the varying lamp features (from lamp to lamp and in time) the residual could be minimised more effectively by applying different lamp reference spectra.

Table 4.7 Usage endurance of lamps at the MH98 campaign.

Lamp No	Used from ... until ...	From spectra Number ... to...
1	Sept 05 – Sept 18	0 – 38 563
2	Sept 18 – Oct 02	38 564 – 80 607
3	Oct 02 – Oct 08	80 607 – 101101

Table 4.7 gives the usage endurance of the lamps used at MH98. Figure 4.21 shows the three instrumental functions (435.84 mercury line) relating to the evaluation of the spectra recorded with the three Xe-lamps. The characteristic lamp spectra are shown in Figure 4.22.

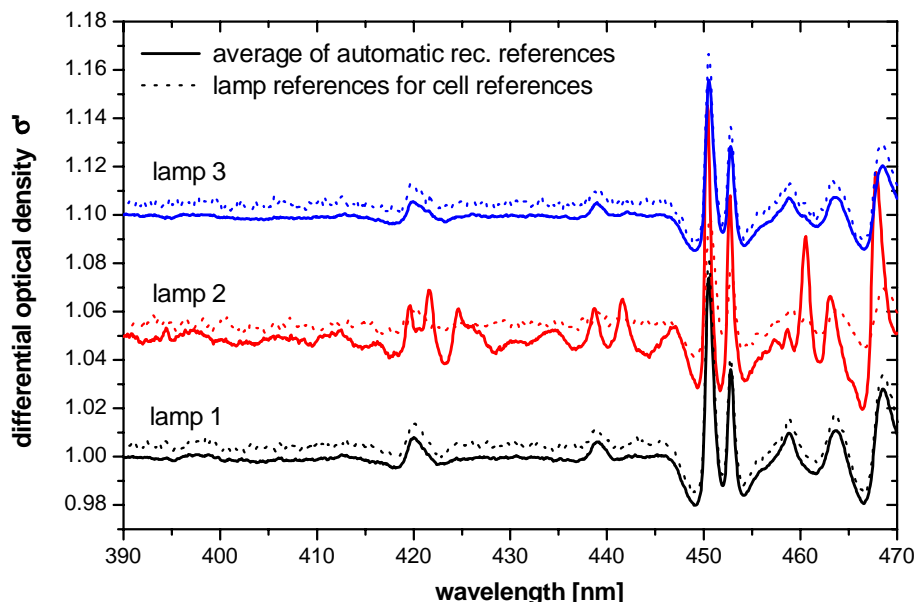


Figure 4.22: Reference spectra of the three different lamps used during the MH98 campaign. Solid lines: ref-spectra, dotted lines: sum-spectra.

As can be seen from the measurement scheme of the MH98 campaign (Figure 4.19), lamp spectra were recorded automatically after every 10th atmospheric measurement cycle. Moreover, lamp spectra have to be recorded as ‘cell-reference background spectra’ to correct the self-recorded references for the lamp structures. Therefore there are two possibilities of composing lamp reference spectra: i) adding up all automatically recorded spectra per lamp and ii) piecing together lamp spectra from reference cell recording. Both types represent the characteristic lamp features, but are slightly different due to the different methods.

The dotted lines in Figure 4.22 show the sum of all these automatically recorded lamp spectra (‘sum-lamp’). The solid lines show the lamp spectra recorded as a lamp reference

to correct the trace gas references for the lamp structures (*ref-lamp*). Therefore these spectra represent only one MCST series. It is obvious that the sum spectra show lower noise levels as they are averages of a larger number of spectra (18, 3 and 22 respectively). Furthermore, the steeper features of *sum-lamp 2* are noticeable, indicating that the quality of the second lamp was relatively bad.

4.3.5 Evaluation of the IO Wavelength Region

The overall wavelength interval recorded for the IO evaluation was 391-468 nm. Figure 4.23 shows an atmospheric spectrum recorded Oct 7 1998, using the MCST.

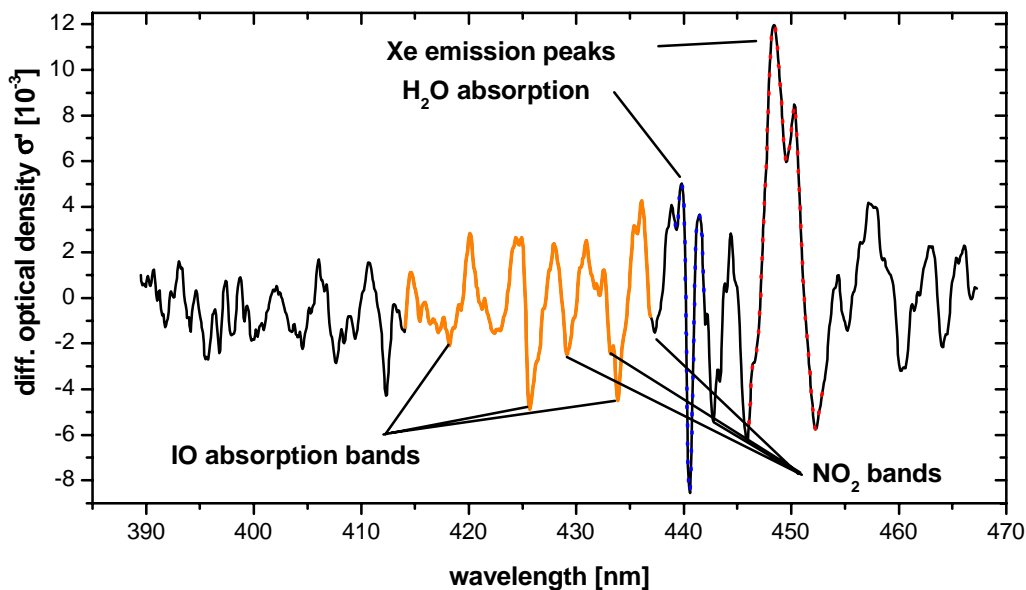


Figure 4.23 Striking features in a MH98 atmospheric spectrum.

Due to very large Xe-lamp emission features in this region and the characteristics of the cross sections applied this interval was divided into two wavelength sections (414 – 437 nm and 429 – 447 nm), which were analysed separately. In order to minimise the residual structure 6 references and a polynomial of the 6th order were applied. Besides the spectral features of the trace gases IO, NO₂ and H₂O two different lamp spectra and an instrumental function were adapted. Depending on wavelength section and lamp, different sets of references were used, leading to 6 sets in total. In order to optimise the relative wavelength position of the references the spectra were shifted relative to an atmospheric spectrum showing clear visible features of all references used. Within the fitting procedure of the evaluation the references were linked to each other, but a linear shift was allowed. That means on the one hand that no relative shift of the references in relation to each other was allowed, but on the other hand that a collective shift in relation to the atmospheric spectrum was legitimate.

The two evaluation intervals were chosen considering the following facts:

- The premier aim was the evaluation of IO, while NO₂ was only the second trace gas of interest in this region. The two largest IO bands are between 420 and 440 nm, whereas the major NO₂ absorption features range from 432 to 450 nm.

- Absorption structures of H₂O are disarranging the evaluation of IO and NO₂ between 440 and 447 nm.
- Large Xe emission features at 437 – 440 nm are producing large residual structures in this interval.

Figure 4.24 shows the two overlapping wavelength intervals of the IO and NO₂ evaluation.

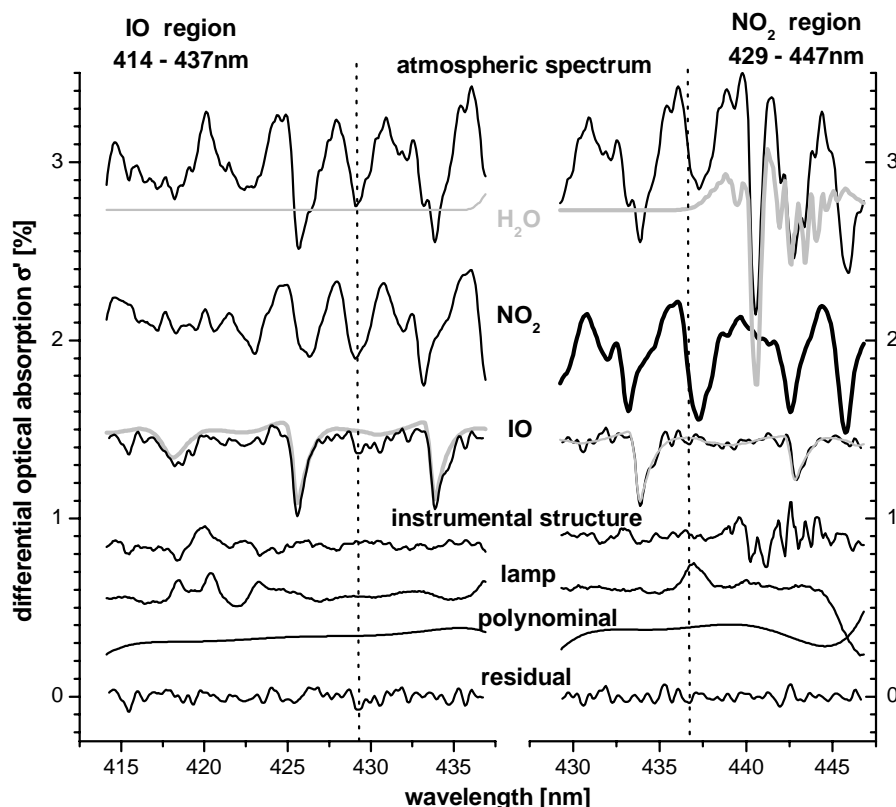


Figure 4.24 Evaluation example of the IO wavelength region (7 Oct 12.25). The left column shows the region of the IO, the right column the region of the NO₂ evaluation. Vertical lines indicate the border of the overlap to the other interval.

a) IO Reference Spectra

The IO reference spectra were convoluted using a literature cross section recorded at our institute by *Hönninger* [1999] and which has been scaled on the basis of measurements made by *Cox et al.* [1999]. For use in this thesis the cross section was convoluted with the 435.84 nm mercury lines as given in Figure 4.21 above. The simulation of the MCST leads to a differential absorption cross section of $\sigma' = 1.9 \times 10^{-17} \text{ cm}^2$ at our spectral resolution of 0.5 nm. For our light path of 14.5 km the differential absorption of 4.5×10^{-3} corresponds to a concentration of $1.6 \times 10^8 \text{ molec cm}^{-3}$.

b) NO₂ Reference Spectra

NO₂ was recorded using the MCST as described in section 4.3.4. As the concentration of the quartz cell is unknown, the recorded absorption spectra have been scaled applying a literature cross section [*Harder et al.*, 1997] (see 3.1.4 b) and c) as well as 4.3.4).

c) *H₂O Reference Spectra*

The H₂O reference spectra were convoluted using the temperature-dependent literature cross section of the HITRAN database at 288 K [*HITRAN*, 1987].

d) *Lamp Reference Spectra*

A very important point is the removal of the characteristic Xe emission features. As all lamps show small differences in their emission feature the sum-lamp spectrum of every lamp is used to evaluate the corresponding atmospheric spectrum. Additionally, the lamp spectrum that shows the most characteristic Xe emission features (*sum-lamp 2*, see Figure 4.22) was used as a reference for each spectrum. To evaluate the spectra recorded with lamp 2 *sum-lamp 2* and *ref-lamp 2* were applied.

e) *Non-Trace Gas Reference Spectra*

Almost every residual shows typical structures that are larger than the noise of the atmospheric spectrum. These features can be caused by

- unidentified absorbers,
- mistakes in the relative shift of the references,
- references that show differences in the shape of the absorption bands due to temperature variations or spectral resolution,
- structures of the lamp spectrum I_0 which slowly vary in time and therefore cannot be removed by fitting a lamp spectrum.

As mentioned above the wavelength region observed is difficult to evaluate as the Xe peaks and the water absorption lines are almost impossible to remove from the atmospheric spectra. As expected the residuals showed typical features in these parts of the spectra. Therefore about 100 residuals (per lamp and per evaluation region) were summed up in a so-called ‘instrumental function’ reference. This reference reduces the influence of the spectral features described above and of unidentified absorbers, but does not influence the fit result of the known absorbers which are adapted [*Ackermann*, 1997].

f) *‘SIGMA’, Other Evaluation Attempts*

In order to avoid these residual features the evaluation software allows to exclude parts of the spectra. The intervals covered by such a ‘SIGMA’ are not considered in calculating the errors of the fit. The SIGMA interval that was necessary to avoid the features caused by the water absorption became relatively large (50 channels = 4 nm from 419 – 423 nm). In addition the average detection limit of all data rose by 50 % from 0.06 to 0.09 ppb. Therefore the possibility of fitting an instrumental function as described under e) was adapted.

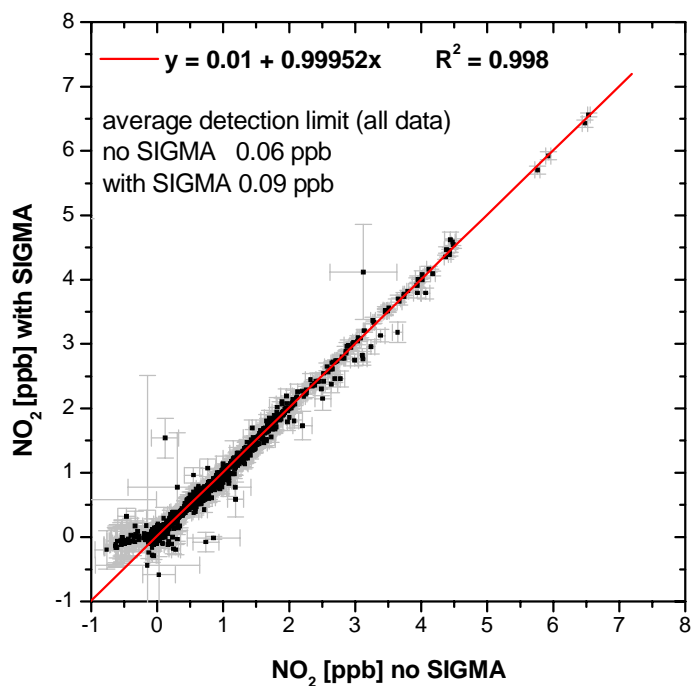


Figure 4.25 Comparison of NO_2 evaluation with and without SIGMA.

4.3.6 Evaluation of the BrO Wavelength Region

The wavelength interval of 312 - 364 nm has been evaluated by *Hönninger* [1999]. Therefore only a short overview of the evaluation concept will be given. The region is influenced by strong absorption structures of ozone. Figure 4.26 shows an exemplary evaluation of the interval.

As mentioned before, this wavelength interval in the UV boundary was measured with not more than half the time resolution of the IO region. Furthermore, the integration times were much higher due to i) lower light intensity of the Xe-lamp and ii) higher light extinction by Rayleigh and Mie scattering (see section 3.1.2). That is why this region was skipped in case of low visibility.

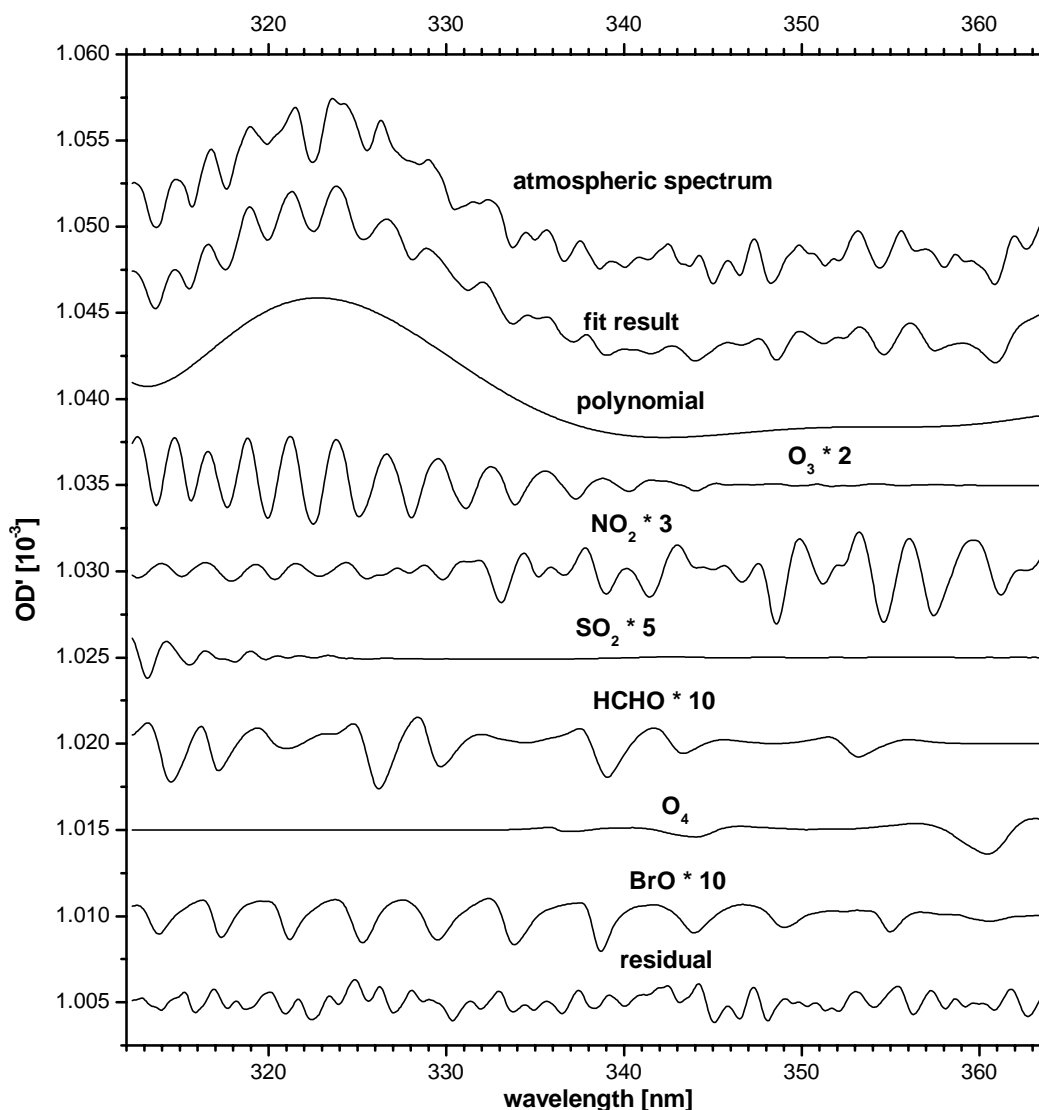


Figure 4.26 Exemplary evaluation of the BrO wavelength interval. The graph shows all species adapted in this region. Note that most of the spectra are scaled up to be shown on one scale (adapted from Hönninger [1999]).

4.3.7 Evaluation of the OIO Wavelength Region

The spectra of the wavelength interval of 545 - 565 nm have been evaluated by Stutz [1999]. Therefore only an evaluation example is given here.

In view of the first detection of IO during MH97, our aim for MH98 was to measure not only IO and its prospective precursors, the halocarbons (HHC), but also the possible product of the iodine oxide self-reaction (R41), iodine dioxide (OIO). No atmospheric measurements of this wavelength interval had been reported before. Figure 4.27 shows an exemplary evaluation that underlines this (first) detection of OIO in the atmosphere.

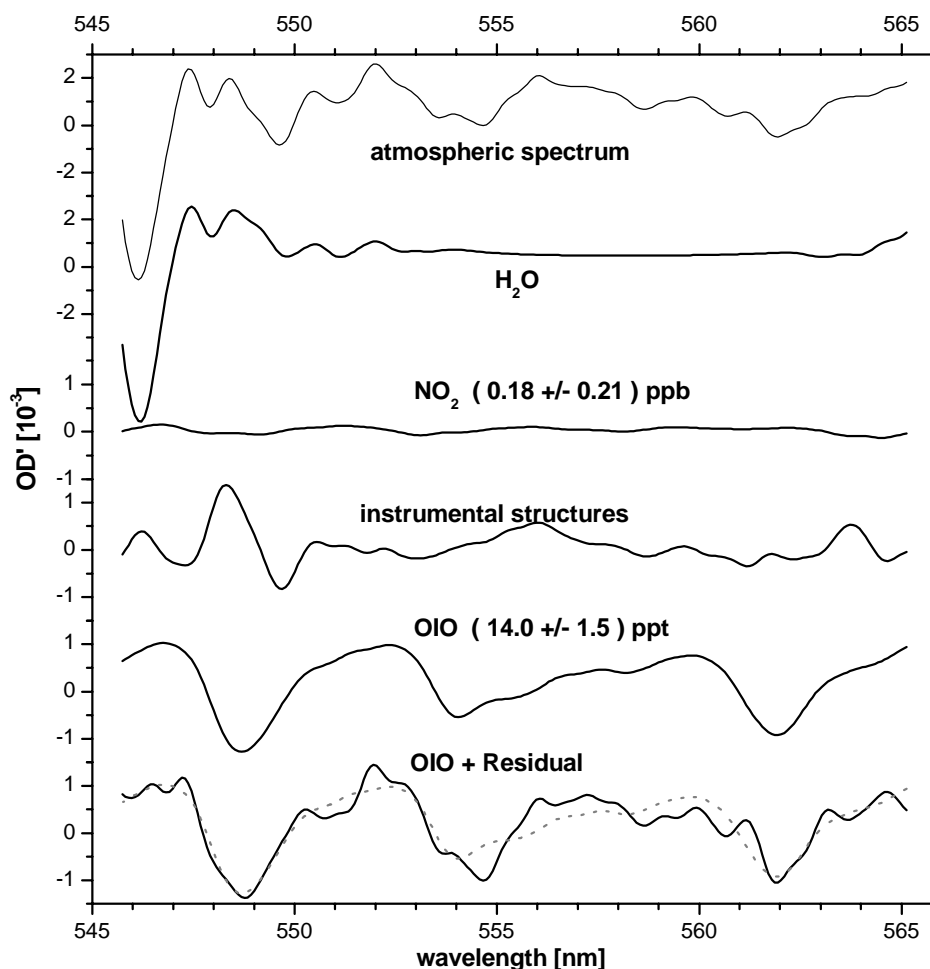


Figure 4.27 Exemplary evaluation of the OIO wavelength interval. The graph shows all species adapted in this region (adapted from Stutz [1999]).

4.3.8 Overview of the DOAS Measurements of MH98

a) Halogen Species

During MH98 we attempted to measure 3 different halogen oxides. As iodine monoxide had already been detected during MH97 (see 4.2.5), evidence of IO in 1998 was not very surprising, even if we had chosen a different season for our measurements. While, in 1997, we detected IO only during 5 days of clean-air westerly conditions, we found daily recurring cycles of IO on over 50 % of the measuring days during MH98. For the first time IO and NO₂ were observed simultaneously. The highest concentration of 8.1 ppt IO was measured in a single event during the polluted period on Sept 26. During the last days of our measurements IO events could be observed on 4 days of easterly flows with excellent visibility, leading to a time series with approx. 15-min time resolution and a detection limit of 0.5 ppt. On the very last day, Oct 7, the IO mixing ratio rose from values below the detection limit to 7.2 ppt. Simultaneously NO₂ dropped by one order of magnitude from 2.3 ppb to 270 ppt.

Iodine dioxide, OIO, was measured for the first time during the 1998 campaign. On several days OIO was found above the average detection limit of 1.7 ppt, especially during the

clean-air periods. Even if a number of OIO events could be observed, we did not find a clear daily cycle or the expected correlation with IO, as will be discussed in chapter 5.1.7 below.

The third halogen oxide, BrO, could not be found during the 4 weeks of our measurements. Even if some points seem to be above the average detection limit of 2.45 ppt, no BrO could be identified in the spectra.

b) Non-Halogen Species

Some of the Non-Halogen species measured by DOAS can be used to indicate the quality of air masses reaching the site. During the first 10 days of our measurements NO₂ and SO₂ showed levels around zero or were scattering around the detection limit of 70 and 190 ppt respectively. During those periods the wind flow remained constant at approx. 20 ms⁻¹ from westerly directions. O₃²² did not show clear daily cycles with maximum values around sunrise and minima in the early afternoon as could be expected for a marine clean-air site. The daily variation of this first period was about ± 10 % around the European background level of 40 ppb over the day. The iodohydrocarbons showed values significantly above the respective detection limit. Diiodomethane, CH₂I₂, the iodinated species with the shortest lifetime, showed a clear daily cycle, as it is rapidly photolysed. Isoprene showed no distinct variations during the first 10 days as expected, as the air masses reached the site from westerly directions. Propane showed one spike on the late afternoon of Sept 9, possibly due to local emissions, while DMS decreased during the first 5 days from 20 to 5 ppt.

On Sept 16 the wind turned from West to East, bringing relatively polluted air masses to Mace Head. Within one day NO₂ rose from 70 to 6000 ppt. Apart from some short peaks due to local pollution HONO exceeded the detection limit of 110 ppt only during this period. HCHO rose to 2.6 ppb within the same period. Simultaneously with the change of the air mass from clean into polluted air O₃ dropped from above 40 to 15 ppb and went up again to the previous level on the following (clean) day. During the polluted period from Sept 19 onwards the daily ozone variation was of the order of up to ± 30 %, strongly correlated with the NO events of up to 1 ppb.

Table 4.8 lists maximum, range of detection limit and average 2σ-detection limit of the trace gases measured at MH98 by DOAS in the halogen oxide wavelength regions from 312 – 565 nm.

²² Only the O₃ data recorded with the in-situ monitor will be taken into account as this data set has the much better time resolution and fewer gaps than the DOAS O₃ data set

Table 4.8 Statistics of trace gases measured by DOAS at MH98 in the halogen oxide wavelength regions (312 – 565 nm).

Species	Maximum	Range of det. limit	Average det. limit
BrO	4.1 ± 4.2 ppt	0.88 - 9.45 ppt	2.45 ppt
IO (long LP)*	7.2 ± 0.3 ppt	0.3 - 6 ppt	0.91 ppt
IO (short LP)*	8.1 ± 2.4 ppt		
OIO	6.7 ± 0.5 ppt	1.4 - 9.3 ppt	3.1 ppt
O ₃	44.0 ± 3.9 ppb	1.4 -15.5 ppb	4.3 ppb
NO ₂ (430 nm)	6.54 ± 0.07 ppb	0.02 - 0.6 ppb	0.07 ppb
SO ₂	5.46 ± 0.1 ppb	0.07 - 0.7 ppb	0.19 ppb
HCHO	2.66 ± 0.6 ppb	0.20 - 2.1 ppb	0.56 ppb
HONO	460 ± 240 ppt	1 - 11200 ppt	110 ppt

* As the highest amount of IO was measured on the short light path resulting in a high uncertainty the highest mixing ratio of the long light path is given as well.

The time series of the different trace gases are shown classified according to wavelength region. Figure 4.30 represents the time series of the species evaluated in the BrO wavelength region. Figure 4.31 shows the DOAS measurements of IO, OIO and NO₂ in the IO wavelength region as well as the in-situ measurements of O₃ and NO.

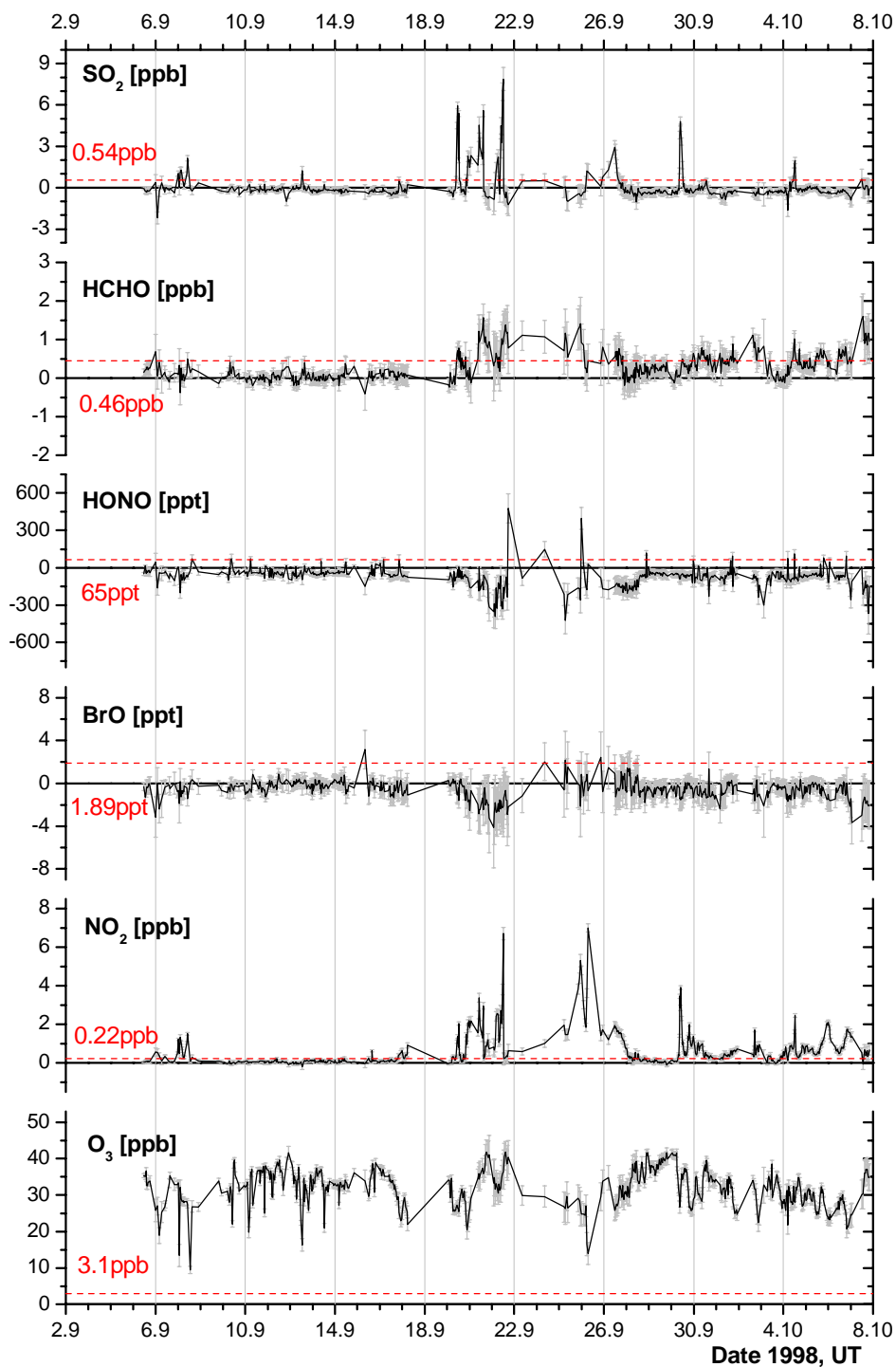


Figure 4.28 Time series of the species evaluated in the BrO wavelength region. Dotted line indicates the the average 2σ -detection limit (adapted from Hönninger [1999]).

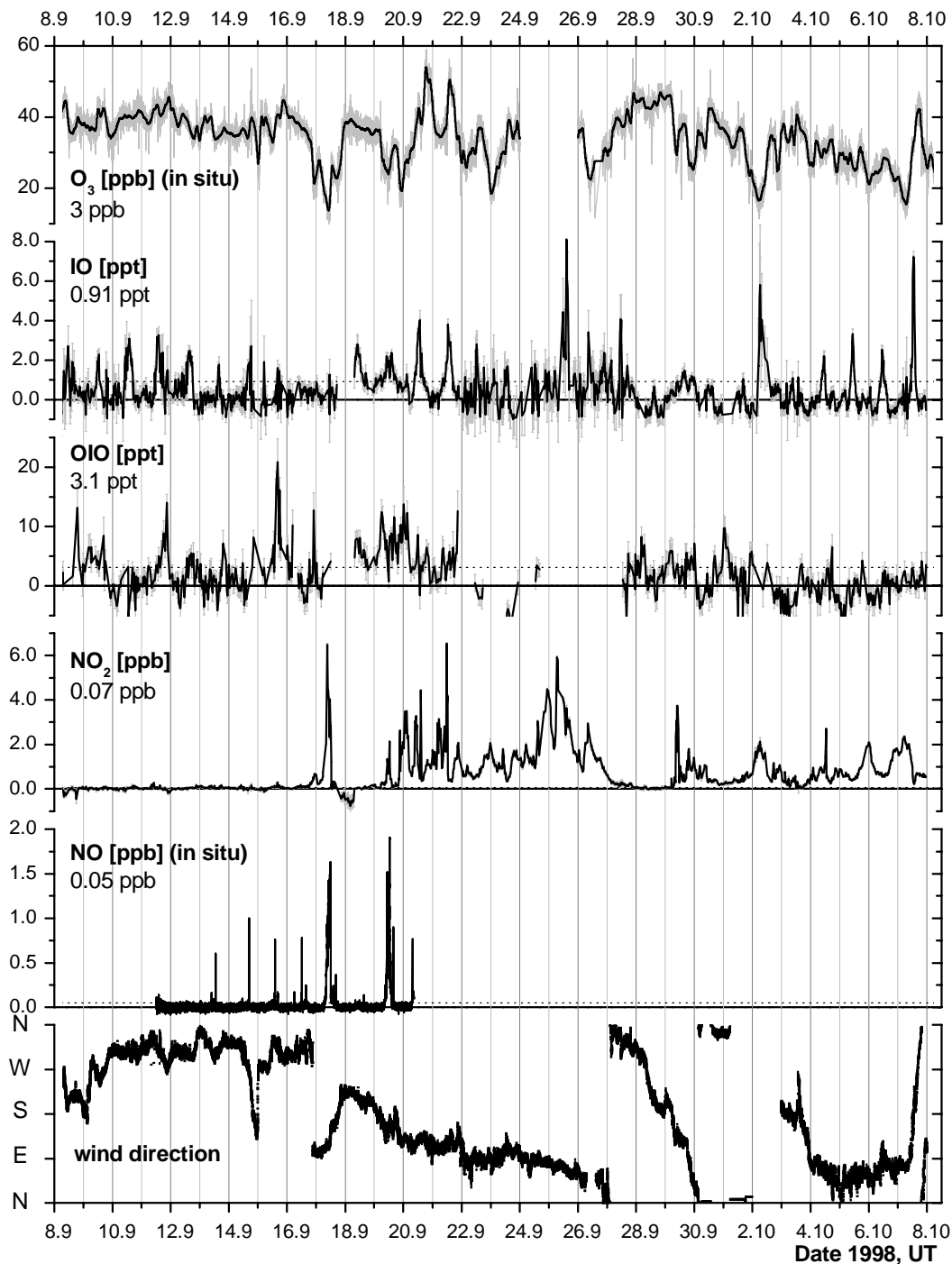


Figure 4.29 Time series of IO, NO_2 (DOAS, 435 nm region), OIO (DOAS, 555 nm), and O_3 and NO, which were measured with in-situ monitors. Dotted line indicates average 2σ -detection limit.

4.3.9 Non-DOAS Measurements of MH98

Within the framework of the *PARFORCE* project, several particle counters were applied in the course of the campaign. As these data are of secondary interest for this thesis they will not be presented here. For more details about the particle data refer to <http://macehead.physics.nuigalway.ie/parforce/>.

Measurements of *Non-Methane Hydrocarbon (NMHC)* were performed as well. C2 - C6 alkanes, C2 - C5 alkenes, benzene, toluene, acetylene and DMS were determined by Lewis [1999] using a GC instrument with detection limits ranging between 0.5 and 4 ppt [Lewis *et al.*, 1998; Lewis *et al.*, 1996]. Samples were taken every 50 - 55 minutes from Sept 8 until Oct 1. As Halogen oxides are known to oxidise DMS forming DMSO (R28), this time series is represented in Figure 4.30. From all *Volatile Organic Compounds (VOC)* measured isoprene and propane are shown as a proxy of biogenic and anthropogenic influences respectively. Isoprene shows daily recurring peaks in the afternoon due to higher biological activity, propane the expected daily noon minimum due to OH oxidation.

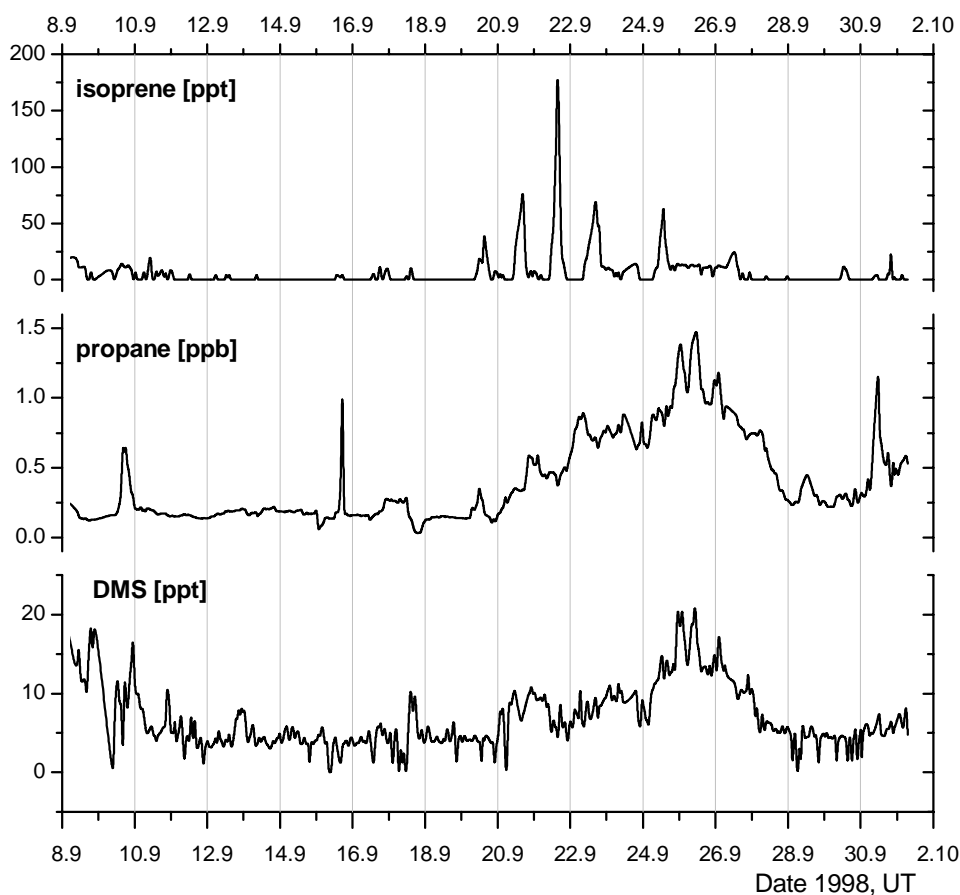


Figure 4.30 DMS, isoprene (mostly biogenic) and propane (anthropogenic) measured at MH98 [Lewis, 1999].

A group of the UEA, Norwich performed measurements of halocarbons [Carpenter *et al.* 2000] using the GS-MS technique with an detection limit of 0.02 ppt, These species are supposed to be potential precursors of RHS (Figure 4.31). These data will be discussed in greater detail later in section 4.4.

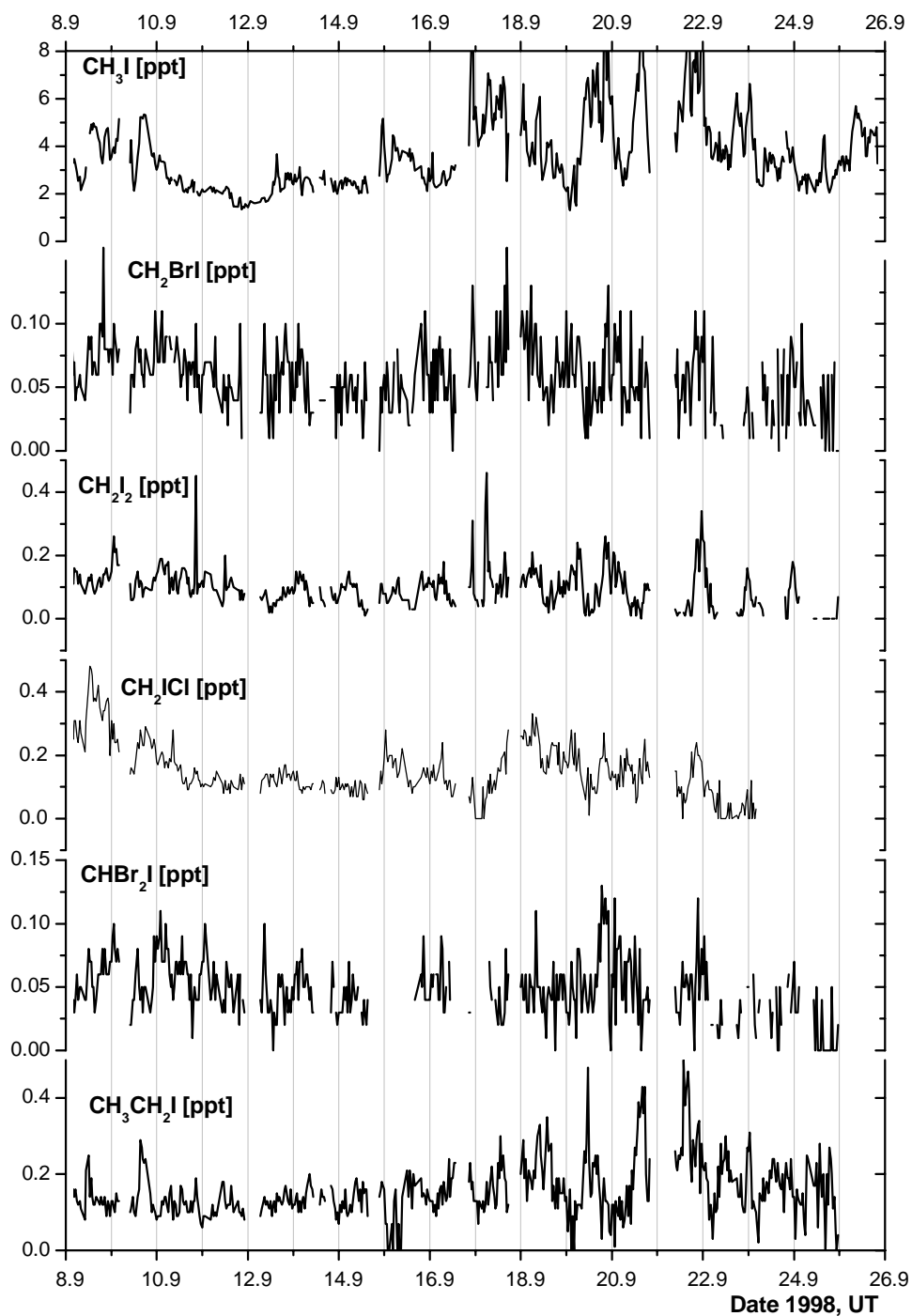


Figure 4.31 HHC time series of MH98 [Carpenter et al., 1999]. Only species including iodine compounds are considered here.

4.4 Results of MH98:

Iodine Oxide in the Marine Planetary Boundary Layer

At the beginning of this chapter a short section will deal with the data-processing routine in order to explain the way most of the data will be presented. It will be shown that the mixing ratio of IO is dependent on a number of parameters. With respect to the potential precursors, the short-lived halogenated hydrocarbons (HHC) or halocarbons for short, solar radiation (SR) and wind direction (WD) a direct dependence can be assumed. With respect to tidal height²³ (TH) and wind speed (WS) the dependence is indirect, as the natural emission of precursors by macroalgae is supposed to increase under low-tide conditions [Carpenter *et al.*, 1999] and as higher wind speed enhances the water-air exchange due to a rougher sea. Furthermore, the precursors themselves are also dependent on SR, as will be explained below. Another parameter which needs to be considered is the NO_x level: The reaction of IO with NO₂ is expected to be one of the most important IO sinks besides the IO self-reaction. Summarising the last paragraph in one equation, one gets:

$$\begin{aligned} IO &= IO(HHC, NO_2, SR, TH, WD, WS) \\ &= IO[HHC(TH, SR, WD, WS), NO_2(WD, SR), SR] \end{aligned} \quad \text{Equ 29}$$

In the following sections different parameters influencing emission and photodissociation of these species will be discussed. Evidence will then be presented that halocarbons are important iodine oxide precursors and the HHC influencing parameters will be discussed in terms of their influence on the IO mixing ratio.

As will be shown below, solar radiation is a parameter of major importance concerning HHC as well as the IO mixing ratios. Unfortunately, SR, given in Wm⁻², was not determined during the whole period of our measurements. Therefore, in order to use a consistent set of data, photopic flux (PF), given in units of kilolux (klx), will be used instead to indicate solar intensity.

4.4.1 Data Processing

The evaluation of the DOAS spectra is described in detail in section 3.1.4. Since the detection limit of a DOAS instrument depends on different varying parameters, such as the intensity of the light received and the length of the light path (which was varying in the case of the Mace Head campaigns), it is not constant. Furthermore, especially in the case of trace gas measurements close to the detection limit, negative concentrations may occur as long as they are compatible with zero within their errors.

A number of correlation plots are shown in order to compare the variations of several trace gases in time and in dependence on WD. In these kinds of presentations strict relations between two parameters can be caused by chemical effects or by transport phenomena.

²³ Calculated on the basis of the TH prediction program of the NUI Galway

Furthermore, parameters can show different relations to each other depending on the time scale of the observations.

a) Temporal Variation

The time series measured at a higher time resolution are averaged to the low-resolution measurements. Between the start and stop times of the low-resolution measurements²⁴ mean values of the more highly resolved data set are generated. This procedure considers measurement or sampling interruptions (e.g. due to changing the DOAS wavelength interval): The values of the highly resolved data set are strictly related to the measurement or sampling intervals of the low-resolution data set. An example of this averaging process is given in the Appendix.

b) Classification of Data

As some parameters show high variations in time, it is sometimes more meaningful to classify the data set. That is why most of the correlation plots represented here do not show the highly resolved data but values classified in a number of intervals, e.g. in the case of diiodomethane (CH_2I_2) versus solar radiation (approximately 500 data points) 8 CH_2I_2 average values related to classes à 9 klx (0 - 9, 9 - 18, ..., > 63 klx) are shown. As a first approximation the square root of the number of data points per class is inversely proportional to the uncertainty of this value. Therefore I estimated the error, assuming a $(1/n)^{1/2}$ dependence. If a linear fit is applied to the data, the fit result and the 95 % confidence levels are given.

c) DOAS Data and the Detection Limit

The time series²⁵ represented in this chapter always show the full data sets. No individual errors are shown in the graphical representations, as the whole set of error bars would make the plots very complex. Instead, the average detection limit of the respective period is shown. A number of data points shown in the time series are below the detection limit or below zero. All these data will not be considered if data are classified for correlation plots.

d) Concentration Distribution with Respect to the Wind Direction

The dependence of parameters on the wind direction (WD) allows to specify relations between different parameters. WD is given as 1-minute time resolution, which is the highest time resolution of all data considered in this thesis, and can therefore well be associated with all other measurements. If the dependence of a parameter on WD is shown, averaged values of 10° sectors are given in polar diagrams, in which 0° corresponds to north, 90° to west etc..

²⁴ mostly the DOAS measurements, where start and stop value of the integration time is given. Note that stop of one data point is not necessarily equal to start of the following data point.

²⁵ Universal time (UT) will be used instead of local time (LT = UT - 1hr)

4.4.2 Potential Precursors of Iodine Oxides

As halocarbons (HHC) emitted by macroalgae are supposed to be important precursors of RHS in the marine atmosphere (see section 2.2), high amounts of IO were expected for southerly, westerly and northerly winds. During these conditions the air masses were expected to become enriched with HHC while passing over the open sea or even more while reaching the site from directions parallel to the coast lines where fields of algae are located.

After a short overview of the meteorological conditions observed at MH98 a number of parameters influencing the mixing ratio of HHC determined during the campaign will be discussed. Section a) deals with the emission behaviour of macroalgae. As SR is supposed to be a parameter of major importance concerning the HHC emissions and sinks, and therefore concerning the concentration of IO, two possibilities of investigating the dependence of the HHC concentration on SR will be presented. In section b) the relation HHC vs. SR will be analysed, which leads to $\Delta_{HHC}(SR)_{SR}$ ²⁶. After the discussion of the dependence of HHC on WS in section c) the relation between HHC and TH will be analysed in general and, by the separation of daytime and night-time data, with respect to the influence of SR on HHC as well. This leads to the second determination of the dependence of the HHC concentration on SR, $\Delta_{HHC}(SR)_{TH}$ at subsection d).

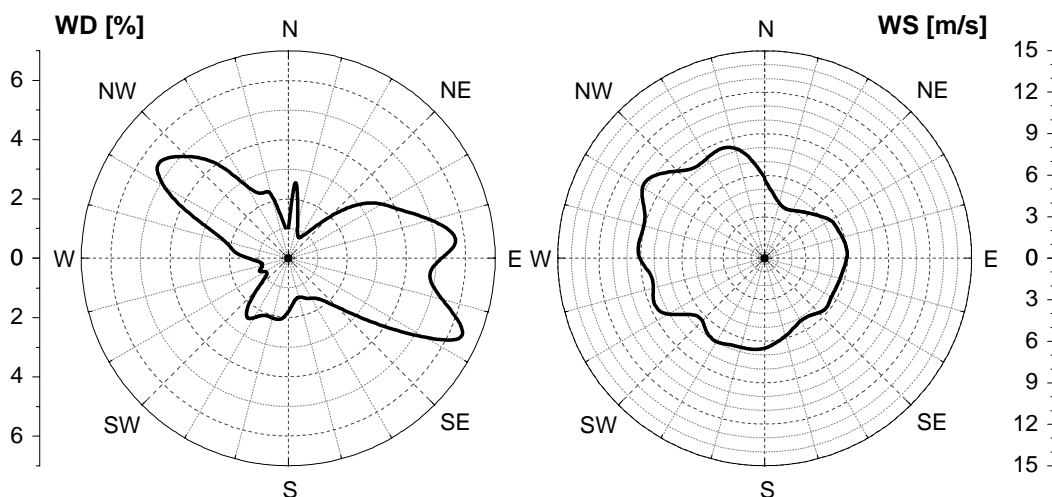


Figure 4.32 Wind direction (WD) frequency and distribution of wind speed in dependence on WD during MH98, 10° sector average values are shown.

The WD frequency count and the dependence of wind speed (WS) on WD is given in Figure 4.32. NW and E have been the dominant wind directions with on average up to 7 % from 110°. Only 1 – 2 % of the air masses reached the site from SE to WSW, while E is the by far dominant wind direction. The average WS data show elevated values from NW/N directions. With respect to the general expectation that HHC-enriched air masses will reach the site from southerly via west to northerly directions, Figure 4.32 indicates that there was a general chance of detecting HHC-enriched air masses during MH98.

²⁶ The index SR indicates that the value has been determined by analysing the dependence of HHC on SR.

As expected, the distribution of WS with respect to WD shows elevated values from the direction of the Atlantic ocean. Additionally the temporal variation of WS is not necessarily equally distributed either. Owing to the location of the site on the Atlantic coast daily periodic variations can be expected. The left diagram of Figure 4.33 represents the average diurnal variation of wind speed of the whole campaign. It shows variations of approximately 15 % (note the suppressed zero line) with higher values around noon. These elevated daytime values may have led to a rougher sea, which influenced surface water → air exchange and therefore possibly enhanced the HHC flux to the atmosphere. Additionally, the aerosol and sea-spray concentration will be enlarged as well.

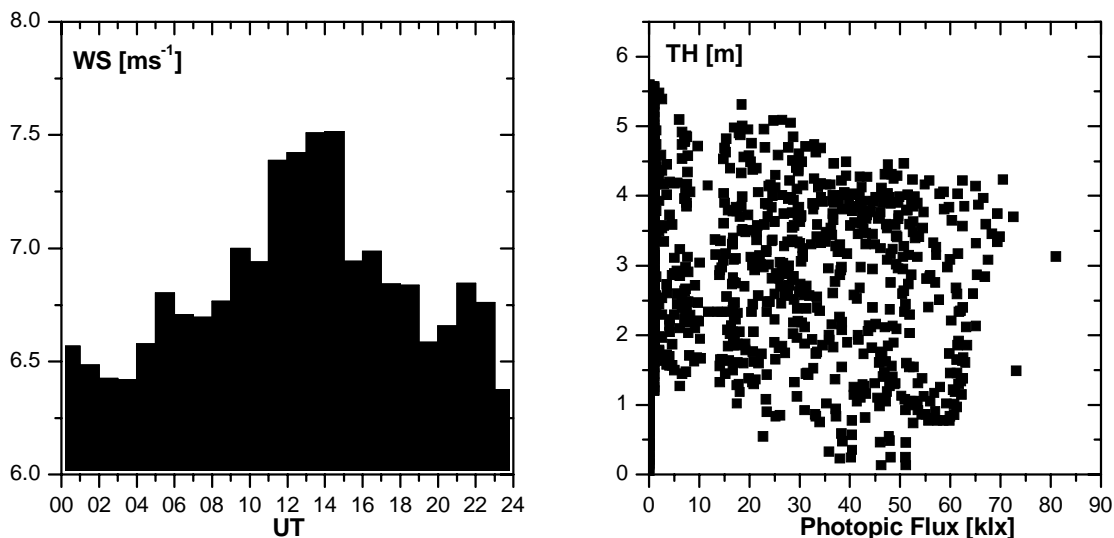


Figure 4.33 Left: Average temporal variation of wind speed, hourly average values of the whole duration of the MH98 campaign from Sept 8 to Oct 7 1998. Right: Tidal height vs. photopic flux during MH98, whole data set.

Tidal height (TH) and solar radiation (SR) are parameters influencing the concentration of HHC, as will be shown below. The TH vs. SR scatter plot (Figure 4.33, right), showing the average values of the 4-week campaign, indicates that both parameters are independent of each other.

a) The Oxidative Stress of Macroalgae

The latest investigations of *Carpenter et al.* [2000] indicate an increase in halocarbon emissions of different *Laminariales*²⁷ species by a factor of 2 to 10 under daylight conditions compared to the respective night-time values. In this study individual plants were analysed with respect to their halocarbon emissions. The species showed significantly higher emissions of HHC if they were exposed to SR, which imposes an oxidative stress on the plants.

With respect to the HHC concentrations determined at the measurement site, and therefore not right above the plants but at a distance of some 100 m to some kilometres, not only the source strength, but also the sinks of HHC need to be considered. As HHC are photo-

²⁷ A macroalgae species which is commonly present on the west coast of Ireland

lytically unstable, their daily periodic cycle is supposed to show minimum values at noon due to a maximum of SR. That is why the formation of inorganic iodine, released via HHC photolysis, is supposed to show maximum values at noon time. The concentration of iodo-hydrocarbons measured under daylight conditions is determined by their sink and production terms. The iodinated compounds with a short photolytic lifetime, which are supposed to lead to the highest production rates of inorganic iodine at Mace Head, are diiodomethane (CH_2I_2) with $\tau_{\text{CH}_2\text{I}_2} \sim 3 \text{ min}$ and bromiodomethane (CH_2BrI) with $\tau_{\text{CH}_2\text{BrI}} \sim 12 \text{ min}$ [Mössinger *et al.*, 1998; Roehl *et al.*, 1997] at mid-latitude noontime conditions. In summary, the concentration of HHC determined at the measurement site depends on the increase in the HHC flux caused by SR, the distance to the source and the photolysis rate of the respective species. The dependence of HHC on SR observed at Mace Head in 1998 will be discussed in subsection b).

b) Halocarbons vs. Solar Radiation

Figure 4.34 demonstrates the influence of SR on the concentration of CH_2I_2 and CH_2BrI . As expected, both species show a negative correlation with SR, which is more distinct in the case of CH_2I_2 . It has to be kept in mind that TH is supposed to influence the HHC emissions as well. Its variation is shown on the smaller panels in the middle of Figure 4.34.

The comparison of HHC concentration and SR underlines the importance of this parameter. Both species analysed here show a pedestal, which is independent of SR, of approximately $[\text{CH}_2\text{I}_2] = [\text{CH}_2\text{BrI}] = 0.04 \text{ ppt}$. Nevertheless, above this pedestal the negative correlation of CH_2I_2 as well as CH_2BrI vs. SR is obvious. The difference between high and low SR, $\Delta_{\text{HHC}}(\text{SR})_{\text{SR}}$, is equivalent to the difference of the abscissa value of the linear fit curve, which corresponds to the HHC concentration under $\text{SR} = 0$, and the independent base of $[\text{HHC}] = 0.04 \text{ ppt}$. It follows $\Delta_{\text{CH}_2\text{I}_2}(\text{SR})_{\text{SR}} = 0.08 \text{ ppt}$ and $\Delta_{\text{CH}_2\text{BrI}}(\text{SR})_{\text{SR}} = 0.024 \text{ ppt}$. It is important to note that these values are not corrected for the influence of TH. Even if SR and TH are independent of each other, as can be seen from Figure 4.33, the TH signal leads to larger uncertainties. However, especially with respect to the release of inorganic iodine to the atmosphere, one has to consider the influence of the higher HHC daytime emissions of macroalgae as mentioned at the beginning of this chapter. Therefore, the flux of HHC to the atmosphere can be expected to be much higher under daylight conditions²⁸, even if the measured concentrations are lower due to the fast photolysis, which over-compensated the increased daytime emissions, as can be seen from Figure 4.34.

²⁸ due to higher oxidative stress by sun and exposure to the atmosphere, see also dependence of HHC on TH

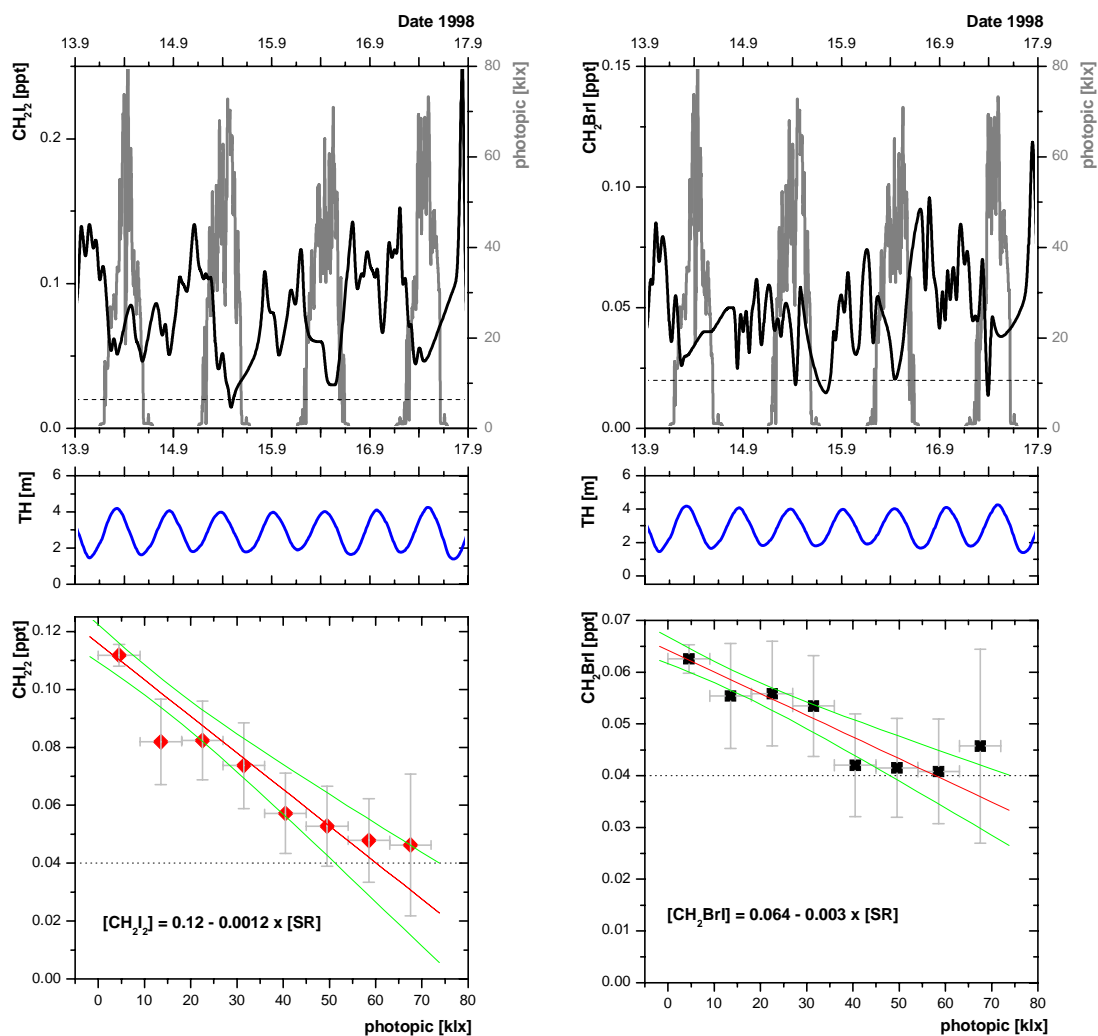


Figure 4.34 Temporal variations of HHC and solar radiation (SR). Upper panel: Time series of HHC and SR during a clean-air period (dashed lines indicate the HHC detection limits). Middle panel: Tidal height (TH). Lower panel: Scatter plot of HHC (9 klx interval average values) vs. SR and linear fit and 95 % confidence level. y-error bars represent the number of data points considered per SR interval, x-error bars show the length of the interval. Dotted line: HHC pedestal independent of SR.

It is important to note that these values are not corrected for the influence of TH. Even if SR and TH are independent of each other, as can be seen from Figure 4.33, the TH signal leads to larger uncertainties. However, especially with respect to the release of inorganic iodine to the atmosphere, one has to consider the influence of the higher HHC daytime emissions of macroalgae as mentioned at the beginning of this chapter. Therefore, the flux of HHC to the atmosphere can be expected to be much higher under daylight conditions²⁹, even if the measured concentrations are lower due to the fast photolysis, which over-compensated the increased daytime emissions, as can be seen from Figure 4.34.

²⁹ due to higher oxidative stress by sun and exposure to the atmosphere, see also dependence of HHC on TH

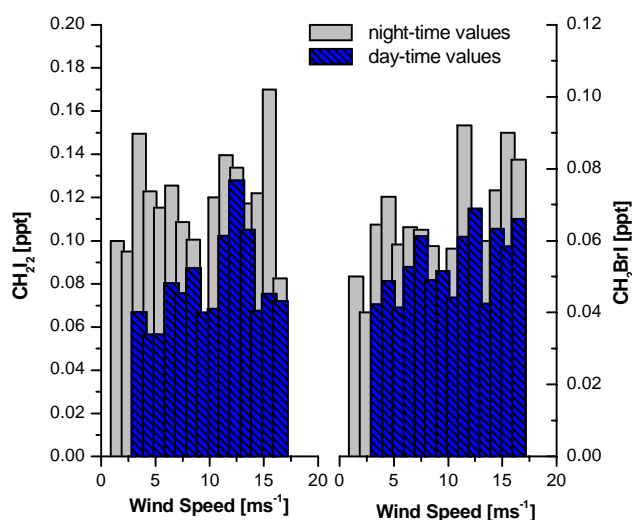
c) *Halocarbons vs. Wind Speed*

Figure 4.35: Correlation of CH_2I_2 (left) and CH_2BrI (right) vs. WS, separated in daytime (dark hatched) and night-time data (grey).

concentrations (section b)). However, only the CH_2I_2 daytime values show a slight trend with higher mixing ratios at higher WS. In general, the influence of WS seems to be negligible.

d) *Halocarbons vs. Tidal Height*

Analysing the dependence of HHC concentrations on TH, one has to take into account the significant dependence on SR. The data set shown in Figure 4.36 is divided into daytime and night-time values to rule out the influence of the ‘disturbing’ HHC sink (and inorganic iodine production) parameter SR. Its influence is automatically eliminated by analysing the separated night-time values. Nevertheless one has to keep in mind that the HHC source strength is also dependent on SR, as pointed out above.

As expected, the daytime data are not significantly dependent on TH as photolysis is the dominant process. In contrast to that, the night-time data, especially in the case of CH_2I_2 , show a negative correlation with higher values during low tide with $r^2 = 0.87$. This dependence of HHC on TH is obvious, but it is not possible to decide whether the decrease with rising tidal height is linear, of higher order or even exponential. To answer this question an observation period of more than only 2.5 weeks is required.

A dependence of HHC emissions on WS can be expected as higher WS usually occurs in combination with a rougher sea. This enlarges the water-air exchange and could lead to an increased flux of HHC to the atmosphere. Figure 4.35 represents the correlation of CH_2I_2 and CH_2BrI vs. WS. As the night-time WS is about 15 % lower than the daytime values (Figure 4.33), the data set is separated into daytime and night-time data. Furthermore, the influence of SR can be ruled out. Figure 4.35 confirms the general behaviour of elevated night-time

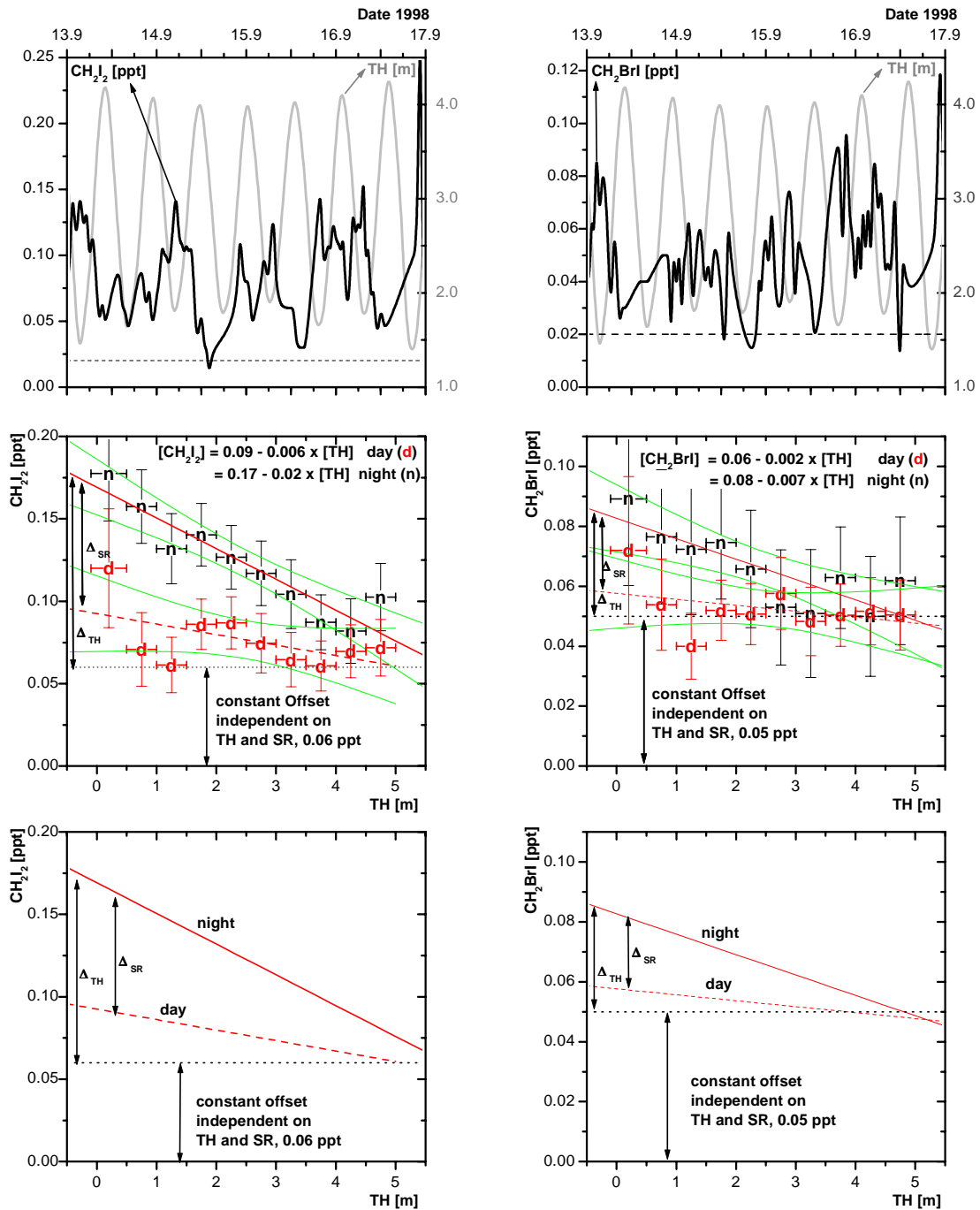


Figure 4.36 Top: Time series of a clean-air period. Middle: Scatter plots of HHC vs. tidal height (TH) of the whole 4-week record, classified in 0.5 m TH values. **d** = daytime (dashed) **n** = night-time (full line) values with the respective linear fit curves and 95 % confidence levels. Bottom: Fit results only.

Assuming, as a first-order approximation, a linear dependence of the HHC mixing ratio on TH, the linear fits of the daytime and night-time values allow to quantify the influence of TH and SR. The ‘offset’ (pedestal) of approximately $C_{CH_2I_2} = 0.06 \text{ ppt}$ and $C_{CH_2BrI} = 0.05 \text{ ppt}$ is clearly visible in both cases, indicating an emission of HHC which is independent of TH, possibly caused by oceanic and not by coastal emissions. Photolysis is eliminated in the case of the night values. Thus the influence of TH ($\Delta_{HHC}(TH)_{TH}$) is given as the difference between the fit curve value at $TH = TH_{\min} = 0 \text{ m}$ and the independent

offset signal. The values derivable from the equations given in Figure 4.36 are $\Delta_{CH_2I_2}(TH)_{TH} = [CH_2I_2]_{night}(TH=0) - C_{CH_2I_2} = 0.11 \text{ ppt}$ and $\Delta_{CH_2BrI}(TH)_{TH} = 0.03 \text{ ppt}$.

The difference between the abscissa intercept of the two linear fit curves (night and daytime values for $TH = 0 \text{ m}$) shows the influence of SR, determined by analysing the TH dependence of the HHC $\Delta_{HHC}(SR)_{TH}$. These values of $\Delta_{CH_2I_2}(SR)_{TH} = 0.08 \text{ ppt}$ and $\Delta_{CH_2BrI}(SR)_{TH} = 0.02 \text{ ppt}$ are in excellent agreement with the values calculated in subsection b). The dependencies of the HHC mixing ratios on SR and TH are summarised in Table 4.9.

Table 4.9 Additional concentration of HHC determined at Mace Head in autumn 1998 which can be related to variations in solar radiation (SR) and tidal height (TH).

Maximal Influence of SR			determined via
$\Delta_{CH_2I_2}(SR)_{SR}$	CH_2I_2	0.08 ppt	SR
$\Delta_{CH_2I_2}(SR)_{TH}$	CH_2I_2	0.08 ppt	TH
$\Delta_{CH_2BrI}(SR)_{SR}$	CH_2BrI	0.02 ppt	SR
$\Delta_{CH_2BrI}(SR)_{TH}$	CH_2BrI	0.02 ppt	TH
Maximal Influence of TH			determined via
$\Delta_{CH_2I_2}(TH)_{TH}$	CH_2I_2	0.11 ppt	TH
$\Delta_{CH_2BrI}(TH)_{TH}$	CH_2BrI	0.03 ppt	TH

It can be concluded that TH and SR have a significant effect on the HHC mixing ratios detected at the site. This general dependence on TH confirms the observations of *Carpenter et al.* [1999], who found a relation between the HHC concentrations and the TH, and *Liss et al.* [2000] and *Carpenter et al.* [2000], who found an increasing flux of HHC if the macroalgae are exposed to oxidative stress. An interpretation of SR and TH with respect to the absolute flux of HHC, and therefore, after photolysis, to the amount of reactive inorganic iodine released, is not possible on the basis of these data as the absolute increase in the HHC emission caused by oxidative stress is still not exactly known. The TH-independent offset of the HHC concentration could presumably be due to oceanic emissions, independent of the release at the shoreline.

e) Dependence of Short-Lived IO Precursors on Wind Direction

In order to locate the source of the precursors Figure 4.37 portrays the distribution of CH_2I_2 and CH_2BrI with respect to the WD in 10° sectors. Daytime and night-time values are shown separately to consider the influence of SR.

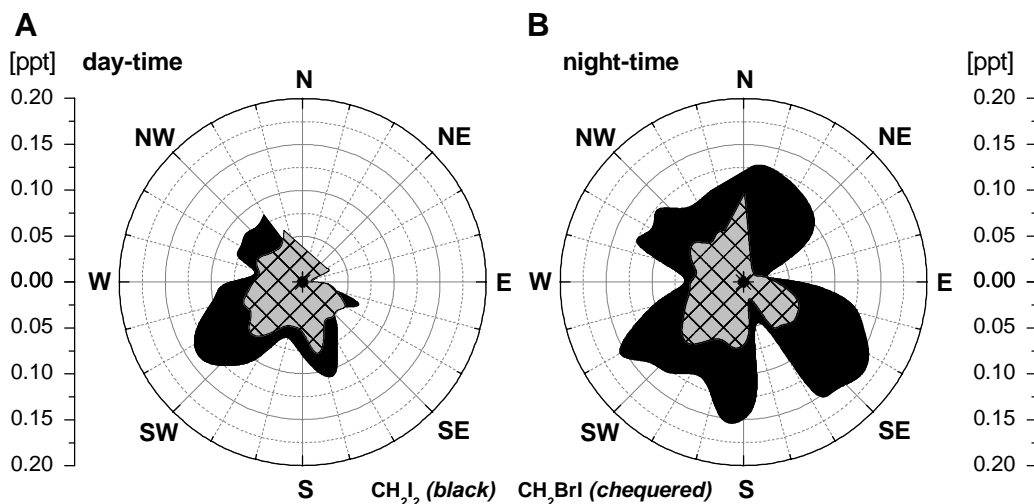


Figure 4.37 Dependence of CH_2I_2 (black) and CH_2BrI (chequered) on wind direction. A: daytime data, B: night-time data (see also Figure 4.39, right panel).

The distribution shows significant differences between daytime and night-time data. First of all, as expected from the time series and correlations plots shown in the last subsections, the absolute values observed during daylight are smaller compared with the values recorded at night. Furthermore, it is noticeable that the night-time data show a large maximum in the SE sector between 110° and 130° .

This difference between daytime and night-time can be interpreted in terms of the distance of the source region of the HHC: Under daylight conditions the photolytic lifetime is $\tau = 3 - 10$ min in the case of CH_2I_2 . Assuming a typical daytime wind speed of $v = 7.5 \text{ ms}^{-1}$, the distance of the HHC source can be calculated to be not more than 1 to 4.5 kilometres.

As can be seen from Figure 4.38, the Irish coastline south-east of Mace Head is very rugged. South-east of the site there are a number of small creeks where large areas covered with seaweed are exposed to the atmosphere during low tide. The circle shown in Figure 4.38 indicates a 4.5-km radius around Mace Head. Remembering that the night-time distribution of HHC with respect to WD showed elevated values from south-westerly directions (Figure 4.37), the two islands south of the site and *Ard Bay* in S/SE directions attract attention. Air masses reaching the site from these directions can take up much more HHC than the air coming from the open ocean. However, under daylight conditions there must be a local source because of the fast photolysis. Therefore the daytime distribution of HHC can only be explained by this assumption of a local source very close to the site.



Figure 4.38 Map of the area around Mace Head (MH), arrow indicates a circle of 4.5 km, the maximal source distance of daytime HHC that can reach MH before being photolysed (see text). Squares indicate 'Irish Grid' with a length of 1 km.

The enhanced night-time values observed in air masses from the north-east and south-east may be associated with sources at a larger distance from the site. *Galway Bay* with an extension of approximately 80 – 100 km is the major HHC source area in the southern sector (see Figure 4.50), while *Bertraghboy Bay* and *Cashel Bay* are potential source regions NE of Mace Head. Especially the daytime minimum found in the direction of the night-time maximum, namely SE, indicates that the night-time sources are located at a larger distance. Due to the missing photolysis at night the HHC can reach the site from a distance of some 10 km. However, even if there are no daytime measurements of HHC from the SE, this sector has to be considered as a potential source region of re-I and IO, especially as the inorganic iodine formed in the HHC photolysis is (re-)generated within seconds. In section 4.4.3 a) it will be shown that SE/E is the most important source region of IO.

In summary one can say that a strong dependence of HHC on TH (as a source-influencing parameter) and SR (as a major sink) has been determined, which was more significant in the case of CH_2I_2 than in the case of CH_2BrI . This confirms the results of *Carpenter et al.* [1999] who found a strong dependence of CH_2ICl , CH_2BrI and CHBr_3 on TH, but a weaker correlation with CH_2I_2 which was more significant here.

However, even if a significant dependence of the HHC concentration on SR and TH has been determined, a significant offset of the order of the variation caused by SR and TH of approximately 0.05 ppt has been found. This pedestal ensures the possibility of determining HHC under conditions of high tide and high solar irradiance and, therefore, the possibility of detecting (low) amounts of IO during these periods of relatively low HHC mixing ratios.

In addition, it is important to note again that the observations related to the dependence of HHC emissions on SR confirm the investigations of *Carpenter et al.* [2000] even if *Carpenter and co-workers* analysed the emissions of some individual plants, while in the case presented here 'integrated concentrations' have been analysed.

4.4.3 IO Dependence on its Precursors and other Parameters

Assuming emissions of HHC to be the primary source of iodine at Mace Head, SR is necessary to transform the non-reactive organic iodine into reactive, inorganic species like IO. The following section deals with IO-relevant parameters. It starts with a comparison of the dependence of IO and HHC on WD, and continues with IO vs. SR and TH respectively.

a) *Dependence of IO, CH_2I_2 and CH_2BrI on Wind Direction*

Possible other sources of IO besides HHC, such as the release from sea salt, have been discussed in chapter 2. They are relatively unlikely, i) as they have not been observed during atmospheric measurements so far and ii) as the iodine content of sea salt is very low ($\sim 2 \times 10^{-5} \%$ [*Holland, 1978*]). From a general point of view one might expect a similar dependence of HHC and IO on WD, as the photolytic lifetime of both species is in the

same order of magnitude (minutes during noon PBL conditions). On the other hand, HHC are finally destroyed after the photolytic decay, while IO is most probably regenerated in the reaction with ozone (cf. chapter 2). Thus a HHC source at a relatively large distance can produce measurable amounts of IO at the site, while no HHC can be measured under daylight conditions due to the fast photolysis. As will be shown below, IO is highly dependent on SR. This leads to a temporal dependence, which also needs to be considered by analysing the distribution with respect to WD. However, only very small amounts of IO can be expected from directions where neither in the daytime nor at night-time any HHC has been detected. Additionally, WS determines the period of time during which the air masses can be enriched with HHC by passing over algae fields, and it influences the water-air exchange as mentioned above.

Figure 4.39 shows the dependence of IO and HHC on WD as 10° average values. The left graph shows the IO values of the whole campaign (chequered) and of the shorter period of the HHC measurements (line), the right graph shows the precursors CH_2I_2 and CH_2BrI .

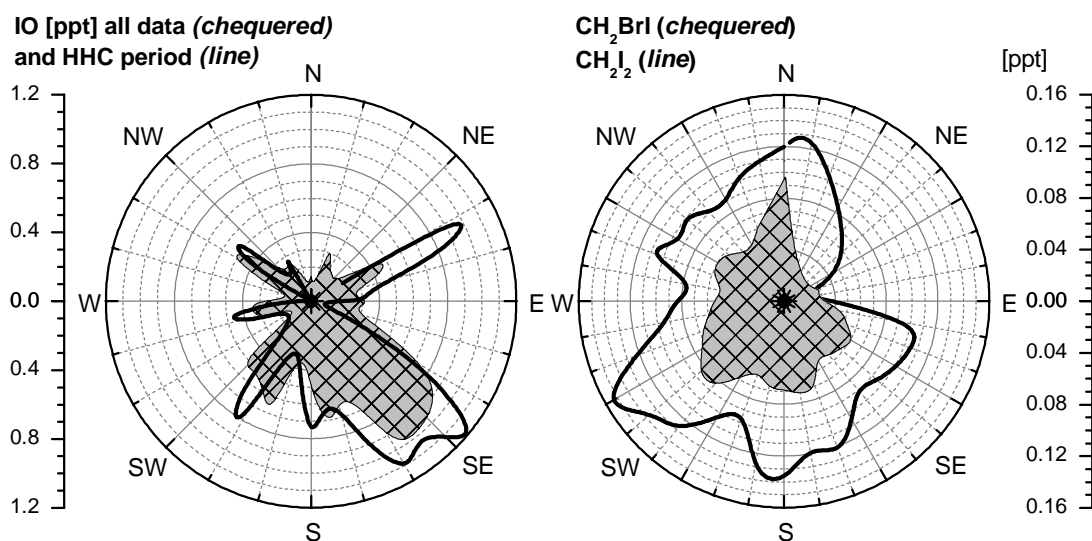


Figure 4.39 Left: Dependence of IO on wind direction (WD) given as 10° average values. Chequered: whole IO measuring period. Line: IO data of the shorter HHC measuring period. Right: dependence of CH_2I_2 (line) and CH_2BrI (chequered) on WD. Figure 4.37 represents the CH_2I_2 and CH_2BrI distribution separated in daytime and night-time values.

From Figure 4.39 it becomes obvious that the south-east sector between 120° and 150° is the direction with by far the highest average values of IO, while, without separating the HHC data set into daytime and night-time values, the dependence of HHC on WD is relatively equally spread apart from the gap at NE/E directions. However, the large maximum in the IO distribution at the SE sector is in excellent agreement with the HHC night-time distribution (Figure 4.37). This underlines the importance of HHC emitted in Galway Bay and in the creeks along the coast south-east of Mace Head, as e.g. Ard Bay, as the primary source of the IO detected at the site. Moreover, no other sources of IO are known in that direction. The origin of the IO detected at the site during SW wind directions may be the coastline of the small islands south of Mace Head.

To verify this conclusion the analyses of the temporal variation of IO and HHC and other relevant parameters affecting IO directly or indirectly via their influence on the precursors are discussed in the following section.

b) Comparison of the Temporal Variation of IO and Halocarbons

Although the SE sector has been detected as the main source region of IO and night-time CH_2I_2 , the dependence of IO and HHC on WD does not show a general resemblance. Comparing the temporal variation of both species it has to be considered that even if HHC are the precursors of IO they do not necessarily have to undergo exactly the same temporal changes. It depends on the time scale and the place of observation whether a positive or a negative correlation is to be expected. Generally speaking, it depends on the flux of the educt (here HHC) to the atmosphere, and therefore the production rate, and the velocity of the different loss processes whether product (here I atoms or IO due to the fast reaction of I with O_3) and educt will vary in positive or even negative correlation with each other. However, from our data set we cannot analyse the flux of HHC (which is the relevant parameter concerning the production rate of organic and, under daytime conditions, also inorganic iodine), which is supposed to be positively correlated with the IO concentration. The HHC concentration determined at the site strongly depends on SR and WD, as has been shown in the last section.

Figure 4.40 represents a comparison of two time series of IO and CH_2I_2 (top) as well as the scatter plot of both species (bottom); the left side shows the whole set of data classified as 0.02 ppt intervals of CH_2I_2 , while the right graph gives all raw data above the respective detection limit.

The time series as well as the scatter plots show a slightly negative correlation of IO and CH_2I_2 . As discussed in the first paragraph of this section, the negative correlation can easily be explained. Assuming the production rate of HHC to be constant during the whole day, the HHC variation is determined by photolysis due to increasing SR. In turn, assuming that the HHC photolysis is the only production process of inorganic iodine, the IO production only depends on the actinic flux as well. As I mentioned above, the production of HHC, and therefore the flux of iodine from the ocean to the atmosphere, increases with increasing SR. However, as long as the photolysis overcompensates the increasing HHC production, the HHC concentration determined at the site will decrease with increasing SR.

In detail, with increasing solar radiation in the early morning hours the frequency of the CH_2I_2 photolysis increases, leading to the photodissociation and the maximum formation of I atoms with $J_{\text{CH}_2\text{I}_2} = (4 - 7) \times 10^{-3} \text{ s}^{-1}$ [Mössinger *et al.*, 1998; Roehl *et al.*, 1997], which corresponds to a photolytic lifetime of $\sim 2 - 4$ min around noon. Assuming 30 ppb of ozone, the reaction of atomic iodine is even faster. With $k_{\text{I}+\text{O}_3} = 1.1 \times 10^{-12} \text{ cm}^3 \text{ molec}^{-1} \text{ s}^{-1}$ the lifetime of I vs. O_3 can be calculated to be approximately 1 second. Therefore the photolysis of HHC is the rate-determining step of the IO production and IO is instantly formed after the HHC photolysis. As IO increases simultaneously with increasing SR (see

next section) and parallel decreasing CH_2I_2 , it becomes obvious that not only the photolysis, but also the flux of HHC is a determining parameter.

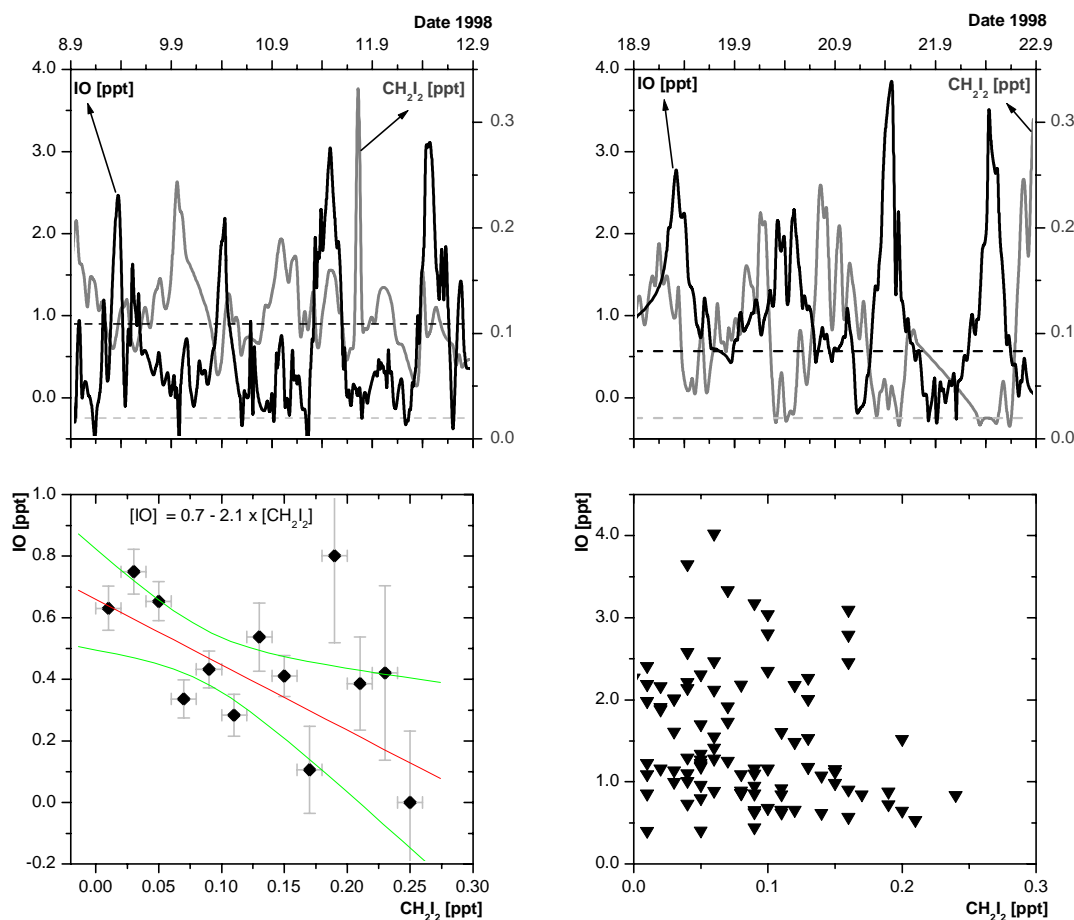


Figure 4.40 Temporal relation of IO and CH_2I_2 . Upper panel: Two time series of both species, dashed line indicates average detection limit of the respective period. Lower panel: IO vs. CH_2I_2 . Left: IO averaged per 0.02 ppt CH_2I_2 intervals with linear fit and 95 % confidence levels. Right-hand side: Raw data.

In summary, a negative correlation of the concentrations of IO and its precursors has been observed. This situation is established as long as the increase in HHC emissions do not overcompensate the increasing photolysis. The IO vs. CH_2I_2 scatter plots of the lower panel of Figure 4.40 show a slightly negative correlation. In the left graph, where the IO values are averaged in classes of 0.02 ppt of CH_2I_2 , the dependence is significant, but the high variability of the data is obvious. The right graph, which shows the raw data, confirms this high variability and the negative correlation: the highest IO values occur at low CH_2I_2 and vice versa. The data representing low concentrations of both species can be caused e.g. by mixing processes.

c) Dependence of IO on Solar Radiation

The actinic flux is a parameter influencing the IO concentration threefold: directly due to the IO photolysis (which essentially leads to a null cycle as IO is photolysed but also regenerated via reaction R1 of I and O_3) and the photolysis of HHC leading to organic iodine, and indirectly, as sunlight increases the flux of the IO precursors, due to photo-

oxidative stress. To investigate the influence of SR on IO, Figure 4.41 shows the average daily cycle of IO and SR of the whole campaign. The values plotted are hourly average values of IO and half-hour values of SR (which was measured with a 5-min time resolution compared to a time resolution of ~20 min in the case of IO) of the whole 4-week data set. Only data above the detection limit are considered, the other values are set to be zero. Thus the absolute values are lower than the mixing ratios observed during high IO events. Considering all data, the average diurnal cycle looks the same with slightly higher values at noon. The daily cycles have not been normalised before the averaging process.

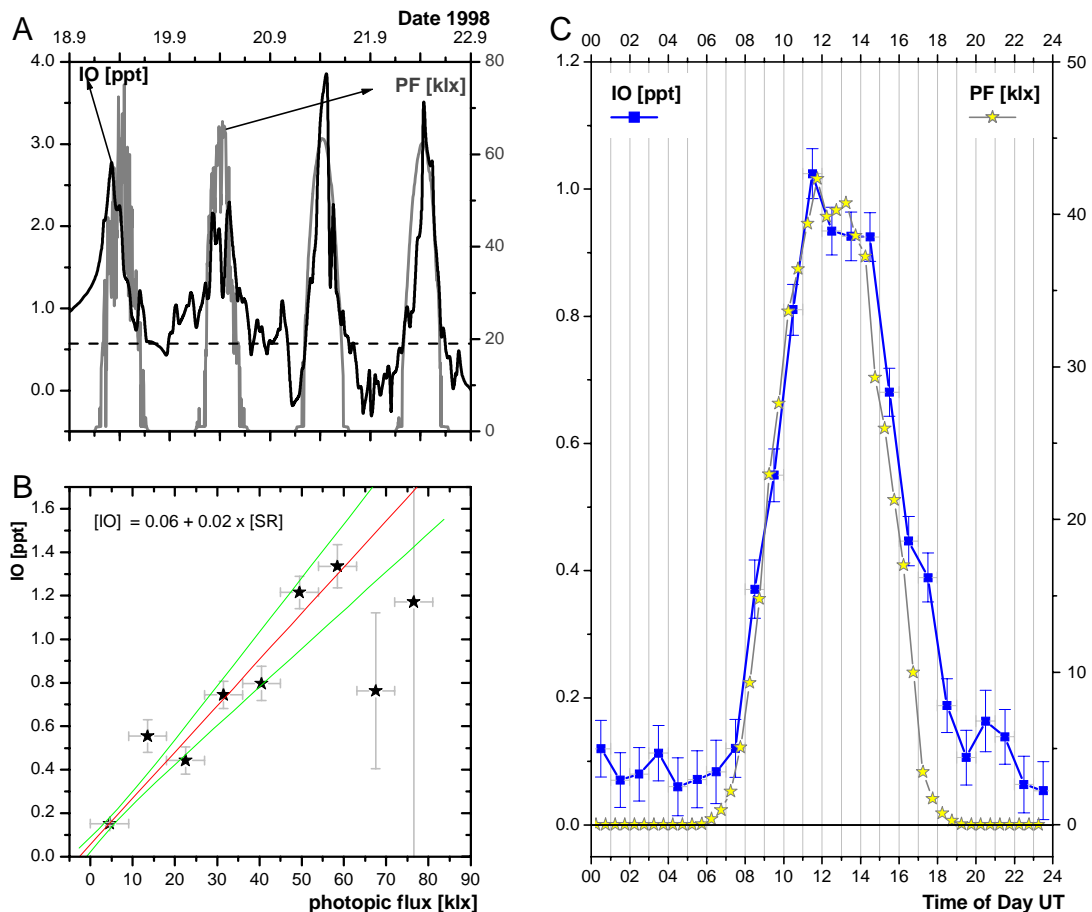


Figure 4.41 IO and solar irradiation, represented as Photopic Flux (PF). **A:** Time series of IO (left) and PF (right abscissa), dashed line indicates the average IO detection limit of this period (0.6 ppt). **B:** IO vs. PF scatter plot, shown as 9 klx classes of all values of the whole campaign above the detection limit and a linear fit with 95 % confidence level. **C:** Average daily cycle of IO (left abscissa) and PF (right abscissa) given as hourly and half-hourly average of all values above the detection limit of the whole period of the campaign. Error bars correspond to the number of data points considered per interval.

The exemplary time series represented in Figure 4.41 (A) represents the averaged overall daily cycle (C) quite well. The agreement of both graphs (IO and PF) shown in diagram C, especially the simultaneous increase at sunrise, attracts attention. IO rises from the average night-time background values of around 0.1 ppt to a noon average of 1 ppt at 11 UT, when the highest local solar zenith angle (SZA) is reached. Well correlated with SR, the average IO mixing ratio decreases to the night-time value of ~0.1 ppt. The scatter plot of IO vs. SR

(given as IO average values of PF classes of 9 klx) shows an excellent linear correlation, except for the two classes of the highest radiation. These last two data points have large errors as the number of the values considered is very small.

d) *Dependence of IO on Tidal Height*

As explained above the elevated flux of HHC to the atmosphere in the daytime during low tide is compensated by the enhanced daytime photolysis rate. Nevertheless, the HHC and thus the iodine flux to the atmosphere increases at low tide (see section 4.4.2 d)). Consequently, TH indirectly influences the IO production rate, and therefore at least the daytime concentrations of IO can be expected to show a dependence on TH.

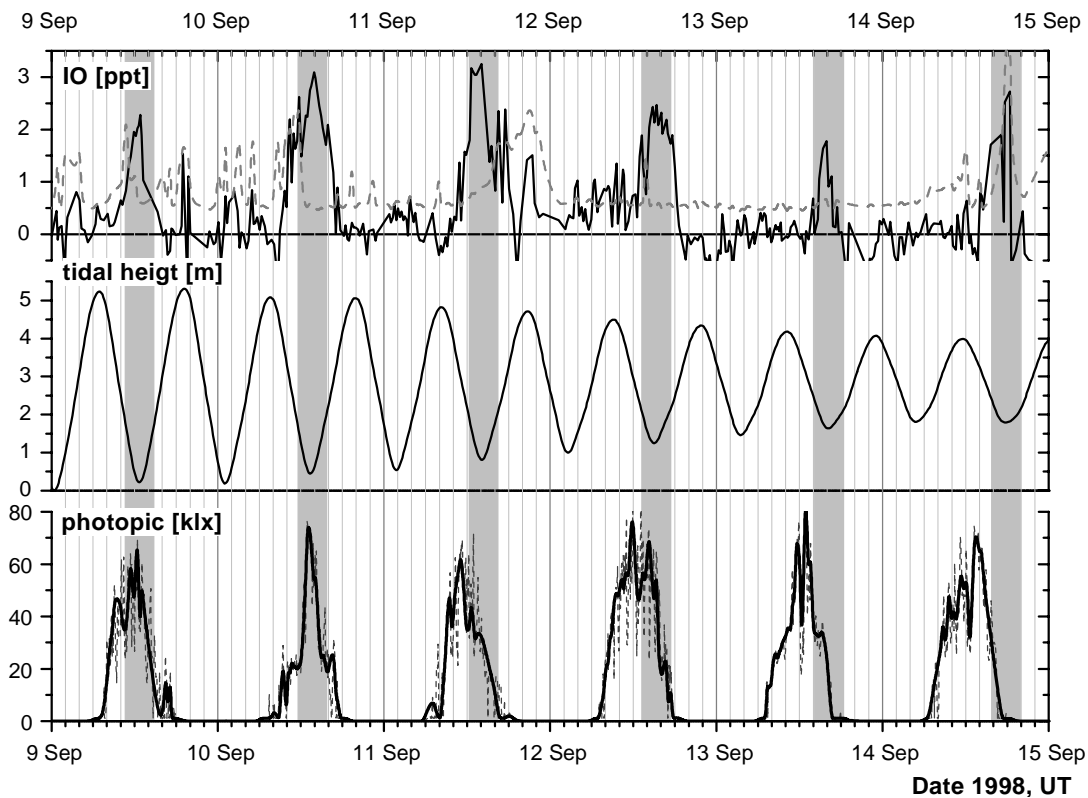


Figure 4.42 IO (dashed line marks the detection limit), tidal height (TH) and photopic flux (5-min time resolution as dotted line and averaged to IO time resolution as full line) time series of MH98. Shaded areas mark the intervals of the daily IO maximum which is clearly shifted in accordance with the low tide minimum.

To point out that there is a considerable dependence of the IO concentrations on TH, Figure 4.42 shows the 6-day time series of Sept 9 – 15 1998, where the point of the daily IO maximum value shifts simultaneously with the minimum in TH (about one hour from day to day). The corresponding times of the day of IO_{max}, TH_{min} and SR_{max} for Sept 9 to 14 are given in Table 4.10. It is obvious that TH, and not SR, as could be expected, is the parameter determining the time of the IO maximum. To stress that this behaviour is not only an event of one single week, but can be observed in general, Figure 4.43 shows three IO vs. TH scatter plots. Daytime values (d), all data (a) and night-time values (n) of the 4-week measuring period are represented, divided into 0.5 m segments of TH.

Table 4.10 Daily shift of IO_{max} with TH_{min} from Sept 9 to 14, 1998.

Date	Time of IO maximum	IO mixing ratio [ppt]	Time of low tide ¹	Time of maximal solar radiation ²
Sept 09	12.51	2.2	12.41	12.30
Sept 10	13.54	3.1	13.23	13.30
Sept 11	14.07	3.2	14.08	11.00
Sept 12	14.50	2.4	15.00	12.00 – 14.30
Sept 13	15.56	1.7	16.00	12.00 – 13.00
Sept 14	18.24	2.7	17.45	13.30

1 Calculated on the basis of the tidal height prediction model of the NUI Galway

2 Period is given if no sharp peak has occurred due to cloud coverage

It is evident that under daylight conditions (**d**) high IO values are associated with low tidal height. The correlation can be described perfectly by an exponential decrease with rising tide ($r^2 = 0.96$). Taking into consideration all data (**a**, incl. night-time values where no IO is formed due to missing photolysis), the negative correlation of IO and TH is still obvious but less distinct. The different behaviour becomes even more distinct in the case of the night-time data, where no dependence on TH can be found as no photolysis of HHC occurs.

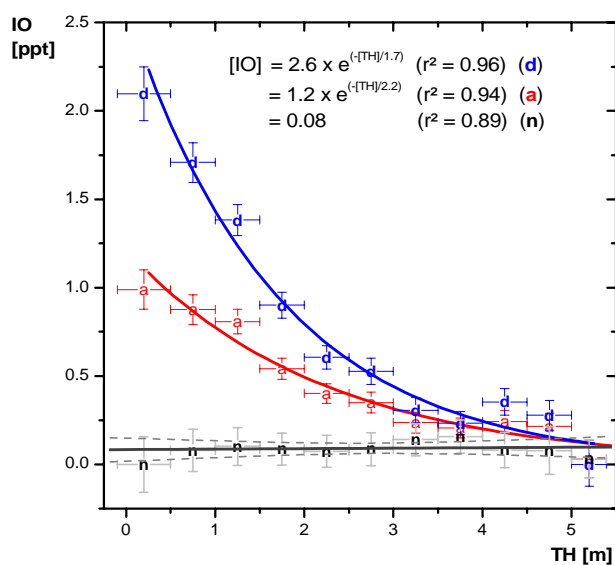


Figure 4.43 IO vs. tidal height (TH), whole data set classified in 0.5 m TH values. All data (**a**), daytime (**d**) (both with exp. decreasing fit) and night-time (**n**) data (linear fit with 95 % confidence bands). The vertical error bars represent the relative frequency of the data, the horizontal error bars the length of the respective interval.

A possible explanation of the non-linear trend could be a non-linear dependence of the HHC emissions on oxidative stress and, consequently, on TH, but this point needs to be further investigated and cannot be decided on the basis of our data. The relation between HHC and IO was not very distinct (see subsection b), Figure 4.40), however, it is expected to be linear if the HHC emission is the only source of IO. If there is another IO source, e.g. the activation of reactive Iodine (re-I) from other reservoirs such as (aerosol) surfaces as second-order processes, the dependence of IO on TH is not necessarily linear.

4.4.4 Iodine – Ozone Interactions at Mace Head, a Modelling Study

Halogens became species of public interest due to their devastating effect on stratospheric as well as tropospheric ozone. In the following subsection the interaction of iodine oxide and ozone will be discussed from a general point of view. A chemical box model is used to describe the observations made at Mace Head *Stutz et al.* [1999].

a) *Model description*

The photochemical box model includes the basic reactions describing boundary layer ozone and halogen chemistry. In the cases discussed here methane, at a mixing ratio of 1.75 ppm, was the only relevant organic species. CO was assumed to be at a level of 130 ppb. The rate constants for the reactions were taken from the review of *Atkinson et al.* [1997] and the photolysis frequencies were calculated with the radiation transport model STAR [*Ruggaber and Dlugi*, 1994]. The iodine reactions included in the model are listed in the Appendix. Tests of the model showed that it correctly describes the expected ozone production and destruction at different NO_x levels.

One of the most important questions we hope to answer with the model concerns the magnitude of ozone destruction and the importance of the different ozone destruction cycles in the marine boundary layer. These cycles have been described and discussed in chapter 2 as HOX and XO Cycle. In a quasi-steady-state mode different NO_x levels were applied to investigate these questions. The change in the ozone mixing ratio was compared in runs with and without iodine chemistry. Thus the importance of the individual chemical reaction cycles with respect to their ozone destruction potential could be characterised.

To achieve a quasi steady state no sources and loss processes for gas-phase species and no transport was included in the model. Since loss processes, e.g. deposition, would be of the same size independent of the addition of iodine chemistry, they do not play an important part in the analysis of the change of the chemical system upon this addition. The solar zenith angle, the temperature and the atmospheric pressure were held constant at 50°, 280 K and 1013 mbar respectively. Typical ozone mixing ratios were ~30 ppb. For a more detailed model description please cf. the publication of *Stutz et al.* [1999].

As discussed in chapter 2, the product channels of several reactions related to iodine chemistry or their respective rate constants are uncertain. For the IO self-reaction recent laboratory studies (e.g. [*Cox et al.*, 1999]) indicate three main reaction channels, while the fate of the reaction products OIO (38 %, R48) and I₂O₂ (50 %, R51) is unclear. In our model we assumed that both photolyse into products with no net O₃-destruction. With respect to the latest laboratory investigations, which show OIO to be photostable [*Cox et al.*, 1999, *Ingham et al.*, 2000], this model estimation is correct concerning the net O₃ destruction. Furthermore, since neither BrO nor ClO exceeded the detection limit during the Mace Head campaigns, no other halogen oxide was included in the model.

b) Model Results

The results of the quasi-steady-state model analysis of the IO mixing ratio (A) and the ozone formation (B) in dependence on the NO_x level are shown in Figure 4.44. For NO_x levels below ~ 1 ppb the reaction of IO with NO and NO_2 is relatively slow compared with the thermal decomposition and photolysis of IONO_2 and INO_2 , as discussed in section 2.3 above. Therefore the IO mixing ratios remain fairly constant. IONO_2 becomes an important reservoir of iodine only at $\text{NO}_x > 1$ ppb.

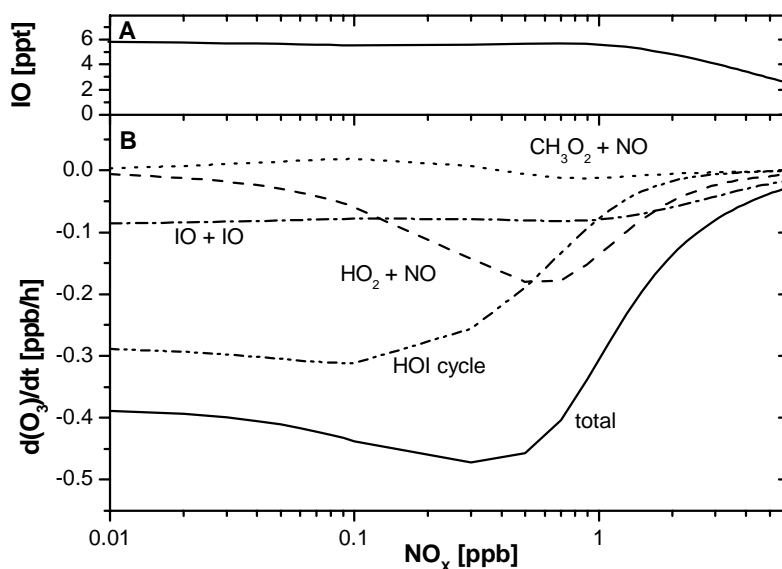


Figure 4.44 Calculated IO mixing ratio (A) and O_3 depletion in the marine boundary layer in dependence on NO_x calculated in a quasi-steady-state model (adapted from Stutz et al. [1999]).

The total ozone destruction rate at $\text{NO}_x < 0.02$ ppb (Figure 4.44) is about 0.4 ppb/h and increases slightly to a maximum of 0.47 ppb/h at 0.3 ppb of NO_x . This is surprising, since neither the IO nor the HOI cycle shows a maximum at this NO_x level. At higher NO_x levels more active iodine is converted into the IONO_2 and INO_2 reservoirs, thus causing a decrease in the ozone destruction rate.

c) Interpretation of the Model Results

The HOI cycle

There are two main ozone depletion processes that have to be considered in the interpretation of the model results. The first is the reaction sequence referred to as HOI cycle in Figure 4.44, which has already been described as cycle B in chapter 2. In summary: HOI is formed by the reaction of IO and HO_2 and afterwards photolysed. The educts X and OH react with O_3 , forming XO and HO_2 respectively. Two ozone molecules net are converted into three oxygen molecules. The HOI cycle is dominant at NO_x mixing ratios below 0.5 ppb. At 0.1 ppb NO_x 0.3 ppb/h ozone are still destroyed in this way. In addition to the reaction of IO with HO_2 also the reaction of IO with CH_3O_2 forms HOI.

Figure 4.45 shows the variation of both peroxy radicals considered in the model in dependence on the NO_x levels for the model runs with and without iodine chemistry.

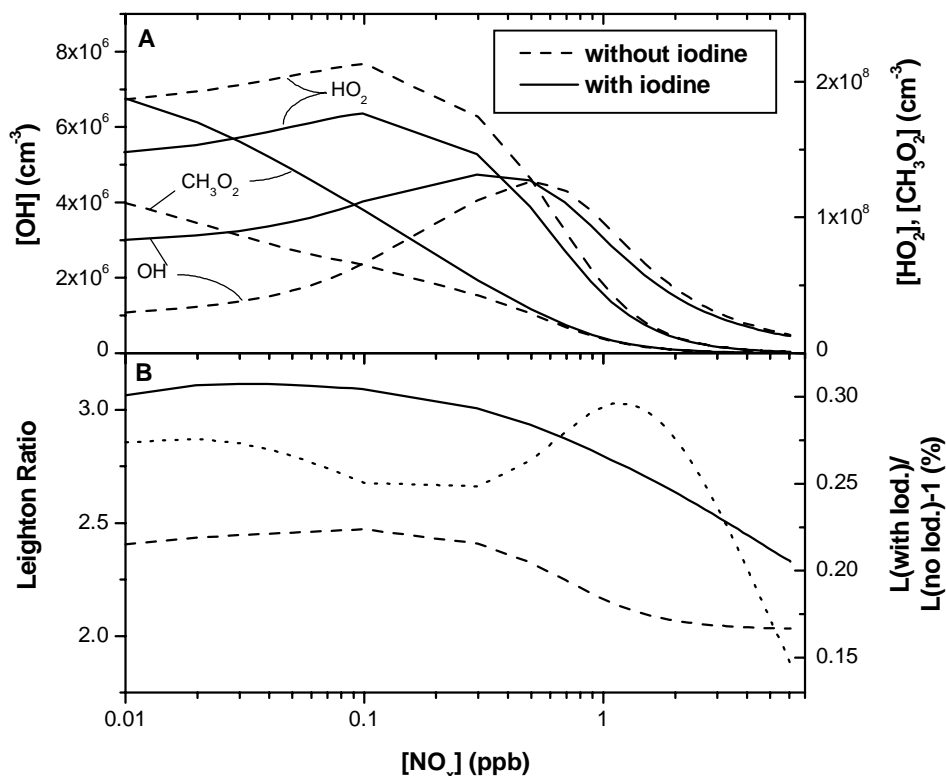


Figure 4.45 A: OH , HO_2 and CH_2O_2 in dependence on NO_x , B: Leighton Ratio L calculated according to Equ 30 with (solid line) and without (dashed line) IO. Relative behaviour of L on addition of iodine (dotted line) [Stutz et al., 1999].

As the concentrations of both peroxy radicals considered in the model are of the same order of magnitude, the path via CH_3O_2 destroys less than 0.01 ppb ozone per hour. The efficiency of the O_3 destruction mainly depends on the photolysis of HOI and the HO_2 and CH_3O_2 concentration, which vary between 0 and $\sim 2 \times 10^8 \text{ molec cm}^{-3}$ in the case with no IO, as can be seen from Figure 4.45. However, for increasing NO_x the concentration of HO_2 decreases and the O_3 destruction via the HOI cycle becomes less important.

The IO Self-Reaction

At levels of 6 ppt IO the IO cycle destroys ~ 0.08 ppb O_3 per hour, which is only $\sim 20\%$ of the total O_3 destruction at low NO_x levels. At higher NO_x levels its relative contribution increases. However, the yield of the IO self-reaction channel that leads to a net O_3 loss is only 12% (R49 and R50). Depending on the fate of OIO (see section 2.3.3.) and I_2O_2 , this mechanism might actually be more important. If all channels contributed to the destruction of ozone, this mechanism would be most important at low NO_x levels with a contribution of 0.56 ppb/h.

Indirect Influences, Reduction of the O₃ Production Channel

An indirect effect of halogens on the O₃ level is the reduction of the O₃ production. As will be described in the following section, where the influence of halogens on the Leighton Ratio will be discussed, the conversion rate of HO₂ to OH and of NO to NO₂ is disturbed by halogen oxide reactions with HO₂ and NO respectively. This reduces the production rate of O₃, which is comparable to a net reduction.

The photolysis of IONO₂ leads to I and NO₃ (see also section 2.3) followed by the photolysis of NO₃ to NO (which is about 10 % of the total NO₃ photolysis of $1.6 \times 10^{-2} \text{ s}^{-1}$), which leads to an additional destruction of O₃ via the reaction of NO with O₃. During the day the model estimated ~0.1 ppt of NO₃. As this reaction would destroy only 0.006 ppb of O₃/h, it is not included in Figure 4.44. Another mechanism destroying less than 0.01 ppb of O₃/h is the reaction channel of IO + CH₃O₂, converting IO to I. This reaction has been simplified in the model, assuming that the bi-radical CH₂O₂ formed in this reaction decomposes to HO₂ and HCHO. Thus CH₃O₂ is converted to HO₂, which indirectly influences the HOI cycle.

All these effects described, the direct destruction of O₃ by halogens as well as the indirect effect of the reduced ozone production, depend on the concentrations of NO_x and HO_x but also on the amount of CO and hydrocarbons available. Assuming 10 times less total iodine, the ozone destruction rates were proportionally reduced by a factor of 10 (see Table 4.11), while the general behaviour is similar. Sensitivity tests have shown that the modelled destruction of O₃ is proportional to the photolysis rates and therefore to the radiative flux in the atmosphere.

Table 4.11 Ozone loss rates from different processes in the boundary layer (BL) [Stutz, et al., 1999].

Process	d(O ₃)/dt [ppb/h]	Comment, Reference
OH production	0.11	calculated by the model
Deposition on the ocean	0.22	estimated for a BL height of 100 m and a deposition velocity of 0.02 cm s ⁻¹ [Warneck, 1988]
Deposition on land	0.43	estimated for a BL height of 500 m and a deposition velocity of 0.2 cm s ⁻¹ [Warneck, 1988]
<i>HOX- and IO-Cycle at:</i> 6.6 ppt IO at 0.1ppb NO _x	0.45	calculated by the model
0.7 ppt IO at 0.1ppb NO _x	0.05	calculated by the model

d) Temporal Ozone Variation at Mace Head in 1998

The temporal variation of the boundary layer ozone occurs on a time scale of minutes to hours. To analyse the changes of the 1-minute time resolution ozone data of the in-situ monitor, the derivation of the ozone mixing ratio with respect to time was calculated. Figure 4.46 shows the O₃ raw data, the smoothed data and the smoothed derivative of the ozone mixing ratio of the whole campaign. It illustrates that ozone formation as well as

ozone loss rates of more than 3 ppb/h have been observed. These large ozone variations may be caused by transport phenomena, which have not been included in the model yet. In general, the daily maximum value of the O_3 variation is by a factor of five to ten higher than the prediction of the model.

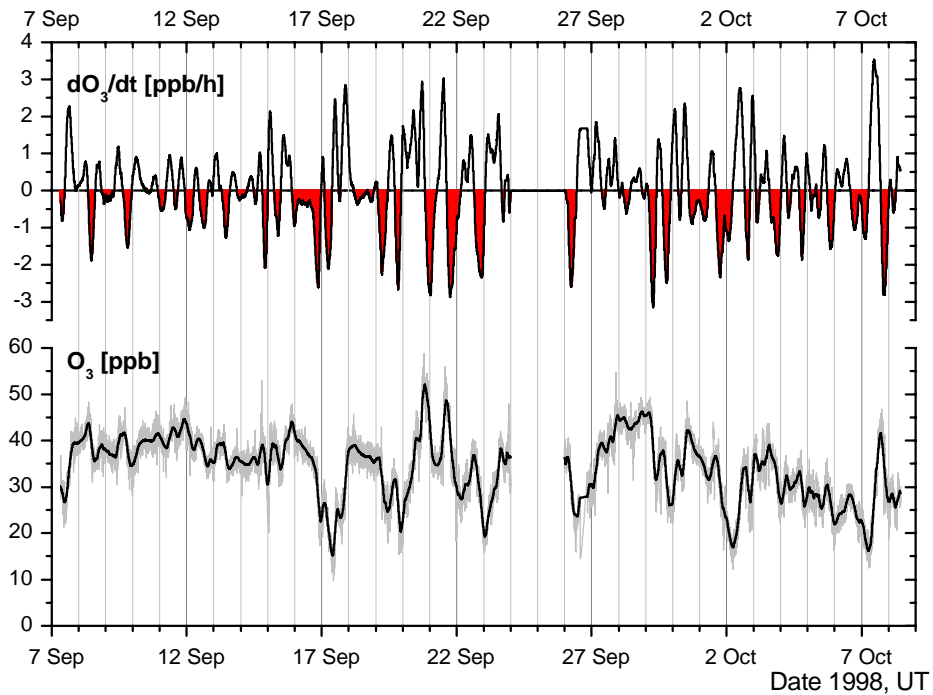
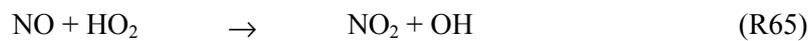


Figure 4.46 Temporal variation of boundary layer ozone observed at Mace Head in 1998. Lower panel: O_3 time series, raw (grey) and smoothed data. Upper panel: Derivative with respect to time of O_3 mixing ratio. Negative values indicate net O_3 destruction and are represented as plane surface below the abscissa.

e) The Leighton Ratio in the Model

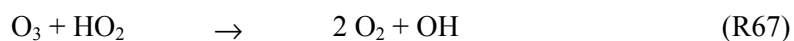
It is self-evident that the Leighton Ratio $L = NO_2/NO$ is a spin-off of the model calculations. L interchanges with the OH to HO_2 ratio via the reaction of NO with HO_2 , NO being oxidised with $k_{R65} = 8.3 \times 10^{-12} \text{ molec}^{-1} \text{ cm}^3 \text{ s}^{-1}$:



followed by the photolysis of NO_2 with $J_{NO_2} = 5 \times 10^{-3} \text{ s}^{-1}$.



At low NO_x levels OH is formed via the reaction of O_3 with HO_2



In the reaction sequence of the HOI cycle (section 2.1.1), which starts with $IO + HO_2$, followed by the rapid photolysis of the product HOI , HO_2 is converted to OH with no net loss of reactive iodine and no oxidation of NO . The decrease of HO_2 and the simultaneous increase of OH caused by 6 ppt of IO is shown in Figure 4.45

At low NO_x levels the model calculates an increase of the OH concentration by a factor of almost 3 with a simultaneous reduction of HO_2 by $\sim 20\%$. As a consequence the OH/ HO_2 ratio increases by a factor of 3.5. The Leighton Ratio is changed by the conversion of NO to NO_2 via the reaction of IO and NO, as no HO_2 is reduced to OH. Followed by the reaction of I-atoms with O_3 and the NO_2 photolysis, this cycle will not directly destroy ozone, but the photostationary state (PSS) between NO and NO_2 will be changed according to Equ 5 (section 2.1.4) or Equ 30 (4.4.5). The modelled variations of L with and without iodine are shown in Figure 4.45. L increases about 25 – 30 % below 2 ppb of NO_x . At a constant NO_x level this leads to a reduction of NO mixing ratios by 25 – 30 % in the presence of iodine.

4.4.5 Influence of Iodine Oxide on the Leighton Ratio

Before the 1998 Mace Head campaign was performed, IO events were expected only during clean-air periods with westerly flows. In 1998 increased IO was observed during conditions of relatively high NO_x for the first time. In this section the measured influence of IO on the *Leighton Ratio* L will be illustrated by two examples. The results will be compared with the model results of the previous section, and the misinterpretation of L, if only peroxy radicals and no halogen oxides are considered, will be given as an example at the end of this section.

Comparing the daily cycle of IO and NO_2 , one would expect both species to be slightly negatively correlated due to their characteristic daily variation: IO shows maximum values at noon, which are well correlated with the photopic flux as shown above. The NO_2 concentration is dominated by the PSS, which is described by the Leighton Ratio as discussed in chapter 2. Due to the maximum in the NO_2 photolysis (J_{NO_2}) around noon NO_2 is expected to decrease during the day, when O_3 generally increases. Figure 4.47 shows the expected anti-correlation of the 24-hour average values of NO_2 and O_3 .

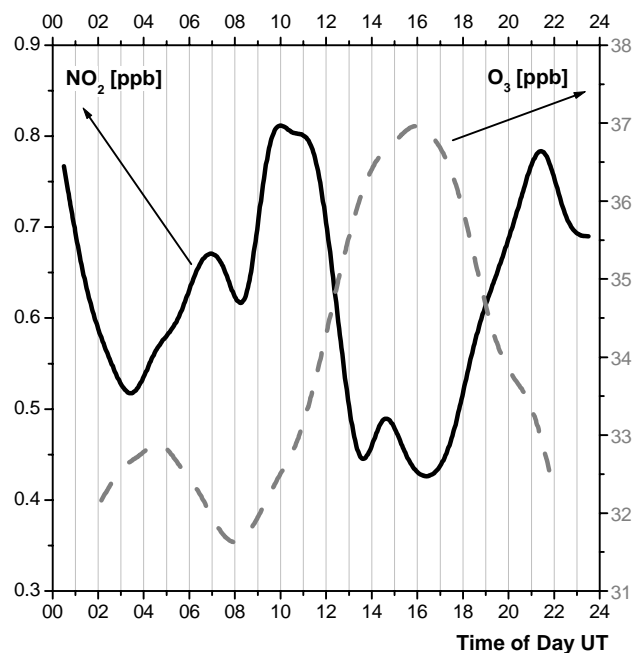


Figure 4.47 NO_2 (full line) and O_3 (dashed) given as hourly average values of all data recorded during MH98.

As already mentioned in chapter 2, besides O_3 and J_{NO_2} there are two important parameters influencing the Leighton Ratio: Peroxy radicals as well as halogen oxides cause an increase of the measured Leighton Ratio L_{measure} , as NO_2 is formed via the oxidation of NO by HO_2 or IO without consuming O_3 (R25-R27). According to Platt and Janssen [1995]

and in consideration of IO as the only halogen oxide species observed at Mace Head L can be calculated from measured parameters as

$$L_{Measured} = \frac{[NO_2]_{Measured}}{[NO]_{Measured}} = \frac{k_{NO+O_3} \cdot [O_3] + k_{NO+HO_2} \cdot [HO_2] + k_{NO+RO_2} \cdot [RO_2] + k_{NO+IO} \cdot [IO]}{J_{NO_2}} \quad \text{Equ 30}$$

It can be seen from the second line of Equ 30 that a number of parameters are necessary to calculate L, while the ‘classical standard’ calculation (first line) only requires the measurements of NO₂ and NO or can be calculated from the most important terms of Equ 30, which, in general, leads to the original calculation where NO₂ and NO are only determined by the photolysis of NO₂ and the reaction of NO with ozone (Equ 31). During MH98 IO was found under low NO_x conditions (NO and NO₂ remained below the detection limits of some 10 ppt) as well as under high NO_x conditions of more than 1 ppb. Due to a gap in the NO measurements only one day of elevated IO mixing ratios can be used to compare the measured Leighton Ratio with varying calculations according to Equ 31 - Equ 34:

$$L_{org} = \frac{k_{NO+O_3} \cdot [O_3]}{J_{NO_2}} \quad \text{Equ 31}$$

$$L_{RO_2} = \frac{k_{NO+O_3} \cdot [O_3] + k_{HO_2+NO} \cdot [HO_2 + RO_2]}{J_{NO_2}} \quad \text{Equ 32}$$

$$L_{IO} = \frac{k_{NO+O_3} \cdot [O_3] + k_{IO+NO} \cdot [IO]}{J_{NO_2}} \quad \text{Equ 33}$$

$$L_{RO_2,RHS} = \frac{k_{NO+O_3} \cdot [O_3] + k_{NO+HO_2} \cdot [HO_2 + RO_2] + (k_{NO+IO} + 0.1 \cdot k_{NO+BrO}) \cdot [IO]}{J_{NO_2}} \quad \text{Equ 34}$$

For this comparison a number of parameters which have not been determined during MH98 need to be approximated by other parameters. However, even if the absolute values of L are uncertain, it is possible to point out significant relative differences of the values calculated according to Equ 31 – Equ 34:

J_{NO_2} has not been measured directly during MH98. In view of the fact that IO has been observed at Mace Head under high and under low NO_x regimes (see e.g. Figure 4.49, Figure 4.51 and Figure 4.52) and that the influence of IO on L should be analysed, it is not meaningful to calculate J_{NO_2} from Equ 31. Because of varying meteorological conditions, such as cloud covering, the calculation of J_{NO_2} by a standard model may cause a number of uncertainties as well. Several radiation parameters have been determined during MH98. As

a first approximation, J_{NO_2} is assumed to be proportional to the actinic flux³⁰. Thus it can be calculated from a radiation parameter like the photopic flux:

$$J_{NO_2} = \alpha \cdot \text{photopic flux} \quad \text{Equ 35}$$

In the case of our measurements during MH98 the proportionality constant α can be calculated by rearranging Equ 30 with respect to the values of NO and NO₂ measured on Sept 19 between 11.00 and 13.00 when NO and NO₂ clearly exceeded the detection limit:

$$\begin{aligned} \alpha &= \frac{J_{NO_2}}{\text{photopic flux}} \\ &= \frac{[NO]_{\text{measure}} \cdot \{k_{NO+O_3} \cdot [O_3] + k_{NO+HO_2} \cdot [HO_2] + k_{NO+RO_2} \cdot [RO_2] + k_{NO+IO} \cdot [IO]\}}{[NO_2]_{\text{measure}} \cdot \text{photopic flux}} \end{aligned} \quad \text{Equ 36}$$

Peroxy radicals (HO₂ and RO₂) are the other parameters of importance which have not been measured during MH98. To close this gap I calculated the sum of [HO₂ + RO₂] following the results of *Carpenter et al.* [1997]. At Mace Head under spring conditions they found the concentrations of peroxy radicals (given in ppt) to be proportional to the first order of the ozone photolysis rate $J(O^1D)$:

$$([RO_2] + [HO_2]) = c \cdot J(O^1D) \quad \text{Equ 37}$$

Following the results of *Carpenter et al.* [1997] I calculated the proportionality constant to be $c \approx 4 \times 10^5 \text{ s ppt}$. During typical clean-air conditions at Mace Head most of the peroxy radicals are expected to be present in the form of HO₂. As the reaction of HO₂ with NO is faster than the reactions of other RO₂ with NO, an upper limit of the influence of peroxy radicals on L can be obtained.

Furthermore, regarding the general formulation of L according to *Platt and Janssen* [1995] given as Equ 5 in section 2.1.4, no BrO above the detection limit has been found during MH98. To obtain an upper limit of the absolute influence of halogens on L, BrO concentrations below the detection limit should not be neglected. Assuming that HHC are also the source of re-Br as well, a comparable variation in the bromine emission can be expected. Therefore, to retain the same variability and to keep the BrO level below the detection limit of ~ 1 ppt, the BrO concentration was estimated to be one tenth of the IO values. With this assumption it is possible to consider low levels of background BrO, even if the absolute influence is very small, as the rate coefficient is $k_{NO+BrO} \approx k_{NO+IO} \approx 2 \times 10^{-11} \text{ molec}^{-1} \text{ cm}^3 \text{ s}^{-1}$. Applying this to Equ 36, one gets

$$\begin{aligned} \alpha &= \frac{[NO] \cdot \{k_{NO+O_3} \cdot [O_3] + k_{NO+HO_2} \cdot [HO_2 + RO_2] + (k_{NO+IO} + 0.1 \cdot k_{NO+BrO}) \cdot [IO]\}}{[NO_2] \cdot \text{photopic flux}} \\ &\approx 1.8 \cdot 10^{-4} \text{ s} \cdot \text{klx}^{-1} \end{aligned} \quad \text{Equ 38}$$

³⁰ correlation plots of SR vs. PF and PF vs. UVA, indicating this linear relation, are given in the Appendix

Figure 4.48 shows the temporal variation of the trace gases related to the Leighton Ratio, the four different calculations of L and the value measured on Sept 19. Again it is important to note that J_{NO_2} , which was used to calculate the different values of L, has not been measured but was assumed to be proportional to the photopic flux, as described above. According to Equ 38 the proportionality constant was calculated to be $1.8 \times 10^{-4} \text{ s klx}^{-1}$, because with this value the 12.00 values of $L_{measure}$ and $L_{RO_2,XO}$ are equivalent. However, this assumption is of minor importance as only the relative changes of the different calculations of L will be compared in the following.

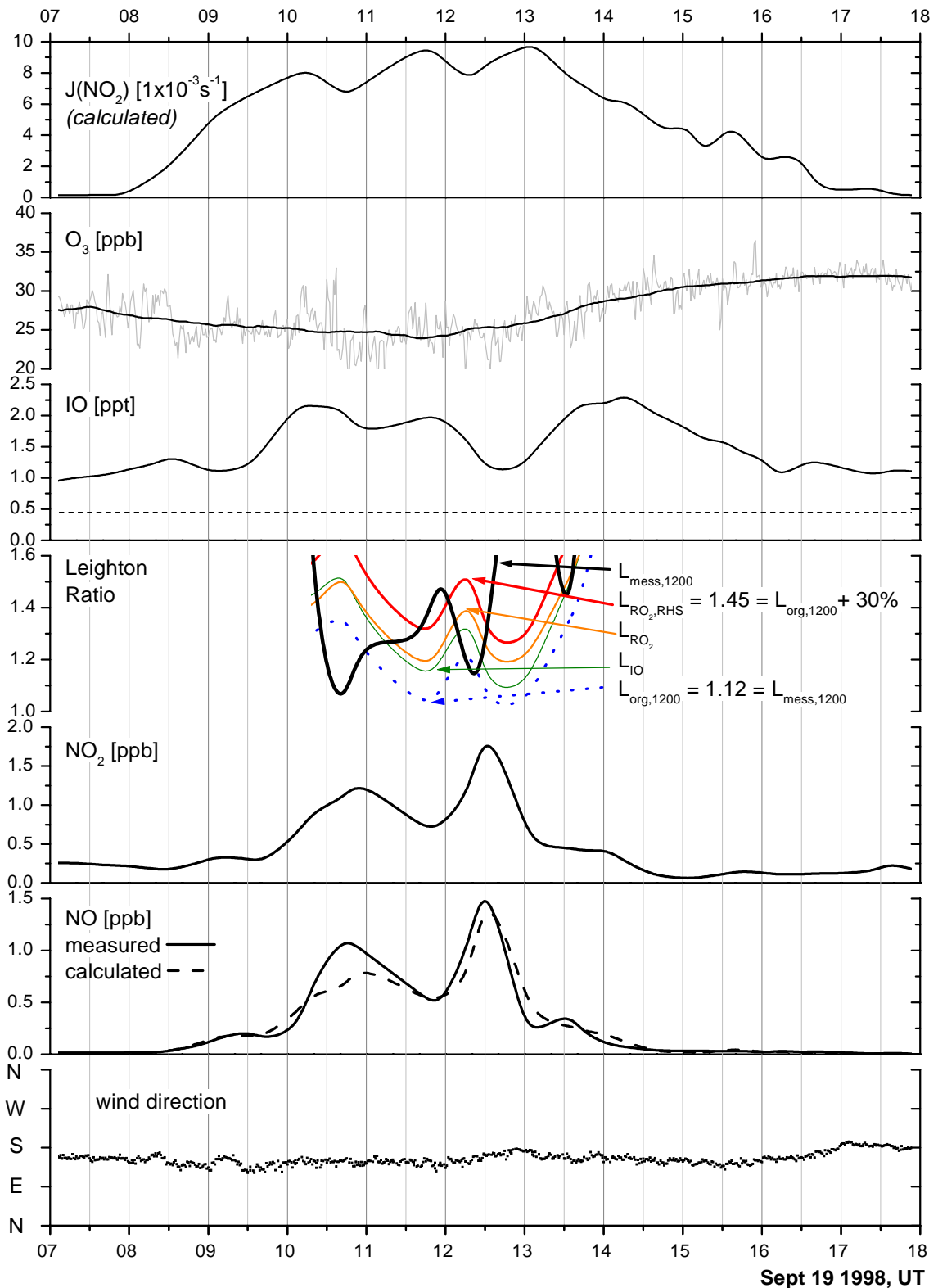


Figure 4.48 Leighton Ratios measured and calculated according to Equ 31 - Equ 34 on Sept 19. $J(\text{NO}_2)$ values were calculated from the photopic flux with respect to the value of L_{measured} of Sept 19, 12.00 (see text). Dotted line indicates the average IO detection limit of this period.

The upper panel of Figure 4.48 shows the calculated values of J_{NO_2} which undergo the expected daily cycle. O_3 varies between 35 and ~ 20 ppb with $\text{O}_{3\text{min}} = 22$ ppb around noon. IO remains relatively low but above the average detection limit of 0.45 ppt of Sept 19. The

two maximum values reached at 10.15 and 14.15 are slightly above 2 ppt of IO. The values of L calculated according to Equ 31 - Equ 34 vary between 1 and 1.3. At noon NO and NO₂ show simultaneous variations with maximum values of 1.3 and 1.7 ppb respectively. As NO has not been measured for the whole period of time, the NO mixing ratio has not only been measured but has also been calculated from Equ 34. Both values are in reasonable agreement. WD remains more or less constant from S/SE.

As can be seen from Figure 4.48, the change in L caused by IO is of the order of 5 to 10 % compared to the original (measured) value (thin line compared to dotted line). The absolute increase in L at 12.00 on Sept 19, taking into account not only halogen oxides but also peroxy radicals, is approximately 30 % ($L_{org} = 1.12$, $L_{RO_2,RHS} = 1.45$). This is in excellent agreement with the model calculations of the last subsection, where an increase of 25 – 30 % was predicted.

The influence of IO becomes all the more important, considering the much higher values observed on some other days of the campaign. The IO level of Sept 19 was only one fourth of the maximum we observed during the campaign. The calculations of L for Oct 7, when IO exceeded mixing ratios of 7 ppt, is represented in Figure 4.49. As no NO was measured on this day, a theoretical NO mixing ratio was calculated following Equ 34 and Equ 30.

During conditions of 7 ppt IO of Oct 7 plus the assumed BrO concentration of 0.7 ppt L changes by 45 % compared to the original calculation. On this day of considerably elevated IO, in contrast to Sept 19, the change in L caused by halogen oxides is larger than the one caused by peroxy radicals. The importance of both of these measurements is pointed out in the example given below.

In general the difference between $L_{Measured}$ (Equ 30, *first line*) and L_{org} (Equ 31) is interpreted in terms of peroxy radicals - without (Equ 39) or with (Equ 40) halogen oxides - by transforming Equ 32:

$$[HO_2 + RO_2] = \frac{L_{Measured} \cdot J_{NO_2} - k_{NO+O_3} \cdot [O_3]}{k_{NO+HO_2}} \quad \text{Equ 39}$$

$$[HO_2 + RO_2] = \frac{L_{Measured} \cdot J_{NO_2} - k_{NO+O_3} \cdot [O_3] - k_{NO+XO} \cdot [XO]}{k_{NO+HO_2}} \quad \text{Equ 40}$$

According to the assumptions made above for the case of Oct 7, 1998 at Mace Head this leads to a difference in the concentration of the peroxy radicals of

$$\Delta[HO_2 + RO_2] = \frac{(k_{NO+IO} + 0.1 \cdot k_{NO+BrO}) \cdot [IO]}{k_{NO+HO_2}} \quad \text{Equ 41}$$

With $k_{NO+IO} = 2.1 \times 10^{-11} \text{ molec}^{-1} \text{ cm}^3 \text{ s}^{-1}$, $k_{NO+BrO} = 2.2 \times 10^{-11} \text{ molec}^{-1} \text{ cm}^3 \text{ s}^{-1}$, $k_{NO+O_3} = 1.55 \times 10^{-14} \text{ molec}^{-1} \text{ cm}^3 \text{ s}^{-1}$ and 7.2 ppt of IO the concentration of peroxy radicals is overestimated by a factor of four (20 ppt).

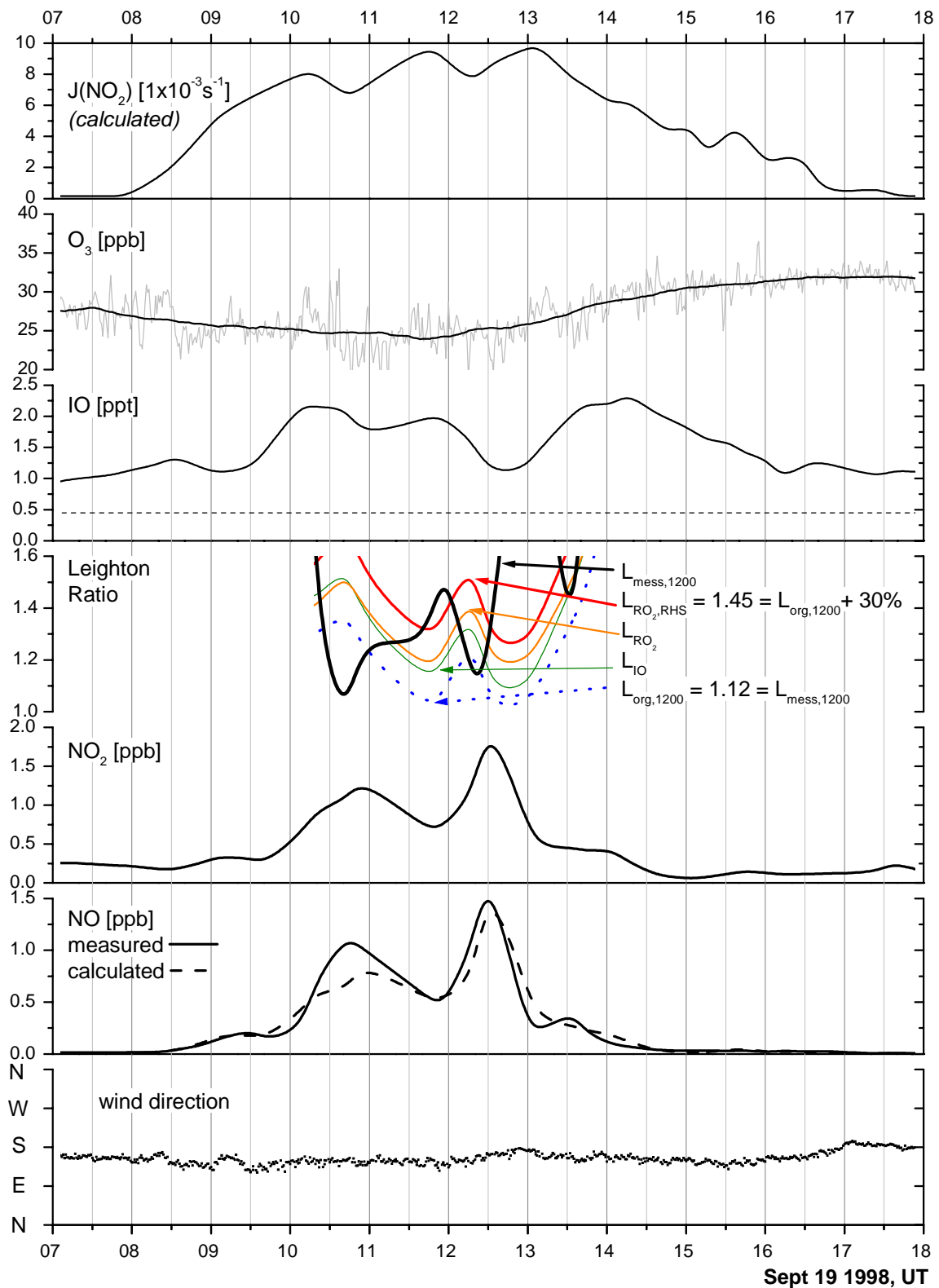


Figure 4.49 Measured and calculated Leighton Ratio on Oct 7, calculated according to Equ 31 – Equ 34. $J(\text{NO}_2)$ values were calculated from the photopic flux with respect to the value of L_{measured} of Sept 19, 12.00 (see text). Dotted line indicates the average IO detection limit of this period of 0.54 ppt.

4.4.6 IO - NO₂ Interactions

In general, IO-enriched air masses are associated with clean-air, NO₂-enriched air masses with polluted conditions. Thus simultaneous measurements of high IO and NO_x mixing ratios are unlikely, especially concerning their distribution with respect to the wind direction. Nevertheless, negative correlations in their temporal changes could be caused by transport phenomena or by chemical processes.

The upper panel of Figure 4.51 shows the time series of Oct 7 and the average diurnal cycle of both species, given as 1-hour average values of the complete 4-week data set (without normalising the daily cycles before the averaging), in the upper panel. While the exemplary day shows a significant negative correlation of both species, the average diurnal cycle of the whole 4-week campaign does not show this behaviour. To point out that the observation of Oct 7 does not represent a single event, Figure 4.52 gives two more examples of this negative correlation. During this period of increased NO₂ mixing ratios (Sept 19 and 20) the negative correlation of both species on a time scale of hours is clearly visible. This comparison emphasises the importance of the respective time scale: As will be shown in the following, there is a negative correlation on the scale of hours but not on the scale of the 4-week average values. The second and the third panel of Figure 4.51 represent the whole 4-week data set as well. The correlation plots of IO vs. NO₂ average values per 0.25 NO₂ interval (middle left) show a slightly negative correlation for the average values below 1.75 ppb NO₂. The higher average values above 2 ppb NO₂ represent only a small amount of data points, indicated by the larger vertical error bars. However, this part of the diagram shows a positive correlation of IO and NO₂. The scatter plot of the raw data shows almost all values in the lower left part of the diagram. Apart from some data points with large uncertainties with respect to their IO value, a negative correlation is more or less confirmed. The third panel of Figure 4.51 compares the average distribution of IO and NO₂ with respect to the wind direction. On average, high NO₂ values were only detected in the NE to SE sector, which is consistent with the geographical location of the site (Figure 4.50). Except for ships passing by, there is no NO₂ source in westerly directions.

The closest NO₂ source of importance is the city of Galway, located at the end of Galway Bay at a distance of ~80 km. Assuming a typical WS of 5 ms⁻¹ from this direction (Figure 4.32), the travel time of an air mass is of the order of some hours. As pointed out in section 4.4.3 a) above, the main sources of IO are located in the same direction, so that right beyond

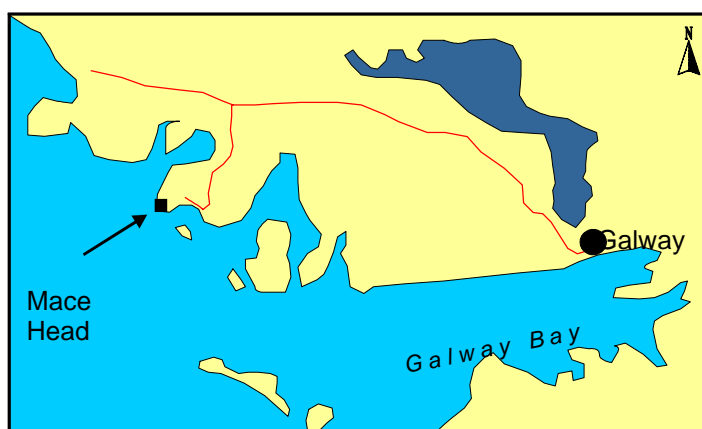


Figure 4.50 Schematic map of Mace Head including Galway Bay, showing the distance from the site to the next source of industrial pollution.

Galway city NO_2 -enriched air masses are influenced by continuous emissions of HHC from the algae of Galway Bay, while the NO_2 source is almost³¹ non-existent. Thus during south-south-easterly conditions a number of IO events have been observed during high NO_x regimes. An example of two days, also showing a clear negative correlation of IO and NO_2 , is given in Figure 4.52.

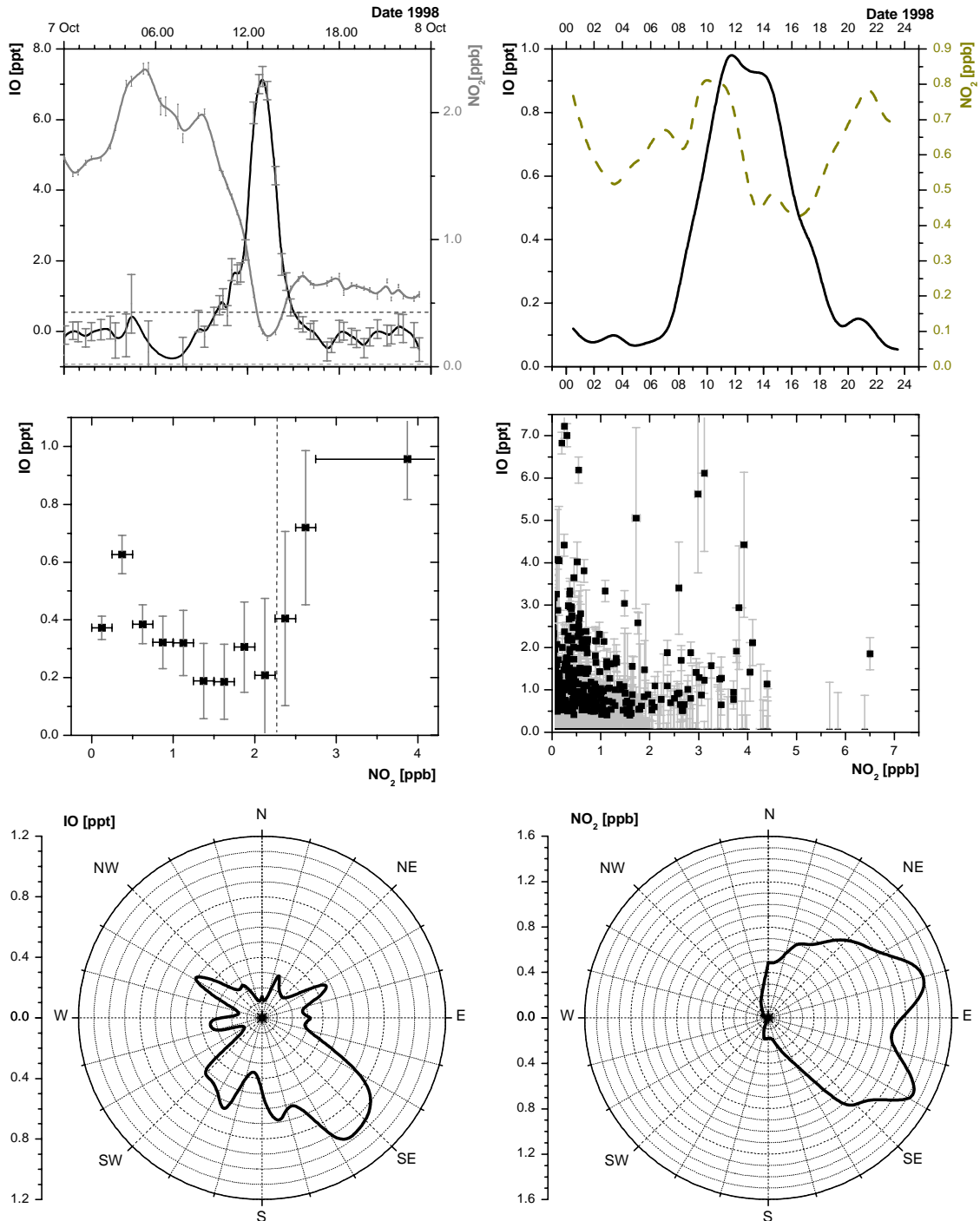


Figure 4.51 Temporal and spatial variation of IO and NO_2 . Top: Time series (left) and daily average cycle of the 4-week data set (right). Middle: IO vs. NO_2 scatter plots of the 4-week data set. Left: IO averages per 0.25 ppb NO_2 interval. Right: raw data without classification. Bottom: Distribution of IO (see also Figure 4.39) and NO_2 with respect to the wind direction.

³¹ There are some emissions of cars and smaller villages along Galway Bay.

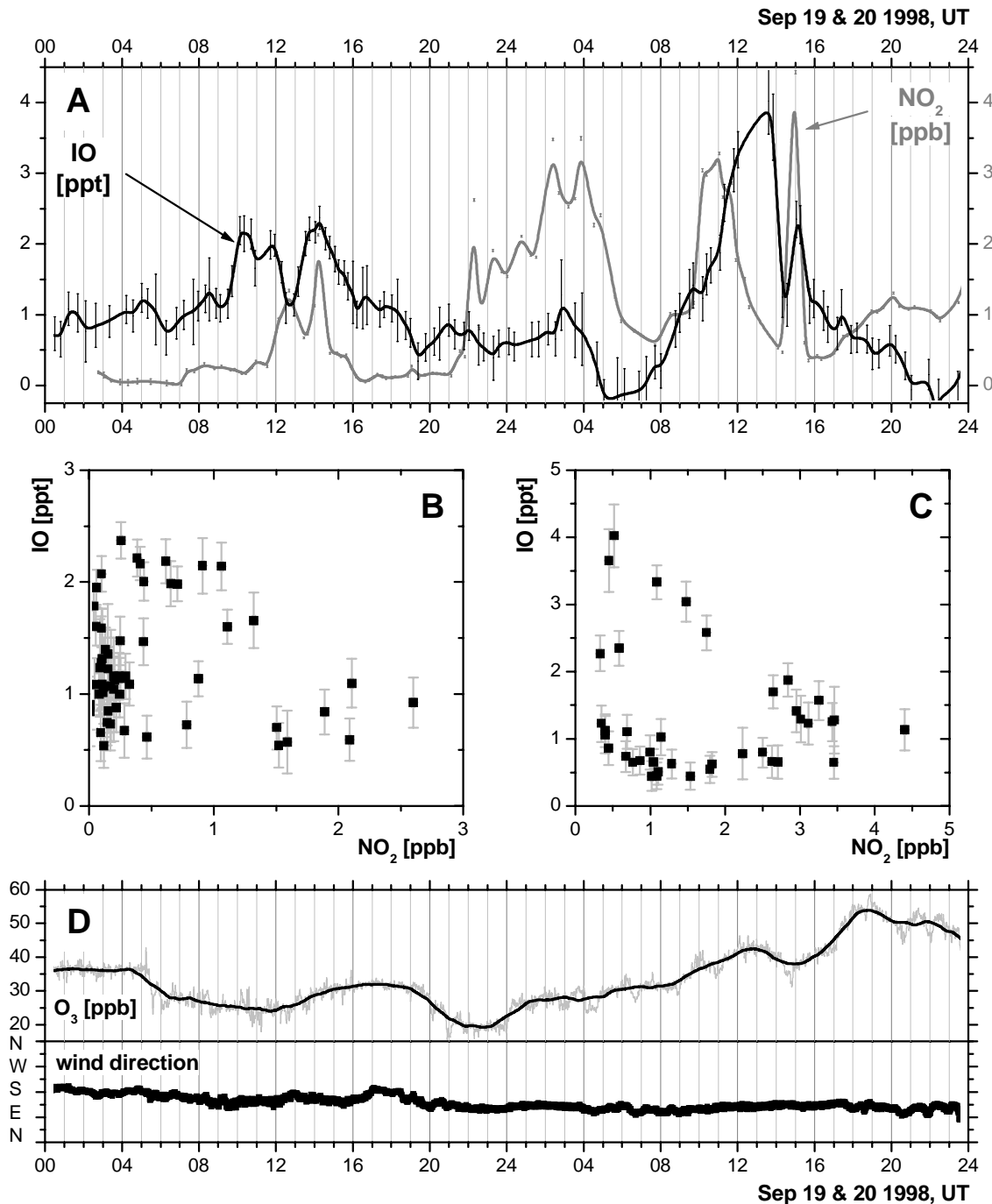


Figure 4.52 IO vs. NO₂. A: time series of anti-correlated IO and NO₂. B/C: corresponding scatter plots (B: Sept 19, C: Sept 20). D: time series of O₃ and wind direction.

The IO, NO₂, O₃ and WD time series and one scatter plot per day are represented. The scatter plots show only IO and NO₂ values above the detection limit of the corresponding period, indicating the negative correlation of IO and NO₂. It is self-evident that low concentrations of both species are observed simultaneously as well. This leads to the characteristic shape of these two graphs, showing all data within the lower left part of the diagram. On Oct 7 (already represented in Figure 4.52) the negative correlation was very distinctive as well. One of the highest IO mixing ratios of more than 7 ppt was observed on this day. Simultaneously with the increasing IO mixing ratio NO₂ decreased from more than 2 ppb to below 0.5 ppb.

On the basis of this observation of simultaneous IO and NO₂ the actual amount of IONO₂ can be calculated from the measured concentrations, assuming steady-state conditions. The thermal decay which regenerates IO and NO₂ was estimated by Jenkin [1992] to be $\Delta_{\text{IONO}_2} = 0.03 \text{ s}^{-1}$ and is still very uncertain. The photochemical degradation with $J_{\text{IONO}_2} = 0.003 \text{ s}^{-1}$ (calculated by 50 nm redshift of J_{BrONO_2} , see e.g. [Atkinson *et al.*, 1997]) and the uptake on aerosol surfaces are assumed to be the other sink of IONO₂. Figure 4.53 shows a schema summarising the processes involving IO and NO₂.

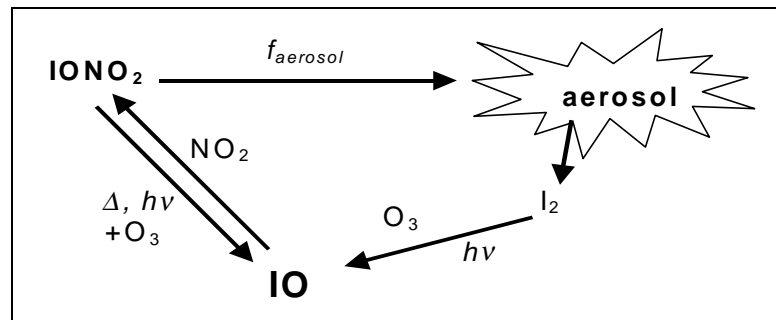


Figure 4.53 Diagram of simplified IO - NO₂ interactions.

According to Fuchs *et al.* [1971] the lifetime on aerosol surfaces can be calculated as

$$\tau_{\text{aerosol}} = \frac{1}{N} \left(\frac{1}{4\pi D} + \frac{3}{4\pi v r^2} + \frac{1-\gamma}{\gamma \pi v r^2} \right). \quad \text{Equ 42}$$

Here N denotes the number of particles per volume, r the particle radius, D the molecular diffusion (typically $10^{-5} \text{ m}^2 \text{ s}^{-1}$), v the velocity ($\approx 250 \text{ m s}^{-1}$) and γ the uptake or accommodation coefficient. The three terms of Equ 42 describe

- the diffusion of the aerosol particle in the boundary layer
- the collision and
- the accommodation or phase transition.

If the observed molecule undergoes a chemical reaction on the aerosol, γ denotes the uptake coefficient. Following the assumptions of Sander *et al.* [1999] and Vogt *et al.* [1999] or Cox *et al.* [1999] the uptake coefficient of IONO₂ is somewhere between 0.1 and 0.01. For this case of $\gamma \leq 0.1$ and particle radii below 1 μm , as is typical for marine background conditions, the first two terms of Equ 42 can be neglected. This leads to a simple relation between loss rate f and aerosol surface per volume given as $A = N4\pi r^2$:

$$f_{\text{aerosol}} = \tau_{\text{aerosol}}^{-1} = \frac{\gamma \cdot A \cdot v}{4} \quad \text{Equ 43}$$

Assuming $\gamma = 0.1$ as an upper limit of the aerosol uptake, $A = 7 \times 10^{-7} \text{ cm}^2 \text{ cm}^{-3}$ as a typical marine value and $v = 250 \text{ m s}^{-1} = 2.5 \times 10^4 \text{ cm s}^{-1}$, one obtains $f_{\text{aerosol}} = 4.4 \times 10^{-4} \text{ s}^{-1}$. Therefore the total IONO₂ degradation frequency is dominated by thermal decay. It is given as

$$\begin{aligned}
 f_{\text{IONO}_2} &= \Delta_{\text{IONO}_2} + J_{\text{IONO}_2} + f_{\text{aerosol}} \\
 &= 3 \times 10^{-2} \text{ s}^{-1} + 3 \times 10^{-3} \text{ s}^{-1} + 4.4 \times 10^{-4} \text{ s}^{-1} \\
 &\approx 3 \times 10^{-2} \text{ s}^{-1} = \Delta_{\text{IONO}_2}
 \end{aligned}
 \tag{Equ 44}$$

It is important to note that a better approximation of the thermal decay of IONO₂ is still not available. However, the approximation of Equ 44 is correct if the relatively uncertain value of Δ_{IONO_2} is correct.

Under steady-state conditions the production and decomposition of IONO₂ is in equilibrium. Thus the IO/IONO₂ partitioning, an indicator of the importance of IONO₂ as a reservoir of reactive iodine, can be calculated by transforming the production – decomposition equation. In this approach the reaction of IO with NO₂ is the only product channel:

$$k_{\text{IO+NO}_2} \cdot [\text{IO}] \cdot [\text{NO}_2] = f_{\text{IONO}_2} \cdot [\text{IONO}_2] \tag{Equ 45}$$

$$\Leftrightarrow \frac{[\text{IO}]}{[\text{IONO}_2]} = \frac{f_{\text{IONO}_2}}{k_{\text{IO+NO}_2} [\text{NO}_2]} \approx \frac{\Delta_{\text{IONO}_2}}{k_{\text{IO+NO}_2} [\text{NO}_2]} \tag{Equ 46}$$

Using the values given above and assuming a minimal NO₂ mixing ratio of 20 ppt (half of the average detection limit), a lower limit of IONO₂ can be calculated:

Low NO_X:

$$\begin{aligned}
 \frac{[\text{IO}]}{[\text{IONO}_2]} &= \frac{3 \times 10^{-2} \text{ s}^{-1}}{3.65 \times 10^{-12} \text{ cm}^3 \text{ molec}^{-1} \text{ s}^{-1} \cdot 5 \times 10^8 \text{ molec cm}^{-3}} \\
 &\approx 16
 \end{aligned}
 \tag{Equ 47}$$

As an upper limit NO₂ is set to be of the order of the highest values observed at Mace Head (around 4 ppb) with still some measurable amounts of IO:

High NO_X:

$$\begin{aligned}
 \frac{[\text{IO}]}{[\text{IONO}_2]} &= \frac{3 \times 10^{-2} \text{ s}^{-1}}{3.65 \times 10^{-12} \text{ cm}^3 \text{ molec}^{-1} \text{ s}^{-1} \cdot 1 \times 10^{11} \text{ molec cm}^{-3}} \\
 &\approx \frac{1}{12}
 \end{aligned}
 \tag{Equ 48}$$

Assuming ~ 3 ppt of IO during conditions of 4 ppb NO₂, as observed on Sept 20, one can calculate an IONO₂ mixing ratio of 36 ppt.

The thermal decay, as well as the photolysis of IONO₂, releases the iodine back to the gas-phase immediately. The thermal decay leads directly to IO and NO₂ within seconds or minutes, the photolysis leads to I and NO₃. The I atom reacts with O₃ and regenerates IO, while NO₃ is in equilibrium with NO, NO₂ and N₂O₅. It reacts with NO forming NO₂ within seconds (see e.g. [Geyer, 2000]). The uptake of IONO₂ on aerosols, even if it was calculated to be about 2 orders of magnitude slower than the (still uncertain) thermal

decay, leads to the removal of iodine from the gas-phase, as the aerosol uptake is followed by the reaction with surface water. This leads to the enrichment of iodine on marine aerosols and its flux from the sea back to the land.

4.4.7 The Formation of OIO

In the first place it is important to note that all OIO mixing ratios presented in this thesis were calculated on the basis of the OIO absorption cross section determined by *Cox et al.* [1999] to be $(1.09 \pm 0.21) \times 10^{-17} \text{ cm}^2 \text{ molec}^{-1}$ at 548.6 nm for a spectral resolution of 1.13 nm FWHM. The value determined by *Ingham et al.* [2000] in a later publication is higher by approximately a factor of three. This fits an earlier publication of *Spietz et al.* [1998], who found values in the range of $(2 - 5) \times 10^{-17} \text{ cm}^2 \text{ molec}^{-1}$ for this OIO band. However, it has to be kept in mind that the OIO mixing ratios presented here eventually need to be scaled down by a factor of 2 - 5. On the other hand, the detection limit has to be scaled down as well in this case. That is why there is no uncertainty concerning the presence of OIO in the marine boundary layer but an uncertainty in the absolute mixing ratios presented here.

In addition to the reaction of IO with NO_2 , the IO self-reaction was pronounced to be the dominant sink of IO in remote regions. The model calculations presented above emphasise the importance of the IO self-reaction for the O_3 destruction. As already described in chapter 2.3.3, the reaction leads to three major product channels, whereby especially the fate of OIO is uncertain. It had not been detected in the atmosphere before the measurements of this thesis were carried out at Mace Head in 1998. Furthermore, the reaction $\text{BrO} + \text{IO}$ leads to OIO as well with a branching ratio which is by a factor of 2, or even more, larger than the one of the IO self-reaction [*Bedjanian et al.*, 1998; *Cox et al.*, 1999] (see also chapter 2.3.3). This is of importance with regards to the partitioning of gas-phase halogen species in general. Even if no BrO has been determined above our detection limit, it has to be considered that there may be some tropospheric background BrO of some tenth of a ppt. However, due to the fact that we did not find any BrO above the detection limit at Mace Head, mainly iodine species will be discussed in the following section.

After the presentation of OIO time series under varying NO_x conditions, an estimation of OIO loss and production rates will be presented for the different regimes.

a) OIO under low NO_x conditions

As described in section 2.3, the visible absorption spectrum of OIO covers 480 – 660 nm, while the dissociation threshold forming IO and $\text{O}(^3\text{P})$ was determined to be 418 nm. Therefore the rapid atmospheric photolysis of OIO is very unlikely. These theoretical and modelled results already described in chapter 2 are supported by our measurements. Figure 4.54 shows the relevant parameters regarding the OIO production and loss processes of Sept 12 and 13, 1998. The diagram gives TH, SR and CH_2I_2 as iodine-source-determining parameters, the iodine oxides IO and OIO, NO and NO_2 as indicators of pollution and reaction partners, and the meteorological parameters WD and WS.

On Sept 12 NO_x concentrations remained very low: only during the afternoon NO_2 exceeded the average detection limit of 35 ppt and NO scattered around the baseline during the whole day. At 16.00 the OIO mixing ratio rose to 5.5 ppt, correlated with IO that peaked exactly at the lowest tide when it rose to 2.5 ppt. This observation indicates that the IO self-reaction is the dominant loss process under low NO_x conditions. OIO decreased over the day parallel to the IO decrease and rose again to 3 – 4 ppt after sunset.

On Sept 13 the IO-peak was much weaker than on the previous day. This might be due to the lower solar radiation that showed a slower increase during the morning hours. As expected, the IO maximum (1.8 ppt) was associated with the minimum tidal height. Over almost the whole period the NO_2 values were significantly higher than on the previous day and showed the expected daily variation of low noon concentrations due to increased photolysis. At 12.00 NO_2 peaked in correlation with a drop in SR, most likely due to cloud-cover formation. NO showed only a small variation between 15 and 50 ppt, which is higher than it was on the previous day, but still below the detection limit of ~40 ppt. The variations become more obvious through the thick line representing NO mean values of IO time resolution.

OIO was observed under daylight conditions on the first of these two days when NO and even NO_2 remained below the detection limit under daylight conditions. Besides the reaction with NO and the deposition on (aerosol) surfaces no other processes are known to remove OIO from the atmosphere. However, a possible explanation of the OIO observation under daylight conditions may be that NO was too low on Sept 12, therefore OIO could survive over the day.

On Sept 13 the average NO_x concentration was slightly higher compared to the previous day. Some of the NO raw data exceeded the detection limit of the monitor. The IO event of Sept 13 was very small and OIO did not exceed the detection limit under daylight conditions. Nevertheless, despite the relatively low IO maximum of only 1.8 ppt, after sunset IO decreased, while OIO rose simultaneously, possibly due to missing loss reactions with NO or OH.

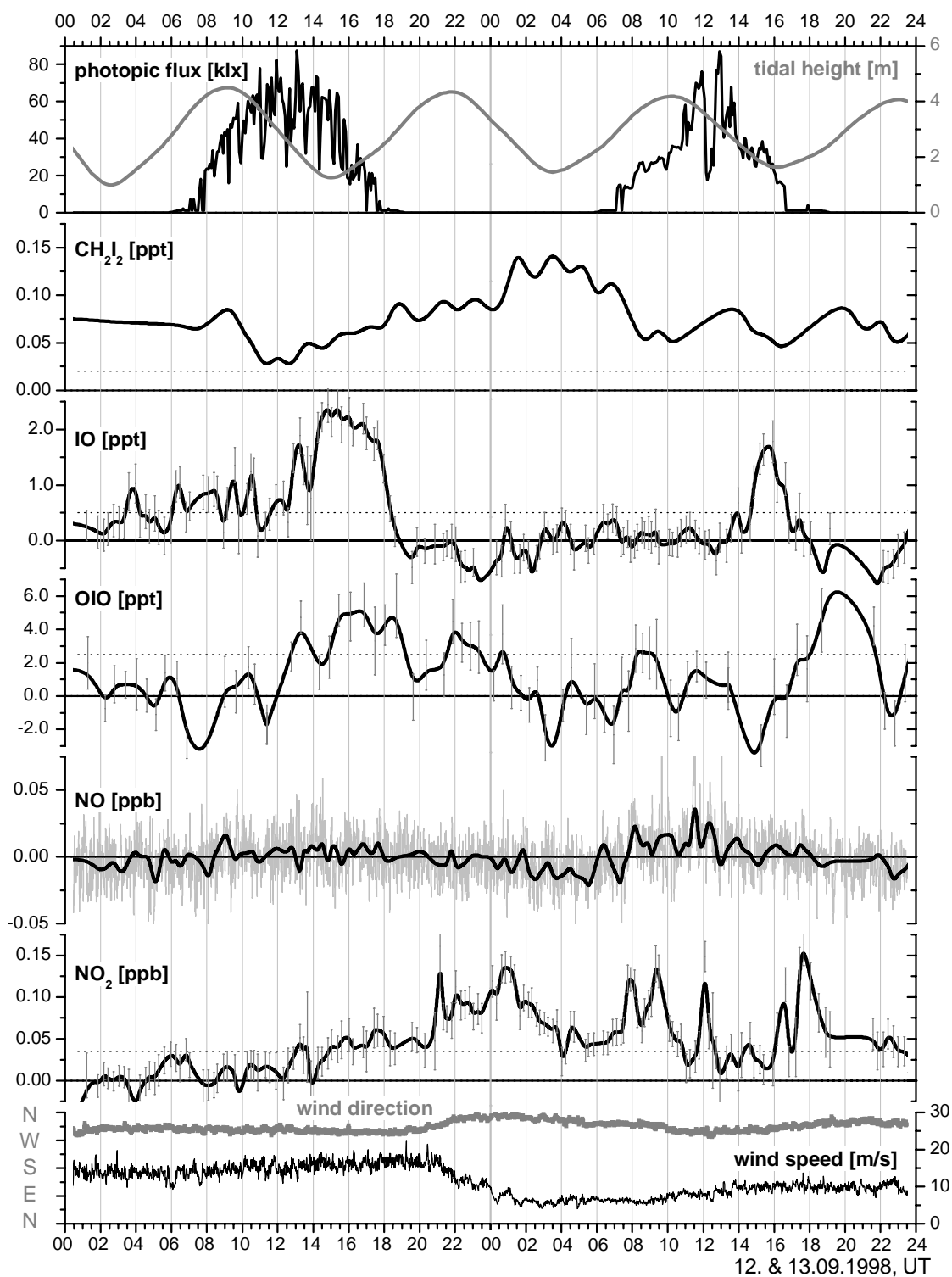


Figure 4.54 Two days of periodic IO events under low NO_x conditions. Dotted lines indicate the respective detection limits.

This observation of increasing OIO after sunset compares well with the measurements of *Allan et al.* [2000] who found OIO to be elevated after sunset. On three days during their measurements at Cape Grim they detected OIO at levels of approximately 2 ppt. This is comparable to our concentrations in consideration of the other absorption cross section applied by this group.

b) *OIO under high NO_x conditions*

Similar, but more distinct observations have been made for NO_x concentrations that were by more than one order of magnitude higher. Figure 4.55 shows the same parameter as Figure 4.54 (NO was calculated according to Equ 34) of Sept 20 and 21. Please note that all trace gas diagrams were scaled up by at least 70 % relative to the clean-air days of Figure 4.54.

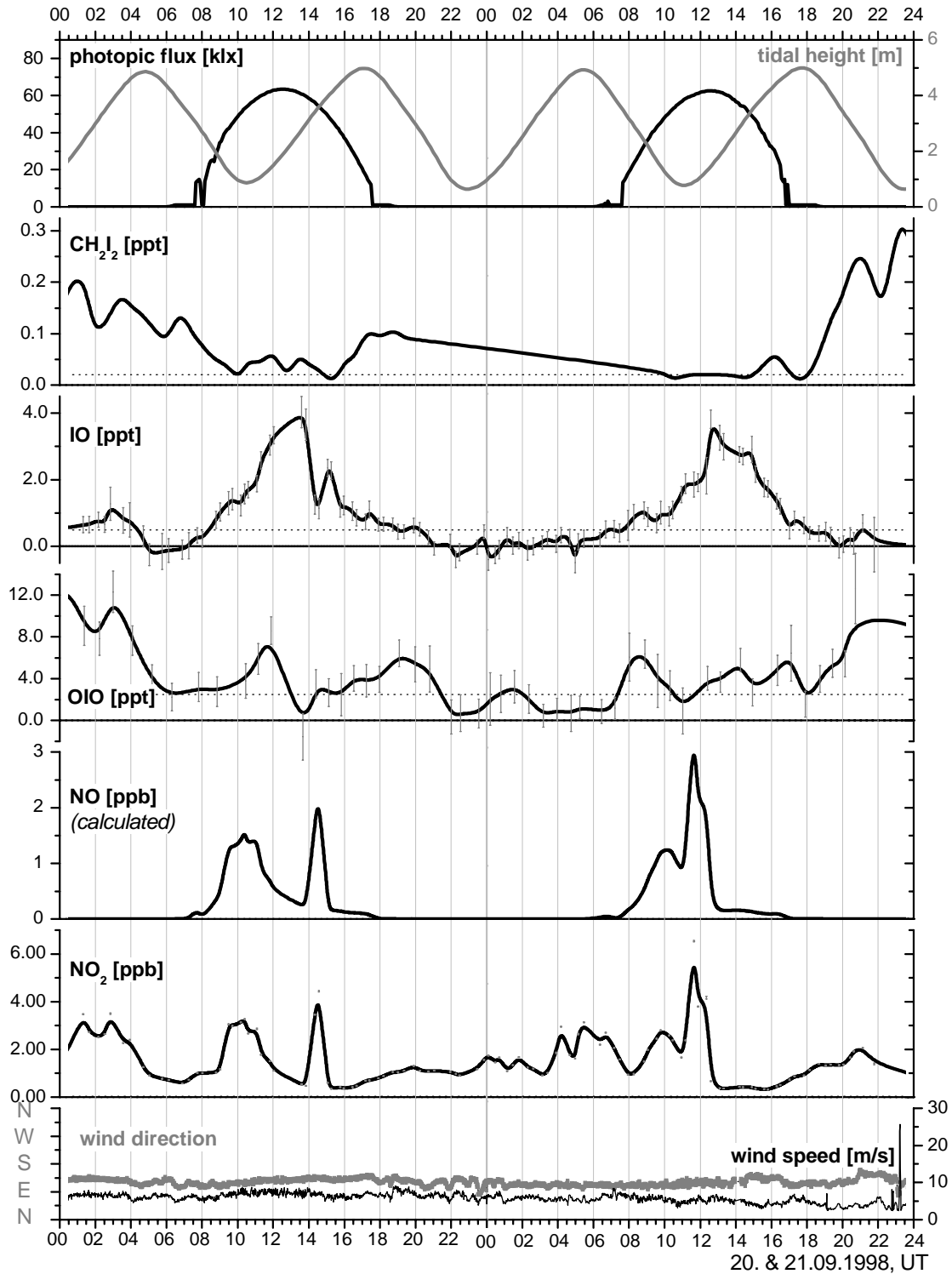


Figure 4.55 Two days of periodic IO events under high NO_x conditions. Dotted lines indicate the respective detection limits.

In the course of Sept 20 and 21 the wind direction remained constant at SE, the primary region of reactive iodine precursors. On these two days with the highest NO_2 amounts of the campaign (up to 6 ppb) IO of up to 4 ppt has been observed. Under these high NO_x levels very high values of OIO have been detected as well.

Figure 4.56 represents the OIO measurements of Oct 4 – 7. The IO and NO_x levels of these days were slightly lower than those of Sept 20 and 21 (Figure 4.55). On these days the OIO concentration remained below the detection limit almost all the time, although IO rose to more than 7 ppt, one of the highest values of the campaign. No OIO event occurred, neither under daylight conditions nor after sunset, as one might have expected in view of the measurements presented above.

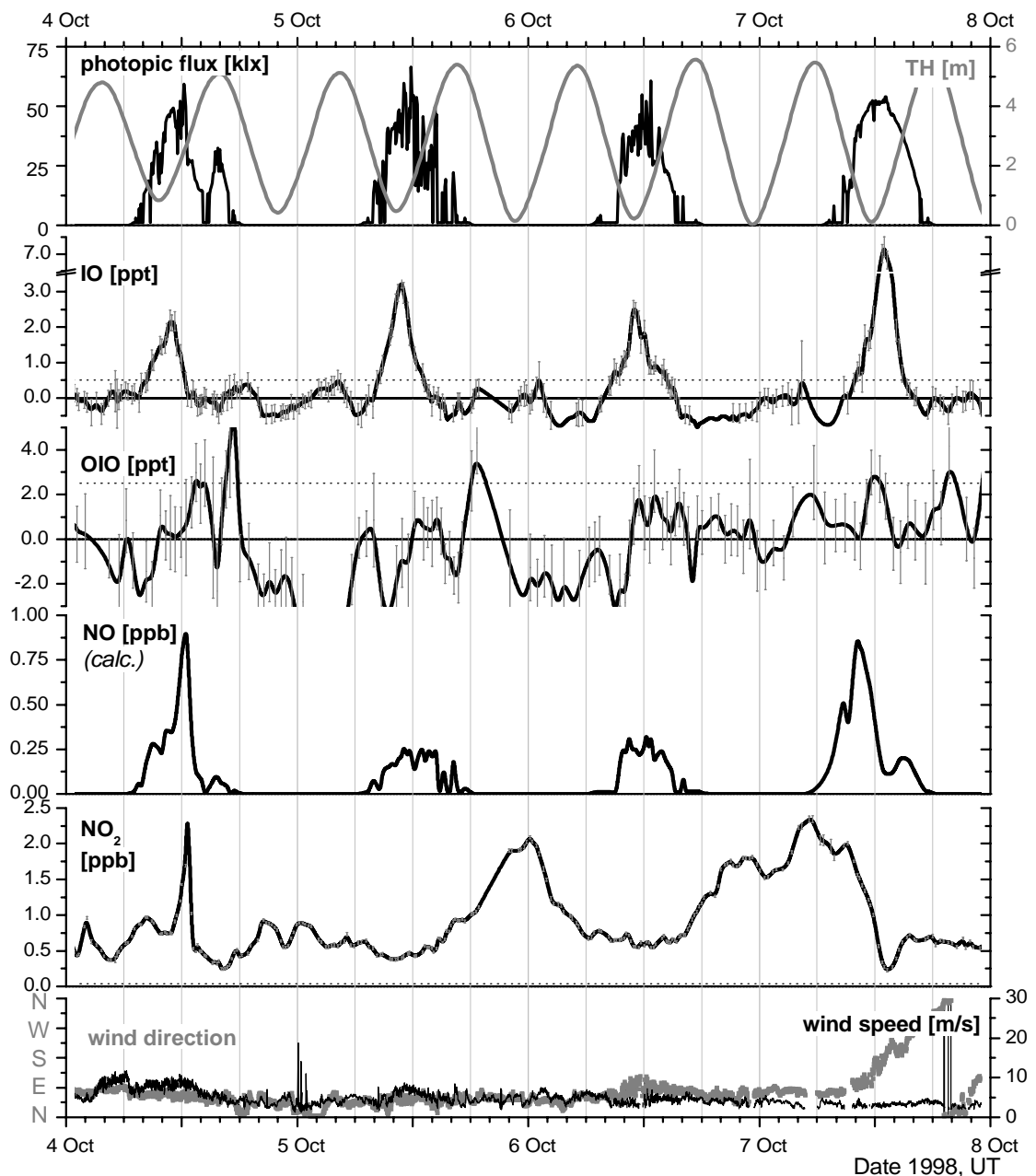


Figure 4.56 OIO time series of the relatively polluted days Oct 4 - 7. Dotted lines mark the detection limits. NO was calculated according to Equ 34, see text.

The absolute value of the OIO mixing ratios presented here is still uncertain due to the uncertainty of the absorption cross section of OIO, as pointed out at the beginning of this section. As we used the lowest value to calculate our concentrations, it may be possible that all OIO mixing ratios presented here need to be scaled down by a factor of 2 - 5.

c) *Production Rate and Loss Rates of OIO*

In consideration of these uncertainties it is possible to calculate the OIO production rate, P_{OIO} , from the IO concentrations determined at Mace Head. As BrO was below the detection limit during the whole campaign, the IO self-reaction is regarded as the only production channel of OIO. Assuming steady state conditions, the OIO production rate must be equivalent to its loss rate. Applying the degradation frequency l_{OIO} and the conditions of Sept 12 (2 ppt of IO) P_{OIO} can be calculated:

$$\begin{aligned} P_{OIO} &= \frac{d}{dt} [OIO]_{prod} = \frac{d}{dt} [OIO]_{loss} = [OIO] \cdot l_{OIO} \\ &= 0.38 k_{IO+IO} [IO]^2 = 0.38 \cdot 8.2 \cdot 10^{-11} \cdot (5 \cdot 10^7)^2 \text{ molec cm}^{-3} \text{ s}^{-1} \\ &\approx 8 \cdot 10^4 \text{ molec cm}^{-3} \text{ s}^{-1} \end{aligned} \quad \text{Equ 49}$$

The factor 0.38 considers the branching ratio of the IO self-reaction. Taking into account the OIO concentration of ~ 4 ppt of Sept 12, the l_{OIO} can be calculated:

$$l_{OIO} = \frac{P_{OIO}}{[OIO]} = \frac{8 \cdot 10^4 \text{ molec cm}^{-3} \text{ s}^{-1}}{1 \cdot 10^8 \text{ molec cm}^{-3}} = 8 \cdot 10^{-4} \text{ s}^{-1} \quad \text{Equ 50}$$

For a first-order loss process the lifetime τ_{OIO} is equivalent to the reciprocal of l_{OIO} :

$$\tau_{OIO} = \frac{1}{l_{OIO}} = \frac{1}{8 \cdot 10^{-4} \text{ s}^{-1}} = 1.25 \cdot 10^3 \text{ s} \approx 20 \text{ min} \quad \text{Equ 51}$$

As the OIO photolysis cannot be expected to occur (see section 2.3.3), the reaction with NO seems to be the most important loss process of OIO. Thus the loss rate l_{OIO} can be replaced by $l_{OIO} = [NO]k_{OIO+NO}$. This loss rate being inserted in Equ 51, the rate coefficient k_{OIO+NO} can be calculated for the conditions of Sept 12 under the assumption of a maximum NO mixing ratio of 10 ppt:

$$\begin{aligned} k_{OIO+NO} &= \frac{P_{OIO}}{[OIO][NO]} \\ &= \frac{8 \cdot 10^4 \text{ molec cm}^{-3} \text{ s}^{-1}}{1 \cdot 10^8 \text{ molec cm}^{-3} \cdot 2.5 \cdot 10^8 \text{ molec cm}^{-3}} \\ &\approx 3.2 \cdot 10^{-12} \text{ cm}^3 \text{ molec}^{-1} \text{ s}^{-1} \end{aligned} \quad \text{Equ 52}$$

For elevated NO_x conditions (Sept 20, Figure 4.55) the following mixing ratios have to be considered:

$$[OIO] = 8 \text{ ppt} = 2 \cdot 10^8 \text{ molec cm}^{-3}$$

$$[\text{IO}] = 4 \text{ ppt} = 1 \times 10^8 \text{ molec cm}^{-3}$$

$$[\text{NO}] = 1.5 \text{ ppb} = 3.75 \times 10^{10} \text{ molec cm}^{-3}$$

From these mixing ratios the following values of P_{OIO} , l_{OIO} and $k_{\text{OIO}+\text{NO}}$ can be calculated according to Equ 49 - Equ 52:

$$P_{\text{OIO}} = 3.1 \times 10^6 \text{ cm}^3 \text{ molec cm}^{-3} \text{ s}^{-1}$$

$$l_{\text{OIO}} = 1.6 \times 10^3 \text{ s}^{-1}$$

$$\tau_{\text{OIO}} = 6.1 \times 10^3 \text{ s} \approx 10 \text{ min}$$

$$k_{\text{OIO}+\text{NO}} = 4 \times 10^{-14} \text{ molec}^{-1} \text{ cm}^3 \text{ s}^{-1}$$

To sum up, the OIO loss rates and lifetimes calculated for both low and high NO_x conditions are comparable, while the rate coefficient $k_{\text{OIO}+\text{NO}}$ is by two orders of magnitude lower in the high NO_x case. This allows the approximation of an upper and lower limit of that value. The upper limit determined is comparable to the estimate by Cox et al. [1999] of $k_{\text{OIO}+\text{NO}} < 10^{-12} \text{ cm}^3 \text{ molec}^{-1} \text{ s}^{-1}$.

Additionally, $k_{\text{OIO}+\text{NO}}$ can be estimated from the reactions of $\text{XO} + \text{NO}$, which show the following order of rate coefficients for $\text{X} = \text{Cl}, \text{Br}$ and I :

$$1.7 \times 10^{-11} \text{ molec}^{-1} \text{ cm}^3 \text{ s}^{-1} = k_{\text{ClO}+\text{NO}} < k_{\text{BrO}+\text{NO}} \approx k_{\text{IO}+\text{NO}} = 2.1 \times 10^{-11} \text{ molec}^{-1} \text{ cm}^3 \text{ s}^{-1}$$

As the reaction $\text{IO} + \text{NO}$ is faster than $\text{ClO} + \text{NO}$, $\text{OIO} + \text{NO}$ can be estimated to be faster than $\text{OCIO} + \text{NO}$ as well. Thus $k_{\text{OCIO}+\text{NO}} = 3.4 \times 10^{-13} \text{ molec}^{-1} \text{ cm}^3 \text{ s}^{-1}$ indicates that $k_{\text{OIO}+\text{NO}}$ is of the order of $(5 - 10) \times 10^{-13} \text{ cm}^3 \text{ molec}^{-1} \text{ s}^{-1}$.

To compare the loss rates calculated here with the values determined by Allan et al. [2000], who found degradation frequencies of the order of $(10^{-4} - 10^{-5}) \text{ s}^{-1}$, which corresponds to a lifetime of the order of 1 hour, it has to be considered that the data published by this group were calculated on the basis of another OIO cross section. The loss and production rates of OIO, calculated from our measurements by downscaling the OIO mixing ratios by a factor of 2 – 5, can directly be compared with the values of Allan et al. [2000]. Table 4.12 summarises these values.

Table 4.12 Comparison of production and loss rates of OIO under varying NO_x levels. Right column shows these values calculated by Allan et al. [2000] for low NO_x levels.

	σ_{OIO} (1.09 ± 0.21) $\times 10^{-17} \text{ cm}^2 \text{ molec}^{-1}$ at 548.6 nm [Cox et al., 1999]		σ_{OIO} (2 - 5) $\times 10^{-17} \text{ cm}^2 \text{ molec}^{-1}$ at 548.6 nm [Spietz et al., 1998]		
	low NO_x (Sept 12)	high NO_x (Sept 20)	low NO_x (Sept 12)	high NO_x (Sept 20)	Allan et al. [2000]
l_{OIO}	$8 \times 10^{-4} \text{ s}^{-1}$	$1.6 \times 10^{-3} \text{ s}^{-1}$	$(1.6 - 4.0) \times 10^{-3} \text{ s}^{-1}$	$(3.2 - 8.0) \times 10^{-3} \text{ s}^{-1}$	$\sim 10^{-4} \text{ s}^{-1}$
τ_{OIO}	20 min	10 min	4 - 10 min	2 - 5 min	$\sim 1 \text{ hr}$

Our measurements stress the importance of OIO as a product of the IO self-reaction and as an important gas-phase reservoir species under low as well as under – comparatively –

high NO_x conditions in the marine planetary boundary layer. Even if the first detection of IO and OIO reported here is an important step, there are still a number of uncertainties that can only be solved by more laboratory, field and model investigations. Unfortunately, due to a gap in rate coefficient measurements to date, a detailed interpretation of these data is not yet possible.

In summary, our measurements indicate that OIO can be found in the marine planetary boundary layer under daylight conditions as well as after sunset. Furthermore, OIO was detected independently of the NO_x level. Neither the OIO photolysis, nor the reaction with NO therefore seems to be an important loss process in the PBL. Production and sink processes of OIO after sunset and, in general, the importance of the $\text{BrO} + \text{IO}$ reaction as an additional source of OIO are still unclear. With our measurements we can rule out an additional $\text{BrO} + \text{IO}$ production channel for BrO levels above our detection limit which ranges from 0.88 to 2.45 ppt. On the other hand, model calculations of *von Glasow* [2001], using the tropospheric box model MOCCA (Model Of Chemistry Considering Aerosols, see e.g. *Sander et al.* [1999 and 1997]) with respect to the marine boundary layer, required small amounts of BrO (of the order of some 10^{th} of a ppt) to produce the levels of OIO we detected at Mace Head.

4.5 *The Dead Sea Campaign 1997*

During the period from May 26 to June 21, 1997 a comprehensive set of atmospheric trace gas measurements and other relevant meteorological parameters were performed at a site in the Dead Sea Valley, Israel. DS97 was performed within the framework of the *HALOTROP* project as a joint venture of our group and the Environmental Sciences Division of the Hebrew University of Jerusalem, Israel (HUJI). The campaign was additionally funded by the *GIF (German Israelite Foundation)*. After a short introduction to the characteristic features of this continental and southernmost measurement site of this thesis and the chemical composition of the Dead Sea water the meteorological conditions will be illustrated. The evaluation of the DOAS data will be described in section 4.5.4, followed by a brief overview of the non-DOAS instrumental equipment of the campaign.

4.5.1 The Dead Sea Measurement Site

The Dead Sea (DS) Valley is - with about 400 m below sea level - the lowest land area on the face of the earth. As the valley is relatively narrow (at most 30 km) and the mountains on its eastern and western borders are quite high (more than 1000 m above the Dead Sea surface in the east and almost 500 m in the west), the predominance of southerly and northerly wind directions is obvious (compare with section 4.5.3). Figure 4.57 shows the view from the site to south-southwest.



Figure 4.57 View from the DS site to South-Southwest.

The measurements were made from a van, the mobile laboratory of the Hebrew University, situated on a dam between the northern and southern part of the DS. The southern basin is characterised by a higher salinity than the northern part as the Jordan river is the only influx, located at the northern end of the DS brine. This location of the measurement site was chosen because of its proximity to the salt-pans, which were assumed to act as major natural sources of halogen compounds (cf. section 2.2). The main salt-pans are located 23 – 25 km south-south-west of the site. Consequently, as can be seen from Figure 4.58, the detection of halogen oxides was expected above all during southerly wind flows. However, in principle, halogen compounds may also be released from the highly concentrated DS water and the sea salt deposits along the DS basin, which are, in different extensions and concentrations, available north and south of the site.

The transmitting telescope was set up on a rooftop of a hotel at a distance of 3.75 km south of the receiving telescope, the spectrograph and the detector unit, which were placed inside the van. Figure 4.58 shows a map of the north-western part of Israel including the Dead Sea and a north to south sectional drawing of the site.

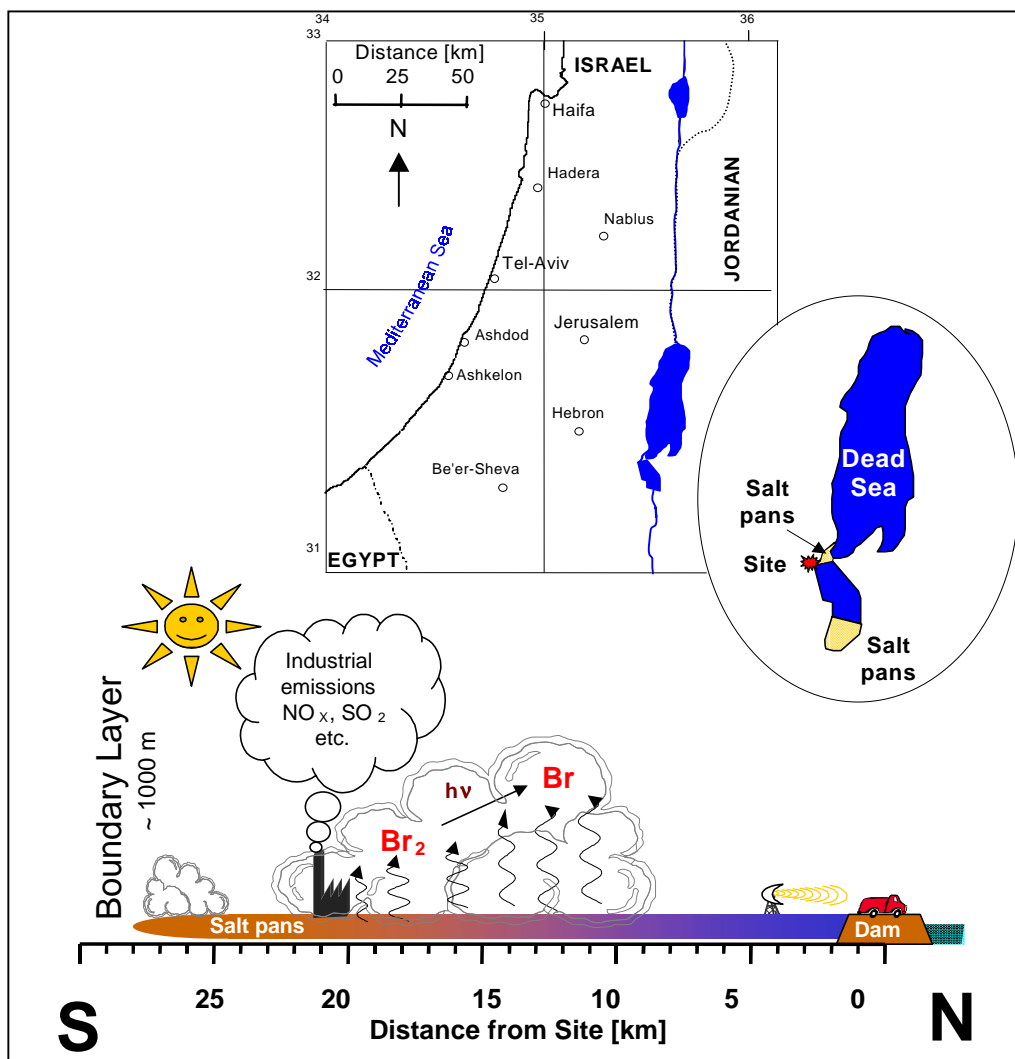


Figure 4.58 Above: Map of the north-western part of Israel and the Dead Sea Valley. Below: Sectional view of the area south of the light path.

The area of the measurements is quite remote from intensive human activities. A regional highway runs along the Dead Sea about 500 m from the site and a tourism centre with several hotels is located 3.7 - 5 km to the south of the site, where the emitting telescope was set up (see section 3.2 for a set-up of the DS DOAS instrument). The primary anthropogenic influences can be expected from the Dead Sea Works factory, located ~20 km south of the site, right in the area of the large salt pans at the southern end of the DS. In addition to industrial emissions like NO_x and SO₂ the Dead Sea Works plant is a potential source of reactive bromine, as it produces Br₂ by the reaction of Cl₂ with Dead Sea solid extracts. An additional source of manmade emissions, which, however, cannot be exactly localised, is the main road passing through the DS Valley.

4.5.2 Chemical Composition of the Dead Sea Water

Compared with normal sea water which contains 0.65 g l⁻¹ Br⁻ and 189.8 g l⁻¹ Cl⁻ (Br/Cl-ratio of 0.0034) [Sverdrup *et al.*, 1942] DS water contains (on average) 5.6 g l⁻¹ bromide and 225 g l⁻¹ chloride (Br/Cl ratio ≈ 0.025) (e.g. [Zak, 1997] or [Gavrieli *et al.*, 1994b] in [Niemi *et al.*, 1997]), resulting in a bromine enrichment factor (ER_{Br} = (Br/Cl)_{DS}/(Br/Cl)_{SMOW}) of 7 compared with SMOW³².

Table 4.13 Chemical composition of the Dead Sea water.

Chemical parameters	DS – halite ²	DS – Upper Water Mass (1960) ³	DS – Lower Water Mass (1960) ³	DS – Water (1985) ⁴	DS – Water (1993) ⁵	Seawater ⁶
Density [g cm ⁻³]	-	1.205	1.229	1.234	1.234	~ 1.024
Na [g l ⁻¹]	41.30	38.51	39.70	38.40	36.40	10.56
K [g l ⁻¹]	7.60	6.50	7.59	7.88	7.81	0.38
Mg [g l ⁻¹]	42.12	36.15	42.43	45.00	45.90	1.27
Ca [g l ⁻¹]	17.60	16.38	17.18	17.50	17.30	0.40
Cl [g l ⁻¹]	224.20	196.94	219.15	224.60	225.00	18.98
Br [g l ⁻¹]	4.50	4.60	5.27	5.20	5.60	0.07
SO ₄ [g l ⁻¹]	0.001	0.58	0.42	0.47	0.41	2.65
HCO ₃ [g l ⁻¹]	-	0.23	0.22	-	-	0.14
TDI ¹ [g l ⁻¹]	337.32	299.89	332.06	339.30	338.70	34.44
Cl/Br	50	43	42	40	40	294

¹ Total dissolved ions

² [Epstein, 1976]

³ [Neev and Emery, 1967]

⁴ Calculated from depth profiles in [Gavrieli and Beyth, 1986]

⁵ Calculated from depth profiles in [Gavrieli *et al.*, 1994a]

⁶ [Sverdrup *et al.*, 1942]

The Br enrichment leads to a relative molar ratio between Br⁻ and Cl⁻ of approximately 1:90 in the Dead Sea water [Niemi *et al.*, 1997]. With over 330 g l⁻¹ dissolved ions the salinity of the DS water is 10 times more concentrated than seawater. Furthermore, the acidity of a pH ≤ 6.5 [Fickert *et al.*, 1999] which is needed to promote the oxidation of Br⁻

³² SMOW = Standard Mean Ocean Water

by HOBr (see section 2.1.2) is available, most likely due to industrial emissions of SO_4^{2-} or NO_3^- : the DS waters are characterised by pH values of 6 – 6.35 [Nishri and Stiller, 1997] and therefore are strongly buffered solutions. It is important to note that, in contrast to bulk oceanic sea water, a bromine release via the ‘bromine explosion mechanism’ (see section 2.2) may occur from the DS water and not only from sea salt deposits. The chemical composition of the DS water is summarised in Table 4.13.

4.5.3 The Meteorological Conditions at the Dead Sea

As mentioned above the Dead Sea Valley is delimited by steep mountains of a height of approximately 1000 m. This channel-like situation causes the north-south direction to be the axis of the major wind flow. Moreover, the height of these mountains more or less represents the typical height of the boundary layer.

The meteorological conditions prevailing at the Dead Sea are totally different from the situation during the ‘north European marine’ campaigns at Weybourne and Mace Head. The temperature varied between 22 and 42 °C, the pressure between 776 and 786 torr and the relative humidity (RH) never exceeded a value of 40 %. Wind speed (WS) showed maximum values of 13 ms^{-1} with typical noon values of 2–3 ms^{-1} and wind direction (WD) changed daily from north to south and back. Figure 4.59 gives an overview of the meteorological conditions.

As can be seen, the DS site offers typical daily recurring cycles of almost all meteorological parameters over the whole period of the campaign. Figure 4.60 shows a three-day period underlining this cyclic repetition that makes the Dead Sea basin almost a natural outdoor laboratory, allowing daily recurring observations of nearly the same atmospheric conditions.

This typical daily meteorological cycle can be described as follows: After sunrise around 6 am local time (LT) the temperature rises from night time values of 25 to 40 °C and more, peaking around 3 pm LT. Simultaneously the relative humidity decreases from 40 % at night to 5–10 %. Parallel to the change in solar radiation the wind direction changes every day from northern night-time directions to the south and reaches a stable southern flow approx. one hour before the maximum SR. At 5 pm the wind shifts back to the north and the wind speed increases from 2 ms^{-1} to maximum values of typically 5–8 ms^{-1} .

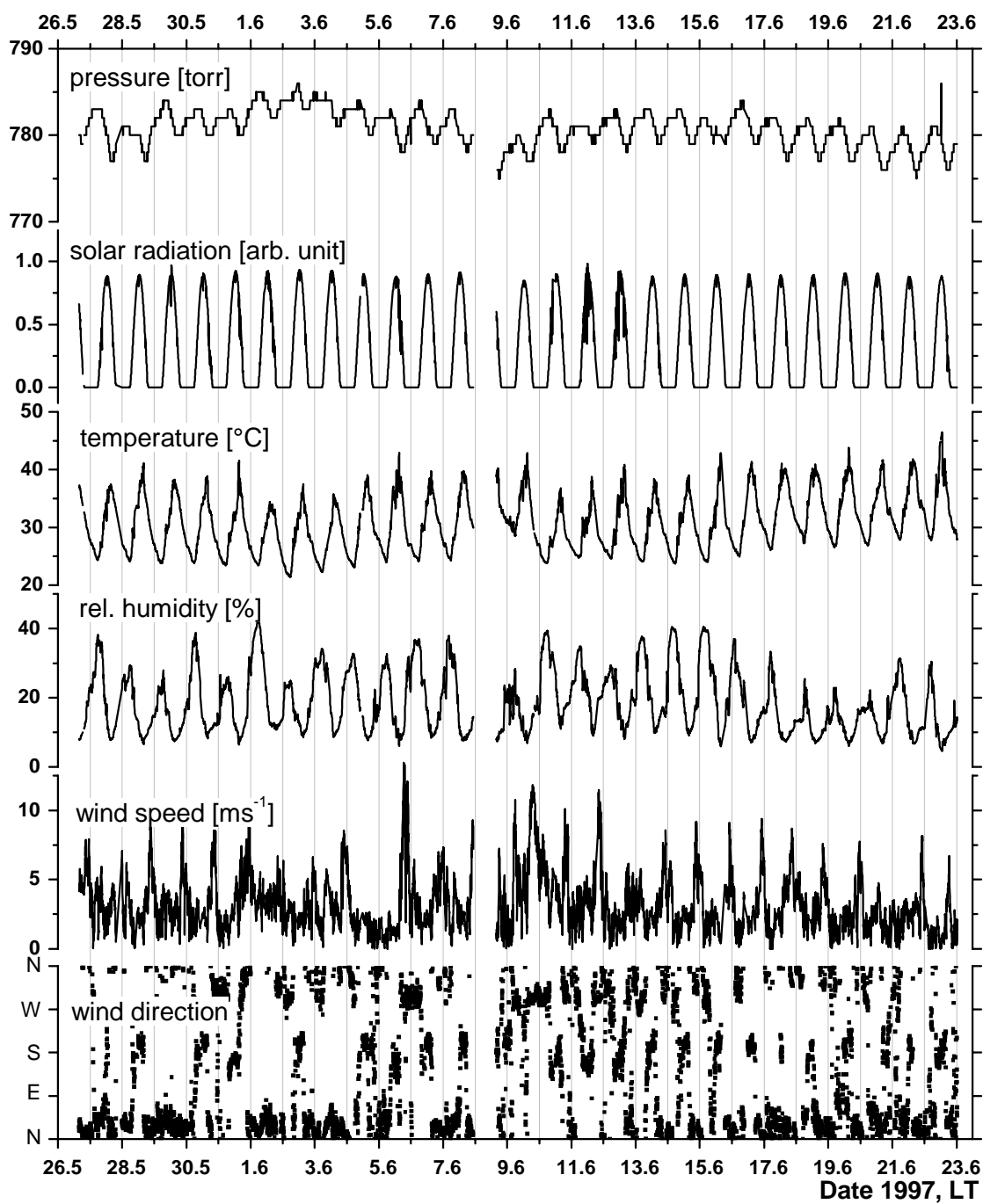


Figure 4.59 Meteorological conditions during the DS97 campaign, the time is given as LT which corresponds to UT + 3 hr.

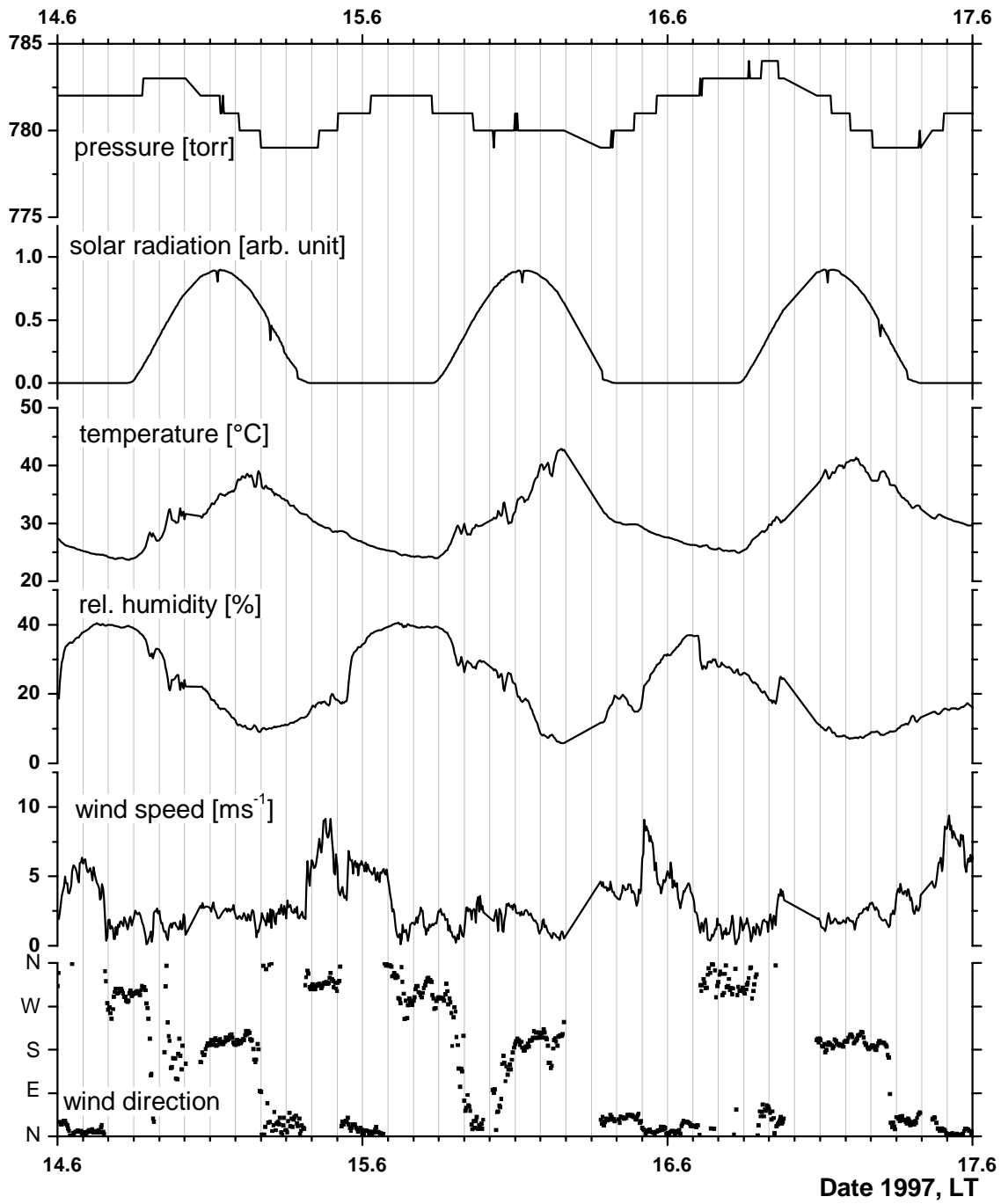


Figure 4.60 Typical three-day section of meteorological conditions during DS97. Major ticks mark the beginning of the day, the time is given as LT (= UT + 3 hr).

Figure 4.61 A shows the frequency count of WD which indicates N/NE as the by far prevailing wind direction in accordance with the topological conditions, the north-south direction as the main flow axis. Graph B shows the hourly average values of solar radiation (SR) (additionally BrO and O₃) and graph C the WD plotted on a 24-hour scale. Every graph considers the data set of the whole period of the campaign. The hourly average values were calculated without normalising the data before.

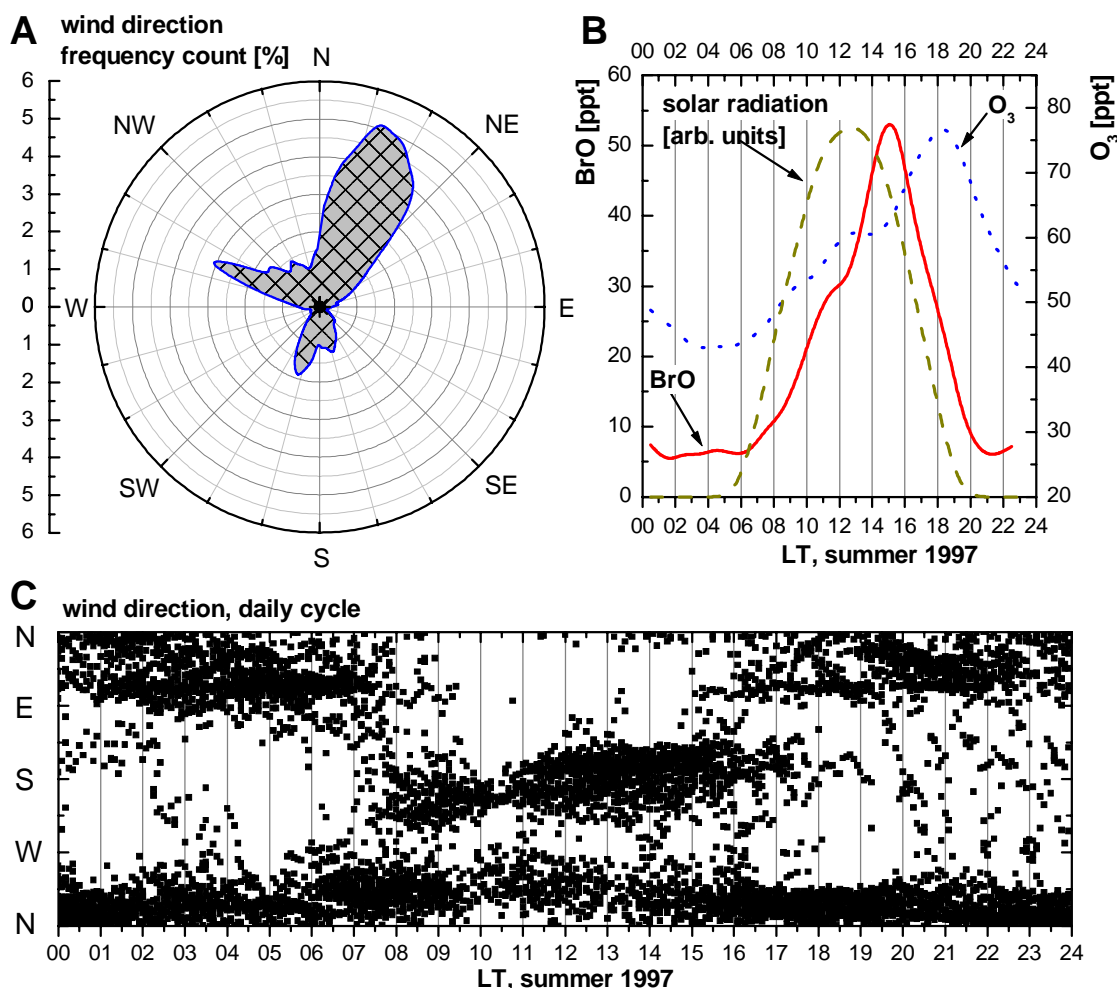


Figure 4.61 A: Frequency distribution of the wind direction (WD), 10° average values. B: Average daily cycle of BrO, O₃ and solar radiation. C: All WD data plotted on a 24-hr scale. All graphs consider the data set of the whole campaign.

The average daily cycle of SR of the whole campaign shows the shape one would expect at a measurement site in Southern Europe. The sun rises around 5.00, reaches its maximum at 12.30 and sets between 20.00 and 21.00. The average daily cycle of BrO and O₃ will be discussed at section 4.6.1.

4.5.4 The DOAS Measurements of DS97

DOAS measurements of BrO, O₃ and NO₂ were performed by analysing the absorption structures of these species in the wavelength region of 337±10 nm with a spectral resolution of 0.25 nm. In an automated measurement routine atmospheric and background spectra were recorded alternately. For the purpose of wavelength calibration atomic Hg

emission lines were sporadically recorded by holding a mercury lamp manually in front of the entrance slit of the spectrograph.

Reference spectra of NO₂ and ozone were recorded twice. As the telescope did not comprise a short-cut system and the lamp was located at the other end of the light path, the light had to pass through the atmosphere before reaching the receiving telescope. The beam having been reflected by the main mirror and the plane mirror, which diffracts the beam by 90° to the entrance slit of the spectrograph, a quartz cuvette filled with NO₂ was held into the beam. As ozone is not photostable a flow-system cuvette was used to record O₃ reference spectra. The O₃ was generated, using an oxygen gas cylinder and a commercial aquarium ozoniser.

As the light has passed through the atmosphere before it transits the quartz cuvette, the atmospheric absorption features have to be removed. Therefore, right after recording the cell and the corresponding background spectrum, an atmospheric correction spectrum (followed by atmospheric background) was recorded. This spectrum represents a kind of lamp emission spectrum, as it includes the spectroscopic lamp features as well as the atmospheric absorption structures.

a) BrO Evaluation

The wavelength-to-channel relation (dispersion) of the DOAS instrument used at the Dead Sea varied in time due to the limited thermal stabilisation of the spectrograph. However, it was possible to correct these variations in the dispersion by comparing the spectral information of the absorbing species in the relevant spectral region of 327 - 347 nm to i) recorded mercury atomic emission lines, ii) clearly visible spectral features of the observed trace gases and iii) the Fraunhofer structures from scattered background sunlight clearly visible observed in our daytime spectra. The shift of the Hg emission lines temporarily recorded as a wavelength calibration is shown in Figure 4.63.

The evaluation procedure consisted of the following steps: The first step included subtraction of the background spectrum followed by band-pass filtration (high-pass: division by a polynomial of the ninth order; low-pass: 5 times adjacent smoothing) of the resulting spectra. After shifting the spectra to correlate wavelength and channel number (to avoid the thermal effects as described above), a logarithm was performed. Using the analysing software MFC [Gomer *et al.*, 1993], a non-linear least-square fit was performed [Stutz and Platt, 1996] for three reference spectra (BrO [Hönninger, 1999], NO₂ (self-recorded as described above), O₃ [Bass and Paur, 1984]), an additional solar spectrum [Kurucz *et al.*, 1984] and a typical scattered-light spectrum. Concurrently, a polynomial of the fourth order was applied to the fitted spectra. Finally, the concentrations were calculated from the fit results adjusted for pressure and temperature variations. Figure 4.62 shows the evaluation of a typical midday spectrum, recorded on June 4, 1997 at 12.56.

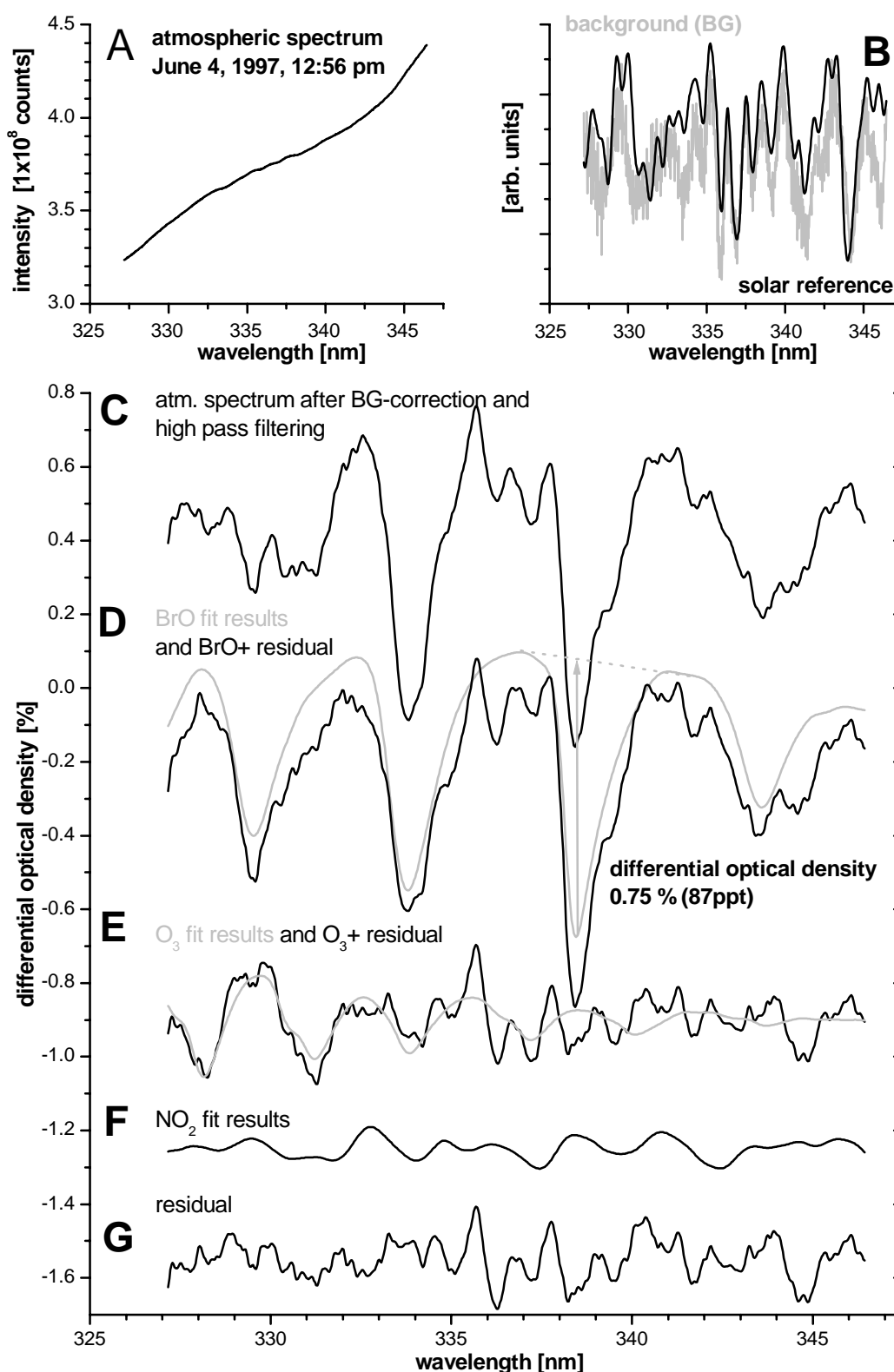


Figure 4.62 Analysis of a typical midday DOAS spectrum: A) Atmospheric raw spectrum, B) background (BG) and solar reference (shown to demonstrate the stray-light compound of the BG), C) Atmospheric spectrum after BG correction and high-pass filtering, D) BrO fit results and BrO + residual(G), arrow marks the differential optical density of the main absorption band, E) O_3 fit results and O_3 + residual, F) NO_2 fit result and G) residual.

Depending on visibility variations caused by aerosols in the atmosphere, the typical time resolution of the instrument was 30 min. A comparison with the BrO reference spectrum of *Wahner et al.* [1988] underlines the first unambiguous identification of this compound in the mid-latitudinal boundary layer [*Hebestreit et al.*, 1999; *Matveev et al.*, 2001; *Stutz et al.*, 1999]. The average detection limit for BrO, using the present set-up, was 7 ppt.

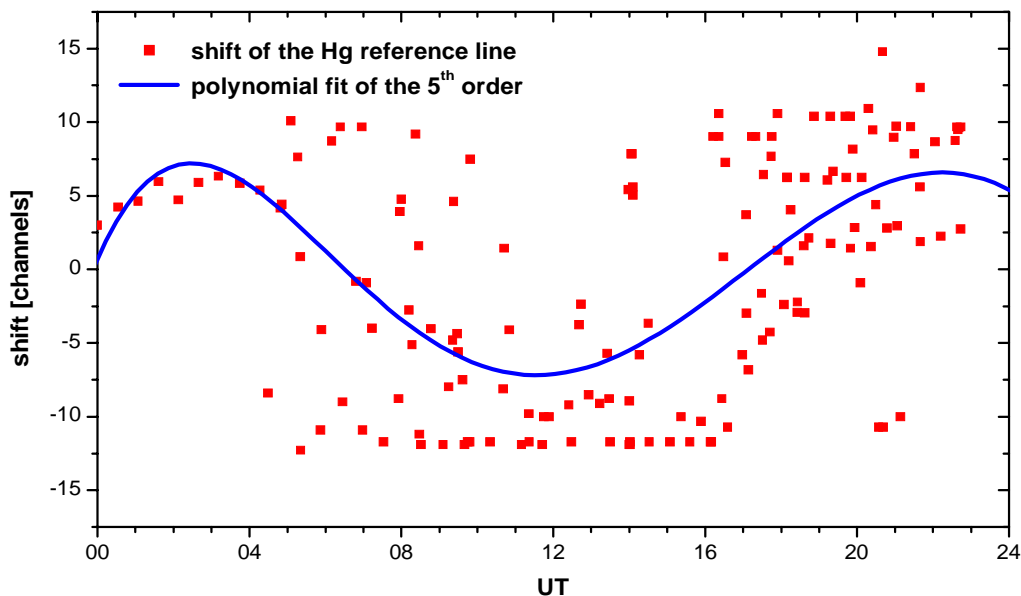


Figure 4.63 Shift of the Hg reference line recorded during the campaign.

b) Evaluation of O_3 and NO_2

The sensitivity for NO_2 and O_3 by the DOAS method was limited by the small absorption cross sections in the observed wavelength region (detection limit 2 ppb and 20 ppb respectively). The NO_2 absorption spectra recorded at the site were scaled, using the cross section of *Harder et al.* [1997], while the O_3 literature reference of *Bass and Paur* [1984] was convoluted to our resolution with a Hg reference line. Because of the availability of independent in-situ monitor data of a higher data quality and better time resolution none of these data are presented in the interpretation part of this chapter (4.6).

4.5.5 Non-DOAS Measurements of DS97

The instrumental equipment included high sensitivity SO_2 and NO/NO_x analysers, O_3 and CO monitors as well as instruments for the continuous monitoring of the common meteorological parameters. The NO_x monitor is based on the detection of NO by chemoluminescence and an additional catalytic converter for NO_2 . It is probably also sensitive to $BrONO_2$ and $BrONO$. The NO_x levels of one to a few ppb measured during high BrO mixing ratios are therefore uncertain. Model calculations (section 4.6.4) indicate that 0.5 – 1 ppb of the NO_x is converted to $BrONO_2$. Consequently, the NO_x signal in the course of the BrO-event may partly be due to $BrONO_2$.

During the measuring period 94 canister samples were collected and then shipped to the University of California (Irvine) Chemistry Laboratory for the bromocarbon analyses,

using gas chromatography techniques with mass spectrometry and electron capture [Blake *et al.*, 1999]. Samples for aerosol analysis were taken on a tandem Teflon/Nylon 47 mm filter pack. The sampled air first passes through the Nylon filter, which retains gaseous nitrates and part of the sulphate, chlorides and bromides. The second Teflon filter traps the remaining nitrate, sulphate and halogen aerosols. The filter samples were collected on a 6-hour basis, for the periods 00-06, 06-12, 12-18 and 18-24 LT. Later the samples were extracted in a 10% methanol-water mixture and analysed for anions using ion chromatography [Luria *et al.*, 1996]. The filter data presented are the sum for both filters. Detailed descriptions of the instruments, as well as their detection limits, are given in Table 4.14.

Ten research flights were performed over central Israel and the Dead Sea during the afternoon hours between July 21 and August 29. The flights were carried out at low altitudes of 300 m above surface level, well within the mixed layer. The instruments on board a Cessna 210 single-engine aircraft included monitors for O₃ and NO-NO_x as well as a global positioning system (GPS), temperature, humidity and pressure sensors and a filter package similar to the system used at the surface site. Aircraft instrumental details are also given in Table 4.14. Both the surface and aircraft measurements were recorded with a 10-second time resolution and averaged over 1-minute periods, using a data-logger computer system.

Table 4.14 List of measurements at the surface site and on board the aircraft.

Parameter	Platform*	Operational principle	Manufacturer	Detection limit
BrO, O ₃ , NO ₂	G	DOAS	In House	7 ppt, 20 ppb, 2 ppb
SO ₂	G	Pulsed Fluorescence	TEII 43S	0.1 ppbV
NO	G&A	Chemiluminescence	TEII 42S	0.1 ppbV**
NO _x	G&A	Chemiluminescence + Mo converter	TEII 42S	0.1 ppbV**
O ₃	G&A	UV Photometric	TEII 49	2 ppbV
CO	G	IR Absorption	TEII 48	100 ppbV
Wind speed	G	3-cup anemometer	Met-One 024A	0.5 ms ⁻¹
Wind direction	G	Wind vane	Met-One 024A	5°
Temperature	G&A	Thermistor	Met-One 060A	0.4 K
Humidity	G&A	Capacitance	Met-One 083	3%
Halocarbons	G	Gas-Chromatograph, MS/ECD detectors	HP-6890 HP- 5973	0.1pptV
Br ⁻ , Cl ⁻ , NO ₃ ⁻ and SO ₄ ⁼	G&A	Ion Chromatography	Dionex DX 500	0.1µg m ⁻³

* G = ground site, A = aircraft ** with no respect to the possible cross sensitivity to BrONO₂

Figure 4.64 shows the NO₂ and O₃ data determined by DOAS in correlation with the respected in-situ monitor data. The offset of the NO₂ monitor values becomes obvious and

can be explained by the possible cross sensitivity regarding bromine nitrates. The differences in the ozone data sets might be caused by the small absorption cross section of ozone in this wavelength region which was optimised for the BrO measurements.

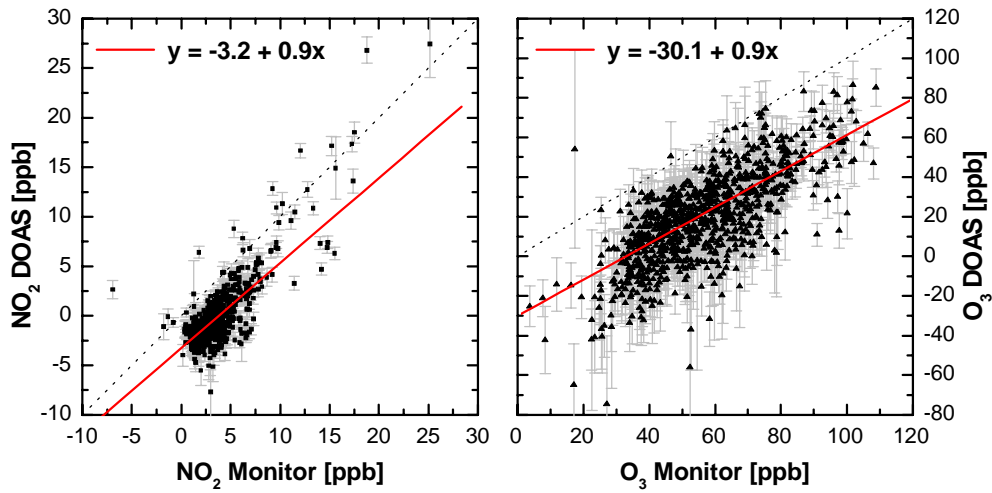


Figure 4.64 Comparison of DOAS and in-situ monitor data of NO₂ (left hand side, black squares) and O₃ (right hand side, black triangles). The dotted line shows the $y = x$ line, underlining that both of the DOAS values are supposed to be too low (or the monitor values too high).

4.6 Results of DS97:

Bromine Oxide – Ozone Interactions at the Dead Sea

In the following subsections it will be shown that the low ozone events (LOE) observed in the course of DS97 are clearly caused by the high BrO levels recorded in daily recurring cycles. Titration of freshly emitted NO_x will be ruled out as a significant O_3 sink at noon-time. After that, the possibility of manmade emitted reactive bromine (re-Br) as the main source of BrO will be excluded. Model calculations will be used to show that the two most probable mechanisms releasing bromine from sea salt, the attack of strong oxidising agents and the autocatalytic uptake of HOBr and BrONO_2 , which have already been discussed in section 2.1.2, can explain the BrO mixing ratio observed. Finally, the results of bromo-carbon and filterable bromine (f-Br) measurements and a subsequent airplane study will be presented.

4.6.1 Average Daily Cycles BrO and Ozone

The time series of BrO (DOAS), O_3 and NO_2 (in-situ monitors) and SR for the entire research period, May 26 to June 22, 1997, are represented in Figure 4.66. Elevated BrO levels were observed on almost every day, while midday O_3 decreases occurred during the major part of the sampling days. Ozone depletion was always correlated with increased BrO levels. During the morning hours the BrO mixing ratios rose above background levels of ~ 10 ppt, which is slightly above the average detection limit of 7 ppt, peaking around noon before returning to background levels or

even below the detection limit around 19.00. During the daytime NO_2 remained relatively low (1 – 2 ppb) as against night-time with a typical maximum of 5 – 10 ppb right around midnight. Peak values occasionally reached 30 ppb. The highest BrO value recorded during the campaign was 176 ppt, the highest mixing ratio ever measured in the atmosphere. The O_3 concentration ranged from maximum values of above 120 ppb down to values below the detection limit of the in-situ monitor (2 ppb). These - temporarily total - O_3 depletion events were observed during high BrO events on almost every day of the campaign. From the time series it becomes obvious that the BrO mixing ratios were mostly elevated during southerly wind directions. Nevertheless, it is still unclear whether time

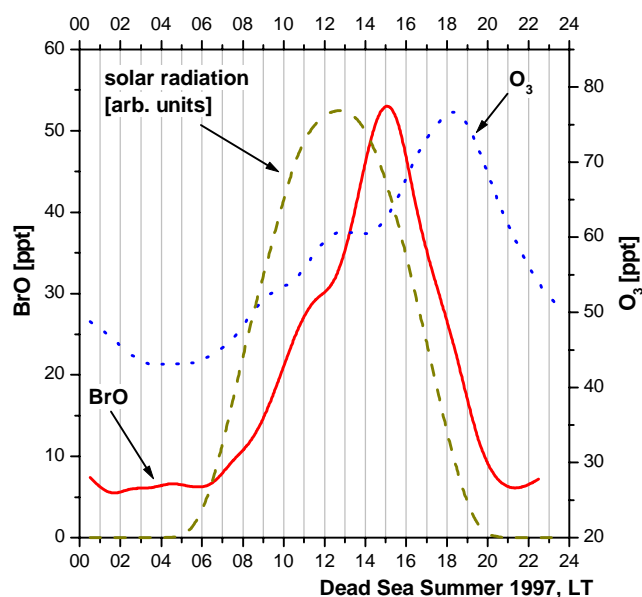


Figure 4.65 Average daily cycle of BrO, O_3 and solar radiation, considering the data set of the whole DS97 campaign.

(and consequently solar radiation) or the change in wind direction is the major reason for these periodically recurring patterns of BrO.

Hourly average values of solar radiation (SR), BrO and O₃, considering the data sets of the whole period of the campaign, are represented in Figure 4.65. These daily averaged cycles were calculated without normalising the data before. As it could be expected from the daily recurring meteorological cycles discussed above (see section 4.5.3), BrO and O₃ show daily recurring cycles as well. Right after sunrise BrO starts to rise and reaches the average maximum mixing ratio of BrO_{max} = 55 ppt in the early afternoon around 15.00. At the local solar maximum at 13.00 the steep BrO increase is interrupted but continues immediately. Values of 5 – 10 ppt, which is comparable with our detection limit, are reached again at 20.00.

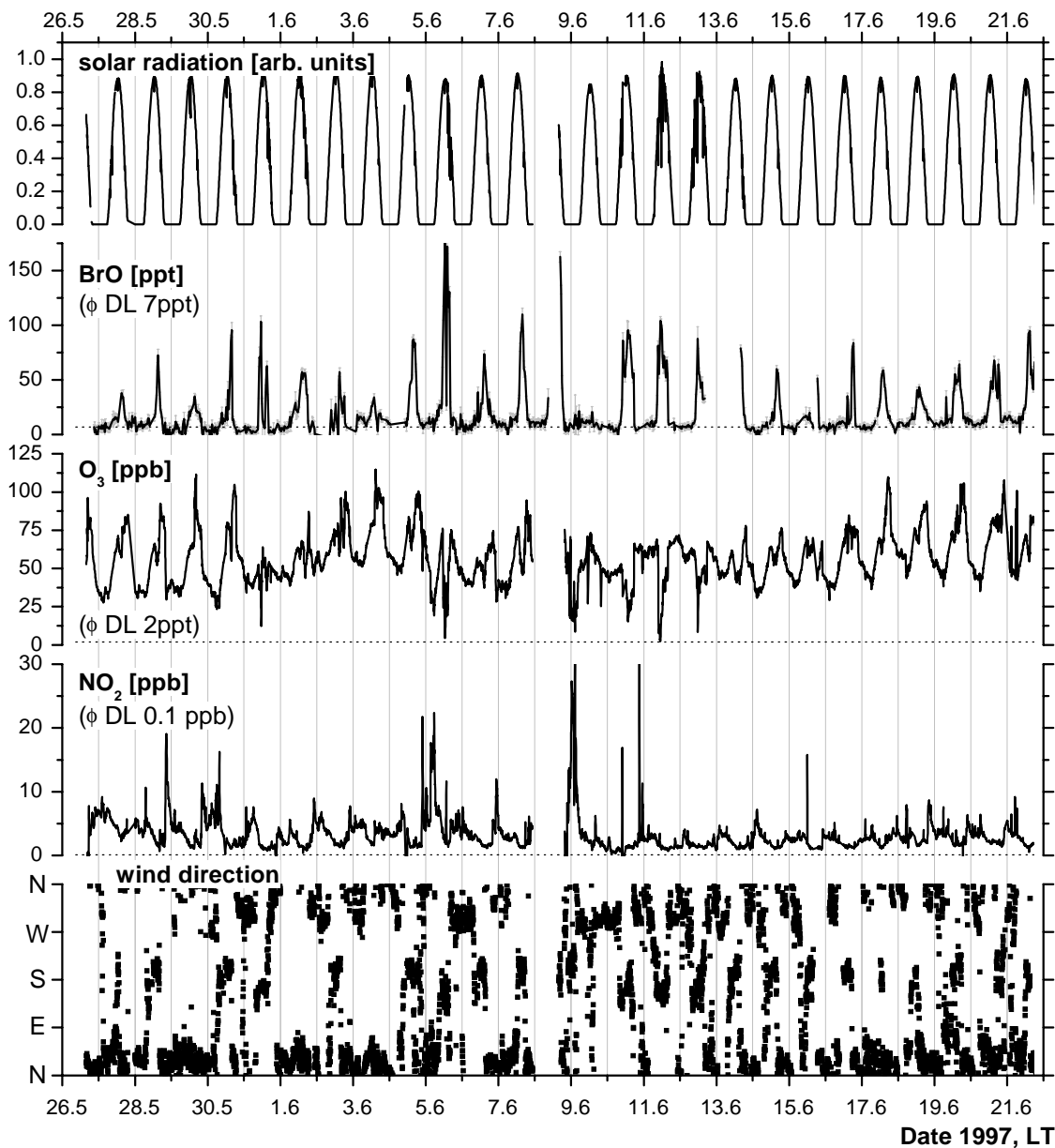


Figure 4.66 Overview of the time series of BrO, O₃, NO₂, wind direction and solar radiation recorded during DS97, indicating the daily recurring cycles of all parameters. Dotted line indicates average 2 σ -detection limit.

However, even if there are some hints on a permanent BrO background level of the order of some ppt, the absolute values are very uncertain and do not allow to conclude significantly that there is permanent BrO background level at the DS. This uncertainty is confirmed by the overall BrO record represented at Figure 4.66. The night-time/early morning mixing ratios of BrO are scattering between zero and the detection limit of 7 ppt in average. O₃ concentrations do not show a minimum correlated with BrO_{max}, but the constant increase in concentration stops at 13.00 at a level of 60 ppb. Afterwards the ozone mixing ratio rises to 75 ppb around 18.00 and decreases rapidly to 50 ppb. The daily O₃ minimum is reached around 03.00 with average levels of 40 ppb. From Figure 4.61 C it became obvious that during the night-time and the early morning hours the wind flowed from northerly directions. At around 08.00 the wind direction changed to the south. This southerly wind continued until the afternoon, when WD changed to the north again. From the WD time series shown in Figure 4.66 it becomes clear that this pattern was consistent for the whole period of the campaign, except for four days when the wind flowed from northerly directions during the entire 24-hour period.

4.6.2 Identification of BrO as the O₃-Destroying Agent

The extensive BrO formation occurring during southerly wind flows is shown in the upper panels of Figure 4.67 which deal with the distribution of BrO and O₃, given as average values of 10° sectors in dependence on WD. The shape of the BrO graph (A) emphasises the southern sector as the direction of major re-Br sources. Unexpectedly, compared to the significant shape of the BrO distribution, the O₃ distribution (B) looks equally spread.

However, to accentuate the variations in the O₃ data it is worthwhile analysing the relative changes of concentrations compared with the overall minimum of the distribution. Graph C and D of Figure 4.67 show the relative variation in the ozone distribution. Both of the distributions are plotted with respect to the 10° segment averages shown as A and B. Given are $\Delta O_3 = (O_3 - O_{3min}) / O_{3min}$ and $\Delta BrO = (BrO - BrO_{min}) / BrO_{min}$ in [%]. As expected, the average BrO mixing ratios of some directions are very low and the BrO mixing ratios show enormous variations of up to 1200 %. The relative O₃ variations show the influence of elevated BrO in the S/SE sector where a significant minimum occurs, while the maximum is about 40 – 50 % higher.

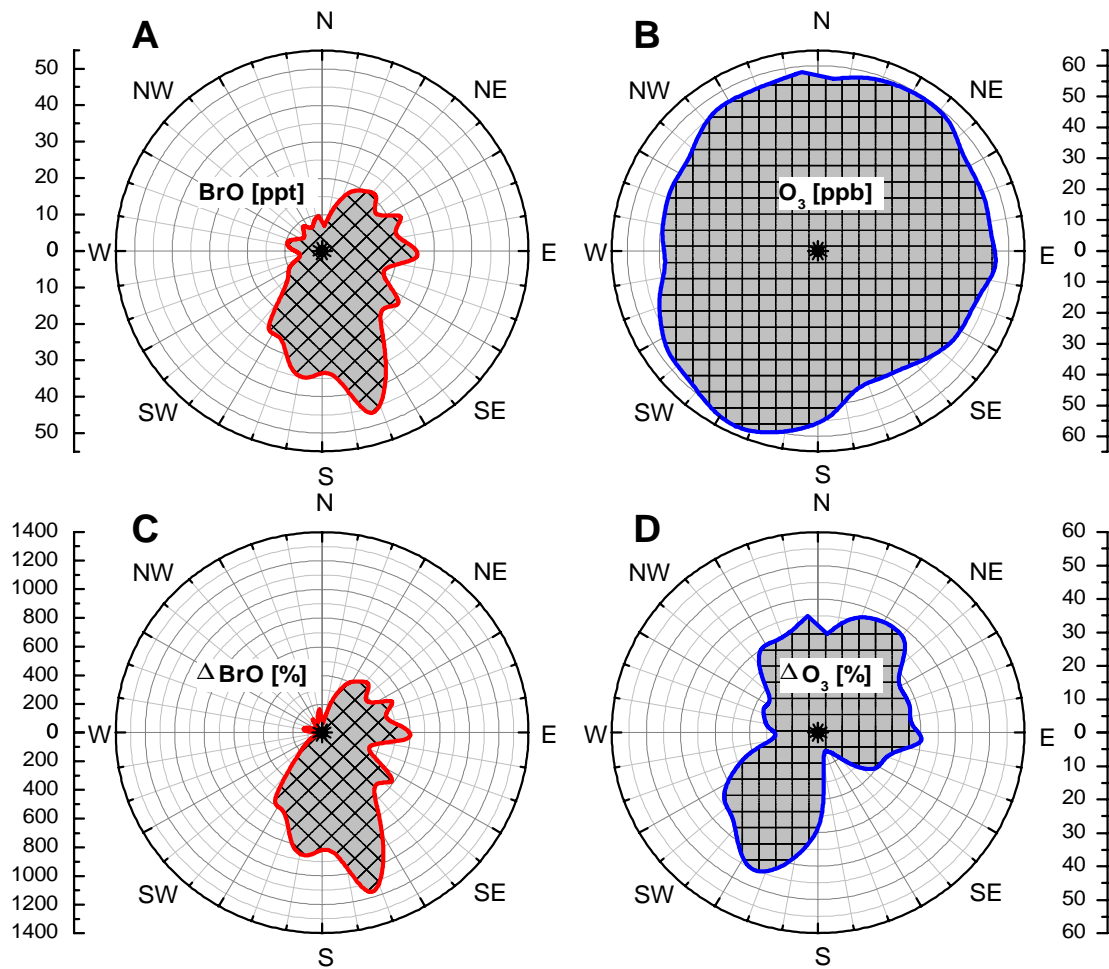


Figure 4.67 The dependence of BrO and O₃ mixing ratios on WD (A,B) indicates the BrO enrichment of southerly airflows. The relative variation (C,D) indicates the O₃ depletion from S/SE.

a) BrO - O₃ Interactions

Figure 4.68 shows a BrO-O₃ scatter plot. All data points of O₃ and BrO above their respective detection limits of 2 ppb and 7 ppt are plotted as BrO averages over 10-ppb O₃ segments, represented by bars. In addition, the data observed during southerly winds in the sector between 150° and 210°, where the dependence on WD shows considerably increased BrO values, have been analysed separately.

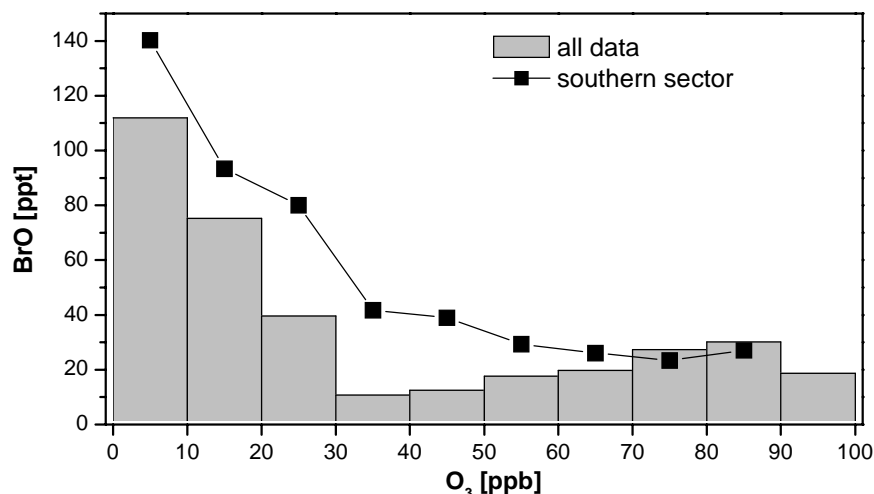


Figure 4.68 *BrO vs. O₃ scatter plot. The entire data set is segmented into 10-ppb O₃ intervals, represented by bars. The squares represent the data recorded during southerly flows between 150° and 210°.*

Both data plots show the anti-correlation of BrO and O₃. High values of BrO correspond to low Ozone, while high Ozone mixing ratios occur only under low BrO conditions. During most of the measurement days performed at the Dead Sea the diurnal wind pattern was consistent, with northerly winds prevailing. Only during midday periods southerly winds prevailed. Owing to this characteristic wind pattern almost all the days with BrO peaks were associated with southerly winds. In the following the interaction of the different parameters under southerly as well as under northerly conditions will be discussed.

b) Ozone Depletion by Reactive Bromine Species

Figure 4.69 shows June 5 as a typical example of a day with periodically changing wind directions, BrO event and O₃ depletion. The wind flowed from the south during the middle hours of the day (09.00 - 15.00) and from the north during the rest of the day.

On June 5 the highest BrO level (176 ppt) was observed, with corresponding O₃ mixing ratios below detection limits. During the LOE no correlation was found between NO and O₃ variations. Thus the possibility of ozone depletion by titration with fresh NO emissions can be ruled out. Furthermore, the NO_x concentrations were quite low (generally below 10 ppb). Hence, all the findings seem to indicate that the O₃ depletion phenomenon is associated solely with the Br-catalysed O₃ destruction cycles A and B of chapter 2. Figure 4.71 shows June 11 as another exemplary day of total O₃ destruction under conditions of high BrO and low NO_x.

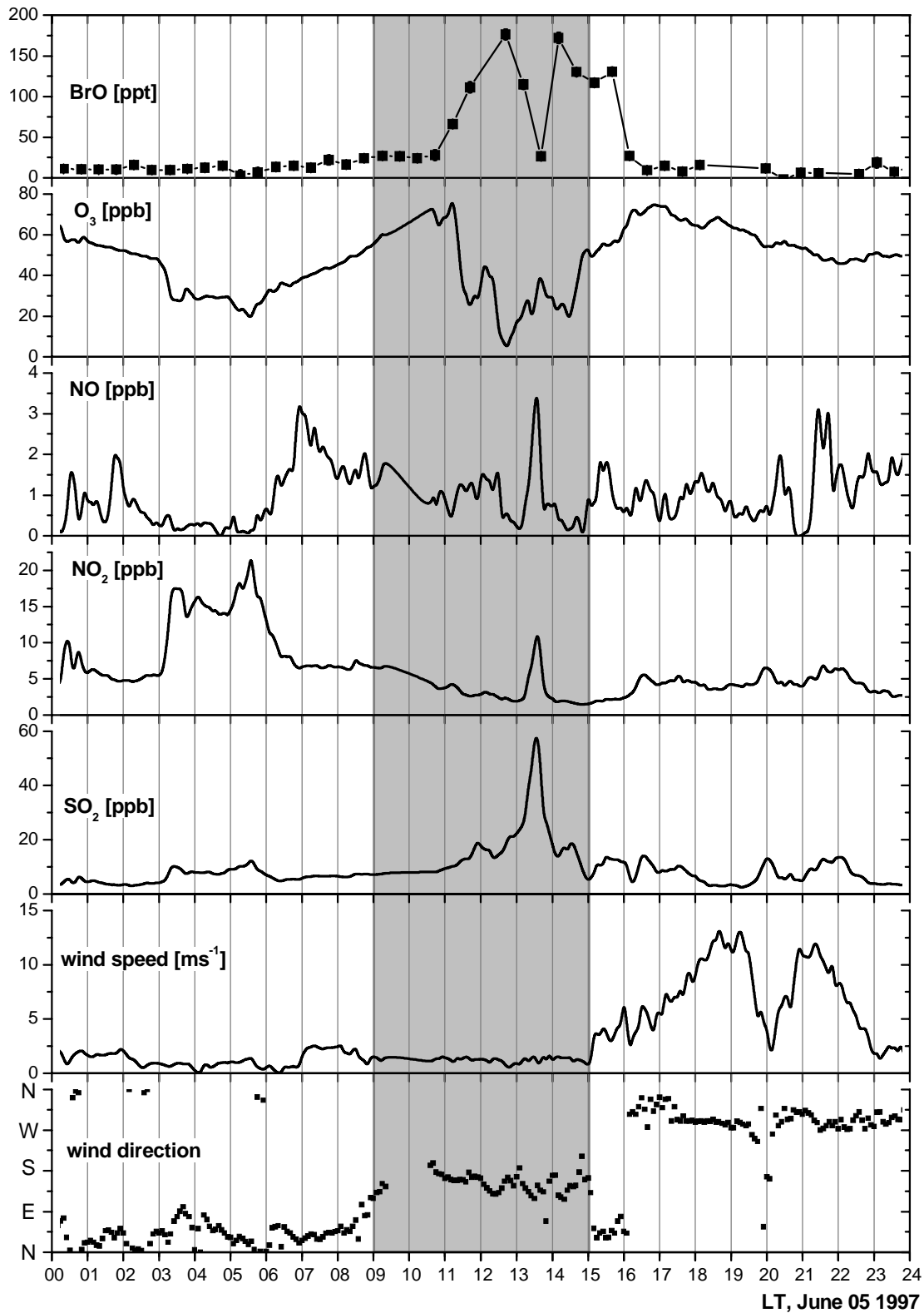


Figure 4.69 Mixing ratios of BrO, O₃, SO₂, NO and NO₂, as well as wind speed and wind direction (WD), of June 5, 1997. The shaded area marks the southerly WD.

4.6.3 Identification of the Sources of Reactive Bromine at the Dead Sea

Since BrO appears to be responsible for the O₃ depletion events, it is important to identify the bromine sources. The environmental conditions at the Dead Sea are extremely different

from those existing in the Arctic during polar sunrise, where O₃-BrO reactions have previously been observed. The temperature is about 40 - 50 K higher and ice surfaces and high breaking waves do not exist.

Potential re-Br sources may include anthropogenic emissions such as bromine from the Dead Sea industries and bromine release from the Dead Sea itself and/or from sources in its vicinity. After a short summary of the natural mechanisms releasing re-Br from salt surfaces, the factory of the Dead Sea Works will be ruled out as the origin of the BrO observed by different observations and calculations.

a) *Short Summary of the Bromine Liberation from Sea Salt*

As described in chapter 2, several heterogeneous processes have been proposed to explain the release of RHS from an - aerosol or ground-deposit - sea salt reservoir [Fan and Jacob, 1992; Mozurkewich, 1995; Sander et al., 1997; Vogt et al., 1996]. The most probable process of autocatalytic ozone destruction and simultaneous release of RHS from sea salt at the Dead Sea is the "bromine explosion" mechanism [Platt and Lehrer, 1997] which is based on the uptake of HOBr on acidic salt surfaces [Fan and Jacob, 1992; Tang and McConnel, 1996]. The ozone destroying sequence can be summarised as the bromine-catalysed net reaction which has already been given in section 2.2 as:



The 'explosion' occurs if less than 50 % of the bromine is lost from the reactive cycle by e.g. the reaction of Br with HO₂ or CH₂O, or BrO with NO₂, forming BrONO₂.

As sea salt is an almost inexhaustible reservoir of halogens, the bromine explosion does not stop before all the O₃ is destroyed. From then on re-Br cannot be regenerated via the reaction with O₃ and will be deposited as HBr, formed in the reaction with unsaturated hydrocarbons, such as alkenes. The acidic environment of a pH ≤ 6.5 [Fickert et al., 1999], which is required to promote the oxidation of Br⁻ by HOBr, is available, as the Dead Sea waters are characterised by pH values of 6 – 6.35 [Nishri and Stiller, 1997] and therefore are strongly buffered solutions. It is important to note that therefore, in contrast to bulk oceanic sea water, a bromine release via the bromine explosion mechanism may occur from the water and not only from sea salt deposits on the ground.

As the bromine explosion leads to an exponential growth of RHS species, very low concentrations of bromine could trigger the reaction chain which is summarised as R34. In general, two mechanisms are possible: bromine release via oxidising species (e.g. NO_x or O₃, see section 2.2) which do not require sunlight, and the photolysis of organohalogen compounds which only proceeds under daylight conditions.

b) *Anthropogenic emissions*

One potential source might be the anthropogenic emissions from the bromine production plant of the Dead Sea Works. The factory produces Br₂ by the reaction of Cl₂ with Dead Sea solid extracts. The potential Br₂ contribution of the Dead Sea Works at the measuring

site can be calculated, using basic diffusion equations. For the calculation of an upper-limit impact value the following assumptions were made:

Emission rate of Br₂ to the air of $\leq 0.1 \text{ kg hr}^{-1}$ [*personal communication Dead Sea Works, 1997*] $\approx 1.25 \text{ mol Br}_2 \text{ hr}^{-1} = 2.5 \text{ mol Br hr}^{-1} = 1.5 \times 10^{24} \text{ molec hr}^{-1}$

Wind speed of 3 ms^{-1} and the highest possible atmospheric stability category during midday hours (Pasquill-Gifford category C) [Roedel, 1992]. The turbulent diffusion perpendicular to the propagation ($x = 20 \text{ km}$) is approx. equivalent to the height z of the mixing layer: $\sigma_y = \sigma_z = 1000 \text{ m} = 10^5 \text{ cm}$

Wind flows direct from the plant to the site.

Based on these assumptions, the highest possible mixing ratio of all gaseous bromine compounds at the sampling site can be calculated to be

$$\frac{1.5 \times 10^{24} \text{ molec}}{\sigma_y \cdot \sigma_z \cdot 2 \times 10^6 \text{ cm}} = 7.5 \times 10^7 \text{ molec cm}^{-3} \approx 3 \text{ ppt} . \quad \text{Equ 53}$$

This upper limit of 3 ppt is by more than one order of magnitude lower than the typical daily BrO mixing ratio of 50 to more than 100 ppt observed at the site . The Br₂ possibly emitted by the Dead Sea Works plant can therefore not explain these large BrO mixing ratios.

c) *Indication of a Natural Bromine Source During Southerly Winds*

Figure 4.69 shows a brief pollution episode with sharp increase of the SO₂ and NO₂ levels at 13.30. The pollution peak is most probably related to emissions from the Dead Sea Works factory, located approx. 20 km south of the measuring site (see e.g. the cross section in the upper panel of Figure 4.72). It is obvious from Figure 4.69 that the pollution episode lasted for not more than 30 minutes, which is much shorter than the BrO-O₃ event which continued for about 5 hours. The pollution peak must therefore be associated with the emissions of a relatively small source, e.g. a single point source. By comparison the BrO emissions are supposed to be associated with release from an event of much longer extension or can, which is most likely, be associated with an area of large extent and therefore a natural source of re-Br. Another exemplary day of complete ozone depletion, elevated BrO and a sharp industrial emission peak, especially of SO₂, is June 11, 1997, shown in Figure 4.71.

In general, the NO_x levels of one to a few ppb measured during periods of high BrO mixing ratios are uncertain because of the possible cross sensitivity to BrONO₂ and BrONO of the NO_x monitor, as mentioned above (see section 4.5). The model calculations discussed below show indeed that about 0.5 - 1 ppb of NO_x is converted to BrONO₂ while the air is travelling to the site. Therefore the NO_x level in the course of BrO-events may partly be overestimated due to BrONO₂.

d) *Indication of a Natural Bromine Source During Northerly Winds*

Figure 4.70 shows the time series of several species of June 1, an example of one of the few days on which the shift of the wind direction did not occur and the northerly airflow continued throughout the entire day. Elevated BrO mixing ratios of up to 57 ppt and a limited O₃ depletion event were observed.

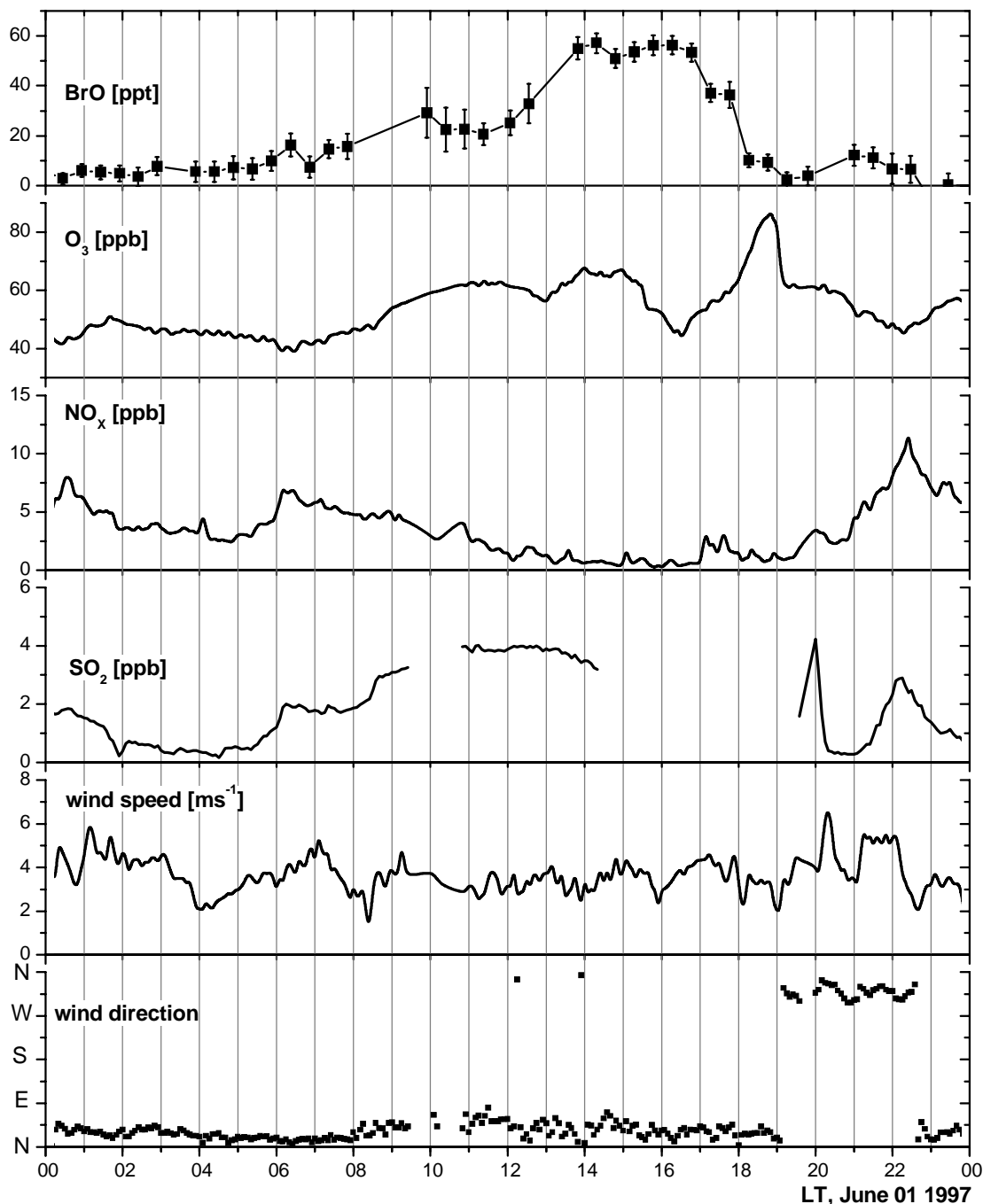


Figure 4.70 *Mixing ratios of BrO, O₃, SO₂ and NO₂, as well as wind speed and direction of June 1, 1997, one of only a few days with constant northerly flows.*

This midday BrO peak, even if the increase in concentration shown in Figure 4.70 is less steep, is evident, although lower than on most of the days with southerly wind directions. The pollution levels (SO₂, NO₂, NO) were moderate, again eliminating the possibility of

associating the O₃ depletion with anthropogenic sources. However, starting from its background (and detection limit) levels of 5 – 10 ppt, BrO rose to values of 50 – 60 ppt.

It is important to stress again that there is no anthropogenic source of re-Br north of the site. The observation of elevated BrO mixing ratios on June 11 under conditions of straight northerly flows therefore confirms the daily recurring BrO events as a natural and not a man-made phenomenon.

To sum up: three different indications for a natural bromine source have been found:

- BrO events have been observed under both northerly and southerly wind flows.
- The shape of the BrO peaks indicates a wide-spread source region.
- The small emissions of the Dead Sea Works factory cannot explain the large amount of BrO detected at the site.

4.6.4 Modelled Description of the BrO and O₃ Observations of DS 97

To analyse the chemical processes taking place in the Dead Sea Valley a photochemical box model with the basic reactions describing boundary-layer ozone chemistry was developed [Stutz *et al.*, 1999]. In the following two different model runs will be interpreted to analyse the measurements represented above. The typical situation observed at the site, which the model tries to describe, is represented in Figure 4.71. The model includes the pertinent O₃, NO_x and HO_x reactions. In the cases discussed here it was assumed that methane at a mixing ratio of 1.75 ppm was the only relevant organic species, CO at a level of 130 ppb was included in the model as well. The rate constants for the reactions were taken from the review of Atkinson *et al.* [1997], while the photolysis frequencies were calculated on the basis of the radiation transport model STAR [Ruggaber and Dlugi, 1994].

The rate constants of the bromine-containing reactions applied are given in the appendix. For more details concerning the model refer to Stutz *et al.* [1999]. The primary aim of the model run was to estimate the amount of total bromine released into the gas phase. In a simple trajectory model of a time frame of 3 hours, which is the typical travelling time of the air masses from the salt pans to the site assuming a WS of 2 ms⁻¹, the solar zenith angle (SZA) and the temperature were held constant at 10° and 320 K respectively. Small NO_x emissions but no mixing and deposition of the main trace gases were included. Since iodine species were neither expected nor measured and no measurements of chlorine oxides existed, only bromine chemistry was considered.

Figure 4.72 shows a scheme of the local topography and two scenarios reproducing the observations of mixing ratios of approximately 100 ppt BrO and the depletion of 50 – 100 ppb O₃ which occurred regularly at the site. Additionally, a small emission of bromine was assumed for the factory (see 4.6.3 b)). Two different release processes were simulated: the release of re-Br via the uptake of oxidising species on salt surfaces and the autocatalytic release following the bromine explosion mechanism described above.

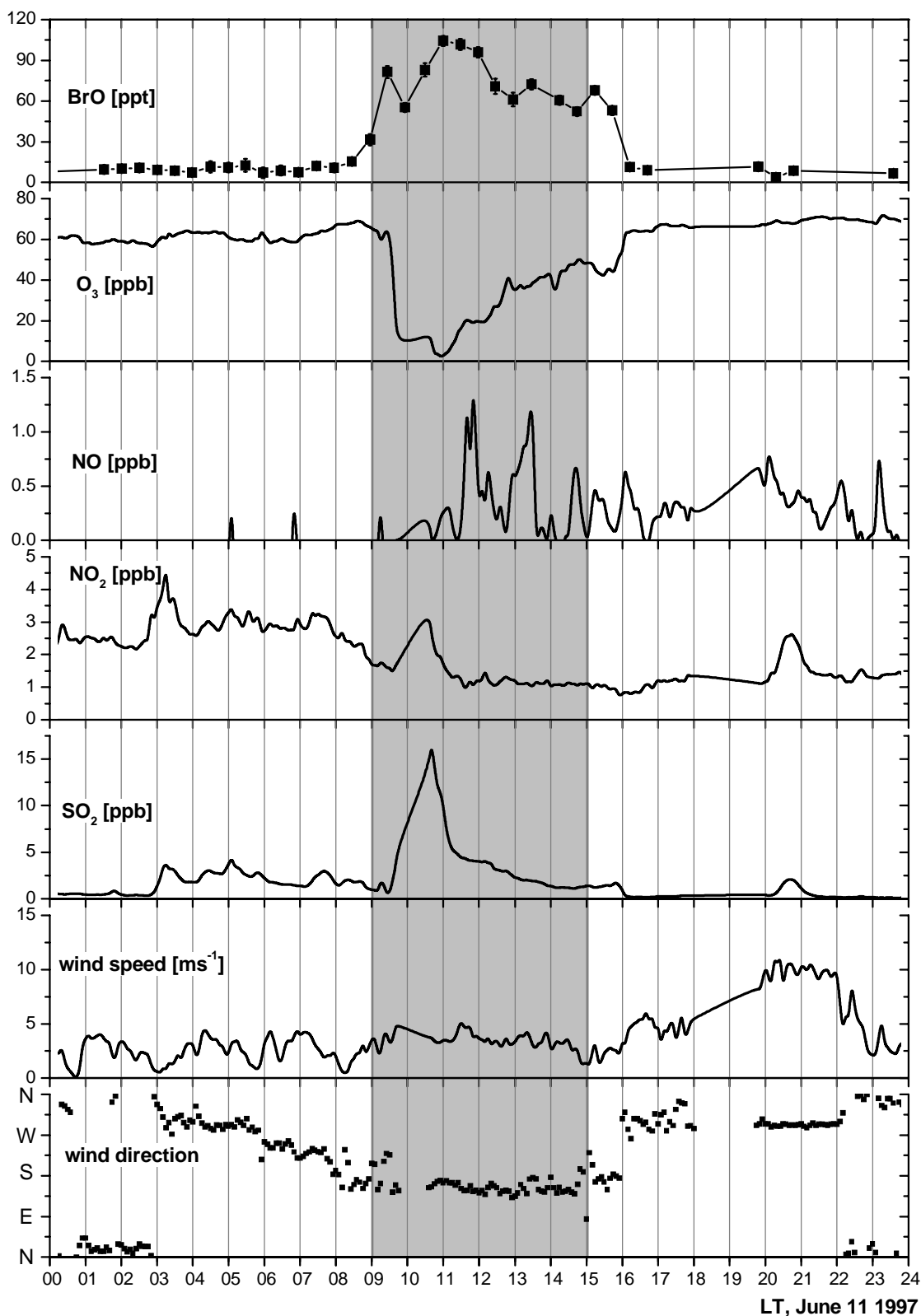


Figure 4.71 Mixing ratios of BrO, O_3 , SO_2 , NO and NO_2 , as well as wind speed and wind direction of June 11, 1997. The shaded area marks southerly flows.

a) *Run A: Re-Br Release via Oxidising Species*

Figure 4.72A shows the release of bromine via the uptake of oxidising species on the salt of the pans, followed by the release of bromine containing compounds from the salt

surface. As the kind and concentration of this species are unknown, this process was parameterised by a constant release of Br_2 over the salt pans. A Br_2 emission of $2 \times 10^7 \text{ molec s}^{-1} \text{ cm}^{-2}$ had to be assumed to explain the typical daily observations made at the site. In this case, no bromine release from the DS water was considered. The centre panel shows the change of total bromine, BrO and O_3 . Total bromine reaches a maximum mixing ratio of 4 ppb, leading to a maximum BrO level of 0.5 ppb. Only such high concentrations can destroy ozone during the relatively short travelling time (2 - 3 hours) to the site.

b) Run B: Autocatalytic re-Br release (Bromine Explosion)

Figure 4.72B shows a scenario describing an autocatalytic release of re-Br via the uptake of HOBr on salt surfaces following the bromine explosion mechanism described above (R27). The uptake of HOBr on the surface was assumed to be $\tau_{\text{HOBr}(g \rightarrow s)} = 3.8 \times 10^{-2} \text{ s}^{-1}$. In contrast to the cases published so far describing arctic (clean-air) chemistry, the uptake of BrONO_2 has to be considered as well. Bromine nitrate is assumed to be hydrolysed to HOBr in the liquid layer on the salt surface with $\tau_{\text{BrONO}_2(g) \rightarrow \text{HOBr}(s)} = 3.4 \times 10^{-3} \text{ s}^{-1}$ [Atkinson *et al.*, 1997]. These reactions would effectively result in an instantaneous release of Br_2 from the surface in line with laboratory data suggesting a very fast liquid-phase chemistry with $\tau_{\text{HOBr}(s) \rightarrow \text{Br}_2(g)} = 1 \text{ s}^{-1}$. Small amounts of bromine compounds could trigger the autocatalytic process. In this case, a small emission of re-Br from the Dead Sea Works was assumed. However, the photolysis of bromocarbons could trigger the reaction chain as well. The release is supposed to continue over the DS water, which is highly enriched with salt and bromine and, as discussed above, characterised by a pH of 6 – 6.35. Thus, in contrast to conditions found at oceanic or Mediterranean sites, where the typical pH value is of the order of 8.2, a bromine release via the bromine explosion mechanism may occur. It starts at the salt pans and continues up to the site. An exponential increase of total bromine and BrO is observed, peaking at 2 ppb and 0.8 ppb at a distance of some kilometres south of the site. At the beginning of the calculation, at a distance of 20 km from the site, no influence on O_3 is noticeable. Right after reaching the maximum bromine mixing ratio, O_3 decreases quickly.

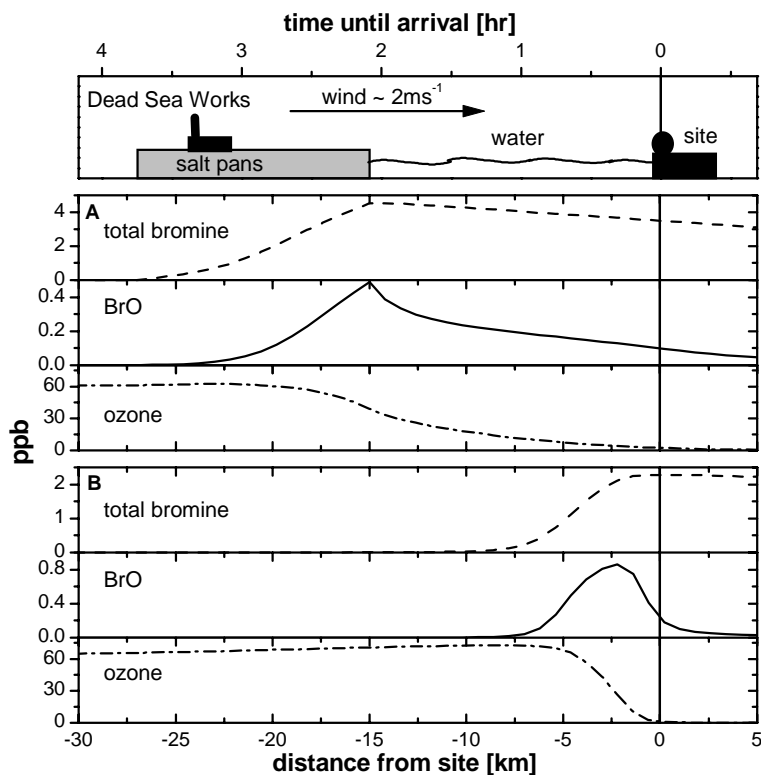


Figure 4.72 Model results of two different attempts to model the BrO - O₃ interaction according to conditions at the Dead Sea and to the local topography (upper panel) A: results assuming a constant release of 2×10^7 molec Br₂ s⁻¹ cm² from the salt pans. B: Autocatalytic release process from the salt pans and from the Dead Sea water. For further explanation see text.

c) Discussion and Comparison of the Different Processes

The smaller mixing ratio of total bromine in the autocatalytic release case (B) compared to the constant release case (A) can be explained by the fast rise in the BrO mixing ratio: less BrO is converted to HOBr and BrONO₂ until the BrO maximum is reached; after that the ozone is totally depleted. The release of bromine must have taken place close to the measurement site, since, assuming the exponential increase in the total bromine concentration, the ozone is destroyed very fast. As can be seen from the lowermost panel of Figure 4.72B, the O₃ mixing ratio drops from more than 60 ppb to zero over the last 5 kilometres, i.e. within less than one hour, assuming a WS of ~ 2 ms⁻¹. Therefore also BrO disappears quickly, because finally the availability of O₃ is the limiting factor of the bromine explosion, as discussed above.

In both cases the main destruction is driven by the BrO self-reaction. Both model runs present lower limits for the required total bromine and BrO mixing ratio, as the mixing of air (from above) with additional O₃ is not included in the model. This assumption is justifiable as the typical time scale of a significant vertical exchange is of the order of half a day, while the total ozone depletion occurs of the order of hours or even faster. An additional uncertainty is the possible presence of chlorine and iodine which cannot be ruled out by the measurements. This would result in a considerably faster O₃ destruction due to

XO + BrO reactions. Less bromine would therefore be required to explain the field observations.

Unfortunately, the measurements show no evidence for neither of the modelled release mechanisms. The behaviour of the BrO and ozone mixing ratios during the transport from the salt pans to the site is characteristic of the individual release process. It should therefore be possible to determine the release mechanism by measuring the O₃ and/or BrO mixing ratios at different locations between the site and the salt pans simultaneously, as is planned for the campaign of summer 2001. The 2 model runs are summarised in Table 4.15.

Table 4.15: Comparison of the two model runs.

Aim: 100 ppt of BrO detected at the site destroys 50 - 100 ppb of O₃

Run A	Run B
Release via uptake of oxidising species	Bromine explosion mechanism
Br release from salt pans, not from DS water	Br release from salt pans and water
Parameterised as constant release $2 \times 10^7 \text{ molec s}^{-1} \text{cm}^2$	Uptake of gaseous HOBr on salt surface $\tau \text{ HOBr(g)} \rightarrow \text{HOBr(s)} = 3.8 \times 10^{-2} \text{ s}^{-1}$ $\tau \text{ BrONO}_2(\text{g}) \rightarrow \text{HOBr(s)} = 3.4 \times 10^{-3} \text{ s}^{-1}$ $\tau \text{ HOBr(s)} \rightarrow \text{Br}_2(\text{g}) = 1 \text{ s}^{-1}$
Maximum total bromine = 4 ppb	Maximum total bromine = 2 ppb
Maximum BrO = 0.5 ppb	Maximum BrO = 0.8 ppb

4.6.5 Bromocarbons at the Dead Sea

The last probable source mechanism of halogen compounds at the Dead Sea is the degradation of organohalogenes emitted by biological processes. As discussed in section 5.1, these photolabile species are emitted by algae and can act as precursors of RHS in the troposphere [Carpenter *et al.*, 1999; Schall and Heumann, 1993; Sturges *et al.*, 1992]. In the case discussed here, bromocarbons are supposed to initiate the bromine explosion described above. Many of these species are present in noticeable concentrations, namely methylbromide (CH₃Br), dibromomethane (CH₂Br₂) and bromochloromethane (CHBr₂Cl). Nevertheless, the production rate of Br atoms is small as the photolytic lifetime of most of these compounds is of the order of days or even months (cf. [Yvon and Butler, 1996]).

The results of the organic bromide compounds (CH₃Br, CH₂Br₂ and CHBr₂Cl) yielded from the 94 canister samples are shown in Figure 4.73. The mixing ratio of CH₃Br varied between 10 and 100 ppt, while the CH₂Br₂ and CHBr₂Cl levels were below 10 ppt and 20 ppt respectively. The CH₂Br₂ daytime values were by about 50 % higher than the night-time values, while CH₃Br and CHBr₂Cl showed no diurnal variations.

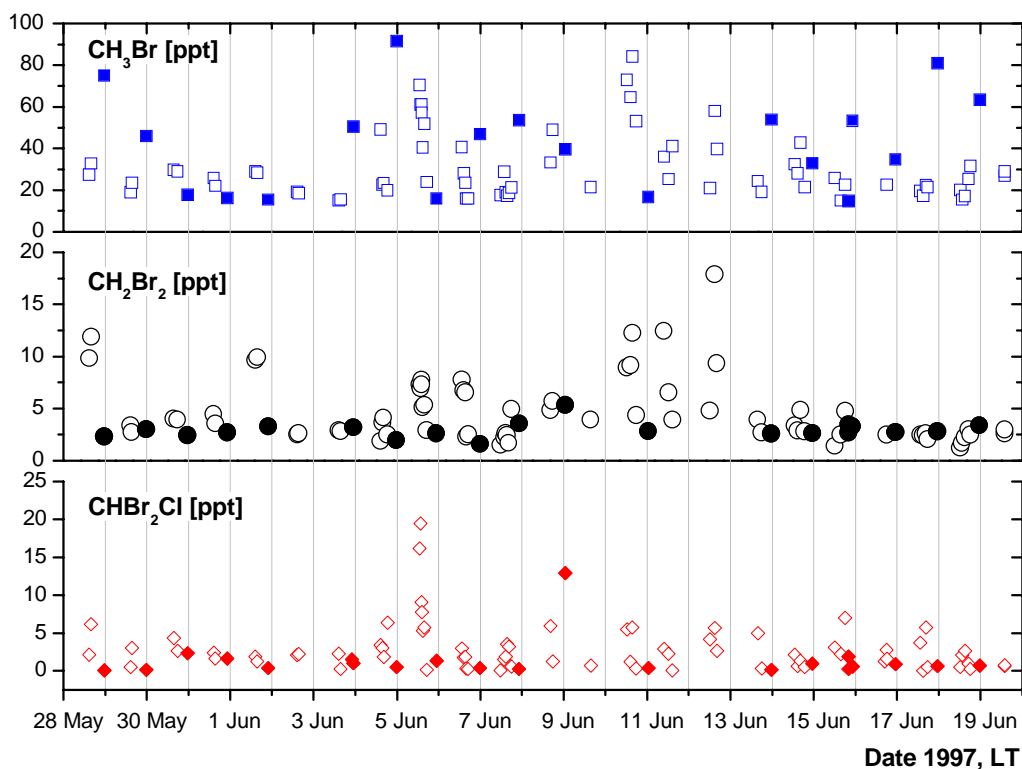


Figure 4.73 Organobromides measured during DS97. Full symbols indicate night-time, open symbols daytime values.

For a more detailed interpretation of the impact of bromocarbon a time series with a better time resolution would be required. However, the data show that a certain amount of organobromides is present at the Dead Sea. Assuming one to a few days as a lower limit of the bromocarbon lifetime and a maximum concentration of 100 ppt, the daily Br production of some ppt cannot explain the BrO concentrations observed, but could trigger the release of re-Br from the salt pans, as mentioned above, although there is no evidence of a distinct diurnal variation.

4.6.6 Total Atmospheric Bromine and Chlorine in the Dead Sea Valley

Between May 23 and June 23, 1997 32 filter samples were taken in the 4 distinct 6-hour sampling intervals 00-06, 06-12, 12-18 and 18-24 LT. The filterable Cl levels of the individual samples ranged from 100 to 1000 ppt, the filterable Br levels from 10 to 60 ppt. With that, the ratio between Br and Cl reflects the relative ratio of these ions in the Dead Sea water (molar ratio of 1:100, compared to a molar ratio of approximately 1:90 observed in the Dead Sea waters [Niemi *et al.*, 1997]). Due to the low time resolution and the limited set of samples (32 filter samples within 4 weeks), which do not represent a complete time series, only the average values of the filterable bromine and chlorine mixing ratios of the respective interval are represented in Figure 4.74, right-hand side. However, from these 4 sampling intervals no diurnal variation in f-Br or f-Cl is visible.

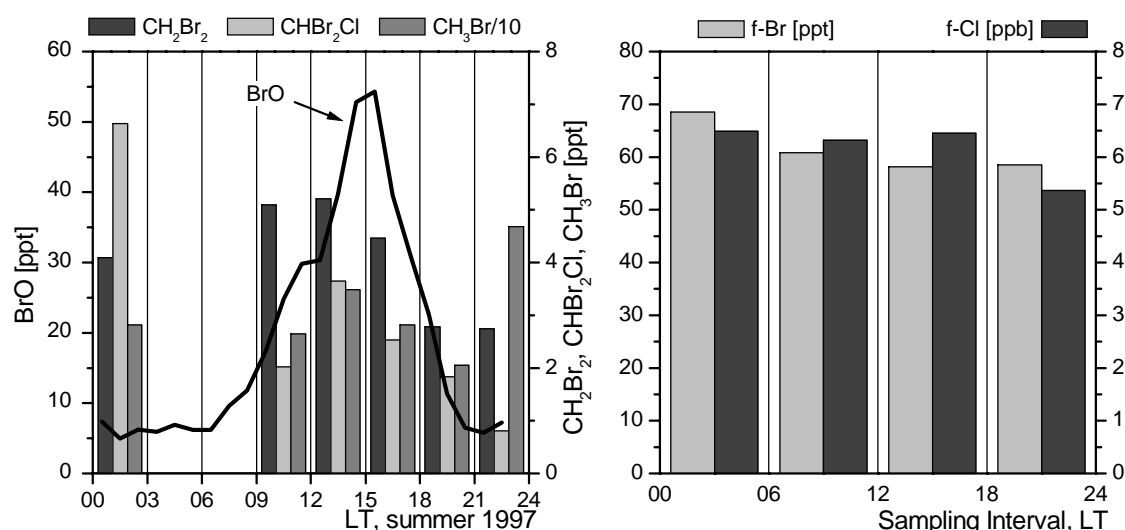


Figure 4.74 Average daily cycle of bromine compounds. Left: Organobromides, measured in 96 canister samples, given as 3-hour average values (CH_3Br scaled down by a factor of 10) and BrO (DOAS, hourly averages). Right: Filterable bromine (left axis, ppt) and chlorine (right axis, ppb) average values of all 32 samples taken during the whole campaign. The individual filters were sampled over 6-hour periods.

The left-hand side of Figure 4.74 shows an overview of the DOAS and canister measurements of bromine species, given as one-hour average in the case of BrO (DOAS) and three-hour average for the bromocarbon measurements. BrO shows a clear diurnal cycle as discussed above, the bromocarbons do not undergo a distinct diurnal variation, even if the noon intervals are slightly elevated compared to the late morning and afternoon values.

In summary, the bromine contents of the aerosol phase (f-Br), bromocarbons (canister) and BrO are all equivalent to 5 to ~100 ppt of the gas-phase Br. Only BrO shows a clear diurnal cycle, while the average levels of aerosol bromides and bromocarbons are essentially unchanged. This may be caused by the limited time resolution of this data set.

4.6.7 Subsequent Air-Plane Study: The Extent of the Ozone Destruction Phenomenon

In a subsequent study related to the DS97 campaign ten O_3 observation flights were carried out from the end of July until the end of August ([Matveev *et al.*, 2001], see Figure 4.75 and Table 4.16). O_3 maximum values over the central parts of Israel were always found to be above 100 ppb, in one case a maximum of more than 240 ppb has been reached. These high values are related to photochemical smog which is typical for central Israel during the summer months. Background levels, outside the urban plume travel path, varied between 45 and 68 ppb. In contrast, over the Dead Sea the O_3 levels were below the detection limit of the instrument (2 ppb) on 7 of the 10 measuring days.

Table 4.16: Summary of the aircraft ozone measurements over the Dead Sea basin. Flights shown in Figure 4.75 are printed in bold type.

Minimum O ₃ [ppb]	Maximum O ₃ [ppb]	Background O ₃ [ppb]	Take-off Time	Landing Time	Date
< 2	156	45	14:06	16:38	21.07.97
60	161	60	13:58	16:03	25.07.97
< 2	132	57	14:41	17:02	31.07.97
< 2	107	50	14:02	16:03	01.08.97
< 2	130	54	14:06	16:06	03.08.97
< 2	161	68	14:05	16:26	07.08.97
< 2	135	61	13:58	16:20	08.08.97
< 2	150	63	13:41	15:53	10.08.97
75	237	65	15:15	17:43	28.08.97
36	188	58	13:41	16:08	29.08.97

Even if the research flights were not performed simultaneously with the surface measurements, they provide information on the regional dimension of the ozone depletion phenomenon. Figure 4.75 shows the estimated distribution of O₃ over central Israel for four out of the ten flights. The Kriging method [Cressie, 1990] with a linear variogram was employed to generate the 2D plots. The first case (July 31, 1997) shows that very low O₃ levels prevail over most of the Dead Sea Valley. In the second case (August 3, 1997) the phenomenon is limited to the southern part, centred over the location of the sampling site of the DS97 campaign. In the third example (August 8, 1997) O₃ is depleted only over the northern part of the Dead Sea, while there is no depletion over the sampling site. In the fourth case (August 28, 1997) no O₃ depletion over the Dead Sea was observed. On that day, one of the more severe smog episodes occurred over Israel. The urban plume from the densely populated metropolitan area of Tel Aviv drifted towards Jerusalem and the Dead Sea. The peak O₃ mixing ratio measured in the plume was almost 240 ppb. It is likely that on that day the anthropogenic pollution may have ‘overwhelmed’ the BrO-catalysed O₃ destruction.

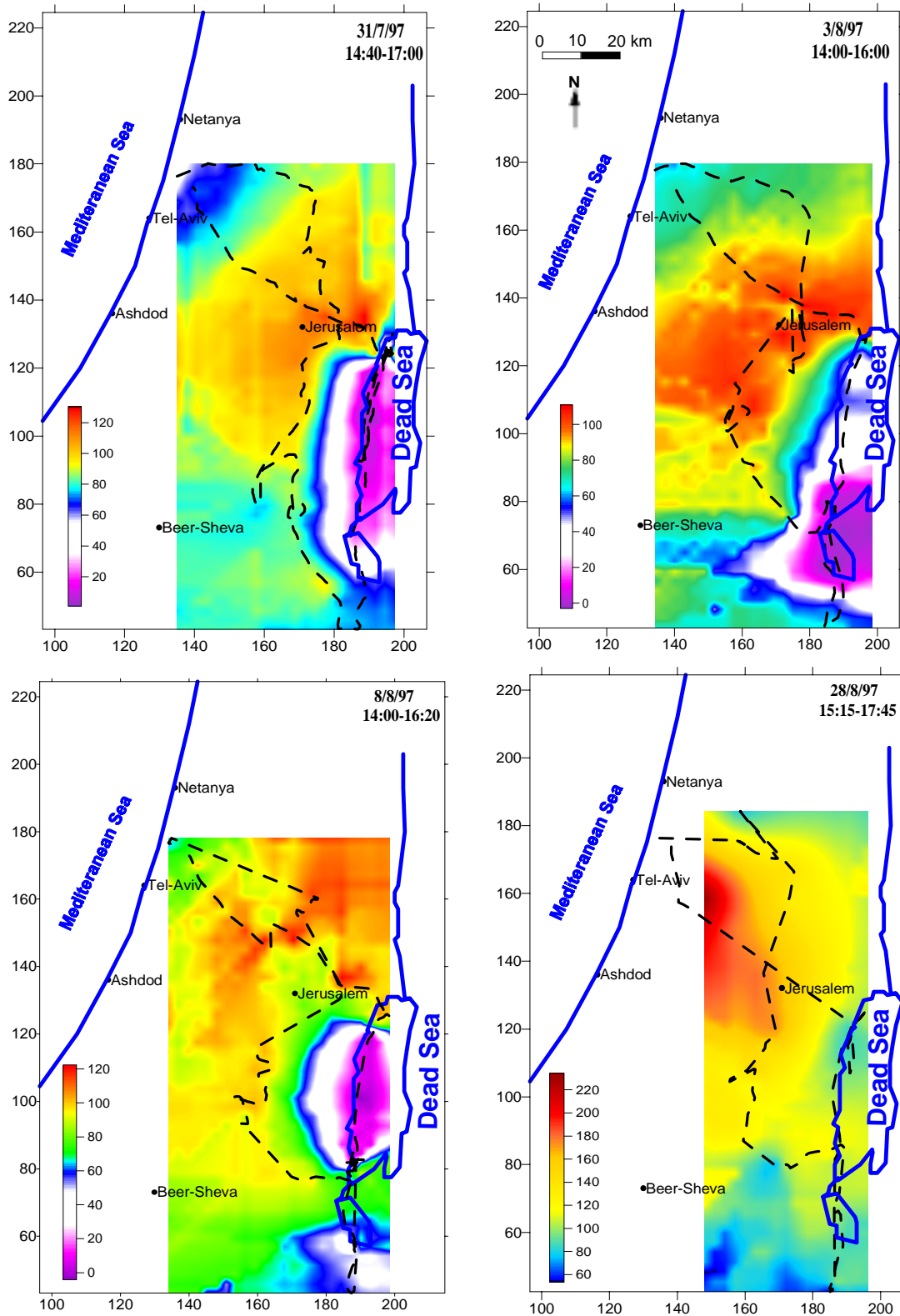


Figure 4.75 Image plots of the O₃ mixing ratios over Israel observed during four sampling flights. Note the O₃ depletion over the Dead Sea Valley on three of the four sampling flights (the white and violet colours) on July 31, August 3 and 8, 1997. The broken line represents the flight path.

Chapter 5

Summary and Outlook

The results of this thesis indicate the importance of halogen chemistry in the mid-latitude planetary boundary layer. It is well-known that reactive halogen species, RHS, play a major role in the chemistry of the polar troposphere. Especially bromine oxide, BrO, is a key species in the ozone depletion events observed during polar sunrise. The so-called 'bromine explosion', the exponential increase in reactive bromine species due to an autocatalytic release of bromine, is relatively well understood today, but there are uncertainties concerning the mechanism inducing this autocatalytic reaction chain. Two possible kick-off mechanisms are presently discussed: the release of RHS from sea salt or the photolysis of short-lived halogenated hydrocarbons.

These two mechanisms are supposed to be the dominant sources of RHS also at mid latitudes, where no halogen oxides had been detected before the measurements relating to this thesis were carried out. Four campaigns have been performed to investigate the influence of RHS at three sites at mid latitudes using the *DOAS (Differential Optical Absorption Spectroscopy)* technique.

During the first campaign at Weybourne, England no halogen oxides could be identified in the spectra, even if some values exceeded the average detection limit of 14 ppt of ClO, 2.6 ppt of BrO and 3 ppt of IO. During the three following campaigns at Mace Head, Ireland in spring 1997 and autumn 1998 and at the Dead Sea, Israel in summer 1997 the detection of IO and BrO succeeded for the first time.

5.1 Mace Head

At Mace Head, a European clean-air site facing the Atlantic Ocean, iodine oxide was observed during both campaigns in spring 1997 and autumn 1998. Short-lived alkyl-iodides released from macroalgae have been identified as the most likely source of reactive

iodine. While in 1997 IO mixing ratios of up to 6.4 ppt were observed during clean-air westerly flows only, in 1998 mixing ratios of more than 7 ppt were detected under conditions of more than 2 ppb NO₂, indicating the importance of iodine nitrate, IONO₂, as a significant reservoir species of the atmospheric iodine cycle.

During the 1998 campaign the average daily variations of the IO mixing ratio were well correlated with the average diurnal solar cycle. Significantly elevated values of IO were observed during low tide, underlining the dependence of the iodocarbon emissions on this parameter as well.

Model calculations show that even a few ppt of IO can have a significant influence on tropospheric chemistry, not only by destroying ozone, but also by altering the photochemistry of the air mass. In particular, a possibly considerable change in the OH concentration and the reduction of ozone production should be a matter of concern. It was found that the importance of IO concerning the ozone destruction is of the order of some 10th of a ppt h⁻¹, which is comparable to conservative O₃ loss processes, e.g. the deposition of O₃. However, the rate of ozone destruction is too small to be noticeable in ozone mixing ratios within the time frame of our measurements, even if our model indicates that at low IO mixing ratios of ~ 0.6 ppt the ozone loss due to iodine chemistry would still constitute 10 – 20 % of the total ozone loss in the PBL.

Furthermore, the detection of OIO in the atmosphere, one of the products of the IO self-reaction, succeeded for the first time. This species is supposed to be one of the major gas-phase reservoirs under conditions of low NO_x. The lifetime of OIO could be determined to be of the order of 10 to 20 minutes, depending on the NO_x level.

Nevertheless, it is still unclear how and how fast the iodine will be removed from the atmosphere. There remains a lot of uncertainty about the temporal and spatial occurrence of reactive iodine, even if measurements by other groups performed on Tenerife and in Tasmania indicate that measurable amounts of IO are widely spread in coastal regions. It is unclear whether a mixing ratio of 8 ppt is a maximum value or whether higher mixing ratios may occur, while 0.6 ppt are below the average detection limit of the instruments. A constant ambient mixing ratio of this size would therefore escape detection.

During the measurements at Mace Head neither ClO (1997) nor BrO (1997 and 1998) could be identified in the spectra, even if some single values exceeded the average detection limits of 34 ppt and ~1.7 ppt (1997) and 2.5 ppt (1998) respectively.

5.2 Dead Sea

High levels of BrO (up to 176 ppt, the highest concentration ever found anywhere in the atmosphere) were observed over the Dead Sea in Israel. These high BrO levels during midday/early afternoon hours coincide with a parallel decrease in the O₃ concentration, frequently to below the detection limit of 2 ppb. Although there are some recent reports of indirect evidence of O₃ destruction by halogens at mid latitudes [Nagao *et al.*, 1999], the present study represents the first observation of its kind at a location outside the polar

regions. Airborne measurements of O₃ levels have shown that the midday O₃ depletion covers large areas over the Dead Sea valley.

The possibility of an anthropogenic release of bromine from the Dead Sea Works, located at the southern shore of the Dead Sea, was examined and ruled out. Modelling investigations could give no definitive answer concerning the halogen release mechanisms at the Dead Sea. To explain the very fast ozone depletion observed, BrO peak mixing ratios of 0.5 to 0.8 ppb are necessary. Depending on the assumed source mechanism, 4 and 2 ppb of total bromine, probably mostly in the form of BrONO₂, are required. Future experiments at the Dead Sea are expected to define the heterogeneous release processes taking place there.

Due to its stable and periodically recurring meteorological conditions the Dead Sea region appears to be an excellent natural laboratory for the further investigation of halogen chemistry. The model considerations are helpful for setting up future experiments aimed at clarifying the observed phenomenon.

5.3 Outlook

In recent years a number of campaigns were carried out at different non-polar sites in order to investigate the influence of halogen oxides in the mid-latitudinal boundary layer. The detection of iodine oxide succeeded in Tasmania and on Tenerife [*Allan et al.*, 2000; *McFiggans et al.*, 2000].

At the Dead Sea an extensive field campaign is planned for the summer 2001. The questions we hope to answer are related to the heterogeneous release processes of RHS from (sea) salt. The difficulties in interpreting the recorded field data, which are caused by transport phenomena, are likely to be ruled out by a more comprehensive set of measurements. The set-up of, at least, three DOAS systems along the Dead Sea valley is planned. By measuring BrO above the salt pans we hope to identify whether or not there is a night-time release of RHS – leading to a BrO peak during sunrise right above the source. In addition, the other halogen oxides besides BrO should be investigated as well.

Wagner [1999] reported elevated levels of BrO at the Caspian Sea via satellite observations and *Stutz and Ackermann* [2000] detected noticeable levels of BrO at Salt Lake City. These investigations indicate that the observations made at the Dead Sea are probably an extreme, but not a unique phenomenon.

Chapter 6

References

- Abbatt, J.P.D., Heterogeneous reactions of HOBr with HBr and HCl on ice surfaces at 228 K, *Geophysical Research Letters*, 21 (8), 665-668, 1994.
- Abbatt, J.P.D., Interactions of HBr, HCl, and HOBr with supercooled sulfuric acid solutions of stratospheric composition, *Journal of Geophysical Research*, 100, 14009-14017, 1995.
- Abbatt, J.P.D., and J.B. Nowak, Heterogeneous interactions of HBr and HOCl with cold sulfuric acid solutions: Implications for Arctic boundary layer bromine chemistry, *Journal of Physical Chemistry*, 101, 2131-2137, 1997.
- Ackermann, R., Messungen von Iodoxid und Quecksilber in der Atmosphäre, Diploma thesis, Ruprecht Karls Universität zu Heidelberg, Heidelberg, 1997.
- Alicke, B., Messungen von troposphärischen Halogenoxidradikalen in mittleren Breiten, Diploma thesis, Ruprecht Karls Universität Heidelberg, Heidelberg, 1997.
- Alicke, B., K. Hebestreit, J. Stutz, and U. Platt, Iodine oxide in the marine boundary layer, *Nature*, 397, 572-573, 1999.
- Allan, B., G. McFiggans, J.M.C. Plane, and H. Coe, Observation of iodine monoxide in the remote marine boundary layer, *Journal of Geophysical Research*, in press, 2000.
- Aranda, A., G.L. Bras, G.L. Verdet, and G. Poulet, The BrO + CH₃O₂ reaction: kinetics and role in the atmospheric ozone budget, *Geophysical Research Letters*, 24, 2745-2748, 1997.
- Atkinson, R., D.L. Baulch, R.A. Cox, R.F. Hampson, J.A. Kerr, M.J. Rossi, and J. Troe, Evaluated kinetic, photochemical and heterogeneous data for atmospheric chemistry: supplement V, IUPAC Subcommittee on gas kinetic data evaluation for atmospheric chemistry, *Journal of Physical and Chemical Reference Data*, 26 (3), 521-1012, 1997.
- Barnes, I., K.H. Becker, and J. Starcke, Fourier-Transform IR spectroscopic observation of gaseous nitrosyl iodine, nitryl iodine, and iodine nitrate, *Journal of Physical Chemistry*, 95, 9736-9740, 1991.
- Barrie, L.A., J.W. Bottenheim, R.C. Schnell, P.J. Crutzen, and R.A. Rasmussen, Ozone destruction and photochemical reactions at polar sunrise in the lower Arctic atmosphere, *Nature*, 334, 138-141, 1988.
- Barrie, L.A., and U. Platt, Arctic tropospheric chemistry: an overview, *Tellus*, 49B (5), 450-454, 1997.
- Bass, A.M., and R.J. Paur, The Ultraviolet Cross-Section of Ozone: I. The Measurements / Atmospheric Ozone, in *Quadrennial Ozone Symposium 1984*, edited by C. Zerefos, and A. Ghazi, pp. 606-616, Reidel, D., Dodrecht, Boston, Lancaster, 1984.
- Bauer, D., T. Ingham, P. Campuzano-Jost, S.A. Carl, G.K. Moortgat, and J.N. Crowley, Gas-phase kinetics and photochemistry of bromine and iodine containing species in the marine boundary layer, *Annual Geophysical Supplement II*, 2 (C716), 1998a.
- Bauer, D., T. Ingham, S.A. Carl, S.M. Moortgat, and J.N. Crowley, Ultraviolet - Visible Absorption Cross Sections of Gaseous HOI and Its Photolysis at 355 nm, *Journal of Physical Chemistry A*, 102, 2857-2864, 1998b.

- Bedjanian, Y., G. LeBras, and P. G., Kinetics and Mechanism of the IO + ClO Reaction, *Journal of Physical Chemistry*, *101* (A), 4088-4096, 1997.
- Bedjanian, Y., G. LeBras, and G. Poulet, Kinetics and Mechanism of of the IO + BrO Reaction, *Journal of Physical Chemistry*, 1998a.
- Bedjanian, Y., G. Poulet, and G. LeBras, Low pressure study of the reaction of Br atoms with alkenes: reaction with propene., *Journal of Physical Chemistry*, *102*, 5867-5875, 1998b.
- Behnke, W., M. Elend, U. Krüger, and C. Zetzsch, The Influence of NaBr/NaCl Ratio on the Br--Catalysed Production of Halogenated Radicals, *Journal of Atmospheric Chemistry*, *34*, 87-99, 1999.
- Blake, N.J., D.R. Blake, O.W. Wingenter, B.C. Sive, L.M. McKenzie, J.P. Lopez, I.J. Simson, H.E. Fuelber, G.W. Sachse, B. Anderson, E., G.L. Gregory, M.A. Carroll, G.M. Albercook, and F.S. Rowland, Influence of southern hemispheric biomass burning on mid-tropospheric distributions of nonmethane hydrocarbons and selected halocarbons over the remote South Pacific, *Journal of Geophysical Research*, *104* (16), 16,213-16,232, 1999.
- Bloss, W.J., D.M. Rowley, R.A. Cox, and R.L. Jones, Kinetic and photochemical studies of iodine oxide chemistry, *Annual Geophysical Supplement II*, *16* (C717), 1998.
- Bottenheim, J.W., A.C. Gallant, and K.A. Brice, Measurements of NO_y species and O₃ at 82°N latitude, *Geophysical Research Letters*, *13*, 113-116, 1986.
- Brauers, T., M. Hausmann, U. Brandenburger, and H.-P. Dorn, Improvement of Differential Optical Absorption Spectroscopy with a multichannel scanning technique, *Applied Optics*, *34*, 4472-4479, 1995.
- Brown, A.C., C.E. Canosa-Mas, and R.P. Wayne, A Kinetic Study of the Reactions of OH with CH₃I and CF₃I, *Atmospheric Environment*, *24A*, 361-367, 1990.
- Carpenter, L.J., G. Malin, F. Kuepper, and P.S. Liss, Novel biogenic iodine containing trihalomethanes and other short lived halocarbons in the coastal East Atlantic, *Global Biogeochemical Cycles*, *14*, 1191-1204, 2000.
- Carpenter, L.J., P.S. Monks, B.J. Bandy, S.A. Penkett, I.E. Galbally, and C.P. Meyer, A study of peroxy radicals and ozone photochemistry at coastal sites in the northern and southern hemispheres, *Journal of Geophysical Research*, *102*, 25417-25427, 1997.
- Carpenter, L.J., W.T. Sturges, S.A. Penkett, P.S. Liss, B. Alicke, K. Hebestreit, and U. Platt, Short-lived alkyl iodides and bromides at Mace Head, Ireland: Links to biogenic sources and halogen oxide production, *Journal of Geophysical Research*, *104* (D1), 1691-1698, 1999.
- Chameides, W.L., and D.D. Davis, Iodine: Its possible role in tropospheric photochemistry, *Journal of Geophysical Research*, *85*, 7383-7398, 1980.
- Chatfield, R., and P. Crutzen, Are there interactions of iodine and sulfur species in marine air photochemistry ?, *J. Geophys. Res.*, *95* (D13), 22,319-22,341, 1990.
- Cox, R.A., W.J. Bloss, R.L. Jones, and D.M. Rowley, OIO and the Atmospheric Cycle of Iodine, *Geophysical Research Letters*, *26* (13), 1857-1860, 1999.
- Cressie, N.A.C., The Origins of Kiriging, *Mathematical Geology*, *22*, 239-252, 1990.
- Crutzen, P.J., and F. Arnold, Nitric acid cloud formation in the cold Antarctic stratosphere: a major cause for the springtime 'ozone hole', *Nature*, *324*, 651-655, 1986.
- Czerny, M., and A. Turner, *Z. Physik*, *61*, 792, 1930.
- Davis, D., J. Crawford, S. Liu, S. McKeen, A. Bandy, D. Thornton, F. Rowland, and D. Blake, Potential impact of iodine on tropospheric levels of ozone and other critical oxidants, *Journal of Geophysical Research*, *101*, 2135-2147, 1996.
- DeMore, W.B., S.P. Sander, D.M. Golden, R.F. Hampson, M.J. Kurylo, C.J. Howard, A.R. Ravishankara, C.E. Colc, and M.J. Molina, *Chemical kinetics and photochemical data for use in stratospheric modeling*, 1997.
- Fan, S.-M., and D.J. Jacob, Surface ozone depletion in Arctic spring sustained by bromine reactions on aerosols, *Nature*, *359*, 522-524, 1992.
- Farman, J.C., B.G. Gardiner, and J.D. Shanklin, Large losses of total ozone in Antarctica reveal seasonal ClO_x/NO_x interaction, *Nature*, *315*, 207-210, 1985.
- Ferlemann, F., Ballongestützte Messung stratosphärischer Spurengase mit differentieller optischer Absorptionsspektroskopie., PhD thesis, Heidelberg, 1998.
- Fickert, S., J.W. Adams, and J.N. Crowley, Activation of Br₂ and BrCl via uptake of HOBr onto aqueous salt solutions, *Journal of Geophysical Research*, submitted, 1999.
- Finlayson-Pitts, B.J., M.J. Ezell, and J.N. Pitts, Formation of chemically active chlorine compounds by reactions of atmospheric NaCl particles with gaseous N₂O₅ and ClONO₂, *Nature*, *337*, 241-244, 1989.
- Finlayson-Pitts, B.J., F.E. Livingston, and H.N. Berko, Ozone destruction and bromine photochemistry at ground level in the Arctic spring, *Nature*, *343*, 622-625, 1990.

- Fitzenberger, R., H. Bösch, C. Camy-Peyret, M. Chipperfield, H. Harder, U. Platt, B.-M. Sinnhuber, T. Wagner, and K. Pfeilsticker, First profile measurement of tropospheric BrO, *Geophysical Research Letters*, 27, 2921-2924, 2000.
- Forte, E., H. Hippler, and H. Van Den Bergh, INO thermodynamic properties and ultraviolet spectrum, *Int. J. Chem. Kinet.*, 13, 1227 - 1233, 1981.
- Fries, U., M.P. Chipperfield, H. Harder, C. Otten, P. U., J. Pyle, T. Wagner, and K. Pfeilsticker, Inter-comparison of Measurements and Modelled BrO Slant Column Amounts for the Arctic Winter and Spring 1994/95, *Geophysical Research Letters*, 26 (13), 1861-1864, 1999.
- Fuchs, N.A., A.G. Sutugin, H. Chemie, Aerosol, and Mathematische Methoden, *High dispersed aerosols*, 1-60 pp., N. Y., 1971.
- Garcia, R.R., and S. Solomon, A new numerical model of the middle atmosphere, 2, Ozone and related species, *J. Geophys. Res.*, 99 (D6), 12,937-12,952, 1994.
- Gavrieli, I., O. Katz, R. Weinstein, and D.A. Anati, A plume of end brines in the transition layer of the southern Dead Sea, pp. 31, Geological Survey of Israel, Jerusalem, Israel, 1994.
- Gershenzon, M.Y., S. Il'in, N.G. Fedetov, and Y.M. Gershenzon, The mechanism of reactive NO₃ uptake on dry NaX (X = Cl, Br), *Journal of Atmospheric Chemistry*, 34, 119-135, 1999.
- Geyer, A., The Role of the Nitrate Radical in the Boundary Layer, Observations and Modeling Studies, Dissertation thesis, Ruprecht Karls Universität Heidelberg, Heidelberg, 2000.
- Gilles, M.K., A.A. Turnipseed, J.B. Burkholder, A.R. Ravishankara, and S. Solomon, Kinetics of the IO Radical. 2. Reaction of IO with BrO, *Journal of Physical Chemistry, A* 101, 853-863, 1997.
- Gomer, T., T. Brauers, F. Heintz, J. Stutz, and U. Platt, MFC (version 1.98) user manual, Institut für Umweltphysik der Universität Heidelberg., Heidelberg, 1993.
- Harder, H., C. Camy-Peyret, F. Ferlemann, R. Fitzenberger, T. Hawat, H. Osterkamp, M. Schneider, D. Perner, U. Platt, P. Vradelis, and K. Pfeilsticker, Stratospheric BrO profiles measured at different latitudes and seasons: Atmospheric observations, *Geophysical Research Letters*, 25, 3843-3846, 1998.
- Harder, J.W., J.W. Brault, P.V. Johnston, and G.H. Mount, Temperature dependent NO₂ cross sections at high spectral resolution, *Journal of Geophysical Research*, 102, 3861-3879, 1997.
- Harwood, M., J. Burkholder, M. Hunter, R. Fox, and A. Ravishankara, Absorption Cross Section and Self-Reaction Kinetics of the IO Radical, *Journal of Physical Chemistry, A* (101), 853-863, 1997.
- Hausmann, M., and U. Platt, Spectroscopic measurement of bromine oxide and ozone in the high Arctic during Polar Sunrise Experiment 1992, *Journal of Geophysical Research*, 99 (25), 399-413, 1994.
- Hebestreit, K., J. Stutz, D. Rosen, V. Matveiv, M. Peleg, M. Luria, and U. Platt, First DOAS Measurements of Tropospheric Bromine Oxide in Mid Latitudes, *Science*, 283, 55-57, 1999.
- Heintz, F., U. Platt, H. Flentje, and R. Dubois, Long-term observation of nitrate radicals at the Tor Starion, Kap Arkona (Rügen), *Journal of Geophysical Research*, 101 (D17), 22891-22910, 1996.
- Hermes, T., Lichtquellen und Optik für die Differentielle Optische Absorptionsspektroskopie, Diploma thesis, Ruprecht Karls Universität Heidelberg, Heidelberg, 1999.
- Himmelmann, S., J. Orphal, H. Bovensmann, A. Richter, A. Ladstätter-Weissenmayer, and J.P. Burrows, First observation of the OIO molecule by time-resolved flash photolysis absorption spectroscopy, *Chemical Physial Letters*, 251, 330-334, 1996.
- HITRAN, HITRAN database 1986 edition, *Applied Optics*, 26 (4058-4097), 1987.
- Holland, H.D., *The chemistry of the atmosphere and oceans*, 351 pp., John Wiley & Sons, New York, 1978.
- Hönninger, G., Referenzspektren reaktiver Halogenverbindungen für DOAS Messungen, Diploma thesis, Ruprecht Karls Universität Heidelberg, Heidelberg, 1999.
- Ingham, T., M. Cameron, and J.N. Crowley, Photodissociation of IO (355 nm) and OIO (532 nm): Quantum Yield for O(³P)/I Production, *in preparation*, 2000.
- Jenkin, M.E., The photochemistry of iodine- containing compounds in the marine boundary layer, *AEA Report, EE-0405*, 1992.
- Jenkin, M.E., R.A. Cox, and D.E. Candeland, Photochemical aspects of tropospheric iodine behaviour, *Journal of Atmospheric Chemistry*, 2, 359-375, 1985.
- Kah, O., Spektroskopische Langzeitmessungen von NO₂, SO₂, O₃, HCHO und HONO in Heidelberg., Diploma thesis, Ruprecht Karls Universität Heidelberg, Heidelberg, 1998.
- Kirchner, U., T. Benter, and R.N. Schindler, Experimental verification of gas phase bromine enrichment in reactions of HOBr with sea salt doped ice surfaces, *Berichte der Bunsengesellschaft für Physikalische Chemie*, 101, 975-977, 1997.
- Klick, S., and K. Abrahamsson, Biogenic volatile iodated hydrocarbons in the ocean, *Journal of Geophysical Research*, 97 (C8), 12,683-12,687, 1992.
- Knoll, P., R. Singer, and W. Kiefer, Improving spectroscopic techniques by a scanning multi channel technique, *Applied Spectroscopy*, 44, 776-782, 1990.
- Kreher, K., P.V. Johnston, S.W. Wood, B. Nardi, and U. Platt, Ground-based measurements of tropospheric and stratospheric BrO at Arrival Heights (78°S), Antarctica, *Geophysical Research Letters*, 1997.

- Kurucz, R.L., I. Furenlid, J. Brault, and L. Testerman, *Solar flux atlas from 296 to 1300 nm.*, National Solar Observatory, Sunspot, New Mexico, U.S.A., 1984.
- Lazlo, B., R.E. Huie, M.J. Kurylo, and A.W. Miziolek, Kinetic studies of the reactions of BrO and IO radicals, *Journal of Geophysical Research*, *102*, 1523-1532, 1997.
- Lazlo, B., M.J. Kurylo, and R.E. Huie, Absorption Cross Sections, Kinetics of Formation, and Self-Reaction of the IO Radicals Produced via Laser Photolysis of N₂O/I₂/N₂ Mixtures, *Journal of Physical Chemistry*, *99*, 11701-11707, 1995.
- LeBras, G., and U. Platt, A possible mechanism for combined chlorine and bromine catalyzed destruction of tropospheric ozone in the Arctic, *Geophysical Research Letters*, *22* (5), 599-602, 1995.
- Lehrer, E., Polar tropospheric ozone loss, Dissertation thesis, Ruprecht Karls Universität Heidelberg, Heidelberg, 2000.
- Lehrer, E., D. Wagenbach, and U. Platt, Aerosol chemical composition during tropospheric ozone depletion at Ny Ålesund/Svalbard, *Tellus*, *49 B* (5), 486-495, 1997.
- Leighton, P.A., *Photochemistry of air pollution*, N. Y., 1961.
- Levenberg, K., A method for the solution of certain non-linear problems in least squares., *Quarterly Applied Mathematics*, *2*, 164-168, 1943.
- Lewis, A.C., NMHC measurements at Mace Head during the PARFORCE campaign, 1999.
- Lewis, A.C., J.B. McQuaid, K.D. Bartle, and S. Walton, Sub-ppt Atmospheric Measurements Using PTV-GC-FID and Real-Time Digital Signal Processing., *Journal of High Resolution Chromatography*, *21*, 181-184, 1998.
- Lewis, A.C., J.B. McQuaid, P.W. Seakins, M.J. Pilling, K.D. Bartle, and P. Ridgeon, Atmospheric Monitoring Of Volatile Organic Compounds Using Programmed Temperature Vaporisation Injection, *Journal of High Resolution Chromatography*, *19*, 686-690, 1996.
- Liss, P., G. Malin, L.J. Carpenter, and W. Broadgate, Do macroalgae influence trace gas emissions and atmospheric chemistry in coastal regions?, NERC Advanced Research Fellow, Norwich, 2000.
- Lovelock, J.E., Natural halocarbons in the air and in the sea, *Nature*, *256*, 193-197, 1975.
- Lovelock, J.E., R.J. Maggs, and R.J. Wade, Halogenated Hydrocarbons in and over the Atlantic, *Nature*, *241*, 194-196, 1973.
- Luria, M., M. Peleg, G. Sharf, D.S. Tov-Alper, N. Spitz, Y.B. Ami, Z. Gawii, B. Lifschitz, A. Yitzchaki, and I. Seter, Atmospheric sulfur over the east mediterranean region, *J. Geophys. Res.*, *101*, 25917-25930, 1996.
- Mano, S., and M. Andreae, Emissions of methyl bromide from biomass burning., *Science*, *263*, 1255-1257, 1994.
- Marquardt, D.W., An algorithm for least squares estimation of non-linear parameters., *Journal Soc. Indust. Applied Mathematics*, *11*, 431-441, 1963.
- Martinez-Harder, M., Messungen von BrO und anderen Spurenstoffen in der bodennahen Troposphäre, Dissertation thesis, Universität Heidelberg, Heidelberg, 1998.
- Martinez-Harder, M., T. Arnold, and D. Perner, The role of bromine and chlorine chemistry for the arctic ozone deletion events in Ny-Ålesund and comparison with model calculations, *Annales Geophysicae*, *17*, 941-956, 1999.
- Matveev, V., K. Hebestreit, M. Peleg, D. Rosen, D.S. Tov-Alper, J. Stutz, U. Platt, D. Blake, and M. Luria, Bromine Oxide - Ozone interaction over the Dead Sea, *Journal of Geophysical Research Letters*, *accepted*, 2001.
- McElroy, C., C. McLinden, and J. McConnel, Evidence for bromine monoxide in the free troposphere during the Arctic polar sunrise, *Nature*, *397*, 338-341, 1999.
- McElroy, M.B., R.J. Salawitch, S.C. Wofsy, and J.A. Logan, Reductions of antarctic ozone due to synergistic interactions of chlorine and bromine, *Nature*, *321*, 759-762, 1986.
- McFiggans, G., J.M.C. Plane, B. Allen, L.J. Carpenter, H. Coe, and C. O'Dowd, A modeling study of iodine chemistry in the marine boundary layer, *Journal of Geophysical Research*, *105* (D11), 14371-14385, 2000.
- Mellouki, A., R.K. Talukdar, A.-M. Schmoltner, T. Gierczak, M.J. Mills, S. Solomon, and A. Ravishankara, Atmospheric lifetimes and ozone depletion potentials of methyl bromide (CH₃Br) and dibromomethane (CH₂Br₂), *Geophysical Research Letters*, *19*, 2059-2062, 1992.
- Misra, A., and P. Marshall, Computational Investigations of Iodine Oxides, *Journal of Physical Chemistry A*, *102*, 9056-9060, 1998.
- Miyake, Y., and S. Tsnogai, Evaporation of Iodine from the ocean, *Journal of Geophysical Research*, *68*, 3989-3993, 1963.
- Molina, L.T., and M.J. Molina, Production of Cl₂O₂ from the self-reaction of the ClO radical, *J. Phys. Chem.*, *91*, 433-436, 1987.
- Molina, M.J., and F.S. Rowland, Stratospheric sink for chlorofluoromethanes: chlorine atom catalysed destruction of ozone, *Nature*, *249*, 810-812, 1974.

- Mössinger, J., D. Shallcross, and A. Cox, R., UC-VIS absorption cross-section and atmospheric lifetimes of CH_2Br_2 , CH_2I_2 and CH_2IBr , *Journal of Chemical Society Faraday Trans*, 94 (10), 1391-1396, 1998.
- Mozurkewich, M., Mechanisms for the release of halogens from sea-salt particles by free radical reactions, *Journal Geophysical Research*, 100 (D7), 14,199-14,207, 1995.
- Murayama, S., T. Nakazawa, M. Tanaka, S. Aoki, and S. Kawaguchi, Variations of tropospheric ozone concentrations over Syowa Station, Antarctica, *Tellus*, 44B, 262-272, 1992.
- Nagao, I., K. Matsumoto, and H. Tanaka, Sunrise ozone destruction found in the sub-tropical marine boundary layer, *Geophysical Research Letters*, 26, 3377-3380, 1999.
- Niemi, T.M., Z. Ben-Avraham, and J.R. Gat, The Dead Sea, The Lake and Its Setting, in *Oxford Monographs on Geology and Geophysics*, edited by H. Charnock, J.F. Dewey, S. Conway Morris, A. Navrotsky, E.R. Oxburgh, R. Price, A., and B.J. Skinner, pp. 286, Oxford University Press, Inc., New York, Oxford, 1997.
- Nishri, A., and M. Stiller, Iron, Magnesium, and Trace Elements in the Dead Sea, in *The Dead Sea, The Lake and Its Setting*, edited by T.M. Niemi, Z. Ben-Avraham, and J. R. Gat, pp. 199-204, Oxford University Press, New York, Oxford, 1997.
- Oltmans, S.J., and W.D. Komhyr, Surface ozone distributions and variations from 1973-1984 measurements at the NOAA Geophysical Monitoring for Climate Change baseline observatories, *Journal of Geophysical Research*, 91, 5229-5236, 1986.
- Oum, K.W., M.J. Lakin, and B.J. Finlayson-Pitts, Bromine activation in the troposphere by the dark reaction of O_3 with seawater ice, *Geophys. Res. Lett.*, 25 (21), 3923-3926, 1998.
- Parrish, D.D., M. Trainer, E.J. Williams, D.W. Fahey, G. Hübler, C.S. Eubank, S.C. Liu, P.C. Murphy, D.L. Albritton, and F.C. Fehsenfeld, Measurements of the $\text{NO}_x - \text{O}_3$ Photostationary State at Niwot Ridge, Colorado, *Journal of Geophysical Research* (91), 5361-5370, 1986.
- Platt, U., Differential optical absorption spectroscopy (DOAS), *Chemical Analysis Series*, 127, 1994.
- Platt, U., Reactive halogen species in the troposphere, in *ISEQS/IUAPPA Conference*, Jerusalem, 1996.
- Platt, U., Freie Radikale - die treibende Kraft der Stoffumsetzungen in der Atmosphäre, *Physikalische Blätter*, 1, 39-41, 1999a.
- Platt, U., Reactive Halogen Species in the Mid-Latitude Troposphere - Recent Discoveries, in *Environmental Challenges for the Next Millennium*, Jerusalem, Israel, 1999b.
- Platt, U., and C. Janssen, Observation and role of the free radicals NO_3 , ClO , BrO and IO in the Troposphere, *Faraday Discuss. Chem. Soc.*, 100, 175-198, 1995.
- Platt, U., and E. Lehrer, Arctic Tropospheric Ozone Chemistry (ARCTOC) - Final Report to the European Union, Heidelberg, 1997.
- Platt, U., and D. Perner, Measurements of atmospheric trace gases by long path differential UV/visible absorption spectroscopy, in *Optical and Laser Remote Sensing*, edited by D.A. Killinger, and A. Mooradian, pp. 95-105, Springer Verlag, New York, 1983.
- Platt, U., D. Perner, and H. Pätz, Simultaneous measurements of atmospheric CH_2O , O_3 and NO_2 by differential optical absorption., *Journal of Geophysical Research*, 84, 6329-6335, 1979.
- Platt, U., and J. Stutz, HALOTROP, results from field, laboratory and modelling studies, Final report of the EU-Project ENV4-CT95-0019-PL950049, Heidelberg, 1998.
- Richter, A., F. Wittrock, M. Eisinger, and J.P. Burrows, GOME observations of tropospheric BrO in northern hemispheric spring and summer, *Geophysical Research Letters*, 25, 2683-2686, 1998.
- Roedel, W., *Physik unserer Umwelt: Die Atmosphäre*, 457 pp., Springer Verlag, Berlin, 1992.
- Roehl, C.M., J.B. Burkholder, G.K. Moortgat, A.R. Ravishankara, and P.J. Crutzen, The temperature dependence of the UV absorption cross sections and the atmospheric implications of several alkyl iodides., *Journal of Geophysical Research*, 102D, 12819-12829, 1997.
- Röth, E., S. Johanning, H. London, and S. Huber-Thives, Description of a photon flux model to determine photodissociation coefficients., *Berichte des Forschungszentrums Jülich*, 1996.
- Rudich, Y., R. Talukdar, and A.R. Ravishankara, Reactive uptake of NO_3 on pure water and ionic solutions, *Journal of Geophysical Research*, D101, 21023 - 21031, 1996.
- Ruggaber, A., and R. Dlugi, Modelling radiation quantities and photolysis frequencies in the troposphere, *Journal of Atmospheric Chemistry*, 18, 171 - 210, 1994.
- Sander, R., MOCCA and MoccaIce, User Manual for Version 64, Air Chemistry Department, Max Planck Institut of Chemistry, Mainz, 2000.
- Sander, R., and J.P. Crutzen, Model study indicating halogen activation and ozone destruction in polluted air masses transported to the sea, *Journal of Geophysical Research*, 101D (9121-9138), 1996.
- Sander, R., Y. Rudich, R.v. Glasow, and P.J. Crutzen, The role of BrNO_3 in marine tropospheric chemistry: A model study, *Geophysical Research Letters*, 26 (18), 2857-2860, 1999.
- Sander, R., R. Vogt, G.W. Harris, and P.J. Crutzen, Modeling the chemistry of ozone, halogen compounds, and hydrocarbons in the Arctic troposphere during spring, *Tellus*, 49B, 522-532, 1997.

- Sauer, C.G., I. Barnes, and K.H. Becker, FT-IR Kinetic and Product Study of the Br Radical Initiated Oxidation of α,β -unsaturated Organic Carbonyl Compounds, *Atmospheric Environment*, **33**, 2969-2979, 1999.
- Savitzky, A., and M.J.E. Golay, Smoothing and Differentiation of Data by Simplified Least Squares Procedures., *Anal. Chem.*, **36** (1627-1639), 1964.
- Schall, C., and K. Heumann, GC determination of volatile organo iodine and organo bromine compounds in seawater and air samples, *Fresenius Journal of Analytic Chemistry*, **346**, 717-722, 1993.
- Schweizer, F., P. Mirabel, and C. George, Heterogeneous Chemistry of Nitryl Halides in Relation to Tropospheric Halogen Activation, *Journal of Geophysical Research*, **34**, 101-117, 1999.
- Seery, D.J., and D. Britton, The continuous absorption spectra of chlorine, bromine, bromine chloride, iodine chloride, and iodine bromide, *Journal of Physical Chemistry*, **68**, 2263-2266, 1964.
- Seisel, S., F. Caloz, F.F. Fenter, H. Van der Bergh, and M.J. Rossi, The heterogeneous reaction of NO_3 with NaCl and KBr: a nonphotolytic source of halogen atoms., *Geophysical Research Letters*, **24**, 2757-2760, 1997.
- Seisel, S., and M. Rossi, The heterogeneous Reaction of HONO and HBr on Ice and on Sulfuric Acid, *Berichte der Bunsengesellschaft der Physikalischen Chemie*, **101**, 943, 1997.
- Senne, T., Pinguinalarm, Diploma thesis, Ruprecht Karls Universität Heidelberg, Heidelberg, 1996.
- Solomon, S., R.R. Garcia, and A.R. Ravishankara, On the role of iodine in ozone depletion, *Journal of Geophysical Research*, **99**, 20491-20499, 1994.
- Solomon, S., R.R. Garcia, F.S. Rowland, and D.J. Wuebbles, On the depletion of antarctic ozone., *Nature*, **321**, 755-758, 1986.
- Spietz, P., S. Himmelmann, U. Gross, J. Bleck-Neuhaus, and J.P. Burrows, A complex approach to investigate the chemistry and kinetics of IOx using flash photolysis and time resolved absorption spectroscopy, in *15th Int. Symp. Gas Kinetics*, Bilbao, Spain, 1998.
- Stolarski, R.S., and R.J. Cicerone, Stratospheric chlorine: A possible sink for ozone, *Can. J. Chem*, **52**, 1610-1615, 1974.
- Sturges, W.T., G.F. Cotta, and P.T. Buckley, Bromoform emission from Arctic ice algae, *Nature*, **358**, 660-662, 1992.
- Stutz, J., Charakterisierung von Photodiodenzeilen zur Messung stratosphärischer Spurenstoffe, Diploma thesis, Ruprecht Karls Universität Heidelberg, Heidelberg, 1991.
- Stutz, J., Messungen der Konzentration troposphärischer Spurenstoffe mittels Differentieller-Optischer-Absorptionsspektroskopie: Eine neue Generation von Geräten und Algorithmen., Dissertation thesis, Ruprecht Karl Universität Heidelberg, Heidelberg, 1996.
- Stutz, J., Evaluation of Mace Head 1998 OIO data, 1999.
- Stutz, J., and R. Ackermann, BrO measurements at Salt Lake City, *personal communication*, 2000.
- Stutz, J., K. Hebestreit, B. Alicke, and U. Platt, Chemistry of halogen oxides in the troposphere: comparison of model calculations with recent field data, *Journal of Atmospheric Chemistry*, **34**, 65-85, 1999.
- Stutz, J., and U. Platt, Numerical analysis and estimation of the statistical error of differential optical absorption spectroscopy measurements with least-squares methods., *Applied Optics* **35**, **30**, 6041-6053, 1996.
- Stutz, J., and U. Platt, Improving long-path differential optical absorption spectroscopy with a quartz- fiber mode mixer, *Applied Optics*, **36** (6), 1105-1115, 1997.
- Sverdrup, H., M.W. Johnson, and R.H. Fleming, *The Oceans, their physics, chemistry and biology*, 1087 pp., Prentice-Hall, Englewood Cliffs, New Jersey, 1942.
- Tang, T., and J.C. McConnell, Autocatalytic release of bromine from Arctic snow pack during polar sunrise, *Geophysical Research Letters*, **23** (19), 2633-2636, 1996.
- Tellinghuisen, J., Resolution of the visible-infrared absorption spectrum of I_2 into three contributing transitions, *J. Chem. Phys.*, **58**, 2821-2832, 1973.
- Toumi, R., BrO as a sink for dimethylsulfide in the marine atmosphere, *Geophysical Research Letters*, **21**, 117-120, 1994.
- Tuckermann, M., R. Ackermann, C. Götz, H. Lorenzen-Schmidt, T. Senne, J. Stutz, B. Trost, W. Unold, and U. Platt, DOAS-Observation of Halogen Radical-catalysed Arctic Boundary Layer Ozone Destruction During the ARCTOC-Campaigns 1995 and 1996 in Ny-Ålesund, Spitsbergen, *Tellus*, **49B**, 533-555, 1997.
- Uthman, A.P., P.J. Demlein, T.D. Allston, M.C. Withiam, M.J. McClements, and G.A. Takacs, Photoabsorption spectra of gaseous methyl bromine, ethylene dibromide, nitrosyl bromine, thionyl chloride, and sulfuryl chloride, *Journal of Physical Chemistry*, **82** (20), 2252 - 2257, 1978.
- Vaida, V., and J.D. Simon, The Photoreactivity of Chlorine Dioxide, *Science*, **268**, 1443-1448, 1995.
- Vogt, R., P.J. Crutzen, and R. Sander, A mechanism for halogen release from sea-salt aerosol in the remote marine boundary layer, *Nature*, **383**, 327-330, 1996.

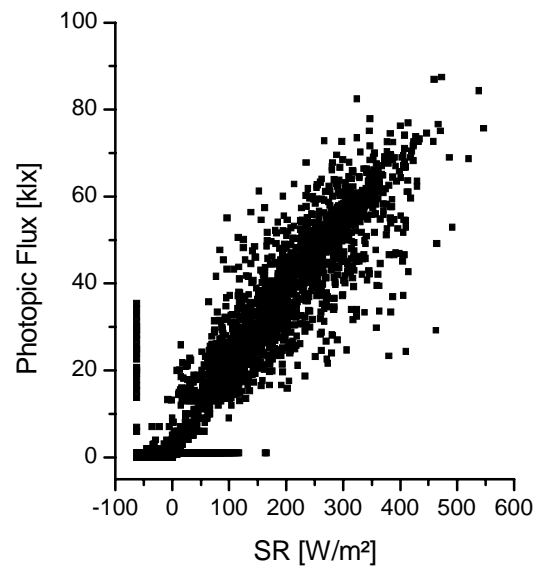
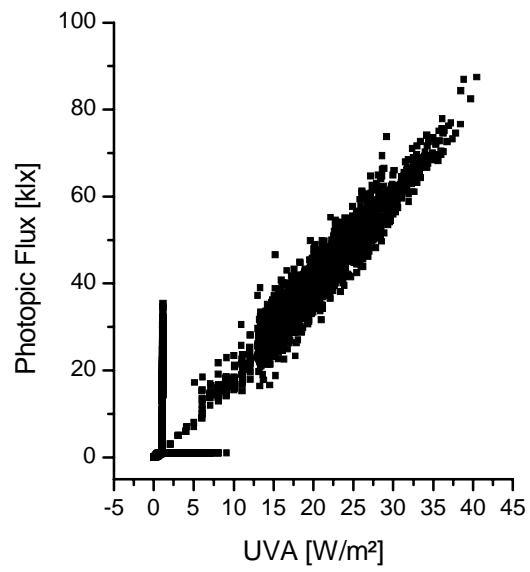
- Vogt, R., R. Sander, R.v. Glasow, and P.J. Crutzen, Iodine Chemistry and its Role in Halogen Activation and Ozone Loss in the Marine Boundary Layer: A Model Study, *Journal of Atmospheric Chemistry*, 32, 375-395, 1999.
- Volkamer, R., Absorption von Sauerstoff im Herzberg I System und Anwendungen auf Aromatenmessungen am European Photo Reactor (EUPHORE), Diploma thesis, Ruprecht Karl Universität Heidelberg, Heidelberg, 1996.
- von Glasow, R., Modelling the gas and aqueous phase chemistry of the marine boundary layer, Ph.D. thesis, University of Mainz, Mainz, 2001.
- Wagenbach, D., F. Ducroz, R. Mulvaney, L. Keck, A. Minikin, M. Legrand, J.S. Hall, and E.W. Wolff, Sea-salt aerosol in coastal Antarctic regions, *J. Geophys. Res.*, 103 (D9), 10,961-10,974, 1998.
- Wagner, T., Observations of halogen oxides from satellite, Dissertation thesis, Ruprecht Karls Universität Heidelberg, Heidelberg, 1999.
- Wagner, T., and U. Platt, Satellite mapping of enhanced BrO concentrations in the troposphere, *Nature*, 395, 486-490, 1998.
- Wahner, A., A.R. Ravishankara, S.P. Sander, and R.R. Friedl, Absorption cross section of BrO between 312 and 385 nm at 298 and 223 K, *Chemical Physics Letters*, 152 (6), 507-512, 1988.
- Warneck, P., Chemistry of the Natural Atmosphere, Academic Press, New York, 1988.
- Wayne, R.P., G. Poulet, P. Biggs, J.P. Burrows, R.A. Cox, P.J. Crutzen, G.D. Haymann, M.E. Jenkin, G.L. Bras, G.K. Moortgat, U. Platt, and R.N. Schindler, Halogen oxides: radicals, sources and reservoirs in the laboratory and in the atmosphere, *Atmospheric Environment*, 29, 2675 - 2884., 1995.
- Wennberg, P.O., Bromine Explosion, *Nature*, 397, 299-301, 1999.
- Wessel, S., S. Aoki, P. Winkler, R. Weller, A. Herber, and H. Gernandt, Tropospheric ozone depletion in polar regions - A comparison of observations in the Arctic and Antarctic, *Tellus*, 50B (1), 34-50, 1998.
- WMO, *Scientific Assessment of ozone depletion: 1998*, World Meteorological Organization (WMO), Global Ozone Observing System, Geneva, Switzerland, 1998.
- Wofsy, S.C., M.B. McElroy, and Y.L. Yung, The chemistry of atmospheric bromine, *Journal of Geophysical Research Letters*, 2, 215-218, 1975.
- Yvon, S.A., and J.H. Butler, An improved estimate of the oceanic lifetime of atmospheric CH₃Br., *Geophysical Research Letters*, 23, 53-56, 1996.
- Zak, I., Evolution of the Dead Sea Brines, in *The Dead Sea, The Lake and Its Setting*, edited by T.M. Niemi, Z. Ben-Avraham, and J.R. Gat, pp. 133-144, Oxford University Press, New York, Oxford, 1997.

Chapter 7

Appendix

A1	PF vs. SR and UVA	ii
A2	Individual Calculation of Average Values	iii
A3	Reactions of Iodine Compounds in the BL Included to the Chemical Box Model	iv
A4	Reactions of Bromine Compounds in the BL Included to the Chemical Box Model	v

(A 1) *PF vs. SR and UVA*



(A 2) Individual calculation of average values

Time A	C_A	Time B	Mid. Time B	C_B	Average C_A
00.00.00	CA1	00.00 – 00.03	00.01.30	CB1	$(CA1+CA2+CA3)/3$
00.01.00	CA2	00.05 – 00.08	00.06.30	CB2	$(CA6+CA7+CA8)/3$
00.02.00	CA3	00.08 – 00.10	00.09.00	CB3	$(CA9+CA10)/2$
00.03.00	CA4
00.04.00	CA5				
00.05.00	CA6				
00.06.00	CA7				
00.07.00	CA8				
00.08.00	CA9				
00.09.00	CA10				
00.10.00	CA11				

(A 3) Reactions of iodine compounds in the BL included to the model

Unless not noted differently rate constants are from [Atkinson *et al.*, 1997]

				k [cm ³ molecule ⁻¹ s ⁻¹]
(I 1)	I + O ₃	→	IO	9.6×10 ⁻¹³
(I 2)	I + HO ₂	→	HI + O ₂	3.6×10 ⁻¹³
(I 3)	HI + OH	→	I + H ₂ O	3.0×10 ⁻¹¹
(I 4)	HOI + OH	→	IO + H ₂ O	2.0×10 ⁻¹³
(I 5)	IO + NO	→	I + NO ₂	2.4×10 ⁻¹¹
(I 6)	I + NO ₃	→	IO + NO ₂	4.5×10 ⁻¹⁰
(I 7)	IO + NO ₂ + M	→	IONO ₂	3.7×10 ⁻¹²
(I 8)	IONO ₂	→	IO + NO ₂	3.2×10 ⁻² s ⁻¹ a
(I 9)	IO + HO ₂	→	HOI + O ₂	8.4×10 ⁻¹¹
(I 10a)	IO + IO	→	I + I + O ₂	1.4×10 ⁻¹¹ b
(I 10b)	IO + IO	→	I + OIO	4.1×10 ⁻¹¹ b
(I 10c)	IO + IO	→	I ₂ O ₂	4.1×10 ⁻¹¹ b
(I 11)	I + NO + M	→	INO	4.1×10 ⁻¹³
(I 12)	INO	→	I + NO	1.4×10 ⁻⁰¹ s ⁻¹ c
(I 13)	INO + INO	→	I + I + NO + NO	7.4×10 ⁻¹⁵
(I 14)	I + NO ₂ + M	→	INO ₂	5.4×10 ⁻¹²
(I 15)	INO ₂	→	I + NO ₂	2.3 s ⁻¹ b
(I 16)	INO ₂ + INO ₂	→	I + I + NO ₂ + NO ₂	2.7×10 ⁻¹⁵
(I 17a)	IO + CH ₃ O ₂	→	I + HCHO + HO ₂	2.5×10 ⁻¹² d
(I 17b)	IO + CH ₃ O ₂	→	HOI + CO + H ₂ O	7.5×10 ⁻¹² d
(I 18)	IO + hv	→	I + O ₃	1.03×10 ⁻¹ s ⁻¹ e
(I 19)	I ₂ O ₂ + hv	→	IO + IO	2.23×10 ⁻³ s ⁻¹ f
(I 20)	IONO ₂ + hv	→	I + NO ₃	1.52×10 ⁻³ s ⁻¹ g
(I 21)	HOI + hv	→	OH + I	4.50×10 ⁻³ s ⁻¹ h
(I 22)	OIO + hv	→	O ₃ + IO	1.03×10 ⁻¹ s ⁻¹ i
(I 23)	INO ₂ + hv	→	I + NO ₂	3.48×10 ⁻⁴ s ⁻¹ j
(I 24)	INO + hv	→	I + NO	1.89×10 ⁻³ s ⁻¹ k

^a [Barnes *et al.*, 1991]

^b [Bloss *et al.*, 1998] ^c [DeMore *et al.*, 1997]

^d estimated based on the BrO + CH₃O₂ reaction [Aranda *et al.*, 1997]

^e [Harwood *et al.*, 1997] ^f 9 × photolysis rate of Cl₂O₂ [Davis *et al.*, 1996]

^g estimated from red-shifting BrONO₂ absorption cross-section by 50 nm ^h [Bauer *et al.*, 1998a] ⁱ assumed equal to J(IO)

^j estimated from red-shifted ClONO absorption cross-section by 100 nm ^k [Forte *et al.*, 1981]

**(A 4) Reactions of Bromine Compounds in the BL
Included in the Chemical Box Model**

Unless not noted differently rate constants are from [Atkinson et al., 1997].

				k [cm ³ molecule ⁻¹ s ⁻¹]
(B 1)	Br + O ₃	→	BrO + O ₂	1.4 × 10 ⁻¹²
(B 2)	BrO + BrO	→	Br + Br + O ₂	2.2 × 10 ⁻¹²
(B 3)	BrO + BrO	→	Br ₂ + O ₂	3.3 × 10 ⁻¹³
(B 4)	Br + HCHO	→	HBr + CO + HO ₂	1.4 × 10 ⁻¹²
(B 5)	Br + CH ₃ CHO + O ₂	→	HBr + CH ₃ COOO	4.2 × 10 ⁻¹²
(B 6)	Br + CH ₃ O ₂	→	HBr + CO + H ₂ O	2.5 × 10 ⁻¹⁴
(B 7)	BrO + CH ₃ O ₂	→	Br + HCHO + HO ₂	5.7 × 10 ⁻¹²
(B 8)	BrO + NO	→	Br + NO ₂	2 × 10 ⁻¹¹
(B 9)	BrO + NO ₂ + M	→	BrONO ₂	2.4 × 10 ⁻¹²
(B 10)	Br + NO ₂ + M	→	BrNO ₂	4.1 × 10 ⁻¹²
(B 11)	BrO + HO ₂	→	HOBr + O ₂	3 × 10 ⁻¹¹
(B 12)	Br + HO ₂	→	HBr + O ₂	2.2 × 10 ⁻¹²
(B 13)	HBr + OH	→	Br + H ₂ O	1.1 × 10 ⁻¹³
(B 14)	BrO + OH	→	Br + HO ₂	7.5 × 10 ⁻¹¹
(B 15)	Br + NO	→	BrNO	3.0 × 10 ⁻¹¹
(B 16)	Br + NO ₃	→	BrO + NO ₂	1.6 × 10 ⁻¹¹
(B 17)	BrO + NO	→	Br + NO ₂	2 × 10 ⁻¹¹
(B 18)	BrO + hv + O ₂	→	Br + O ₃	1.2 × 10 ⁻¹ s ^{-1a}
(B 19)	Br ₂ + hv	→	Br + Br	1.1 × 10 ⁻¹ s ^{-1a}
(B 20)	BrONO ₂ + hv	→	Br + NO ₃	3.1 × 10 ⁻³ s ^{-1a}
(B 21)	HOBr + hv	→	OH + Br	2.6 × 10 ⁻³ s ^{-1a}
(B 22)	BrNO ₂ + hv	→	Br + NO ₂	7.4 × 10 ⁻⁴ s ^{-1b}
(B 23)	BrNO + hv	→	Br + NO	1.6 × 10 ⁻³ s ^{-1c}

^a [DeMore et al., 1997]

^b estimated from red-shifted ClONO absorption cross-section by 50 nm

^c [Uthman et al., 1978]

Danksagung

Zunächst möchte ich mich bei meinem Doktorvater Prof. Dr. Ulrich Platt bedanken, der die Durchführung dieser Arbeit ermöglicht hat. Immer wieder hat er es verstanden, Freiräume in der Organisation und Durchführung meiner Kampagnen und Projekte zu gewähren und dennoch die nötigen Anstöße zu geben, falls es mal nicht so laufen sollte.

Bei Prof. Dr. Frank Arnold möchte ich mich für die Mühen und die Geduld bei der Übernahme des Co-Referates bedanken.

Herzlicher Dank sei auch an Prof. Dr. Jochen Stutz gerichtet, der mich nicht nur abschnittsweise auf meinem Weg durch die Promotion, sondern auch auf eine Messkampagne begleitet hat. Danke Jochen, für die Tipps und e-mails zu mitternächtlichen Stunden.

Ein weiterer herzlicher Dank gebührt Björn und Gerd, mit denen ich jeweils einen Mace Head Aufenthalt erleben durfte. Ohne fliegende Mäuse, Sprinter und Surf Boards und natürlich die unentbehrlichen Beilegscheiben und Kässpätzle wären die Kampagnen sicher nur halb so erfolgreich und das Guinness sicherlich nur halb so lecker gewesen.

Zum Gelingen der Kampagnen haben zu großen Teilen die jeweiligen local heros beigetragen, so dass es nun an der Zeit ist vorerst ins Englische zu wechseln.

First I would like to thank Gerry Spain, not only for boating and diving at Mace Head – ‘actually in fact’ to stress macroalgae – but also for providing O₃ data and everything else which was required to promote a successful field campaign. Many thanks go out to Mick Geever, who was for me the kind spirit of Mace Head. From the first visit on he gave me a hand wherever he could.

Furthermore, I would like to thank Wends for picking Ecki and me up at our first *HALOTROP* meeting at Edinburgh and for introducing me to the field of scientific conferences, meetings and the social events related thereto. Good luck in Sweden and thanks for all.

Thanks as well to Bev, Sal, Luce, Ally, Wends, Gill, Mathew, Lee, Leonie, Eva, Sebastien, Frithjof, Bill, Collin and all the others of the Mace Head Crew of 97 & 98 for sharing a number of interesting results and last but not least a lot of wonderful days at the western coast of Ireland. Thank you Mary and Harry for the remarkable accommodation of MH98.

In connection with a number of important data related to this thesis I would like to thank Luce for measuring HHC, Christoph from Galway and Andrew from Birmingham, and Mathew and Ally for organising and calculating trajectories of the Mace Head campaigns. Finally thanks to the modellers and biologists Nic (thanx for the discussions about perambulators at Nice and anywhere else, you still owe me a dirty talk...), Gordon (my Honda is still not running well), Roland and Frithjof for helpful discussions about halogen chemistry and stressed macroalgae, and Klaus for all these fruitful conversations about IO, OIO and, öiö, guess I will miss it in a real job in the real life!

To survive the change from the Green Island to the desert-like conditions at the Dead Sea it was important to find kind and committed colleges at the southern end of Europe as well. That's why I want to thank Mordechai, Menachem, Valeri, David and Lelach for taking care of me during my campaign at Israel and for organising everything from accommodation to the measurements down in the Dead Sea Valley.

Besides the campaigns related to my thesis the work in the tropospheric research group gave me the chance to take part in a number of research projects with lots of friendly colleagues from Heidelberg and other Institutes. This gives me the chance to switch back to German.

Auch wenn vieles, womit ich auf Kampagnen gelockt wurde, im Vorfeld so etwas wie Urlaub versprach, war es doch meist harte Arbeit (Freiklettergefühle auf D2 und Strommasten bei Pabstthum, Cappuccino und Tennis in Mailand, Schneesturm am Schneesfernerhaus, etc.). Dennoch möchte ich allen danken, die mich für diese schwierigen Unterfangen verpflichtet haben, vielen Dank also Birgit, Ralf, Andi, Björn, Gerd, Richi und nochmals Herrn Platt, der uns immer wieder ins Feld schickt und uns allen diese Forschungsabenteuer ermöglicht hat.

Im ‚Laden‘ selber gibt es natürlich auch viele gute Geister, die mir die Arbeitszeit versüßt und bei vielen Problemen zur Seite gestanden haben. Hier ist besonders Gerd zu nennen, der bei so vielen Fragen immer die richtige Adresse war und auch trotz eigener Hektik immer für einen Tipp gut

war. Vielen Dank auch nochmals für das Korrekturlesen meiner Arbeit und die Geduld die du, auch dabei, aufgebracht hast. Ich bin schon gespannt auf ‚Neue Erkenntnisse zur Halogenchemie‘, [Hönniger 2001].

Besonders in der Endphase der Arbeit hatten neben denen, die sich meinem Werk auch schon „im frühkindlichem Stadium“ zu nähern wagten (Danke Juliane, Gerd, Sebastian, Andi, Hartmut und Björn), auch meine (Zimmer-) Kollegen Ralf, Hans, Simon und die Gäste Jutta und Nicole unter meiner Zusammenschreibphase zu leiden. Danke, dass ihr mich in dieser Verfassung ertragen und mir hin und wieder Trost und Nahrung gespendet habt. Auch den Olivers (F und S) und Hansi sei gedankt für ihre permanente Soft- und Hardware- Problem-Sprechstunde, und Tom, nicht nur für offene Diskussionen auf langen Autobahnfahrten.

Großes Lob verdienen auch die Damen der Verwaltung und des Sekretariats, die dort neben ihren Job auch mit den Marotten der Wissenschaftler zu kämpfen haben und diese zu ertragen wissen.

Zum Glück wird das Institut sehr durch seine Vielseitigkeit geprägt. Auch wenn der Kontakt zu den Glazis im Laufe der Zeit immer mehr einschief, fand ich doch bei Dietmar immer ein offenes Ohr, danke für die Tipps auf und neben der Piste, fahr weiter so!

Neben den Kollegen sind nun natürlich all die Freunde und Bekannten (gell Chris, wie du zum Beispiel!) zu nennen, mit denen ich einige meiner Zeit im Geschäft verbringe durfte. Diskussionen mit Ecki, Uwele, der Hex und Herrn Fischer waren sowohl im Laden als auch bei den leider seltener gewordenen DoKo-Abenden mit dem Mäusle eine Wonne.

Dem Heidelberger Pack, ehemals auch als Bacardi Front verschrien (Dank an Ingeborg für diese Namensgebung, keiner von uns trinkt das Zeug...) sei herzlichst dafür gedankt, dass es existiert und immer da ist, wenn man es braucht! Es ist einfach großes Glück solche Freunde zu haben, die einem auch die eine oder andere Macke verzeihen. Jutta möchte ich noch für die viele Zeit danken, die sie mir Hannah vom Rechner fern gehalten und damit mich zum Arbeiten getrieben hat. Toll, dass unsere 3 Kurzen sich so super verstehen.

Da bin ich nun endlich bei meiner kleinen Familie angelangt, ohne deren hundertprozentige Unterstützung eine solche Arbeit meiner Meinung nach nicht zu schaffen ist. Hannahs Lächeln entschädigt in Augenblicken für die geraubten Schlafstunden und ohne Katis Einsatz hätte diese Arbeit nie ihre jetzige Form erreicht. Danke für den Einsatz all deiner Energie, besonders in den letzten Monaten vor der Abgabe, aber auch für das Verständnis, das du mir in all den Jahren in Heidelberg immer wieder entgegengebracht hast.

Abschließend möchte ich Anni für ihren unglaublichen Einsatz und Willen danken, das Englisch dieser Arbeit in eine für sie verträgliche Form zu bringen. Ihr Engagement für uns war und ist wunderbar. Die richtigen Worte für Wolli, Siggie, Frauke und Pit zu finden fällt mir sehr schwer. Euch sei für die jahrelange Unterstützung aus der Ferne, euer Verständnis für meinen Weg und die Hilfe gedankt, die ich in all den Jahren von euch bekommen habe. Danke, dass ihr für mich da wart, wenn ich euch brauchte, so wünsche ich mir eine Familie.